# Experimental investigation of the deep mantle melting properties

Giacomo Lo Nigro

**N° d'ordre : D. U. 2137**

**Université Blaise Pascal-Clermont-Ferrand II**
(U.F.R. Science et Technologies)

ECOLE DOCTORALE DES SCIENCES FONDAMENTALES
N° 678

**THESE**

Présentée pour obtenir le grade de
**DOCTEUR D'UNIVERSITE**

*Spécialité : Pétrologie expérimentale*

Présenté par

Giacomo LO NIGRO

Diplômé d'Etudes Approfondies

# Experimental investigation of the deep mantle melting properties

Soutenue publiquement le 24 06 2011, devant la commission d'examen composée de :

| | | |
|---|---|---|
| Isabelle Daniel | Professor, UCB, Lyon 1 | Rapporteur |
| Sébastien Merkel | Professor, UMET, Lille | Rapporteur |
| Anne-Line Auzende | Maître de Conférence, IMPMC, Paris | Examiner |
| Tahar Hammouda | Maître de Conférence, LMV, Clermont-Ferrand | Examiner |
| Hervé Martin | Professor, LMV, Clermont-Ferrand | Examiner |
| Denis Andrault | Professor, LMV, Clermont-Ferrand | Thesis Adviser |

**N° d'ordre : D. U. 2137**

**Université Blaise Pascal-Clermont-Ferrand II**
(U.F.R. Science et Technologies)

ECOLE DOCTORALE DES SCIENCES FONDAMENTALES
N° 678

**THESE**

Présentée pour obtenir le grade de
**DOCTEUR D'UNIVERSITE**

*Spécialité : Pétrologie expérimentale*

Présenté par

Giacomo LO NIGRO

Diplômé d'Etudes Approfondies

# Etude expérimentale des propriétés de fusion du manteau inférieur

Soutenue publiquement le 24 06 2011, devant la commission d'examen composée de :

| | | |
|---|---|---|
| Isabelle Daniel | Professeur, UCB, Lyon 1 | Rapporteur |
| Sébastien Merkel | Professeur, UMET, Lille | Rapporteur |
| Anne-Line Auzende | Maître de Conférence, IMPMC, Paris | Examinateur |
| Tahar Hammouda | Maître de Conférence, LMV, Clermont-Ferrand | Examinateur |
| Hervé Martin | Professeur, LMV, Clermont-Ferrand | Examinateur |
| Denis Andrault | Professeur, LMV, Clermont-Ferrand | Directeur de Thèse |

# Remerciements

Tout d'abord je tiens à remercier mon directeur de thèse Denis Andrault, qui m'a initié à la pétrologie expérimentale (je ne connaissais pas grand-chose…) et pour son apport fondamental pendant les manipes au Synchrotron. Je le remercie aussi pour le rapport amical pendant ces trois ans et demi.

Je remercie les créateurs du programme c2c (projet Marie Curie) pour l'énorme possibilité de travail.

Je tiens aussi à remercier le jury d'avoir accepté de juger mon travail : les rapporteurs Isabelle Daniel et Sébastien Merkel, et les examinateurs Anne-Line Auzende, Tahar Hammouda et Hervé Martin.

Je remercie aussi Nathalie (la seule avec qui je pouvais parles en italien…au moins jusqu'à l'arrivée de Lucia), Ali et Ken, (et oui ça une équipe très internationale) et tous les autre membres petro-X pour leur aide direct au indirect).

Je remercie Sylvain Petitgirard et Armando Solé pour les discussions sur la fluorescence aux rayons-X.

Je remercie, Jean-Luc (mister microsonde), Jean-Marc (ou Jean-MEB), Mohamed et tous les autres techniciens du labo.

Merci à mon prof. de master M. Merli qui m'a donné les contacts pour commencer cette aventure.

Et maintenant les remerciements rigolos…pour tous les pots qui étaient, qui sont et…bref je commence par ces qui sont plus au labo comme Ben, Beto, Carolina, Daniel, Géraldine, Guillaume, Marion, Sarah pour continuer avec Anaïs (et oui la France et toujours en grève), Célia (la copine de voyages -congres), T. Giachetti, K. Martelli et Y. Sonzogni (mais ils sont partout ces italiens ?!), Ahmed (on serat jamais d'accord sur l'équipe à supporter), Hanika (enfin quelqu'un d'autre de vraiment latin), Aude, Fanny, Noël, Oscar, Yannick, pour finir avec les premiers années Asmaa, Amélie, Batiste, Gareth, Gabrielle….Et encore Nico (l'ultras), Lydie, David, Greg, Anne-Sophie….

Grazie à Seb L. (un frère d'Italie), Mathieu (c'est bien la pause café…) et qui encore ….ah ah oui, comment oublier mes pots de bureau Julia et Seb V. (ça manquera, peut être, votre bla-bla mais j'ai toujours gardé mon self-control en restant zen). Je veux ajouter quelque mot pour mes co-bureaux, que « malgré tout » ont été des copains des voyages super et qui ont tolérés le chaos sur mon bureau (moi je bosse, eheheh). Je vous attends tous sous le soleil de Sicile.

Per finire una piccola dedica in italiano per i miei amici di Palermo (che non sto qua ad elencare, grazie a tutti) e soprattutto alla mia famiglia che anche se a una distanza notevole mi ha sempre sostenuto durante questo lungo periodo.

# Experimental investigation of the deep mantle melting properties

During the final stage of accretion, terrestrial planets experienced violent and highly energetic giant impacts. As a consequence of impact heating, the early Earth was partially or wholly molten, forming a magma ocean in the outer layer of Earth. Subsequent cooling of the magma ocean has led to fractional crystallization of the primitive mantle. Many unknowns remain about accretion of the early Earth, such as extension depth and life time of the magma ocean(s), role of mantle recrystallization on the chemical segregation between the different Earth reservoirs, and so on. The knowledge of melting properties of the deep mantle is also important to investigate the possibility of partial melting at the present time.

The aim of this study was to tackle a few major questions concerning the Earth lower mantle: What is the melting sequence between the main lower mantle phases? Can we explain the ultra-low-velocity zones (ULVZ) by partial melting of pyrolitic (or chondritic) mantle? How does iron partition between liquid and solid silicate phases in the deep mantle? Can we provide new information on the properties of the deep magma ocean based on the melting curve of the primitive mantle?

Melting curves and melting relations have been investigated using the laser-heated diamond anvil cell (LH-DAC) for pressure between 25 and 135 GPa and temperature up more than 4000 K, i.e. at P-T conditions corresponding to the entire Earth's lower mantle. Compositions investigated were the join between MgO and $MgSiO_3$ and a model chondritic-composition for the Earth mantle. Two different *in situ* synchrotron radiation techniques have been used to infer melting properties at high pressures; X-ray diffraction and X-ray fluorescence spectroscopy.

The new results obtained in this study include:

a) *Eutectic melting curve in the MgO-$MgSiO_3$ join*; for this simplified model-composition, the eutectic melting temperature is found to be 4830 ±150 K at 135 GPa. It plots at ~700 K higher than the solidus for a chondritic type mantle composition (see below).

b) *Liquidus and solidus melting curves for a chondritic mantle composition*; at 135 GPa, solidus and liquidus temperatures were measured at 4150±150 K and 4725±150 K, respectively. Our measurements also confirmed that $MgSiO_3$-perovskite is the liquidus phase in the deep lower mantle. When the solidus melting curve is compared with the different temperature profiles available for the lower mantle and the D" region, it suggests that partial melting in the lower mantle is unlikely, except in the D"-layer if the core is very hot and/or for a mantle material containing a high concentration of incompatible elements (i.e. Na, K, H or $CO_2$), in order to decrease the melting point compared to that of the mean mantle. Concerning properties of the Early Earth, our results suggest that complete melting of the Earth's mantle is incompatible with a reasonable surface temperature. Thus, it is unlikely that the mantle has experienced complete melting after the Earth has been accreted completely.

c) *Calcium and iron partition coefficients between liquid and solid mantle*; this work provides maps of elemental (Ca and Fe) and phase fractions for sample of chondritic-type compositions that have been partially molten in the LH-DAC at the lower mantle P-T conditions. The Fe partitioning coefficients extracted from the maps show a large preference of Fe for the liquid phase. This behavior could be compatible with the production of dense liquids when the lower mantle encounters partial melting, which can be related to sinking down of liquid phases.

*Keywords: partial melting, lower mantle melting curves, properties of the magma ocean, phase relations, high-pressure experiments in LH-DAC, partition coefficients, iron.*

# Etude expérimentale des propriétés de fusion du manteau inferieur

Au cours de la dernière phase d'accrétion, les planètes terrestres ont connus des impacts géants violents et très énergétiques. A la suite du chauffage causé par les impacts, la Terre primitive était partiellement ou totalement fondue, et un océan magmatique a été formé dans la couche externe de la Terre. Le refroidissement successif de l'océan magmatique a causé la cristallisation fractionnée du manteau primitif. Cependant, ils restent beaucoup d'incertitudes à propos de l'accrétion de la Terre primitive, comme la profondeur et la durée de vie d'un (ou plusieurs) océan(s) magmatique(s), l'effet de la recristallisation du manteau sur la ségrégation chimique entre les différents réservoirs de la Terre et ainsi de suite. La connaissance des propriétés de fusion du manteau profond est important aussi pour examiner la possibilité d'une fusion partielle actuellement.

L'objectif était d'aborder quelque problème concernant le manteau inferieur terrestre: Quelle est la séquence de fusion entre les phases dominantes dans le manteau inferieur? Est-ce qu'on peut expliquer la zone à ultra-basse vélocité (ULVZ) avec la fusion partielle d'un manteau pyrolytique (ou chondritique)? Quel est le partage du fer entre les phases silicatées liquides et solides dans le manteau profond? Est-ce qu'on peut donner des informations nouvelles sur les propriétés d'un océan magmatique profond à partir des courbes de fusion du manteau primitif?

Dans cette étude les courbes de fusion et les relations de fusion ont été analysés en utilisant la cellule à enclume de diamant chauffé au laser (LH-DAC) pour des pressions entre 25 et 135 GPa et des températures jusqu'à plus que 4000 K, i.e. pour des conditions de P-T qui correspondent au manteau inferieur terrestre entier. Les compositions utilisées ont été le raccord entre MgO and $MgSiO_3$ et une composition de type chondritique pour le manteau terrestre. J'ai utilisé deux techniques in-situ de radiation-synchrotron pour déduire les propriétés de fusion à hautes pressions; la diffractométrie au rayons-X et la fluorescence au rayons-X.

Les nouveaux résultats obtenus dans cette étude sont :

a) *La courbe de fusion eutectique pour le system MgO-$MgSiO_3$ ;* pour ce type de model simplifié, on a trouvé une température de fusion eutectique à 4830 ±150 K et 135 GPa. Elle est à ~700 K au dessus du solidus pour une composition du manteau chondritique (voir ci-dessous).

b) *Les courbes de fusion de liquidus et solidus pour une composition du manteau chondritique;* Les températures de solidus et liquidus mesurées à 135 GPa, sont respectivement 4150 ±150 K et 4725 ±150 K. Ces mesures ont confirmé que la $MgSiO_3$-perovskite est la phase liquide dans le manteau inferieur. Donc, on a mis en comparaison ces résultats avec les profiles de températures disponibles pour le manteau inferieur et la région-D", et on en conclue que la fusion partielle dans le manteau inferieur est improbable, sauf dans la région-D" si le noyau est très chaud et/ou pour un matériel mantellique avec une concentration élevée des éléments incompatibles (i.e. Na, K, H ou $CO_2$) qui baissent le point de fusion comparé à celui du manteau moyen. Pour ce qui concerne les propriétés de la Terre initiale, ces résultats suggèrent qu'une fusion complète du manteau terrestre est incompatible avec les températures superficielles attendues. Donc, est vraiment improbable que le manteau ait subie une fusion complète une fois que la Terre a terminé son accrétion.

*c) Les coefficients de partage pour le calcium et le fer entre le manteau liquide et solide ;* cette étude donne les cartographies des fractions pour les éléments (Ca et Fe) et pour les phases, dans le cas d'un matériel chondritique qui a été partiellement fondue dans une LH-DAC pour les conditions de P-T du manteau inferieur. Les coefficients de partage obtenues à partir de ces cartographies, montrent que le fer préfère la phase liquide. Ce comportement pourrait être compatible avec la production des liquides denses quand le manteau subie une fusion partielle, et ça peut être corrélé avec une préférence des phases liquides à plonger.

*Mots-clés : fusion partielle, courbes de fusion dans le manteau inferieur, propriétés de l'océan magmatique, relations des phases, expériences de hautes pressions, coefficients de partage, fer.*

# Contents

# Preface

## Context: Earth's lower mantle

The Earth's lower mantle is the region of the planet at depth between 670 km (transition zone) and ~2900 km (outer core). This portion of the Earth presents extreme conditions of pressure and temperature, i.e. 25<P<135 GPa and ~2000<T<~3800 K. The main problem for the investigation of the deep mantle is its inaccessibility by direct observation, since we have no rock samples from this region.

Three major methods are at present used for the understanding of this inaccessible layer: 1) computational interpretation of seismic data; 2) study of isotopic data (i.e. Sm/Nd and Hf/W; Boyet and Carlson, 2005) in comparison with primitive meteorites; 3) experiments at high pressure like this work. Then, understanding of Earth's deep mantle is straightly linked to the improvement of experimental techniques based on high pressure observations, such as in situ diamond anvil cell experiments.

The lower mantle is mainly composed by three phases, for both pyrolite or chondrite model: Al-bearing $(Mg,Fe)SiO_3$ and $CaSiO_3$ perovskites and (Mg,Fe)O ferropericlase, resulting from transformation of majorite garnet and olivine at high pressure (P>25GPa). Obtaining new constrains on the properties of these primary constituents of lower mantle is fundamental to our understanding of the dynamics of this deep terrestrial region.

Two more heterogeneities are present in the lowermost mantle: the ultra-low velocity zone (ULVZ) and the D" region at the core-mantle boundary. In particular, the presence of ULVZ has been interpreted as the result of partial melting (Williams and Garnero, 1998).

## Scientific issue

Partial melting has been an important factor during terrestrial accretion and differentiation and it still remains extremely important for the mantle evolution, because it induces segregation of incompatible elements and could be responsible for the most of the mantle heterogeneities.

Phase relations have been largely studied using the multi-anvil press (MAP) apparatus up to ~35 GPa (Ito and Takahashi, 1987; Zhang and Herzberg, 1994; Presnall et al., 1998; Litasov and Ohtani, 2002; Ito et al., 2004; Liebske et al., 2005).

At higher pressures, experimental studies have been performed using the DAC up to ~65 GPa (Zerr and Boehler, 1998; Boehler, 2000). However, no more information is available for pressure above 65 GPa, except for shock wave experimental data at ~130 GPa (Holland and Ahrens, 1997; Luo et al., 2004) or ab initio calculations (Stixrude and Karki, 2005).

More recently, using the LH-DAC Fiquet et al. (2010) determined melting curve for peridotite composition.

My PhD thesis is focused on the investigation of melting properties of constituents of the lower mantle and determination of the partitioning coefficients of iron between liquid and solid in this deep region of the planet. Geophysical implications for early to present day Earth mantle are also discussed. During my study, in situ experiments have been carried out in LH-DAC using X-ray diffraction and X-ray fluorescence techniques for $Mg_2SiO_4$ and Cl-chondrite starting materials, in the interval of pressure and temperature typical of lower mantle ($25<P<135$ GPa and more than 4000 K).

## Plan of the manuscript

This manuscript is made up of five chapters briefly described below:

1) The first chapter is an introduction that presents both preliminary works and current knowledges on early melting and crystallization of the Earth. It details why it is important to study composition and thermal structure of the terrestrial planet, in order to better constrain and understand the early Earth's differentiation. Previous determinations of partition coefficients between minerals and liquids, and density inversions are also discussed.
2) The second one gives a description of experimental and analytical techniques used during my thesis. In particular a detailed description of X-ray diffraction (XRD) and X-ray fluorescence (XRF) techniques using laser-heated diamond anvil cell is made, in order to explain how I carried out my experiments. Moreover, I extensively describe the different methods to calibrate and quantify XRF data.
3) The chapter three presents the eutectic melting curve determined for the $MgO$-$MgSiO_3$ system. This eutectic curve, compared with previous works, has been found in agreement at lower pressures. At the same time, is reported the melting curve of platinum which extends our knowledges on this metal melting up to ~100 GPa.
4) The fourth chapter presents results of recent study on solidus and liquidus profiles of chondritic mantle at very high pressures and temperatures. In this chapter, we present a discussion on thermal structure and melting in D" region. We show also our observations about formation and extension of magma oceans across Earth history. This chapter corresponds to a paper already published (Andrault et al., 2011).

5) The chapter five describes a new is-situ method consisting on the use of coupled XRD and XRF at the ERSF (Grenoble), to determine iron partitioning coefficients between liquid and solid phases. Moreover, it presents major implications on compositional and thermal properties of deep mantle, and especially on floatability of silicate liquids at the same extreme conditions. Buoyancy of liquids and density crossovers are of primary importance for the comprehension of dynamics in the Earth lower mantle. This chapter will be submitted for publication in a close future.

# Chapter 1: introduction

## 1.1 The structure of the Earth's mantle

The interior structure of the Earth, similar to the outer, is layered. These layers can be defined by either their chemical or their rheological properties. Recording of both compressional and shear waves (P- and S-waves respectively) generated by earthquakes or large explosions, as well as oscillations of the entire planet caused by large earthquakes, make it possible to derive the elastic-wave velocities and density as a function of depth.

Primary waves (P-waves) are pressure waves that are the initial set of waves produced by an earthquake. Their speed ($V_P$) is function of $\rho$, $K_S$ and $\mu$:

$$V_P = \sqrt{\frac{K_S + \frac{4}{3}\mu}{\rho}} \tag{1.1}$$

where $\rho$, $K_S$ and $\mu$ are density, bulk modulus and shear modulus, respectively.

Secondary waves (S-waves) tipically fellow P-waves during an earthquake and deplace the ground to the direction of propagation. The speed of S-waves depends on $\rho$ and $\mu$:

$$V_S = \sqrt{\frac{\mu}{\rho}} \tag{1.2}$$

Since propagation speed of wave depends on material properties, discontinuities of earth's mantle are evidenced when phase transitions of minerals phases occur at specific pressures and depths.

Moreover, S-wave cannot travel through liquids and molten materials when the shear modulus ($\mu$) is zero or weak (Fig. 1.1).

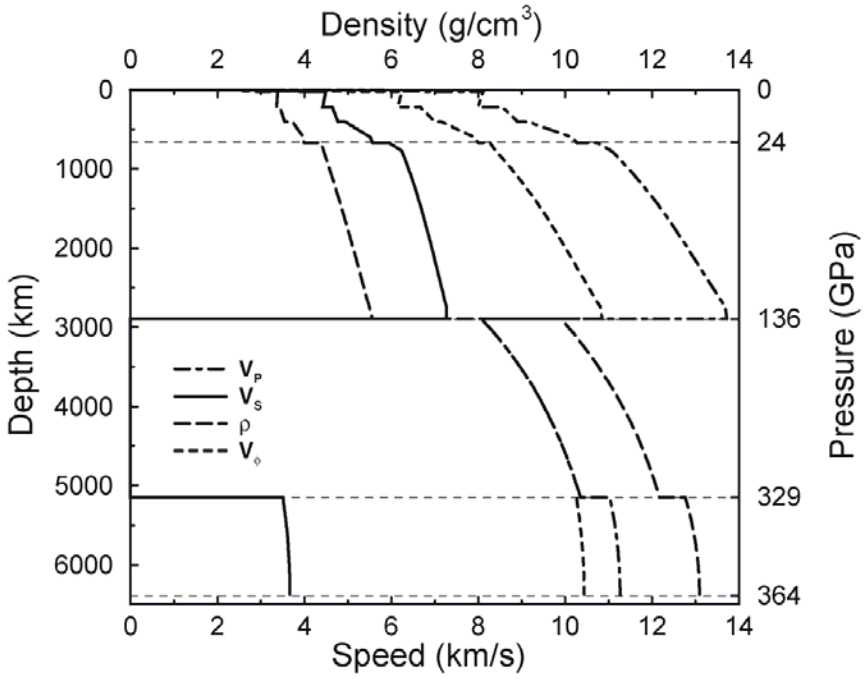


**Figure 1.1** Profiles for Earth's properties: density, $\rho$; speed waves $P$, $V_P$; speed waves $S$, $V_S$; and $V\phi$ ($V\phi = \sqrt{V_P^2 - 4/3V_S^2}$). Reproduced from PREM model (Dziewonski and Anderson, 1981).

The mantle is the ~2850 km thick shell of rock surrounding the metallic core of the Earth. Because it contains the bulk of the planet's rocky material, the mantle is the ultimate source of the silicate magmas that cause volcanic eruptions, even though the mantle itself is predominantly crystalline, not molten.

In particular, the top of the mantle is identified by the depth at which the velocity of compressional waves jumps discontinuously from values typically less than 7 km/s to greater than 8 km/s (the Mohorovicic discontinuity). The base of the mantle, at a depth of 2890 km, is defined by the disappearance of rigidity. Unlike the mantle, the outer core is liquid; also, it is far denser than the overlying rock. Indeed, the core-mantle boundary is the most significant discontinuity of the Earth in that the contrast in observed properties is even greater than that between the atmosphere and crust.

Two smaller but still significant discontinuities in seismic-wave velocities define the primary subdivision of the mantle, transition zone, and lower mantle (Fig. 1.2). These velocity jumps appear to be globally present at about 410- and 650-km depths, although the exact depths can vary by a few tens of kilometers from one location to another.

At a more subtle level, there are at least three additional structures that are pervasive, and are considered important: the low-velocity zone (ULV), in the upper mantle, the D" region at the base of the mantle (Bullen, 1942; Kellogg et al., 1999; Merkel et al., 2007) and the ultra low velocity zone (ULVZ) (Williams and Garnero, 1996; Stutzmann et al., 2000) at the core-mantle boundary (CMB). Tomographic inversions of seismic data yield maps of seismic-wave speed heterogeneity throughout the mantle, with a resolution greater then 1000 km (Fig. 1.3). These regions, which are explained by partial melting (Revenaugh and Sipkin, 1994; Revenaugh and Mayer, 1997; Lay et al., 2004; Labrosse et al., 2007; Mosenfelder et al., 2009; Hernlund and Jellinek, 2010), have not been detected to be laterally continuous and have a thickness ranging from a few kilometers up to about 50 km (e.g. Thorne and Garnero, 2004; Garnero and McNamara, 2008).

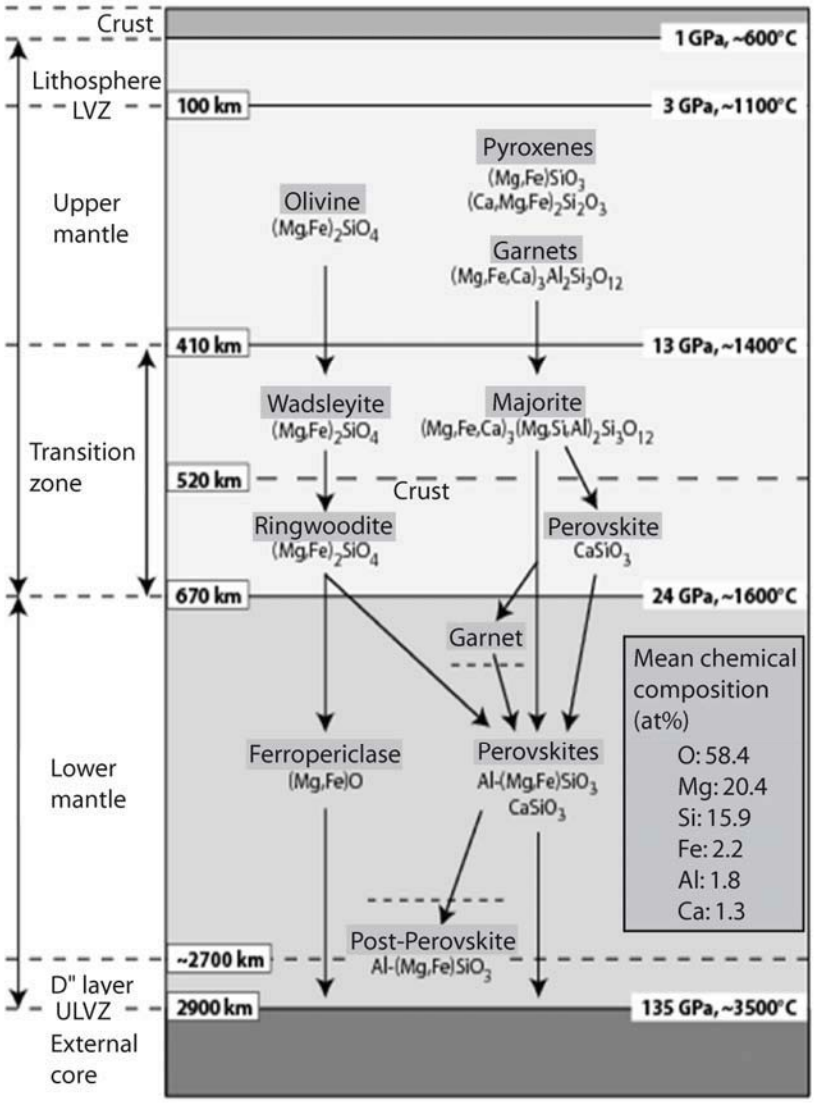


**Figure 1.2** Earth's mantle mineralogy for a pyrolitic composition (Andrault, personal communication).

Briefly, several mechanisms have been proposed for the origin of ULVZs: a) partial melting of the mantle, which is the most probable scenario (Williams and Garnero, 1996); b) core-mantle reactions (Knittle and Jeanloz, 1991); c) lateral infiltration of core material in the CMB (Kanda

and Stevenson, 2006); d) subduction and segregation of late Archean banded-iron formations (Dobson and Brodholt, 2005); e) upward compaction of sediments crystallizing from the outer core (Buffett et al., 2000); f) highly Fe-enriched forms of PPv (Mao et al., 2006); g) and more recently, iron rich (Mg,Fe)O as a robust candidate for a compositionally distinct ULVZ (Wicks et al., 2010; Bower et al., 2011).

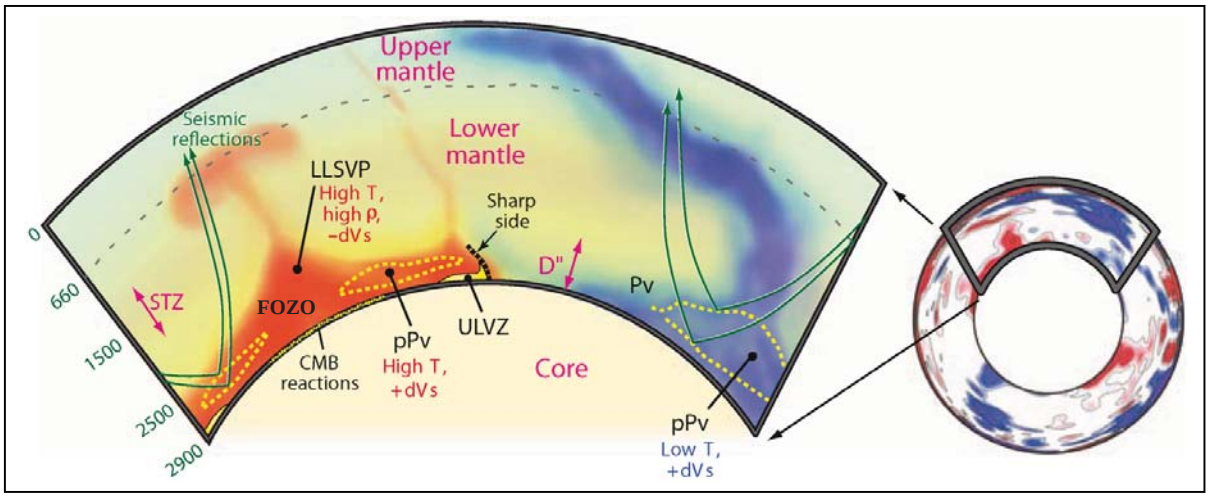


**Figure 1.3** Tomographically high and low seismic shear velocity variations in Earth's mantle (blue and red, respectively) are shown in an equatorial cross section (right) viewed from the south, along with an enlarged panel (left) depicting several seismic findings in the D" region. LLSVP is a large low-shear-velocity province found beneath the Pacific Ocean and Africa. ULVZ is the ultralow-velocity zone in the CMB and can be swept around in lateral currents. STZ is the spin transition zone at ~1500 km depth and represents a change in the spin state of $Fe^{2+}$ to $Fe^{3+}$. Reproduced from Garnero and McNamara (2008).

## 1.2 Early Earth differentiation

The first 860 My of the Earth's lifetime are generally referred to as the "Hadean" (4.6-3.8 billion years ago), a stage during which the Earth underwent major episodes of differentiation. During this time, the metallic core separated from the silicate mantle, and the silicate mantle may have developed much of its internal characteristics.

The final stages of terrestrial planetary accretion involved violent and tremendously energetic giant impacts among core-segregated Mercury to Mars sized objects and planetary embryos (Fig. 1.4) (Canup, 2008; Wetherill, 1990). As a consequence of impact heating, the early Earth was at times partially or wholly molten (Fig. 1.5 and 1.6), increasing the likelihood for high pressure and high temperature equilibration among core and mantle forming materials (Walter and Trønnes, 2004). During its accretion period, Earth would have periodically had an extensively molten outer layer (a magma ocean) of variable thickness. In summary, the Earth accreted over a period of at least $10^7$ years from smaller bodies, most of which had already segregated metallic cores.

High velocity impacts of planetesimals into the growing Earth have been considered to occur during accretion, which results in degassing of volatiles contained in the Earth forming planetesimals (as a consequence of rocks melting). The result was a ($H_2O$-$CO_2$)-rich atmosphere surrounding the accreting Earth. This steam atmosphere formation from vaporization of rocks (Nagahara and Ozawa, 1996), for temperature above 1700-1800 K, prevents rapid cooling of a magma ocean (Abe and Matsui, 1988; Zahnle et al., 1988). Such rock vapor atmosphere conducts heat easily so that the magma ocean would cool down in a few thousand years (~20 ky), as reported by Karki and Stixrude (2010), before the magma ocean surface temperature comes back to 1700-1800 K (Sleep et al., 2001).

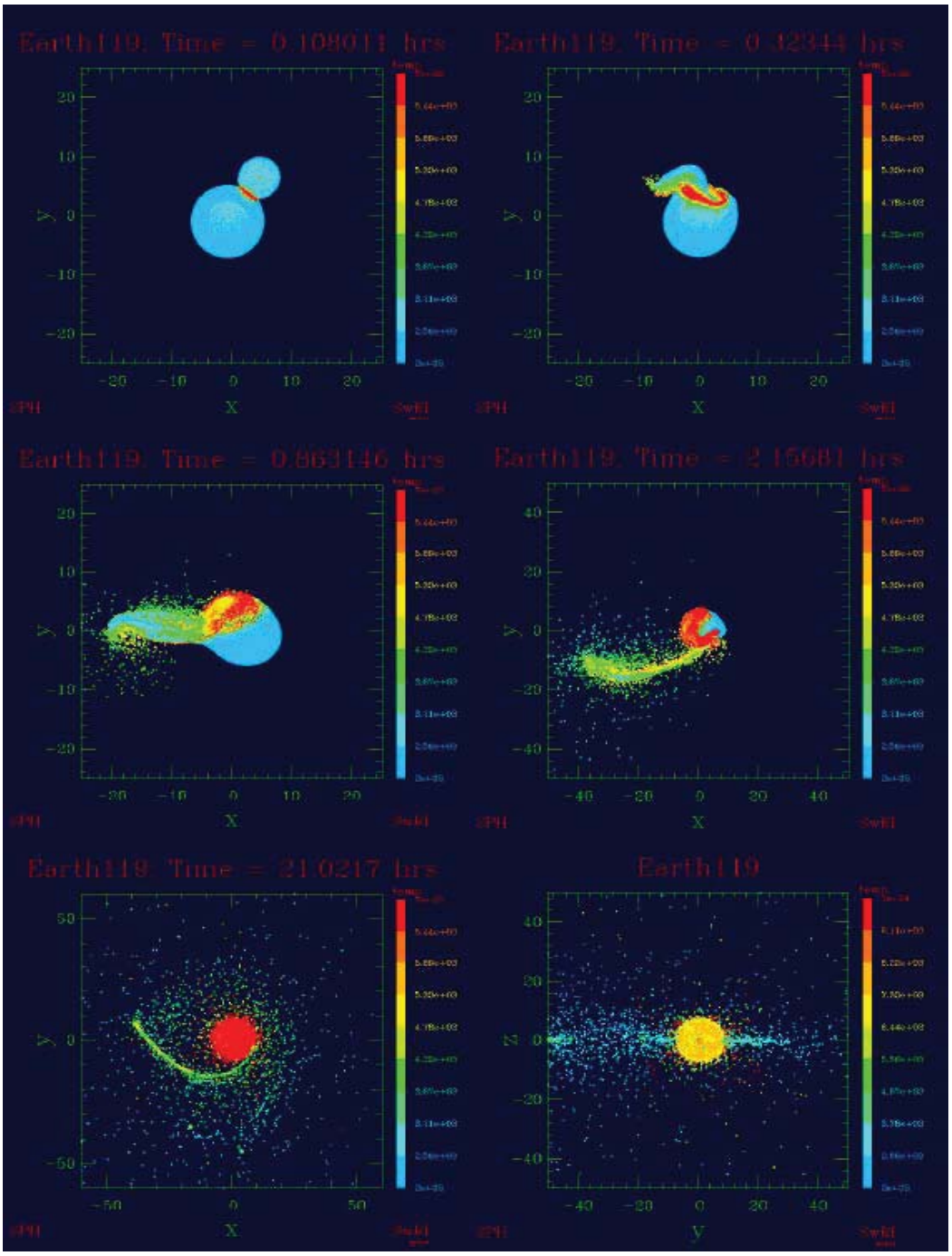


**Figure 1.4** The leading current theory, about Moon formation, is that a huge ball of rock about the size of Mars struck Earth a glancing blow. The impact melted both planets, and a huge plume of molten rock spewed off and began orbiting the single remaining planet. Gradually this splash of rock condensed to form the Moon (From Canup, 2004).

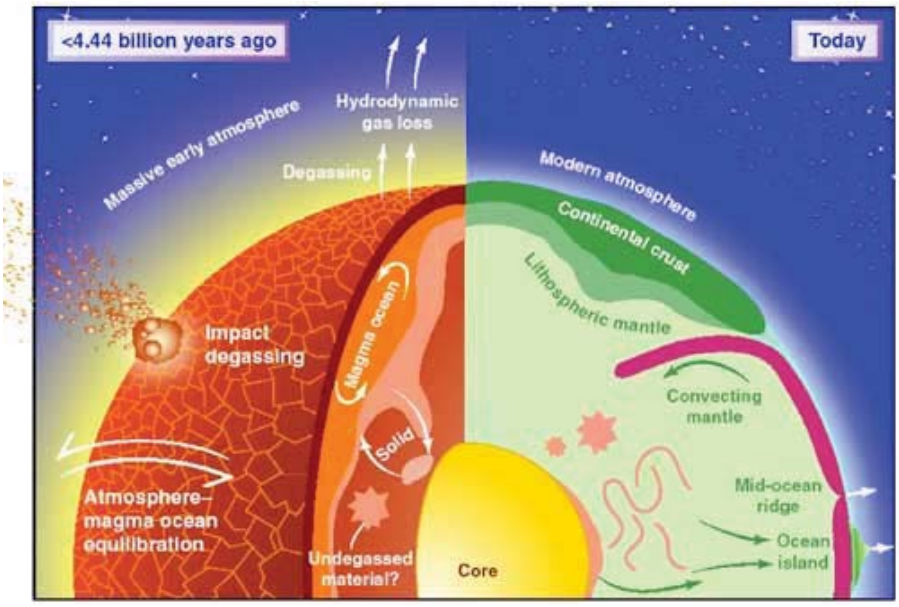


**Figure 1.5** Cutaway view of Earth in the Hadean and today (from Ballantine, 2002). During accretion, large bodies are efficiently degassed on impact (left), yet noble gas measurements suggest that reservoirs within Earth's mantle remain volatile-rich today (right).
In this sketch is shown an overview of the Earth's accretion, differentiation and fractionation causes (i.e. giant impacts, steam atmosphere, magma ocean formation, and convection).

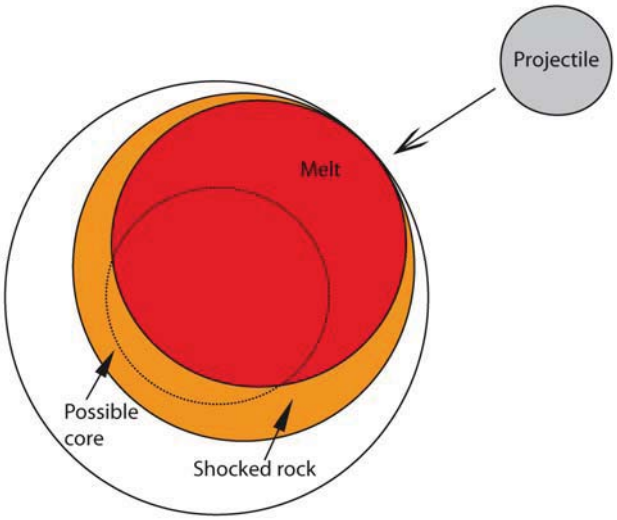


**Figure 1.6** Schematic illustration of the pattern of heat deposition in a planet struck by a projectile of comparable size (between Mars and the young Earth sizes). Adjacent to a melted region roughly twice the projectile's diameter, the shock level, and thus temperature, falls off steeply with increasing distance from the impact site. From Melosh (1990) modified.

### 1.2.1 Core formation

Many meteorites are samples from the asteroid belt between Mars and Jupiter, and are probably a remnant of the early days of accretion. The occurrence of distinct populations of iron and achondritic silicate meteorites attests to early differentiation in planetesimals that were subsequently destroyed during collisions (Taylor and Norman, 1990). Parent/daughter fractionation of short and long lived radionuclides during core formation generates isotopic signals that constrain the timing of accretion and core formation in terrestrial objects. In particular, tungsten isotopes ($^{182}$Hf-$^{182}$W, Kleine et al., 2002) confirm early core formation and place strict time limits on the timing of segregation of metal from silicate (Yin et al., 2002). Thanks to this method, it has been estimated that core formation in the terrestrial planets and the formation of the Moon must have occurred during first ~30 million years of the life of the Solar System (Kleine et al., 2002).

Radiogenic isotope tracers are often used to understand the chemical evolution of planetary bodies. The $^{182}$Hf–$^{182}$W systematics of meteoritic and planetary samples provide firm constraints on the chronology of the accretion and earliest evolution of asteroids and terrestrial planets and lead to the following succession and duration of events in the earliest solar system.

The strong fractionation of lithophile Hf from siderophile W during core formation makes the Hf–W system an ideal chronometer for this major differentiation event. However, for larger planets such as the terrestrial planets the calculated Hf–W ages are particularly sensitive to the occurrence of large impacts, the degree to which impactor cores re-equilibrated with the target mantle during large collisions, and changes in the metal-silicate partition coefficients of W due to changing $f_{O2}$ in differentiating planetary bodies. Hafnium–tungsten chronometry also provides

constraints on the duration of magma ocean solidification in terrestrial planets (Kleine et al., 2002).

In an other system, Sm decays to Nd via two radioactive decay schemes: $^{146}$Sm-$^{142}$Nd and $^{147}$Sm-$^{143}$Nd. Both Sm and Nd are refractory lithophile (prefer silicates over metal) elements, whose relative abundances should not be affected by either volatile loss or core formation. $^{147}$Sm-$^{143}$Nd system has been widely used to trace planetary-scale processes such as the evolution of the bulk silicate Earth (BSE, defined as all the Earth except for its metallic core) and its chemical differentiation into crust and mantle over Earth's history. The early epic of Earth's differentiation is better investigated with the short-lived chronometer $^{146}$Sm-$^{142}$Nd (Boyet and Carlson, 2005).

Growth of the Earth from planetary embryos and planetesimals resulted in the substantial partitioning of siderophile elements into the metallic core, leaving lithophile elements in the silicate mantle. Primitive mantle is estimated from analyses of mantle peridotites (McDonough and Sun, 1995; Allegre et al., 1995), bulk Earth from the compositions of undifferentiated protoplanetary material, represented by the Cl carbonaceous chondrite meteorites (chondritic reference model) and the core is obtained by calculating the difference (Wood et al., 2006).

## 1.3 Differentiation of Earth's mantle and floatability of silicate melts

Except for the first 50-100 million years of the Earth's history (during this period most of the mantle was molten), the differentiation of Earth's silicate mantle has been controlled by solid-state convection (Abe, 1997; Lee et al., 2010). As the mantle upwells and decompresses across its solidus, it partially melts. These low-density melts rise to the surface and form the continental and oceanic crust, driving the differentiation of the silicate part of the Earth. Because many trace elements, such as U, Th and K (heat-producers) and noble gases, preferentially partition into melts, when melt separates and forms crust, it concentrates these incompatible elements into the crust or atmosphere in the case of noble gases. Then, nearly half of the Earth's amount of these elements now is concentrated into the crust.

In contrast, the upper mantle is depleted in incompatible elements. For this reason, it is inferred that the other half of these incompatible elements resides in the Earth's interior. The most accredited hypothesis is that this reservoir represents primordial material never processed by melting or degassing. Lee et al. (2010) suggest that during the Earth's first billion years a whole-mantle convection (van der Hilst et al., 1997) occurred, resulting in the production of dense liquids that crystallized and sank into lower mantle. These sunken phases would present primordial chemical signatures.

Alternatively to the primordial layer, Fe-rich layers formed by sinking of Hadean magma ocean liquids or by subduction of oceanic crust have been proposed (Christensen and Hofmann, 1994; Abe, 1997; Boyet and Carlson, 2005; Stixrude et al., 2009).

The behavior of liquids tends to change depending on high-pressure conditions and iron content. For example, peridotite partial melts at 9-23 GPa (270-660 km) are suggested to be denser than

solid peridotite, because such liquids are Fe-rich and more compressible than solids (Herzberg et al., 1996; Miller et al., 1991; Stolper et al, 1981; Suzuki et al., 1998).

In order to determine the floatability of liquid silicate, the knowledge of Fe partitioning coefficient between liquid and solid phases is primordial (Lange and Carmichael, 1987; Ohtani and Maeda, 2001).

At pressures lower than 10 GPa (<300 km) and higher than 14 GPa (>410 km), liquids are less dense than the Preliminary Reference Earth Model (PREM) (Dziewonski and Anderson, 1981) and hence rise (Fig. 1.7). However, in the range of pressure 10-14 GPa, partial melts of peridotite are denser than PREM. This means that melts generated within the transition zone, buoyant in this region, are denser than PREM in the interval 10-14 GPa. For pressures higher than 22 GPa and the upper part of the lower mantle, the melts tend to sink down because its Fe-content preferentially partition into ferropericlase (Lee et al., 2010).

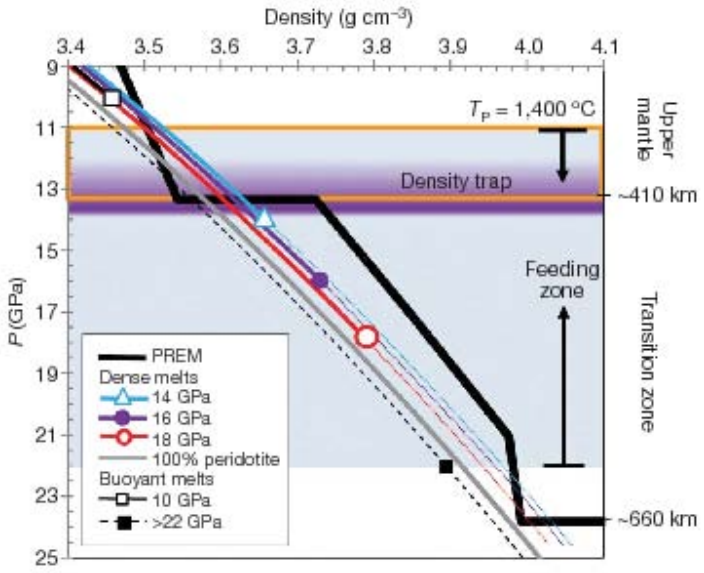


**Figure 1.7** Density crossovers for silicate melts (Lee et al., 2010). Densities of 10, 14, 16 and 18 GPa are from Herzberg and Zhang, 1996 and Ohtani and Maeda, 2001; density of 22 GPa is from Trønnes and Frost, 2002.

Not much additional information is available for the lower mantle, except the proposition by Lee et al. (2010) that Fe-rich rock should sink into the lower mantle, eventually forming a Fe-rich layer (FOcus ZOne or FOZO) at the core-mantle boundary.

Recent works on diamond anvil cell (Nomura et al., 2011) and shock wave experiments (Mosenfelder et al., 2009) confirm this hypothesis (Fig. 1.8). In Figure 1.8, density for ferropericlase (Ricolleau et al., 2009), Ca-Perovskite (Komabayashi et al., 2010) and PREM (Dziewonski andAnderson, 1981) are also shown for comparison. In particular, Ricolleau et al. (2009), calculate densities of KLB-1 peridotite up to 112 GPa and T=2000 K; Komabayashi et al. (2010) calculate calculate densities for $Mg_{0.86}O_{0.14}$ and T=1600-1900 K; Nomura et al. (2011) determine densities for (Mg, Fe)$SiO_3$ liquid and ($Mg_{0.92}Fe_{0.08}$) $SiO_3$ perovskite up to 140 GPa and T=4000 K.

These studies (Mosenfelder et al., 2009; Nomura et al., 2011) show density crossovers at very high pressures typical of deep mantle. As shown in Fig. 1.8, it is evident that melts become denser than surroundings minerals at P>76 GPa (Melt (No-11)) and P>130 GPa (grey and red Melt (Mo-09)) depending strictly on Fe partitioning. Recent works on first principles molecular dynamics (FPMD) simulations (Wan et al., 2007; Stixrude et al., 2009) agree with this suggestion and propose a pressure above 120 GPa and T>4000 K to obtain liquid denser than solid, with possible enormous implications on deep lower mantle properties.

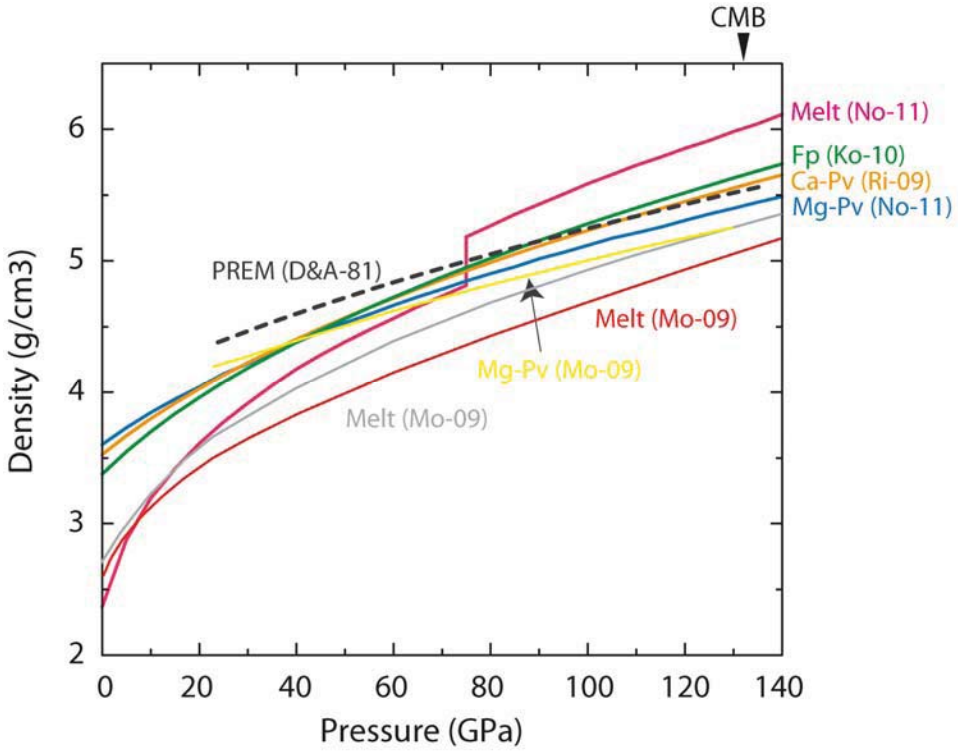


**Figure 1.8** Density of silicate melts and phases calculated with Birch-Murnaghan EoS. Density of (Mg,Fe)$SiO_3$ liquid (Melt (No-11); Nomura et al., 2011) coexisting with $(Mg_{0.92}Fe_{0.08})SiO_3$ perovskite (Mg-Pv (No-11); Nomura et al., 2011) is calculated at 4000 K. Are also shown those for: $(Mg_{0.86}Fe_{0.14})O$ ferropericlase (Fp (Ko-10); Komabayashi et al., 2010); Ca-perovskite (Ca-Pv (Ri-09); Ricolleau et al., 2009). And for comparison: $MgSiO_3$ perovskite (Mg-Pv (Mo-09); Mosenfelder et al., 2009); liquid densities along $MgSiO_3$ and $Mg_2SiO_4$ liquidus (red and grey Melt (Mo-09), respectively; Mosenfelder et al., 2009); and PREM (PREM (D&A-81); Dziewonski and Anderson, 1981).

These conclusions have major consequences for the dynamics of mantle upwellings and therefore hot spots (Williams and Garnero, 1998) and plume characteristics (Kumagai, 2008). Indeed, it is well known that plume or superplume interactions with phase transition generate a thick thermal boundary (Brunet and Yuen, 2000).

In Figure 1.10 (Arndt, 2000) are different model of plumes. In model A, a plume that raises from the boundary between lower and upper mantle forms a head after it reaches the lithosphere (White and McKenzie, 1989). In model B, a plume grows a large, and cooler, head as it ascends from a source at the CMB (Campbell and Griffiths, 1990). In model C, in which a plume stalls at the boundary between the lower mantle and the upper mantle and gives rise to smaller "plumelets" (Thompson and Tackley, 1998; Brunet and Yuen, 2000).

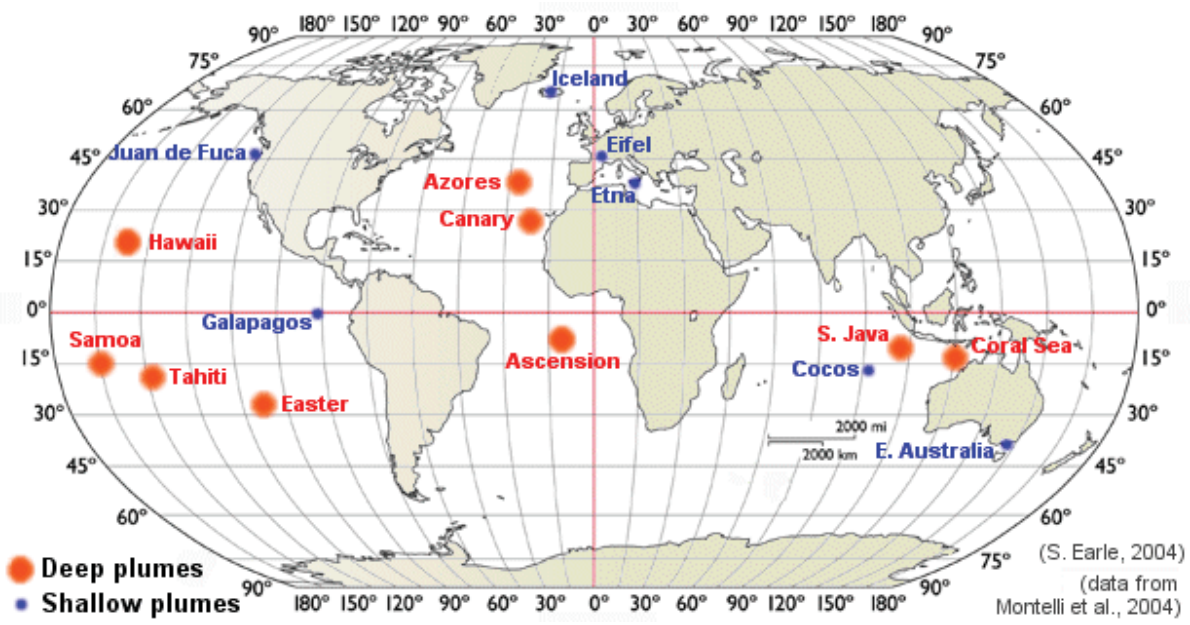


**Figure 1.9** Mantle plume world map

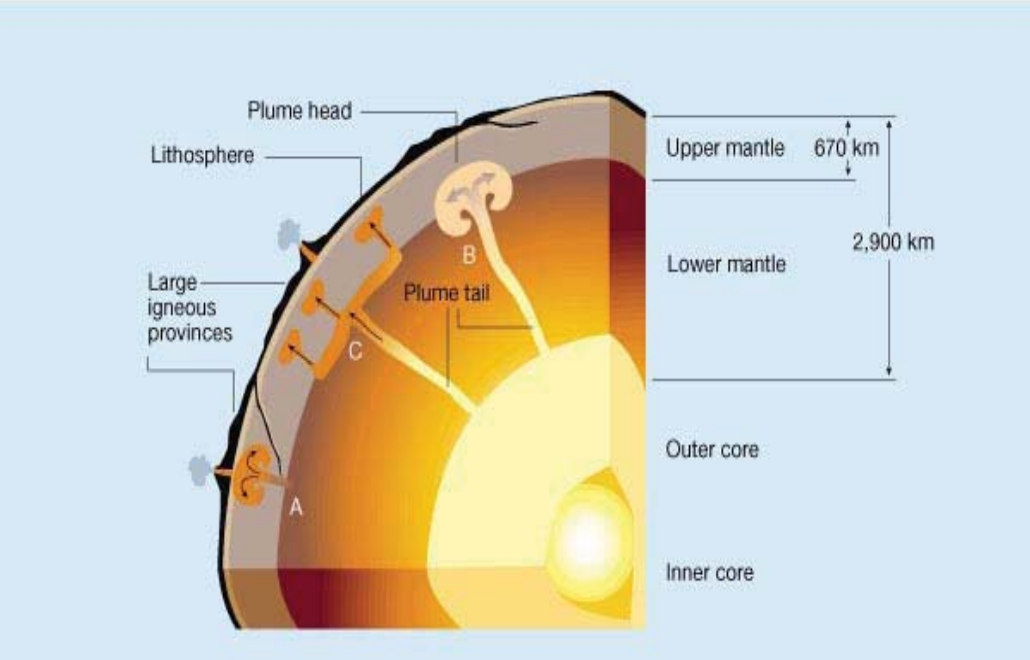


**Figure 1.10** Different models for mantle plumes, Arndt (2000).

## 1.4 The composition of the Earth

Establishing the composition of the silicate Earth (or primitive mantle) is critical to understanding of the composition of the Earth. The determination of the chemical composition of the Earth depends on three main sources of information:

1. The seismic profile of the Earth and its interpretation (see paragraph 1.1);
2. Comparisons between primitive meteorites (i.e. chondrites) and the solar nebula composition;
3. Chemical and petrological models of peridotite-basalt partial melting (i.e. the pyrolite model).

Elements can be classified in lithophiles, siderophiles, chalcophiles and atmophile (see Table 1.1). The two major divisions of the Earth are the metallic and silicate portions, the core and the mantle (including the crust), respectively.

The silicate portion of the Earth is subdivided into the crust, upper mantle, transition zone and lower mantle, with each region separated by a seismic discontinuity and having a distinct seismic velocity gradient. Present mantle is ~99% of the Earth silicate portion. The core, or metallic Earth, is subdivided into an outer liquid shell and inner solid region that is dominantly composed of a mixture of Fe and Ni, which is assumed to be in chondritic proportions (Fe/Ni ≈17).

| | |
|---|---|
| ***Lithophile elements* (*rock/oxygen*-loving):** | |
| Refractory | Be, Al, Ca, Sc, Ti, V, Sr, Y, Zr, Nb, Ba, REE, Hf, Ta, Th, U |
| Transitional | Mg, Si, Cr |
| Moderately volatile | Li, B, Na, K, Mn, Rb, Cs |
| Highly volatile | F, Cl, Br, I, Zn |
| ***Siderophile elements* (*iron*-loving):** | |
| Refractory | Mo, Ru, Rh, W, Re, Os, Ir, Pt |
| Transitional | Fe, Co, Ni, Pd |
| Moderately volatile | P, Cu, Ga, Ge, As, Ag, Sb, Au |
| Highly volatile | Tl, Bi |
| ***Chalcophile elements* (*sulphur*-loving):** | |
| Highly volatile | S, Se, Cd, In, Sn, Te, Hg, Pb |
| ***Atmophile elements* (*gas*-loving):** | |
| Highly volatile | H, He, C, N, O, Ne, Ar, Kr, Xe |

**Table 1.1** Classification of the elements as a function of their preferred host phases and volatile attitude.

For the upper mantle has been proposed the pyrolite model (Ringwood, 1962). Pyrolite is a theoretical rock consisting of about three parts peridotite and one part basalt, which correspond to PYRoxenes and OLivine (PYROLite). This rock yields to basaltic magmas by partial melting.

For a pyrolitic model, the upper mantle is composed of $(Mg,Fe)_2SiO_4$ olivine, pyroxenes $(Ca,Mg,Fe)(Mg,Fe,Al)(Si,Al)_2O_6$ and garnets $(Ca,Mg,Fe)_3(Mg,Fe,Al)_2(Si,Al)_3O_{12}$ (see Fig. 1.2).

The transition zone, at 410 km and 13 GPa, is attributed to the phase transition of olivine to its high pressure polymorph wadsleyite (e.g. Katsura and Ito, 1989; Morishima et al., 1994). Wadsleyite transforms within the transition zone at ~520 km to another $(Mg,Fe)_2SiO_4$ polymorph ringwoodite (e.g. Katsura and Ito, 1989).

Regarding to the lower mantle, the composition is assumed to be similar to that of the upper mantle. For pressures higher than 17-18 GPa, $CaSiO_3$ perovskite forms from majoritic garnet (Canil, 1994). These phases transform to a mixture of $MgSiO_3$ perovskite (76%), (Mg,Fe)O magnesiowüstite (17%) and $CaSiO_3$ perovskite (7%) in the lower mantle (Wood, 2000). In

particular, the transition of ringwoodite to magnesian perovskite is considered to cause the seismic discontinuity at 670 km (Ito and Takahashi, 1989).

A second class of models can be referred to as the CI chondrite type, where the Earth is assumed to have a bulk "major-element" composition equal to that of CI chondrites (McDonough and Sun, 1995). CI carbonaceous chondrites, the most primitive of the chondritic meteorites, possess the highest abundances of the moderately-volatile and volatile elements relative to the refractory elements, and have a composition that closely matches that of the solar photosphere. A CI chondritic model is a good starting point from a historical perspective (see Table 4.1 for composition in this study). Earth mantle, compared with CI carbonaceous chondrites, is depleted in Mg and Si relative to the refractory lithophile elements.

In the table 1.2 are shown different compositions for pyrolitic and chondritic models.

| | Pyrolitic models | | | Chondritic model | CI | |
|---|---|---|---|---|---|---|
| | 1 | 2 | 3 | 4 | 5 | 6 |
| $SiO_2$ | 45.00 | 45.16 | 45.00 | 48.34 | 49.60 | 49.90 |
| $TiO_2$ | 0.201 | 0.217 | 0.17 | 0.15 | 0.00 | 0.16 |
| $Al_2O_3$ | 4.45 | 3.97 | 4.40 | 4.30 | 3.40 | 3.65 |
| $Cr_2O_3$ | 0.384 | 0.46 | 0.45 | 0.63 | 0.00 | 0.44 |
| MnO | 0.135 | 0.13 | 0.11 | 0.16 | 0.00 | 0.13 |
| FeO | 8.05 | 7.82 | 7.60 | 3.44 | 8.48 | 8.00 |
| NiO | 0.25 | 0.27 | 0.26 | 0.11 | 0.00 | 0.25 |
| MgO | 37.80 | 38.30 | 38.80 | 40.00 | 35.10 | 35.15 |
| CaO | 3.55 | 3.50 | 3.40 | 2.49 | 3.30 | 2.90 |
| $Na_2O$ | 0.36 | 0.33 | 0.40 | 0.38 | 0.00 | 0.34 |
| $K_2O$ | 0.029 | 0.031 | 0.003 | 0.02 | 0.00 | 0.022 |

**Table 1.2** Different compositions (Wt%) for the mantle. 1) McDonough and Sun (1995); 2) Jagoutz et al. (1979); 3) Green et al. (1979); 4) Allègre et al. (2001); 5) Andrault et al. (2011); 6) Taylor and McLennan (1985).

In this study (chapter 4-5) we chose a chondritic material in order to model the primitive mantle after core segregation.

## 1.5 Magma ocean hypothesis

Current understanding of the last stages of planetary accretion suggests that mass and energy accumulation are dominated by a few large impacts (i.e. the giant collision of a Mars-sized impactor with proto-Earth, which caused the formation of the Moon). An important thermal consequence of such impacts is melting and the formation of a large melt pond, which upon isostatic readjustment would spread like a blanket over the surface, forming a deep magma ocean (Hayashi et al., 1979; Melosh, 1990; Tonks and Melosh, 1993; Canup, 2008). The extent and depth of the magma ocean (see chapter 4) depend on many factors including the impactor/target mass ratio, impact velocity and initial temperatures of the objects.

Experimental melting studies show that crystallization in the deep mantle (>~700 km) would be dominated by Mg-Perovskite, with minor amounts of Ca-Perovskite and ferropericlase, whereas crystallization at shallower levels would be dominated by olivine and its high-pressure polymorphs, majorite garnet, and lesser amounts of pyroxenes (Ito et al., 2004; Trønnes and Frost, 2002; Zhang and Herzberg, 1994; Andrault et al., 2011).

Magma ocean solidification process is sensitive to many factors, including surface temperature, cooling rate, crystal nucleation and growth rates and melt crystal-mush viscosities (Ito et al., 2004; Solamotov and Stevenson, 1993).

Anyway, the conventional view is that differentiation of a magma ocean occurs by fractionation of perovskite at the bottom of the ocean (Miller et al., 1991; Liebske et al., 2005; Solomatov, 2000). Opposed to this scenario, Mosenfelder et al. (2009) assert that cooling of a deep magma ocean could result in crystallization from the top down (or near the top, at pressures corresponding to the modern-day transition zone).

## 1.6 The magma ocean models

### 1.6.1 Tonks and Melosh, 1990

In this work the term magma ocean refers to a global magma layer of approximately uniform depth formed by giant impacts on the Earth with thermal effects on the terrestrial planet, including vaporization and melting. Because impacts between the proto-Earth and bodies with masses larger than Mercury may occur several times during late accretion (Wetherill, 1990), multiple magma ocean formation episodes may have taken place.

In this model, the melt generated from the impact can form a magma ocean in one of two ways.

a. The shock wave produced by the giant impact generates a large, intact volume of melt (Fig. 1.12a). Some of this melt is excavated in the cratering flow; the remainder stays behind. They refer to this as the "retained melt". If sufficiently thick, the excavated melt could spread out to approximately uniform depth on the surface after emplacement. Additionally, the resulting crater and the retained melt body are not isostatically stable.
b. Consequently, the retained melt may be extruded onto the surface by isostatic adjustment of the planet (Fig. 1.12b). A magma ocean formed by this process occurs only if the isostatic adjustment time scale of the planet is short compared to the magma cooling time.

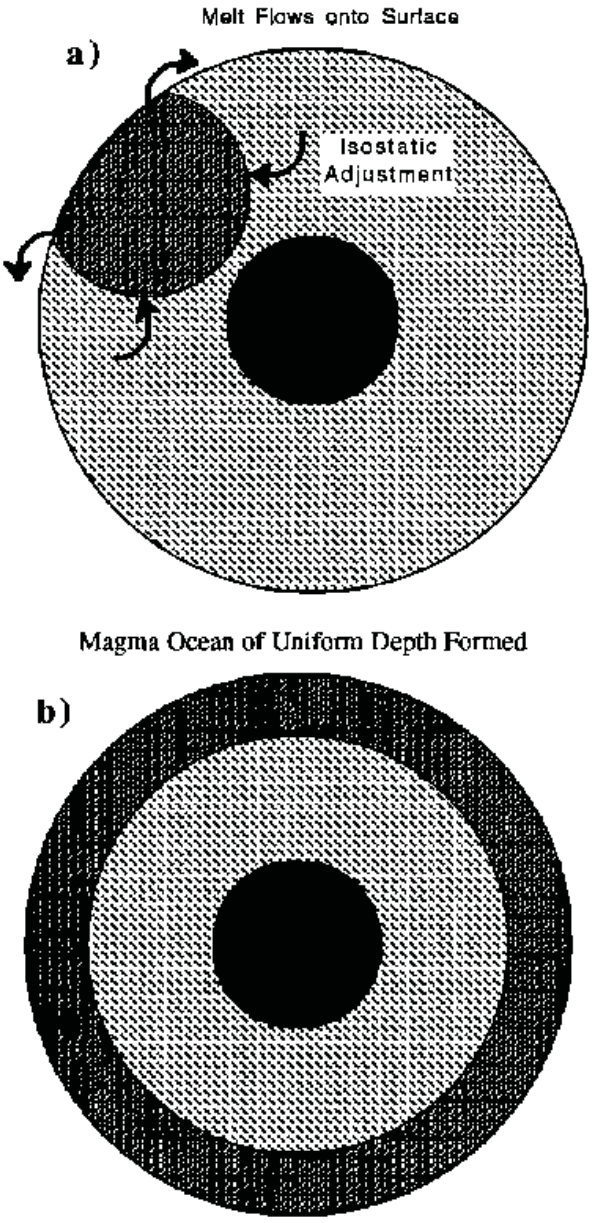


**Figure 1.12** Mechanism of a magma ocean from Tonks and Melosh (1993).

### 1.6.2 Abe, 1997

In this study, Abe asserts that there are several types of magma oceans.

a. Firstly, he distinguishes between “sustained” and “transient” magma oceans. If the growing Earth has a thick blanketing atmosphere, the surface temperature of the Earth is kept above the melting temperature and a magma ocean is sustained during accretion of the Earth. On the contrary, a deep magma ocean formed by a single impact would cool and solidify within a relatively short period, if there is no atmospheric blanketing effect.
b. Secondly, he distinguishes between “deep” and “shallow” magma oceans. The chemical differentiation of a deep magma ocean may be very different from that of a shallow one, because the former may be affected by fractionation of high pressure minerals.
c. Thirdly he distinguishes “soft” and “hard” magma oceans. The soft magma ocean is characterized by high melt fraction and low viscosity, whereas the hard magma ocean is characterized by low melt fraction and solid-like viscosity. In the soft magma ocean, vigorous convection disturbs melt-solid separation and prevents chemical fractionation (Abe, 1993; Miller et al., 1991; Solomatov and Stevenson, 1993; Tonks and Melosh, 1990). In the hard magma ocean, on the contrary, convective mixing is less vigorous and chemical fractionation may proceed.

Abe concludes that there are three cases of magma ocean evolution depending on the cause of magma ocean.

1. A giant impact would produce a “transient deep” magma ocean and differentiation at lower mantle pressure seems unlikely. However, if a thick transient atmosphere is formed, differentiation likely proceeds. On the contrary, differentiation at the upper mantle pressure proceeds irrespective of lower mantle differentiation;

2. The blanketing effect of a solar-type proto-atmosphere likely produces “sustained deep” magma ocean and differentiation proceeds at the lower mantle pressure. Then, composition of the early mantle is affected by fractionation of high pressure minerals such as Mg- and Ca-perovskite;
3. The blanketing effect of impact-induced steam atmosphere likely produces “sustained shallow” magma ocean and differentiation proceeds mainly at the upper mantle pressure. Then, the composition of the early mantle is not affected by fractionation of high pressure minerals. Even in this case, however, lower mantle composition is affected by chemical differentiation in the upper mantle, because differentiated materials are buried in deep mantle owing to growth of the Earth.

For all three cases, differentiation at the upper mantle pressure is indicated. It means that all models of Earth formation suggest a differentiated early upper mantle.

### 1.6.3 Solomatov, 2000

A giant impact melts a significant part of one hemisphere of the Earth. Isostatic adjustment quickly redistributes the mass to create a more stable spherically symmetric configuration. In the beginning of crystallization of the magma ocean, the temperatures in the deepest parts of the Earth were probably near the solidus and depended on the poorly constrained pre-impact thermal state of the mantle. This implies that some portion of the lower mantle could retain substantial amounts of primordial volatiles.

In this model, crystallization is assumed to start from the bottom and in less than 1000 yr propagates through the lower mantle. The product of this period of crystallization is essentially undifferentiated mantle with the remaining shallow partially molten layer. Small amounts of crystals might settle down and contribute to the formation of a Fe-rich D" layer.

The shallow magma ocean is the only part of the mantle that undergoes any substantial differentiation.

In Figure 1.13 is illustrated a possible thermal structure of the growing proto-Earth: a shallow magma ocean where crystal settling/flotation and segregation of liquid Fe delivered by impacts take place; a solid lower mantle with liquid Fe diapirs and a liquid Fe core. The bottom of the shallow magma ocean is located at P= 28 GPa (Li and Agee, 1996; Righter et al., 1997; Righter and Drake, 1997).

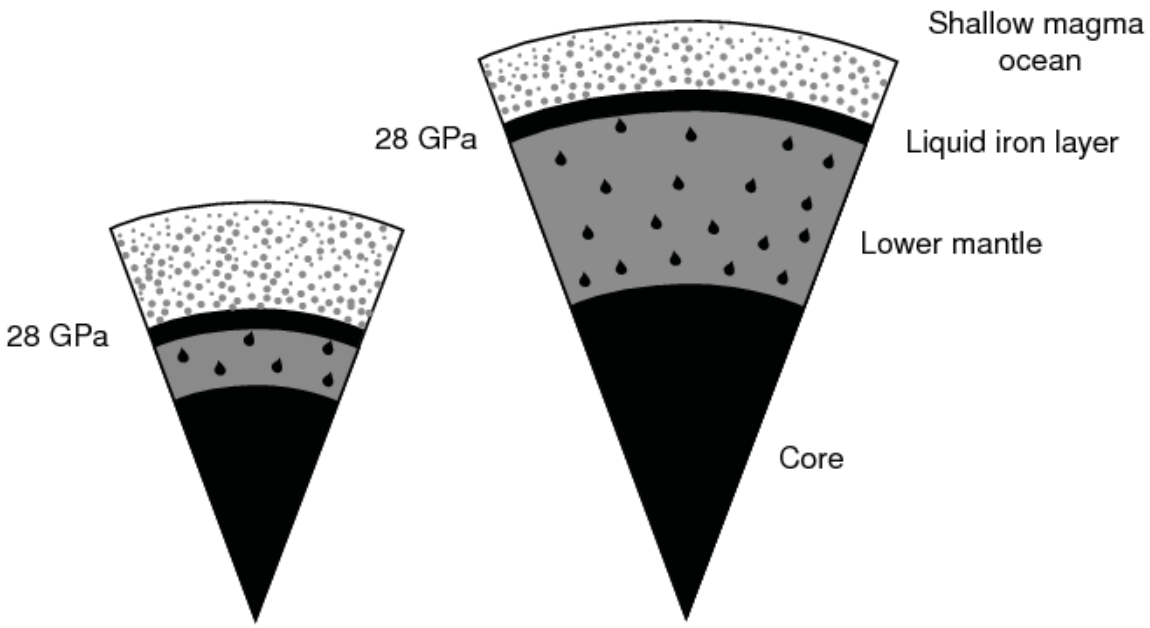


**Figure 1.13** A possible thermal structure of the growing proto-Earth, from Solomatov (2000).

### 1.6.4 Liebske et al., 2005

The existence of Earth's deep magma ocean during the Hadean (4.5-3.8 Ga before present) may have led to significant chemical differentiation and possibly stratification of the mantle by crystal fractionation (Fig. 1.14). Liebske envisaged three possible scenarios for the evolution of the Earth's mantle.

1. Crystal fractionation at lower mantle pressure took place and resulted in the formation of a chemically distinct reservoir in the lower mantle. This reservoir was not remixed with the overlying mantle by subsequent solid-state state convection.
2. Crystal fractionation took place but the crystal cumulate and the overlying mantle were extensively or completely re-homogenized by whole-mantle convection.
3. Magma ocean crystallization occurred without any significant amount of fractionation and subsequent initial mantle differentiation.

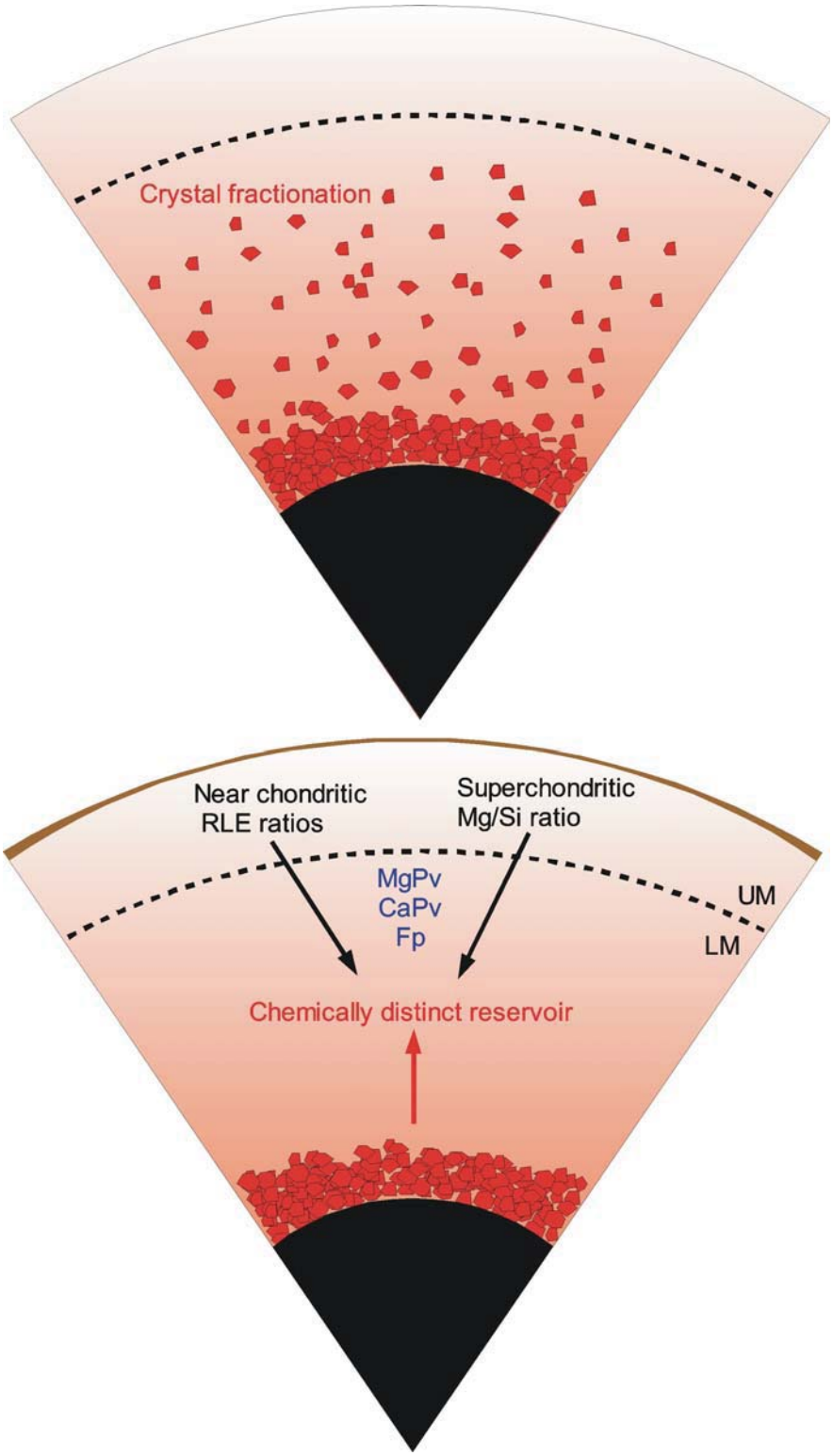


**Figure 1.14** Possible processes during magma ocean crystallization. Reproduced from Liebske (2005).

### 1.6.5 Wood et al., 2006

Numerical simulations (Abe, 1997; Solomatov, 2000) indicate that a magma ocean extending to the core-mantle boundary would be short-lived and that the lower mantle would crystallize in a few thousand years. A shallower, partially molten layer would crystallize much more slowly, however, and could remain as a mixture of crystals and melt for 100 Myr. Considering these results and the energetics of impact and core segregation leads to a dynamic view of the growing Earth in which the outer molten part deepened and shallowed many times after episodic impact. The pressure and temperatures recorded by core-mantle partitioning are therefore values averaged over numerous cycles of metal accumulation and segregation such as that depicted in Fig. 1.15.

Impacting planetesimals disaggregate and their metallic cores break up into small droplets in the liquid silicate owing to Rayleigh-Taylor instabilities. These droplets descend slowly, re-equilibrating with the silicate until they reach a region of high viscosity (solid), where they pond in a layer. The growing dense metal layer eventually becomes unstable and breaks into large blobs (diapirs), which descend rapidly to the core without further interaction with the silicate.

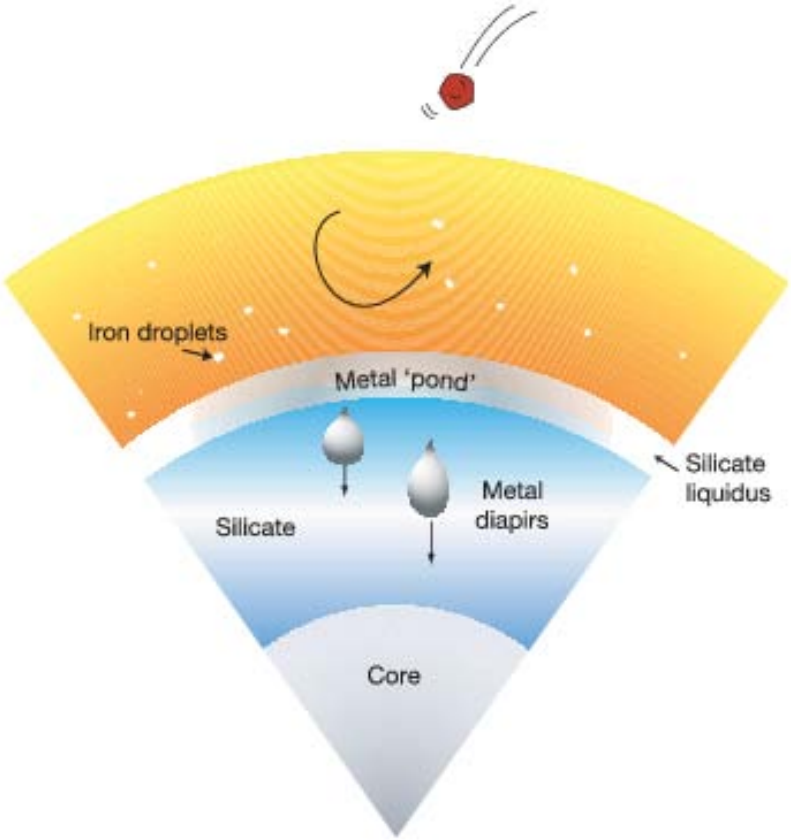


**Figure 1.15** Woods's deep magma ocean model. Reproduced from Wood et al. (2006).

### 1.6.6 Labrosse et al., 2007

The existence of patches of dense partial melt at the base of the Earth's mantle (Williams and Garnero, 1996), together with estimates of melting temperature for deep mantle phases (Zerr et al., 1998; Andrault et al., 2011), indicates the presence of a deep melting occurrence in the past.

In this model is shown that a stable layer of dense melt formed at the base of the mantle early in the Earth's history would have undergone slow fractional crystallization, and would be an ideal candidate for an unsampled geochemical reservoir hosting a variety of incompatible species for an initial basal magma ocean thickness of about 1.000 km (Labrosse et al., 2007).

This model is schematically illustrated as in Figure 1.16:

a. Iron-rich liquid descends as a rain of droplets in the shallower magma ocean, accumulates on top of the solid mantle and undergoes diapiric instability and rapid transport to the core;
b. The molten layers formed at the top and the bottom of the mantle crystallize, and deposit material onto a solid mantle layer that grows upward at the top and downward at the bottom at two vastly different rates;
c. After the surface magma ocean has fully crystallized, the slowly cooling basal melt layer fractionally crystallizes increasingly Fe–enriched solids that are deposited upwards onto the bottom of the solid mantle;
d. After a substantial part of the basal magma ocean has frozen, the solid that forms may itself contain enough dense components to become stable against complete entrainment in the solid mantle, hence forming piles under upwelling currents.

The remaining thin mushy layer of melt is thicker where mantle flow converges along the core-mantle boundary, leading to seismically detectable ultralow-velocity zones. Solid-state

convection in the mantle controls the rate of crystallization of the bottom magma ocean and the possible entrainment of FeO-enriched dense material accumulating at the base of the solid mantle (dark grey in c and d of Fig. 1.16).

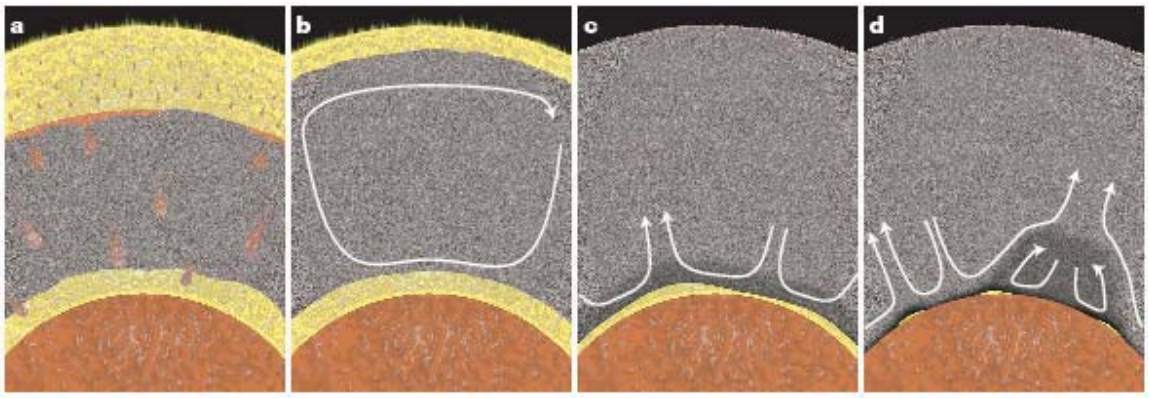


**Figure 1.16** Schematic illustration of the formation and evolution of an Earth's magma ocean at the base of the mantle. Reproduced from Labrosse et al. (2007). Yellow zone is the ocean magma; grey zone is the mantle; orange zone is the core.

### 1.6.7 Elkins-Tanton, 2008

In this model Elkins-Tanton affirms that magma ocean solidification and subsequent planetary evolution proceeds through three major phases (Fig. 1.17).

a. First, the magma ocean solidifies, partitioning volatiles between solid cumulates, evolving liquids, and a growing primordial atmosphere. These cumulates are gravitationally unstable to overturn (Elkins-Tanton et al., 2003).
b. In step two, the unstable solidified mantle cumulates overturn to a stable configuration. The overturn process creates a mantle that is gravitationally stable and therefore resistant to the onset of thermal convection. Hot cumulates that formed deep in the magma ocean rise to shallower depths during overturn and may melt adiabatically, producing the earliest basaltic crust.
c. In step three, the planet conducts heat through its solidified mantle and radiates it to space through the primordial atmosphere formed in step one.

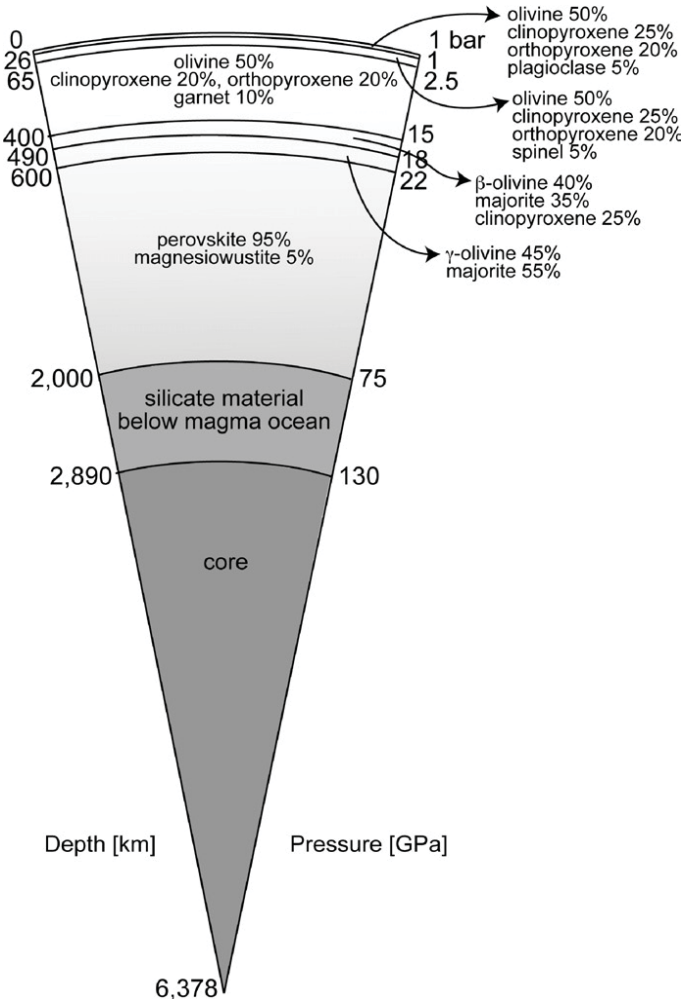


**Figure 1.17** Mineral phases assumed to solidify from a 2000-km deep terrestrial magma ocean (Elkins-Tanton, 2008).

### 1.6.8 Nomura et al., 2011

During Earth's history any melts that form below ~1800 km depth sink and accumulate at the base of the mantle, while any crystals that form owing to cooling of this dense magma will rise upward into the solid mantle (Fig. 1.18a). Perovskite crystals forming in the basal magma ocean (BMO) would have been relatively depleted in iron and floated to the top of magmas below 1800 km depth. Then, Fe-poor perovskite crystallization leaves a residual liquid enriched in FeO and depleted in $SiO_2$ and crystals forming from this evolved liquid may become dense enough to form thermo-chemical piles at the base of the solid mantle (Fig. 1.18b). The finals stage of crystallization (Fig. 1.18c) involves a composition close to wüstite, leaving behind a very dense thin layer that is consistent with the seismic properties inferred inside ULVZs (Wicks et al., 2010). Such material would be maintained at or near the solidus over geological scale time scales because the residual liquid will sequester incompatible species that in turn depress the melting temperature.

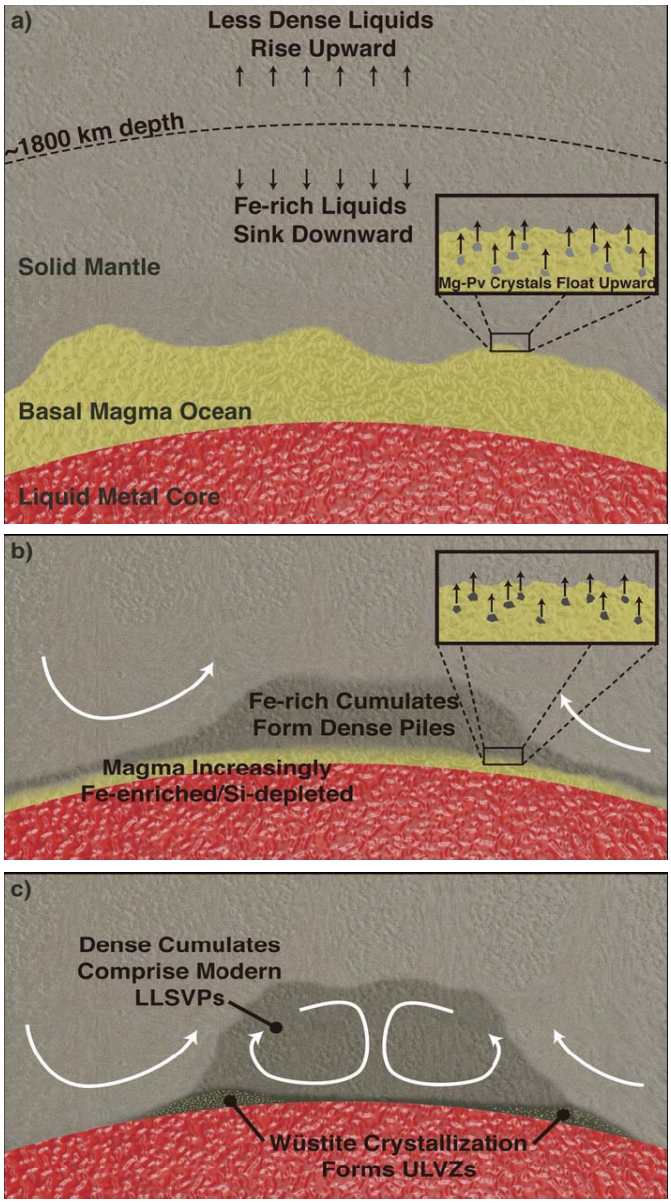


**Figure 1.18** Evolution and crystallization of dense melts in the deep mantle (Reproduced from Nomura et al., 2011). White arrows indicate schematic flow patterns in the convecting solid mantle. White arrows indicate schematic flow patterns in the convecting solid mantle.

### 1.6.9 Summary of different magma ocean models

There three main scenarios for the evolution of the Earth's mantle (Liebske et al., 2005):

1. Crystal fractionation at lower mantle conditions and subsequent formation of a chemically distinct reservoir in this region (Abe, 1997; Labrosse et al., 2007). This reservoir was not remixed by solid-state convection;
2. Crystal fractionation with partial or complete re-homogenization of crystal cumulates by solid-state convection (Abe, 1997). Convection and chemical fractionation are function of melt fraction amount and viscosity, i. e. for high melt fraction and low viscosity conditions we have a vigorous convection which prevents chemical fractionation (Abe, 1997; Miller et al., 1991; Solomatov and Stevenson, 1993; Tonks and Melosh, 1990).
3. Crystal formation without fractionation and subsequent mantle differentiation (Abe, 1997).

In this paragraph are summarized (Table 1.3) main theories of magma ocean formation from our (Andrault et al., 2011) and previous works.

| Authors | Magma Oceans | Properties |
|---|---|---|
| *Tonks and Melosh, 1990* | Large volume of melt | Melt flows into surface |
| *Abe, 1997* | SUSTAINED<br><br>TRANSIENT<br>DEEP<br>SHALLOW<br>SOFT<br><br><br>HARD<br><br><br>TRANSIENT DEEP<br><br><br>SUSTAINED DEEP<br><br><br><br>SUSTAINED SHALLOW | Because of a blanketing atmosphere<br>No blanketing effect<br><br><br>High melt fraction and low viscosity>>vigorous convection>>no fractionation<br>Low melt fraction and high viscosity>>less vigorous convection<br>No differentiation at lower mantle pressure (LMP), no transient atmosphere<br>Differentiation at LMP and blanketing effect>> fractionation of Ca- and Mg-Pv<br>No differentiation at lower mantle pressure (LMP), steam atmosphere |
| *Solomatov, 2000* | Isostatic adjustement and stable spherically configuration | Crystallization from the bottom (at 28 GPa).<br>Differentiation only in a shallow magma ocean |
| *Liebske, 2000* | Crystallization at LMP and distinct reservoir in the LM<br>Crystallization at LMP<br>Crystallization | No remixing by convention<br><br>Remixing by convection<br>No fractionation, no differentiation |
| *Wood et al., 2006* | Crystallization | P of equilibrium (Peq) = 40 GPa and 3150 K<br>Metallic cores break up into droplets in the liquid silicate |

| | | |
|---|---|---|
| *Labrosse et al., 2007* | Basal magma ocean (~1000 km thick)<br>Fe droplets in shallow magma ocean<br>Crystallization at the top and the bottom<br>Basal magma ocean frozen | Fractionated crystallization, solid rich in Fe<br>Diapirs to the core<br><br>Different rates of crystallization<br>Solid formed |
| *Elkins-Tanton, 2008* | Magma ocean solidifies | Unstable mantle cumulates become stable |
| *Nomura et al., 2011* | Basal magma ocean<br><br>Cumulates rich in Fe and depleted in Si | Pv depleted in Fe and float to the top (below 1800 km) |
| *This study (Andrault et al., 2011)* | Transient magma ocean<br><br>Fully molten chondritic mantle at Peq<br>If T>1700-1800 K, no blanketing effect<br>Basal magma ocean for | No blanketing effect, Peq= 40 GPa and 3150 K<br>Surface T=2450 K, transient magma ocean<br>Quick cooling<br><br>1) composition enriched in incompatible elements<br><br>2) middle-depth solid mantle is mainly composed of Al, Mg-Pv |

**Table 1.3** Summary of magma ocean models from previous works and this study.

## 1.7 Temperature profiles of the lower mantle

We can obtain more direct information on temperature in the mantle by associating phase transformations with seismic discontinuities, if the phase boundaries of selected transformations are reliably defined (Ito and Katsura, 1989; Hernlund et al., 2005; Ono and Oganov, 2005; Katsura et al., 2010). In order to obtain a better description of the Earth's composition and thermal structure, seismic data must be compared with mineralogical data and thermodynamic models (Wang, 1972; Brown and Shankland, 1981; Anderson, 1982; Ito and Kastura, 1989; Stacey, 1992). Moreover, because of uncertainties and limitations in previously used models, there are considerable discrepancies between the various proposed descriptions of the Earth's thermal and compositional structure (da Silva, 2000).

The agreement between body wave and normal data suggest that the lower mantle is likely to be nearly adiabatic (Masters, 1979; Dziewonski and Anderson, 1981; Bunge et al., 2001) and modeled geotherms have been found in good agreement with the adiabat (Shankland and Brown, 1985). Therefore, an adiabatic geotherm is used as a reference mantle temperature profile (Dziewonski and Anderson, 1981; Matas et al., 2007), which assumes that the convective mantle is homogeneous and adiabatic. Then, geotherms are derived by comparison with the PREM model (da Silva, 2000).

A constraint of the Earth density profile is given by the observation of the Bullen parameter $\eta$ (Bullen, 1963),

$$\eta = V_\phi^2 \left( \frac{d\rho}{dr} \right) \left( \frac{dP}{dr} \right)^{-1} \tag{1.3}$$

where the bulk sound velocity $V_\phi$ $\left(V_\phi^2 = V_p^2 - 4/3V_S^2\right)$ is deduced from a radial body-wave model, and $(d\rho/dr)/(dP/dr)$ reflects the actual density-pressure relationship along a radial profile of the Earth. The Bullen parameter is observed to be 1±0.02.

In a homogeneous mantle, the departure of $(d\rho/dr)/(dP/dr)$ from the adiabatic value $(\partial\rho/\partial P)_S = V_\phi^{-2}$ can only be due to the fact that the mantle geotherm $(dT/dr)_E$ is not adiabatic and one has

$$\left(\frac{d\rho}{dr}\right)\left(\frac{dP}{dr}\right)^{-1} = V_\phi^{-2} + \frac{\alpha}{\rho g}\left[\left(\frac{dT}{dr}\right)_E + \frac{\alpha g T}{C_p}\right] \tag{1.4}$$

where $\alpha$, $C_p$ and $g$ are the thermal expansion, the specific heat, and the gravitational acceleration, respectively. The Bullen parameter would, therefore, be $\eta_H$ where

$$\eta_H = 1 + V_\phi^2 \frac{\alpha}{\rho g}\left[\left(\frac{dT}{dr}\right)_E + \frac{\alpha g T}{C_p}\right] \tag{1.5}$$

and $\eta_H$=1 in a homogeneous mantle implies a so-called adiabatic geotherm defined by

$$\left(\frac{dT}{dr}\right)_E + \frac{\alpha g T}{C_p} = 0 \text{ (Turcotte and Schubert, 1982)} \tag{1.6}$$

While temperatures are relatively well constrained in the shallow mantle due to anchoring by phase transitions at 410 km and 670 km depth in $(Mg,Fe)_2SiO_4$ (Ito and Katsura, 1989), the profiles of temperatures are determined using the adiabatic geotherm (eq. 1.5) to the lower mantle conditions (Fig. 1.19). Differences in adiabatic geotherms are up to ~250 K at the bottom of the mantle yielding in general 2500 K±250 at 2700 km depth (Brown and Shankland, 1981; Bunge et al., 2001; Stacey and Davis, 2004).Whereas models using inversion of seismic radial profiles

indicate hotter temperatures of 2800 to 3400 K at 2700 km (Matas et al., 2007), dependent on the Mg/Si ratio.

The adiabatic temperature gradient gradually decreases with increasing depth without a phase transition, and abruptly changes in association with phase transitions. Then, the temperature at the 410 km discontinuity has been re-evaluated by comparing the depth of the discontinuity with the olivine-wadsleyte transition pressure (Katsura et al., 2010). The temperature at a depth of 2700 km is found to be 2730±50 K (Katsura et al., 2010).

Earth's temperature profile in the D"-region has been mostly constrained in light of the new post-perovskite phase of $MgSiO_3$ (Murakami et al., 2004; Ono and Oganov, 2005). It was proposed that the observation of pairs of positive and negative S-wave velocity discontinuities in the D"-region are due to double-crossing of the perovskite to post-perovskite transition (Hernlund et al., 2005).

Regarding the outer core temperature, it is generally estimated extrapolating the adiabatic temperature profile from the inner-core boundary (ICB) through the outer core. However, the range of ICB temperatures is very large.

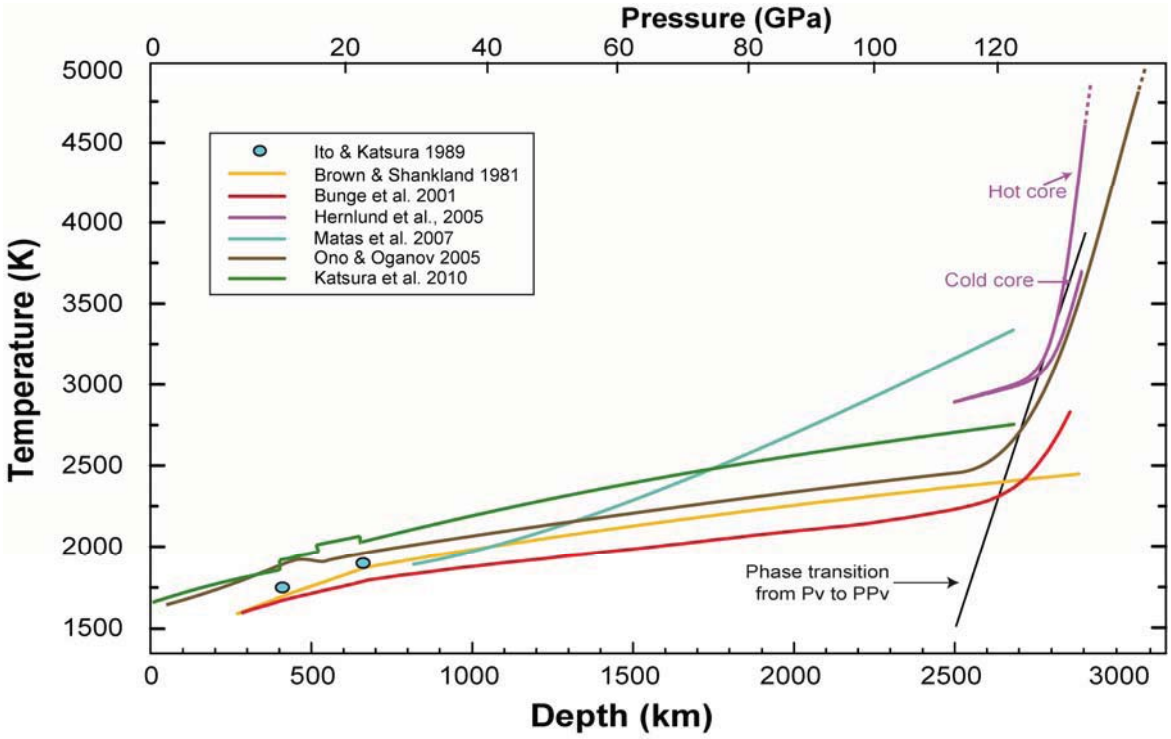


**Figure 1.19** Temperatures profiles estimated for the lower mantle. Are reported estimates of the mantle geotherm (Brown and Shankland, 1981; Bunge et al., 2001; Hernlund et al., 2005; Ono and Oganov, 2005; Matas et al., 2007; Katsura et al., 2010) and temperature anchor points (Ito and Katsura, 1989). Phase transition Pv/PPv (Black line) is from Ono and Oganov (2004).

## 1.8 Liquidus and solidus phase relations in the lower mantle

In order to understand the details of the early melting and crystallization history of the Earth, melting phase relations of the mantle at very high pressures must be known.

The system MgO-$MgSiO_3$ is the most fundamental starting point for development of an understanding of these phase relations (Presnall et al., 1998; Liebske et al., 2005). In Figure 1.20 is reported the eutectic melting curve for this system at pressures between 10 and 22 GPa, obtained using a multi-anvil press (Presnall et al., 1998 (P-98 in Fig. 1.20)). Melting of $(Mg,Fe)SiO_4$ olivine was determined using shock-wave experiments (Ahrens and Holland, 1997; Luo et al., 2004 (L-04 in Fig. 1.20)) and was reported at 4300 K and 130 GPa. Regarding to the classic pyrolite model for the lower mantle, many information are available for pressures up to ~60 GPa (Litasov and Ohtani, 2002; Trønnes and Frost, 2002; Zerr et al., 1998 (LO-02, TF-02, and Z-98 respectively in Fig. 1.20)).

Recently, have been determined liquidus and solidus melting curves for peridotite compositions between 36 and 140 GPa, using laser-heated diamond anvil cell (LH-DAC) (Fiquet et al., 2010 (F-10l and F-10s in Fig. 1.20)). In particular, it has been shown that for peridotite compositions, olivine is the liquidus phase up to 13-16 GPa (Takahashi and Scarfe, 1985; Walter, 1998), but is replaced at higher pressures by majorite (Mj) garnet (Ito and Takahashi, 1987; Herzberg et al., 1990; Zhang and Herzberg, 1994). At 22-23 GPa, the liquidus phase is ferropericlase (Fp) (Zhang and Herzberg, 1994; Trønnes and Frost, 2002; Fiquet et al., 2010). At higher pressures, P>30 GPa, ferropericlase is replaced by $MgSiO_3$ perovskite (Mg-Pv) as liquidus phase (Ito et al., 2004; Fiquet et al., 2010).

The melting curve of end-member phases is relatively well determined using the LH-DAC technique (Boehler, 2000 (B-00 in Fig. 1.20)) or shock-wave experiments (Luo et al., 2004 (L-04

in Fig. 1.20)). However, for phase relations of chondritic compositions, at pressure higher than ~30 GPa, not much information is available. Anyway, it is well known that olivine is the liquidus phase up to ~10-15 GPa (Herzberg et al., 1990; Ohtani et al., 1986), majorite replaces it up to approximately 24-25 GPa (Ohtani et al., 1986) and Mg-perovskite is observed to replace majorite at 25 GPa (Ito et al., 2004).

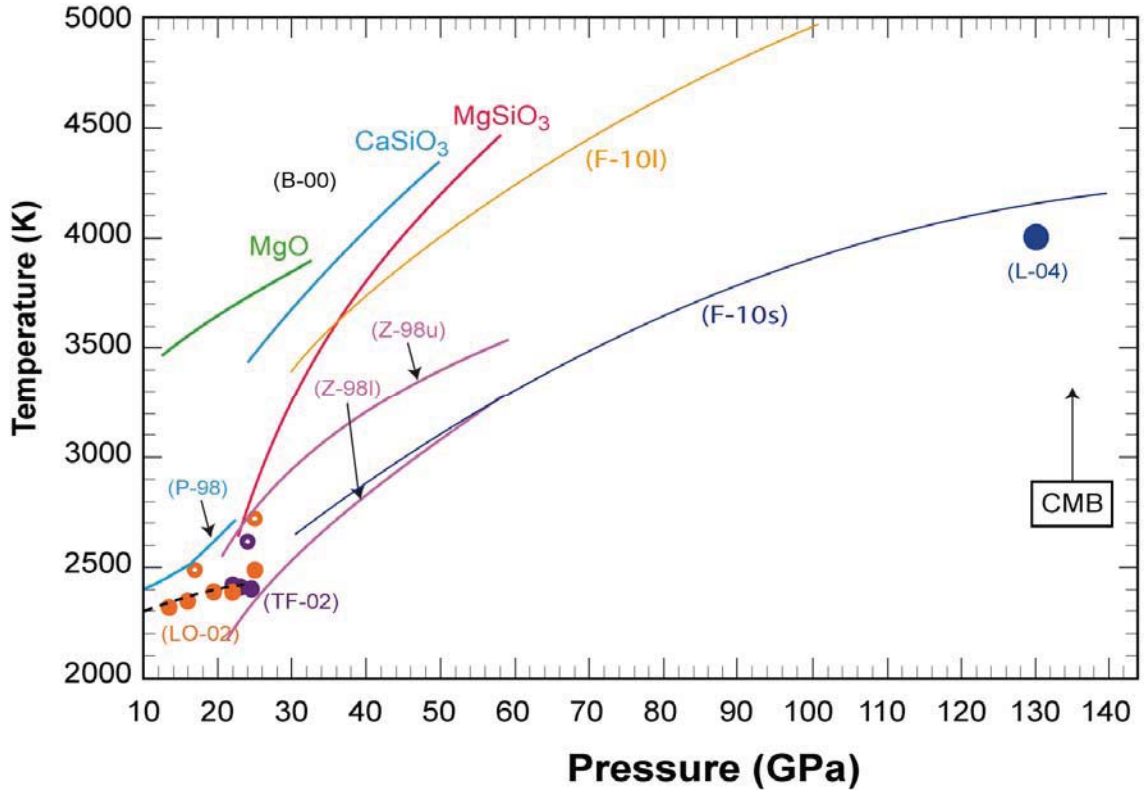


**Figure 1.20** Melting points and curves from previous works on the melting of lower mantle materials. Where: MgO-$MgSiO_3$ system: P-98 is Presnall et al., 1998; Olivine: L-04 is Luo et al., 2004; Peridotite: F-10l and F-10s is Fiquet et al., 2010 (liquidus and solidus); Pyrolite: LO-02 is Litasov and Ohtani, 2002; TF-02 is Trønnes and Frost, 2002; Z-98 is Zerr et al., 1998; Simple oxides: B-00 is Boehler, 2000.

## 1.9 Partition coefficient

Simple concentration ratios between two phases are termed *partition coefficients* (Denbigh, 1966), and will be given the symbol D (Nernst, 1891). Phases can be minerals, liquids or gases.

Here we present the partition coefficients following the terminology of Beattie et al. (1993), which is an extension of that suggested by Takahashi and Irvine (1981) and Yardley (1989).

According to the terminology of Beattie et al. (1993), partition coefficient is written as:

$$D_M^{\alpha/\beta} = {}^{\alpha/\beta}D_M = C_{MO}^{\alpha} / C_{MO}^{\beta} \quad (1.7)$$

Where, subscripts refer to the element M of interest and superscripts refer to the phases α and β concerned. $C_{MO}$ is concentration (C) for a component *MO*. Here we will use this terminology for Ca and Fe partitioning between minerals and melts as: $D_{Ca}^{Min/Melt}$ and $D_{Fe}^{Min/Melt}$, respectively (Min = mineral, i.e. Garnet, Ca- and Mg- perovskites, Magnesiowüstite, Olivine) (see also the chapter 5).

Determination of $D_{Ca}$ and $D_{Fe}$ is of primary importance for the understanding of the lower mantle properties up to the core mantle boundary and for modeling differentiation in the early Earth (Agee, 1998; Mosenfelder et al., 2009). Indeed, it is well known that density crossovers and floatability of liquids in the deep mantle depend on many factors including Fe partitioning between solid and liquid (Agee, 1998).

Calcium and iron partitioning coefficients between solid and liquid phases have been at the center of a number of studies (Fig. 1.21 and 1.22-1.23, respectively). These values concern pressures up to 35 GPa, using multi-anvil press (MAP) apparatus (Agee, 1990; Corgne et al., 2002, 2005; Drake et al., 1991, 1992, 1993; Gasparik and Drake, 1995; Hirose et al., 2004; Ito et al., 2004; Kato et al., 1988, 1996; Liebske et al., 2005; Longhi, 1995; McFarlane et al., 1990, 1991, 1992, 1994; Ohtani et al., 1989, 1991, 1995, 1998; Taura, 2001; Trønnes and Frost, 2002; Walter et al.,

2004; Zhang and Herzberg, 1994) and up to ~90 GPa, using the diamond anvil cell (DAC) (Nomura et al., 2011) and various mantle compositions such as pyrolite, peridotite and chondrite. Ca is strongly compatible with Ca-Pv and incompatible with liquidus phases up to 35 GPa, for higher pressures no information is available (Fig. 1.21).

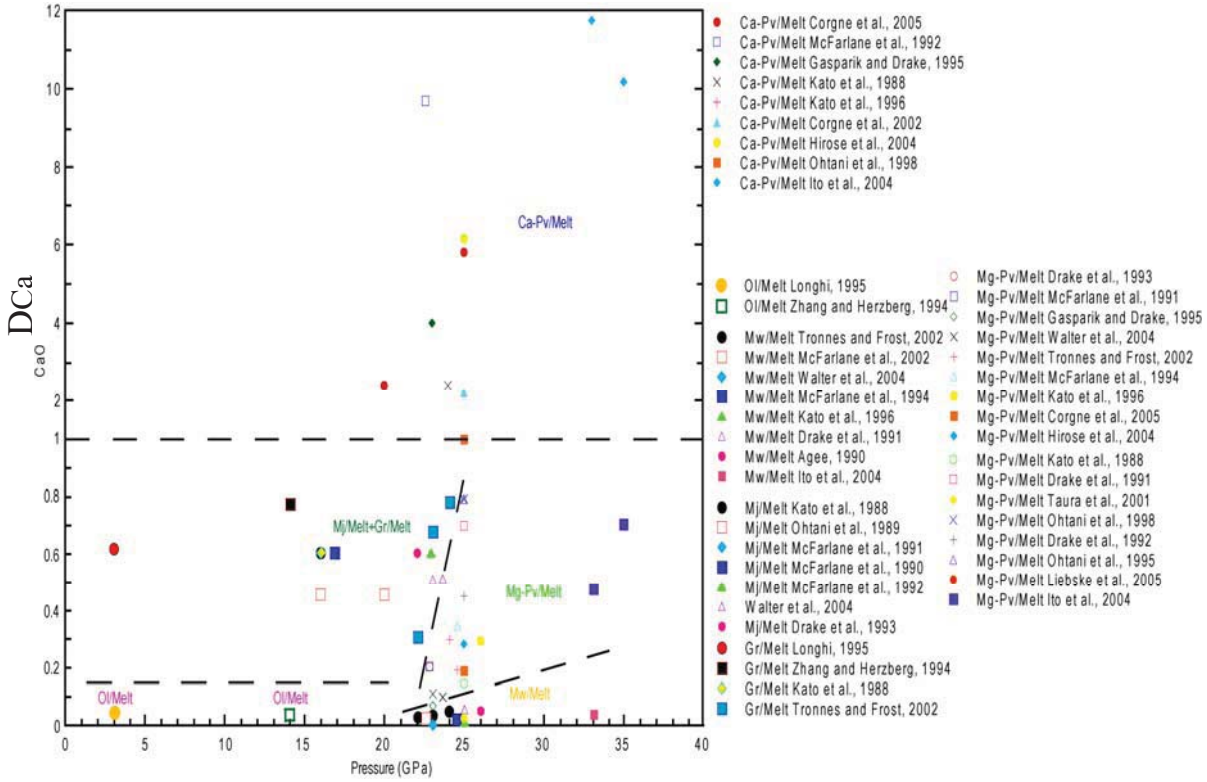


**Figure 1.21** Several previous works for $D_{Ca}$ between phases and silicate melts for various mantle materials and pressures up to 35 GPa.

$D_{Fe}$ has been reported to vary from ~0.3 to ~0.7 when we consider partitioning between liquidus (solid phases) and melts, and pressures up to 35 GPa (Fig. 1.22). At higher pressures, exists a recent study (Nomura et al., 2011) that reports a decrease of $D_{Fe}^{Pv/Melt}$ from ~0.4 to ~0.06, for pressures between 35 GPa and 85 GPa (Fig. 1.23). These results imply an increasing incompatibility of iron at increasing pressure. Data reported in chapter 4 confirm the incompatible character of Ca and Fe elements, in the extended range of pressure up to ~113 GPa.

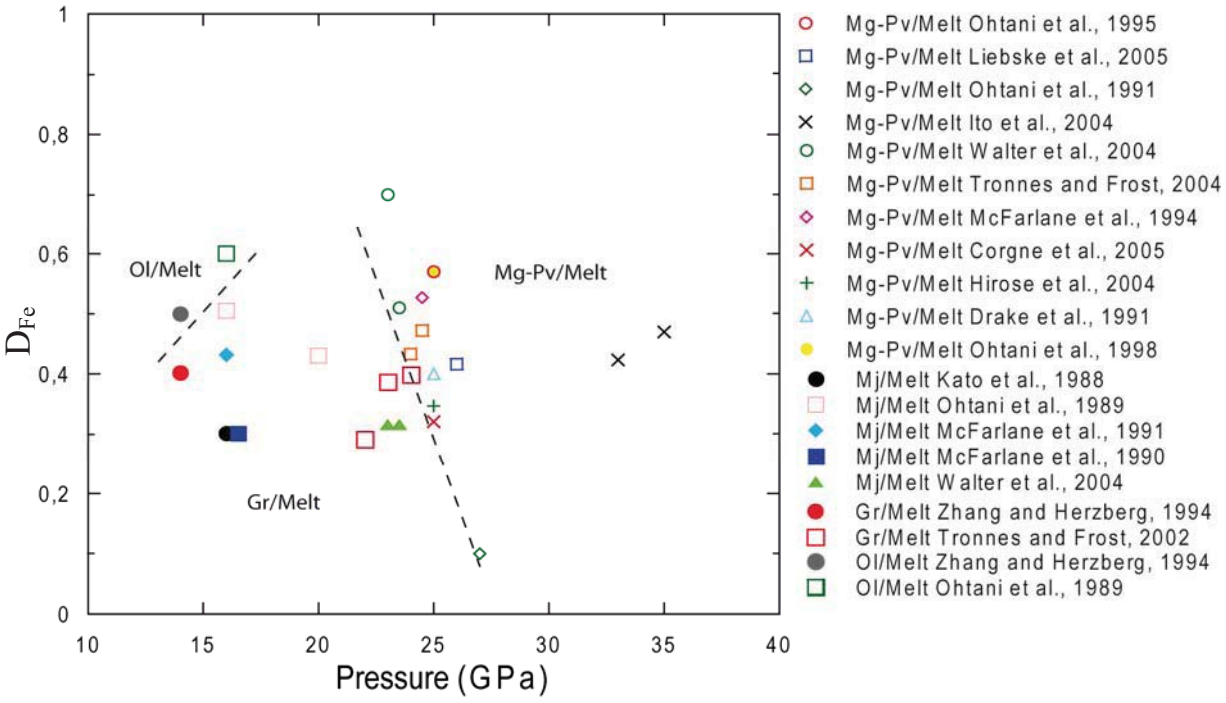


**Figure 1.22** Several previous works for $D_{Fe}$ between phases and silicate melts for various mantle materials and pressures up to 35 GPa.

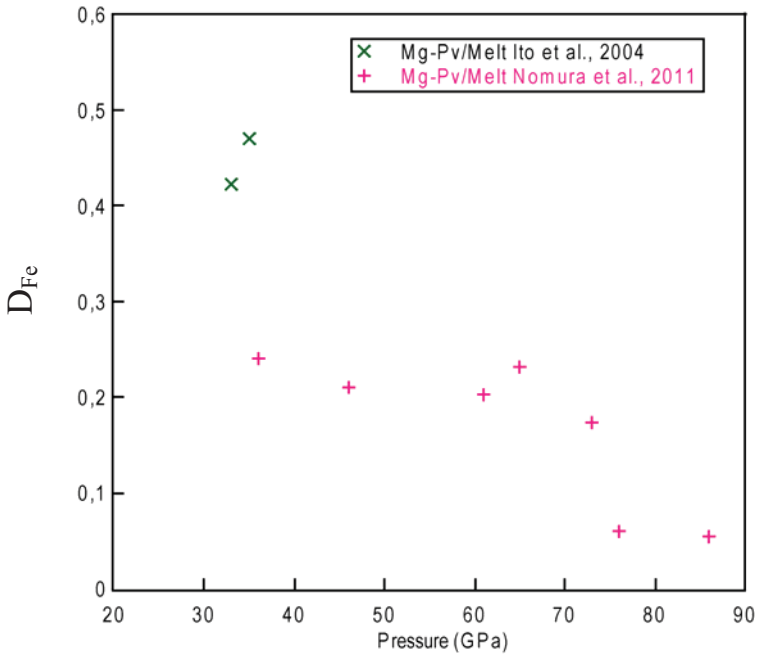


**Figure 1.23** Comparison of previous works for $D_{Fe}$ between Mg-perovskite phase and silicate melt for different mantle materials from MAP (Ito et al., 2004) and DAC (Nomura et al., 2011) experiments.

# Chapter 2: experimental and analytical methods

## 2.1 Starting materials and sample assembly

### 2.1.1 Chondritic composition

The starting material concerning the studies on melting curves and iron partitioning coefficients (chapter 4 and 5, respectively), consisted of a synthetic glass with a model composition for a C1-chondritic mantle (McDonough and Sun, 1995; Wasson and Kallemeyn, 1988). The bulk composition was prepared from oxide and carbonate mixes through repeated cycles of grinding and fusion at around 1800 K and rapidly cooled to obtain a glass of homogeneous composition (Bouhifd and Jephcoat, 2003). In order to make sure that we have a glass, we did Raman spectroscopy. Therefore, we used microprobe in order to choose glasses with the same color.

Our sample consisted of a synthetic CMASF glass with oxide contents in chondritic proportions (except for iron) so as to model the primitive mantle after core segregation (Wasson and Kallemeyn, 1988) (Table 2.1). We did not include minor and trace elements, which most abundant are Na (4900 ppm) and K (560 ppm).

| | Chondritic mantle (this study) | | Pyrolite |
|---|---|---|---|
| **Oxide** | **(Wt%)** | **(Mole %)** | **(Wt%)** |
| **$SiO_2$** | 49.6 | 43.5 | 45.1 |
| **$Al_2O_3$** | 3.4 | 1.8 | 3.3 |
| **FeO** | 8.48 | 6.2 | 8.0 |
| **CaO** | 3.3 | 2.6 | 3.1 |
| **MgO** | 35.1 | 45.9 | 38.1 |

**Table 2.1** Composition of starting material used in this study, as measured by electron microprobe analyses. At lower mantle P-T conditions, the Ca-Pv, Mg-Pv, and Fp phase proportions are expected to be 4.5, 75.7, and 19.8 mol%, respectively. This composition is representative of a chondritic-type mantle (Wassen and Kallemeyn, 1988), and it is also quite close to pyrolite (Ringwood, 1975).

### 2.1.2 Forsterite

The forsterite specimen used for calorimetric measurements, of industrial origin, was given by O. Jaoul (Université Paris XI). Its composition, as determined from electron-microprobe analyses with the automated CAMEBAX microprobe of the Université Paris VI is 0.11 (2) wt % $A1_20_3$, 42.61 (3) wt% $SiO_2$, 57.36 (4) wt% MgO and 0.05 (2) wt % CaO, total of 100.15 (6). This compares favorably with the nominal composition, namely 42.70 and 57.30 wt% $SiO_2$ and MgO, respectively. The lattice parameters = 4.760( 1), b = 10.201(2 ) and c = 5.985(1 ) Å were derived from an X-ray powder diffraction pattern in which the reflections of only forsterite were apparent (Gillet et al., 1991).

The Raman spectra were recorded with the multichannel microprobe (Microdil 28, from Dilor) of the MLRO service of the University of Nantes. The light was collected in the backscattering

direction through a Leitz UTK 40 or UTK 50 objective (focal distance of 8 or 18 mm; numerical aperture of 0.63 or 0.32, respectively). The spectra were obtained from about 10 accumulations lasting each 20 to 40 s, and peak positions were identified within $\pm 1 cm^{-1}$.

### 2.1.3 Sample assembly

Our samples consisted of 5 to 10 μm thick pellets of:

1. $Mg_2SiO_4$-forsterite mixed with a YAG-laser absorber embedded between two MgO pellets: we used Pt as pressure standard;
2. CMASF glass embedded between two NaCl or KCl pellets as thermal insulators: for this chondrite-sample we did not mix it with any YAG-laser absorber or pressure standard.

We used rhenium (forsterite) or tungsten (Cl-chondrite) gaskets pre-indented to a thickness of 30-45 μm and laser-drilled to diameters of 50-80 μm (Fig. 2.1).

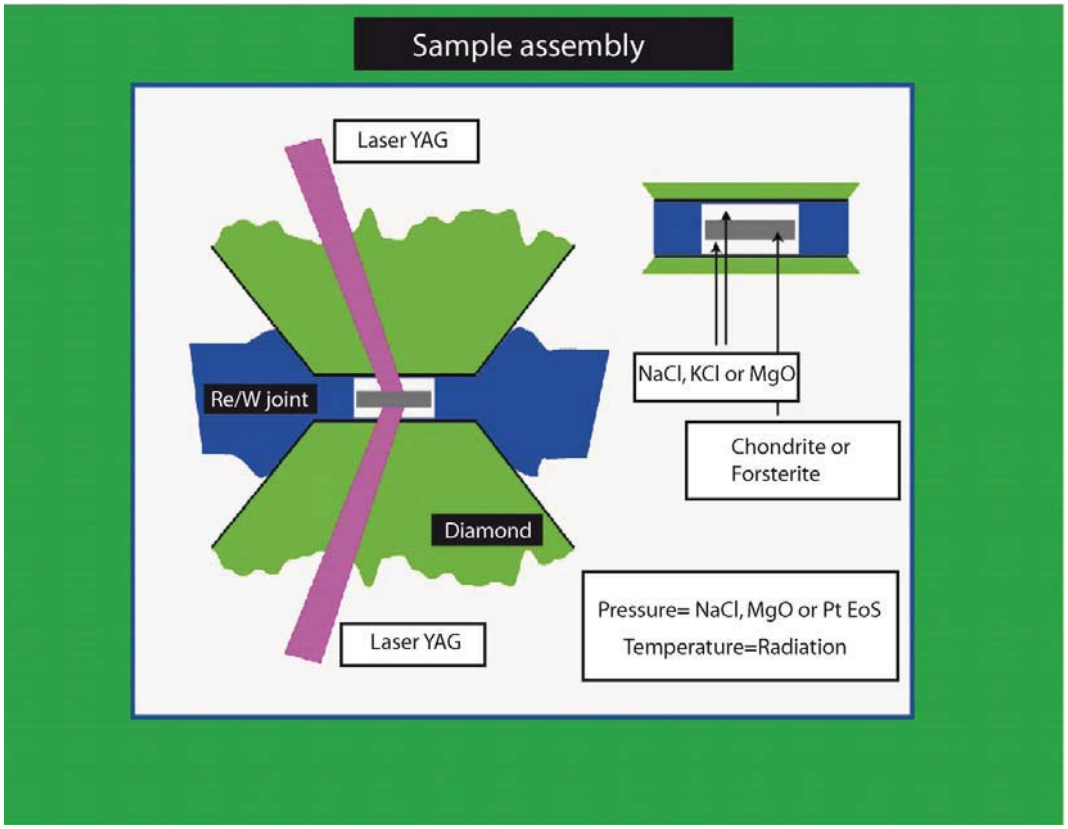


**Figure 2.1** Sample assemblies in this study.

## 2.2 ESRF and ID27

### 2.2.1 The European Synchrotron Radiation Facility (ESRF)

ESRF was the first third generation synchrotron source, starting its user operation in 1995. Located in Grenoble, France, it is one of the three high energy 3rd generation SR sources operational worldwide (Fig. 2.2).


**Figure 2.2** The European Synchrotron Radiation Facility (ESRF).

The source is optimized to produce hard X-rays in the 1 to 100 KeV range. The ID27 beamline uses an insertion device (ID) as a source point which generates high fluxes and brilliance in the 20 to 90 KeV range of photon energy.

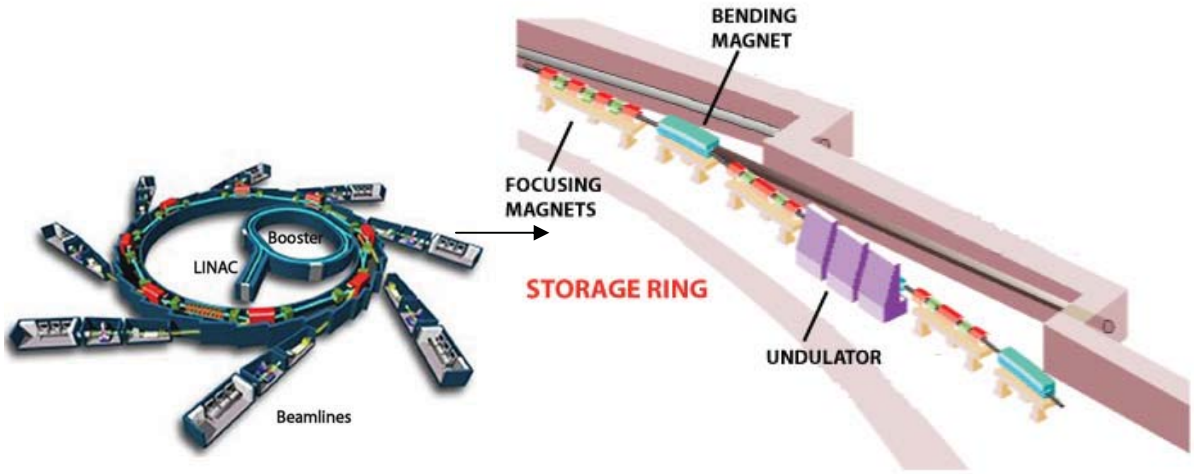


**Figure 2.3** ESRF circular track off which beamlines branch and an internal image of the storage ring.

Figure 2.2 and 2.3 show different parts of ESRF. Electrons are produced with an electron canon and accelerated with a linear accelerator (LINAC). The booster accelerates particles up to a relativistic speed and energy of 6 GeV. Once accelerated, electrons are injected into the ring storage with a circumference of 844 m.

The ESRF consists of 40 beamlines. Beamlines placed on the bending magnets (BM) are intercalated between the beamlines that work with undulators (ID).

### 2.2.2 The ID27 beamline

ID27 is specialized in high-pressure applications employing diamond-anvil and large-volume cells. ID27 is fully optimized for monochromatic high-resolution XRD under extreme pressure and temperature for diamond anvil cell experiments. The monochromatic beam is selected using a nitrogen-cooled Si(111) monochromator and focused on the sample using multilayers mirrors in the Kirkpatrick-Baez (KB) geometry (Fig. 2.4). These mirrors possess a very board energy band pass from 6 KeV to 80 KeV with a maximum of 80% reflectivity at 30 KeV.

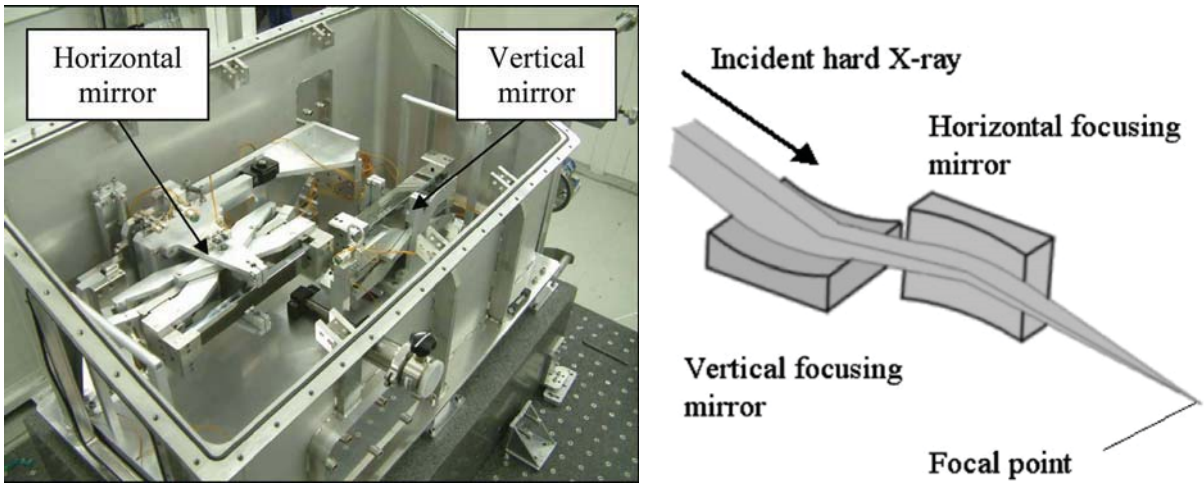


**Figure 2.4** Photograph of the pair of 300 mm-long KB mirrors (Mezouar et al., 2005) and its focusing system.

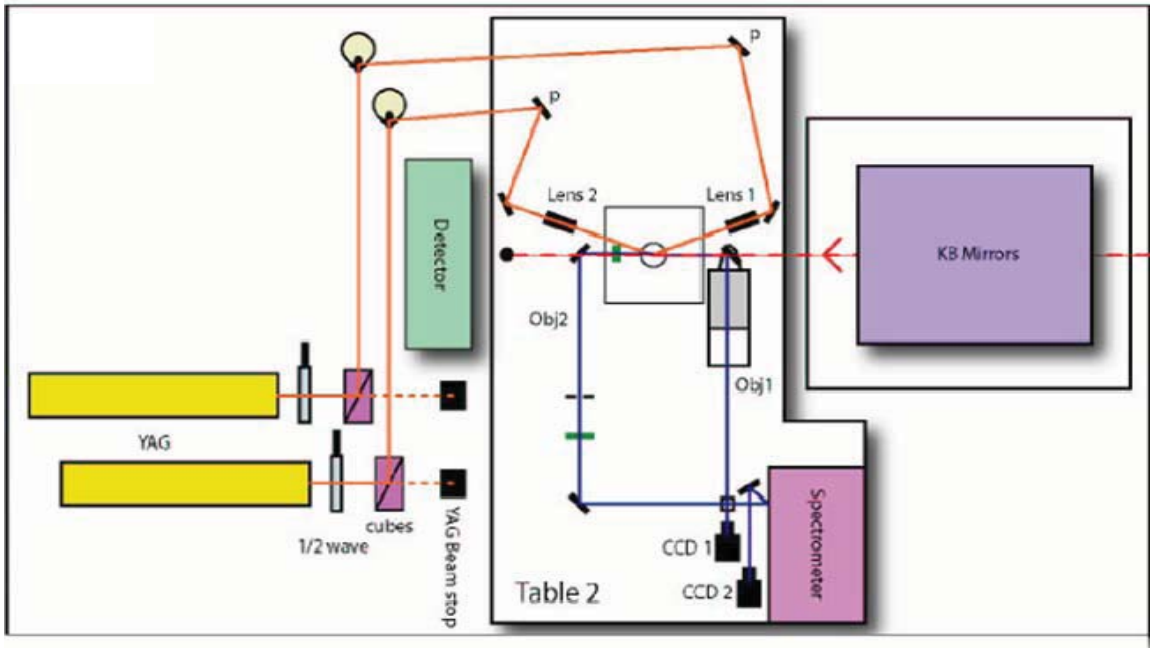


**Figure 2.5** Schematic diagram of the laser heating system at the ID27 beamline (Mezouar, 2010). The experimental hutch (at 48 m from the X-ray source) is equipped with an XYZ translation to accommodate the high-precision two-circle diffractometer suitable for powder and single crystal

diffraction in DACs. The diffraction signal is collected on a Bruker CCD detector or a MAR345 image plate that are easily interchanged using high-precision motorized translations (Fig. 2.5).

In this study, the hutch was equipped with an energy dispersive solid-state Si(Li) Vortex detector to X-ray fluorescence experiments. In fig. 2.6 is an image of ID27 hutch during my experiments of X-ray diffraction and X-ray fluorescence.

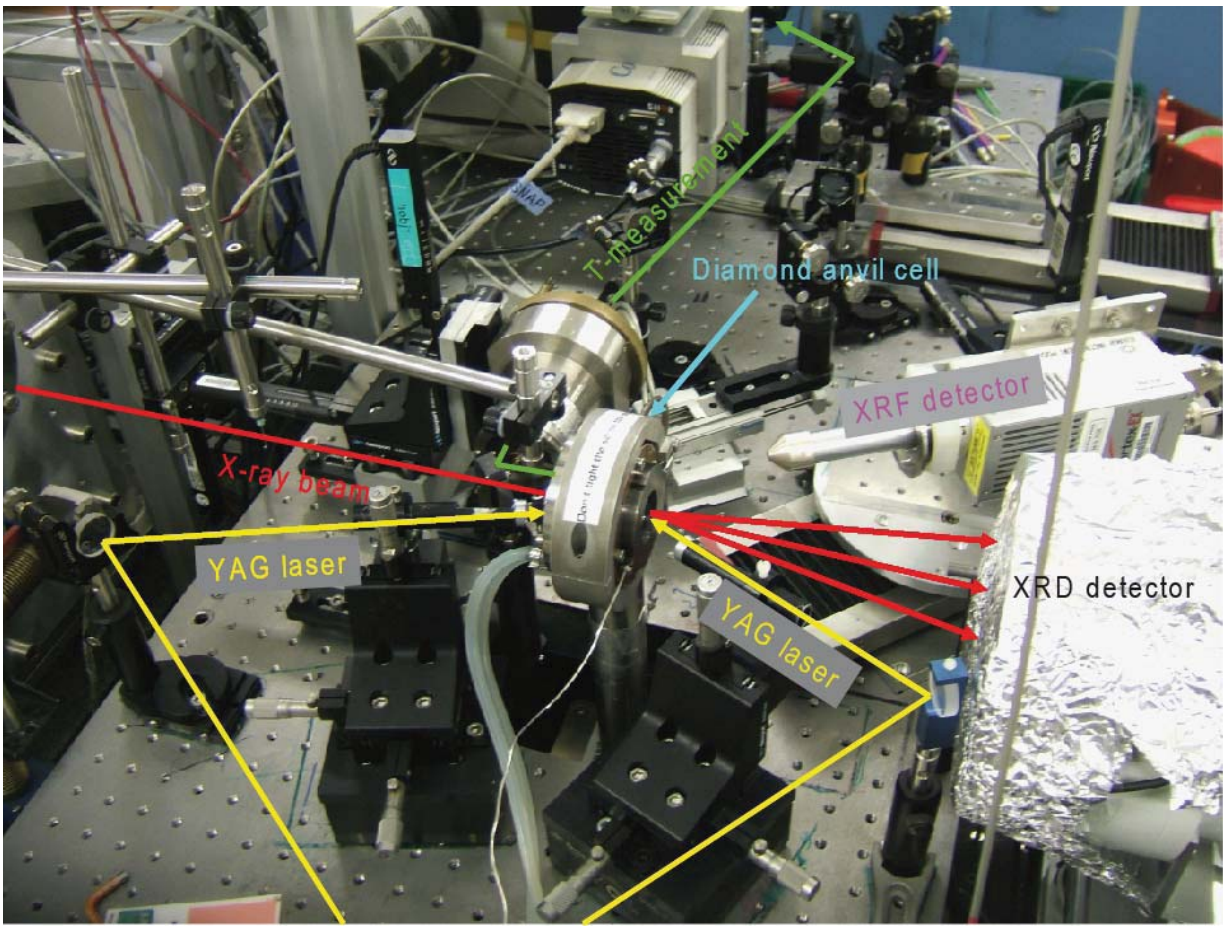


**Figure 2.6** Image of ID27 assembly during my XRD and XRF experiments.

### 2.2.3 Mirrors

Focusing of hard X-rays has long been considered unfeasible. This was mainly the consequence of the weak refraction of this type of electromagnetic radiation with matter, resulting in a refractive index $n$ very close to unity. While lenses for visible light are made of a transparent material with an index of refraction substantially different from 1, there is no equivalent material for X-rays. First solutions for X-ray focusing were proposed by M.A. Kumakhov, and were originally thought out as the total reflection of X-rays from smooth surfaces (Gibson and Kumakhov, 1992). Today, several focusing solutions exist for hard X-rays also including refractive and diffractive optics as illustrated by Fig. 2.7. There has been tremendous progress over the last ten years in X-rays optics. An extrapolation of the current trend is shown in Fig. 2.8.

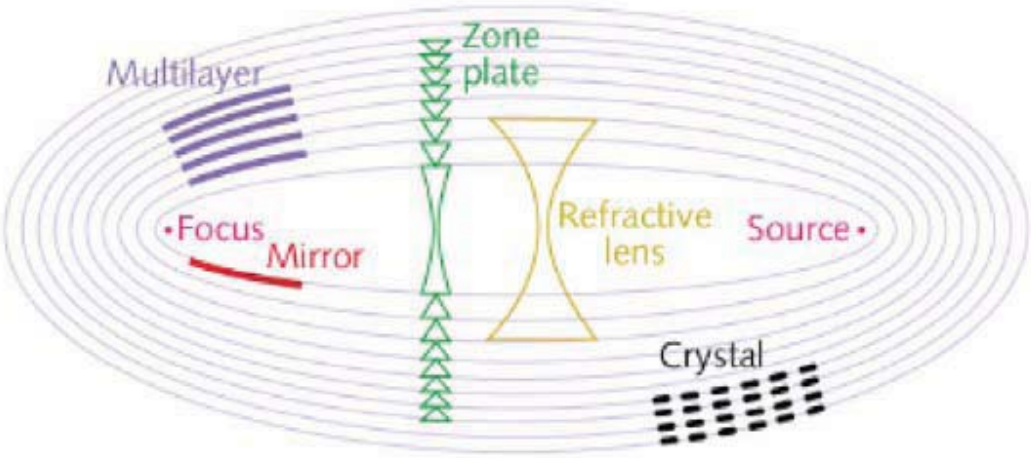


**Figure 2.7** Schematic illustration of various X-ray optical elements. Reproduced from Bouvet et al. (2007).

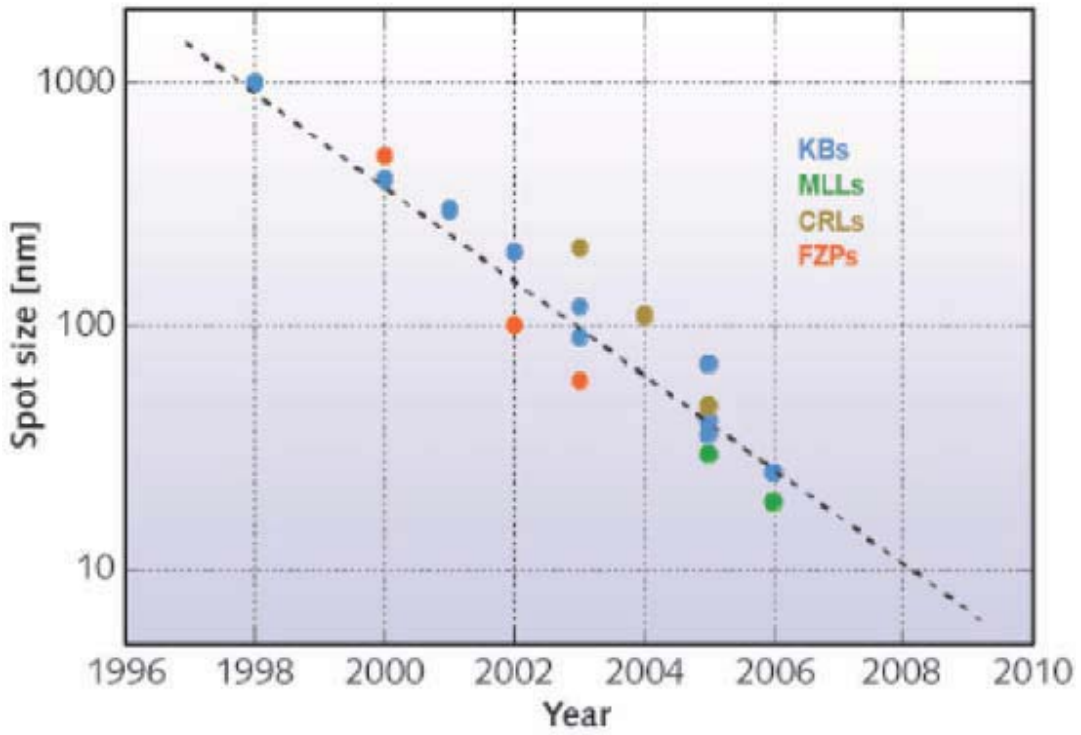


**Figure 2.8** Historical evolution of the measured spot size for different hard X-ray focusing elements. KB: Kirkpatrick-Baez mirror pair; MLL: multilayer Laue lenses; CRL: compound refractive lenses; FZP: Fresnel zone plate. Reproduced from Bouvet et al. (2007).

A classical way of focusing an X-ray beam is using mirrors. To achieve total external reflection of the high-energy X-rays, the incident angle has to be extremely small, typically around 0.5 degrees, a value which reduces for higher energies. The mirror thus acts as a low-pass, i.e. it filters out high energy X-rays, an effect which can be useful for e.g. the elimination of higher harmonics from the monochromatized beam. The focusing effect of a mirror always originates from the way it is curved. Two designs are commonly used. A toroidal mirror is curved in two directions, called tangential and sagittal.

The Kirkpatrick-Baez (KB) design uses two separate elliptical mirrors, each of which focuses the beam in one direction. The most prominent advantage of KB mirrors is the ability to capture the

primary beam in a large collection angle and focus it with high transmission efficiency in an achromatic manner down to μm or sub-μm diameters. Another advantage is that they can be combined with bent graded multi-layers, where alternating layers of a high and low electron density material are deposited by a lateral thickness gradient on the surface of the substrate to account for the variation of the Bragg angle, which allows mono-chromatisation and focusing at the same time (Hignette et al., 2005).

## 2.3 High pressure and high temperature experiments

### 2.3.1 Diamond anvil cell

When a material is pressurized using two opposed anvils, a uniaxial force is applied on the sample. Pressure undergone by material is dependent on applied force and the sample contact with the surface. Fortunately, the Re or W gasket helps to transform this uniaxial pressure into a hydrostatic pressure.

The best material for the anvils is the diamond because of: its extreme hardness (10 in the hardness scale) and it is transparent over a large range of wavelengths (from the ultraviolet up to the far infrared). The diamond transparency allows us to do spectrometric analyses and in-situ observations. Diamond anvil cells are generally made of tungsten carbide (WC) or steel. Physical properties of diamond and WC allow big conical opening of the seat for diamond cells. Thanks to conical opening and transparency of diamond, laser heating of sample and X-ray diffraction are possible for high pressure and high temperature conditions. The main inconvenient for the DAC is the little size of the sample, ~50-100 μm in diameter.

Le Toullec and Chervin refined the concept of "membrane" diamond anvil cell (Le Toullec et al., 1988; Chervin et al., 1995). These DACs allow performing X-ray diffraction at high pressure and high temperature with a large diffraction cone. These cells have been optimized to obtain an opening at the bottom of diamond very large. The pressurization system is separated from the body of the cell. Pressure is transmitted to the diamond by a steel membrane blown up with helium gas. It is injected onto the membrane with an external pump. During my thesis I used both Le Toullec and Chervin cell (Fig. 2.9 and 2.10-2.11 respectively).

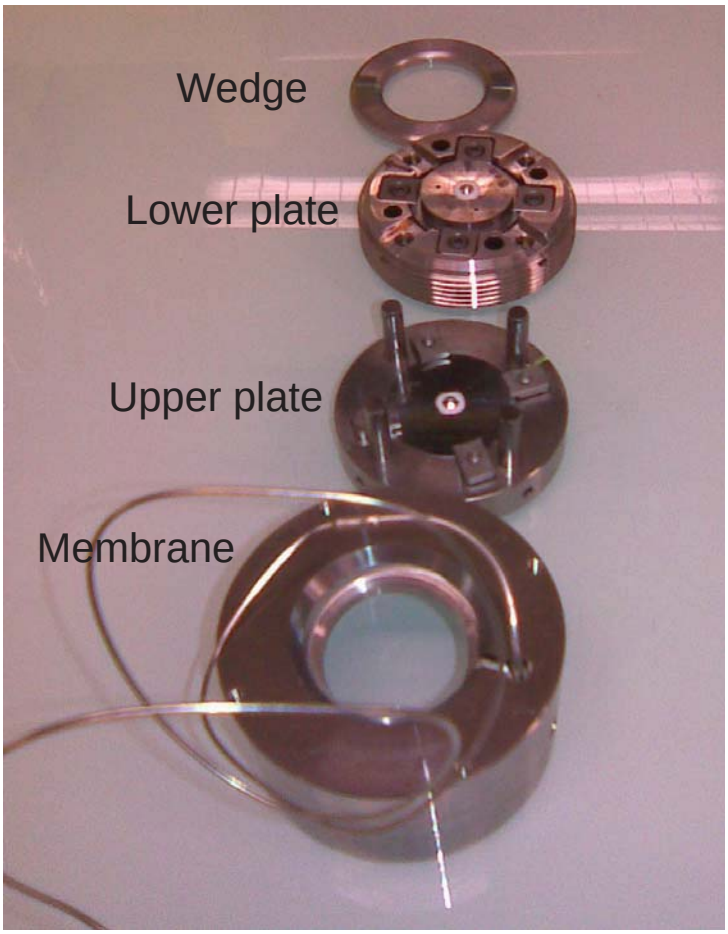


**Figure 2.9** Diamond anvil cell, Le Toullec type.

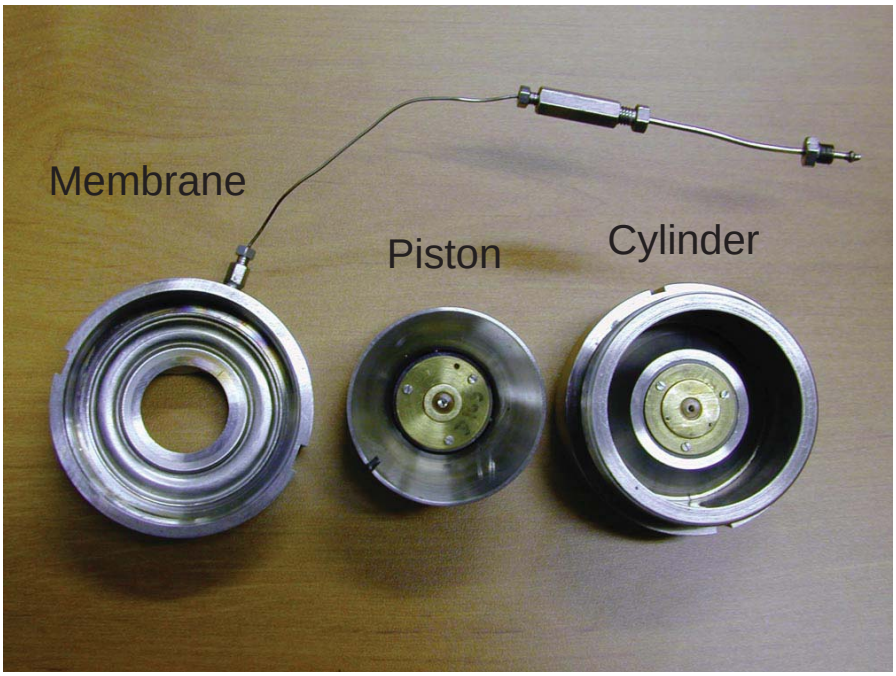


**Figure 2.10** Diamond anvil cell, Chervin type.

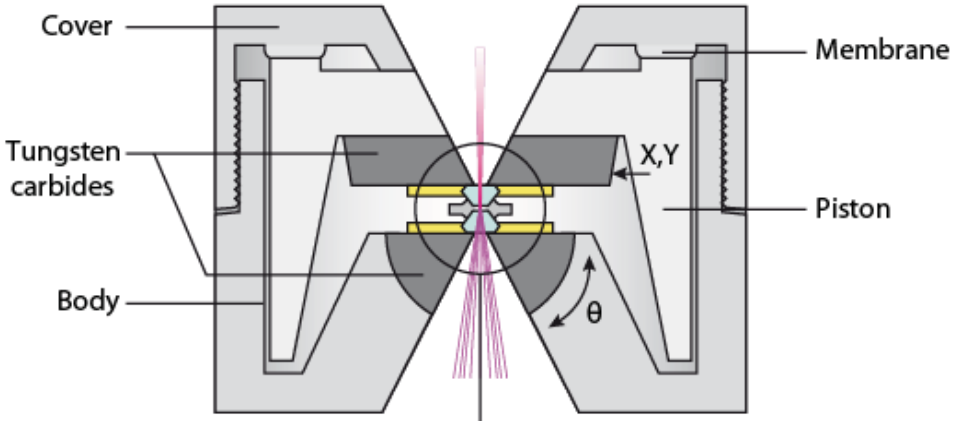


**Figure 2.11** Schema of a DAC Chervin type.

### 2.3.2 Diamonds and sample loading

The choice of the diamond culet is directly linked to the maximum pressure applicable. The, so-called “bevel” diamonds allow to obtain very high pressures by truncating the diamond edges in order to prevent the contact during deformation at high pressure. These bevels, with internal diameter of 70 or 100 μm and external diameter of 300 μm, allow us to reach pressures higher than 70 GPa.

The gasket provides a radial constraint to the sample. It prevents the diamonds to touch each other and the increase of pressure, because plastic deformation of the gasket absorbs part of deformations. In this study I used tungsten or rhenium gaskets, suitable for high pressure, with an initial thickness of about 250 μm.

Firstly, we have to pre-indent the gasket with the diamonds using a membrane pump (Fig. 2.12). Thickness changes from 250 μm to ~40-45 μm. After decompression, we drill a hole in the centre using the laser drilling system available at the ERSF. Ideal diameter of hole is function of the culets size and target pressure. Once the gasket is drilled, it is replaced into the DAC respecting its initial direction to minimize the risk of break diamonds at high pressure (Fig. 2.13).


**Figure 2.12** Membrane pump for diamond anvil cell.

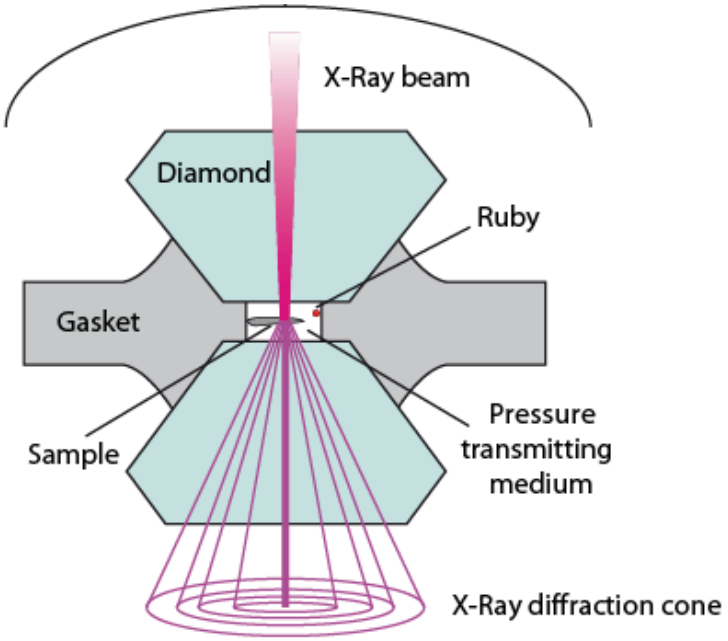


**Figure 2.13** Schema of a classical loading in the DAC.

The sample should be significantly smaller than the gasket hole to leave room for the transmitting medium and to prevent the contact among the diamonds. In this study we used glass pieces or pellets made of powder samples as starting materials.

### 2.3.3 Pressure transmitting medium

In order to obtain correct information about structure, elastic and lattice parameters for phases present in the sample at high pressure, it is required to limit constraints deviations that move pressure from hydrostaticity. To keep hydrostaticity, uniaxial and radial constraint could not be sufficient; it is preferable to add a liquid pressure transmitting medium. However, any material rest in liquid phase for pressure higher than 12 GPa and ambient temperature. For this reason, at very high pressure it is necessary the use of solid pressure transmitting medium. We can choose among several materials in function of sample and pressure. The more a solid is compressible ("soft") the more its shear modulus is weak, the more the medium can be considered hydrostatic. Moreover, it is preferable do not have chemical reactions between transmitting medium and sample. For this, rare gases in the solid state are considered the best materials (e.g. He, Ar, N). We can also use salts or oxides as MgO, $Al_2O_3$ or $SiO_2$; during my experiments I used MgO (chapter 3), NaCl or KCl (chapters 4-5). Briefly, we have to choose materials in function of experiments.

We used the pressure transmitting medium as an internal pressure standard mixing standard and sample.

### 2.3.4 High temperature and temperature gradient

We can use two types of laser, $CO_2$ or YAG laser in function of the sample characteristics. Wavelengths are 10.6 and 1.06 μm for $CO_2$ and YAG laser, respectively. They produce different size of heating laser spot. I will present briefly the YAG laser, because it was used during the experiments. It works by interaction with valence electrons of metals or transition elements, e.g. Fe in $(Mg,Fe)SiO_3$. The YAG laser is focused on the sample surface with a diameter lower than 10 μm and then it produces very high gradient of temperature. The YAG laser does not heat white oxides, and for this is ideal for pressure transmitting medium as NaCl, KCl, MgO or $Al_2O_3$. This type of laser is particularly appropriate for extreme pressure, and then for this study. The YAG laser can cause elemental migration under chemical gradient (Soret diffusion), even if the segregation is very limited when the sample is heated between the NaCl insulation layers without additional laser absorber (Sinmyo and Hirose, 2010).

The temperature distribution within the laser-heated sample can be modeled based on the thermal diffusion equation (Li et al., 1996):

$$\rho C \frac{\partial T}{\partial t} = \nabla \cdot k \nabla T + A \qquad (2.1)$$

Where $T$, $\rho$, $C$ and $k$ are temperature, density, specific heat and thermal conductivity of the sample. The absorbed power density is described by $A$.

The accuracy and precision of temperature measurement in the laser heated diamond anvil cell have been much improved in the past with the use of spectral radiometry (Boehler, 1986). This method is adopted in this study. Temperatures are determined by fitting the thermal radiation to the Planck radiation formula, assuming constant emissivity with respect to wavelength:

$$I_\lambda = c_1 \varepsilon (\lambda) \lambda^{-5} / [\exp (c_2 / \lambda T) - 1] \qquad (2.2)$$

where $I_\lambda$ is spectral intensity, ε emissivity, λ wavelength, T temperature, and $c_1 = 2\pi hc^2 = 3.7418 \times 10^{-16}$ W $m^2$, $c_2 = hc / k = 0.014388$ mK, h= Planck constant, c=speed light, k= Boltzmann constant.

## 2.4 X-ray diffraction (XRD)

Thanks to X-ray diffraction of samples we are able to measure volume. It is necessary an X-ray beam focalized and highly energetic, as that of ID27 beamline at European Synchrotron Radiation Facility in Grenoble, France.

### 2.4.1 Principle

Diffraction phenomena are linked to the crystal structure. A crystal is homogeneous and periodic: it is composed of a pattern, a set of atoms arranged in a particular way, and a lattice exhibiting long-range order and symmetry. Crystal structure of a material can be described in terms of its unit cell (a spatial arrangement of atoms).

The unit cell is given by its lattice parameters: the length of the cell edges and the angle between them. Unit cell is defined by three integer vectors, $\vec{a}, \vec{b}, \vec{c}$ forming angles α, β and γ. Unit cell repeats itself parallelly to α, β and γ angles with translator movement to form direct lattice. In particular a lattice plane intersects three or more vertices of the lattice (the basis) and cut three axes $\vec{a}, \vec{b}, \vec{c}$ at distance from origin equal to a/h, b/k and c/l. h, k and l are Miller indices (Fig. 2.14).

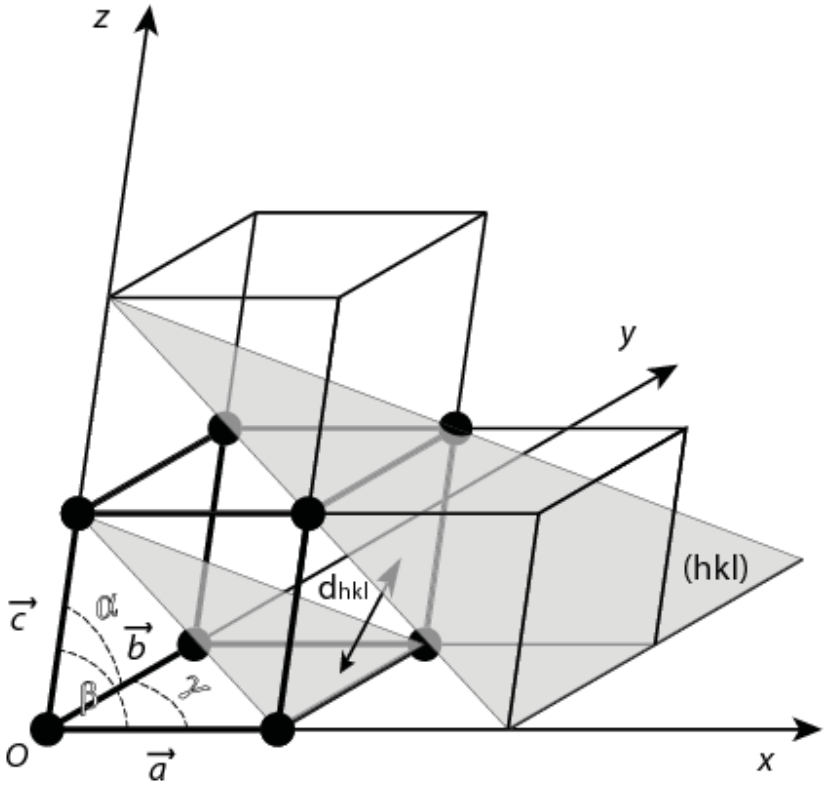


**Figure 2.14** Periodic lattices with parameters and planes of lattice (hkl) equidistant from $d_{hkl}$.

An incident X-ray beam interacts partially in elastic mode with electron orbital of atoms forming crystalline material. Photons scattering from a crystal lattice is directly linked to the equidistance between lattice planes (hkl) in case of constructive interference.

Interference is constructive when the phase shift is a multiple of $2\pi$; this condition can be expressed by Bragg's law (Fig. 2.15):

$$n\,\lambda = 2d_{hkl}\sin\theta \qquad (2.3)$$

where n (an integer) is the "order" of reflection, $\lambda$ is the wavelength of the incident X-rays, d is the interplanar spacing of the crystal, $\theta$ is the angle between incident X-ray and scattering planes.

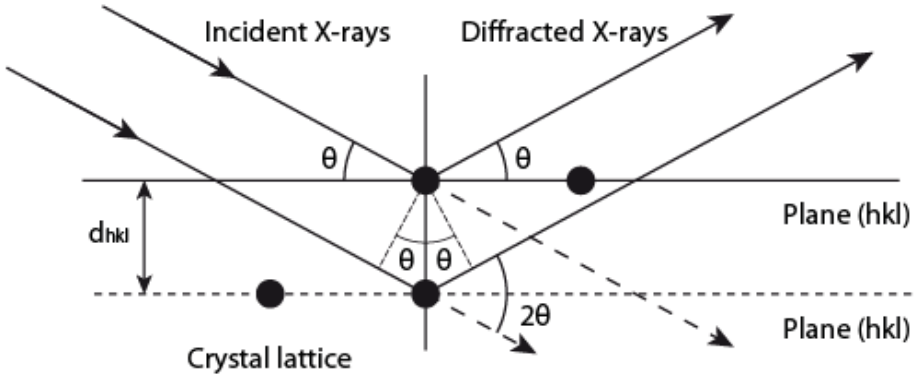


**Figure 2.15** Schema of Bragg's diffraction for a set of planes with spacing distance $d_{hkl}$. X-ray beam deviation is 2θ.

Bragg's diffraction is possible only if $\lambda \leq 2d_{hkl}$. Because $2d_{hkl}$ is only a few Å, λ must be lower or equal to few Å and this is the case of X-rays.

In order to measure d we have two possibilities:

- either we fix λ and determine different θ: this is the angular dispersive diffraction (WDX);
- or we fix θ and use several λ: this is the energy dispersive diffraction (EDX).

In case of angular dispersion, we have to use a monochromatic X-ray beam with, for example, λ= 0.3738 Å at the ID27 beamline of the ESRF.

### 2.4.2 Treatment of data

The pattern of diffraction has to be integrated for all the 2θ values available to give diffraction spectrum (intensity= f (2θ)) exploitable. I used the Fit2d program for integration of patterns (Fig. 2.16a) and GSAS program to treat it (Fig. 2.16b).

Thanks to GSAS program we are able to carry out refinements in Rietveld and Le Bail mode. Diffraction spectra give several information:

- 2θ for each peak, which corresponds to phase $d_{hkl}$. We are able to identify phases with lattice parameters;
- Intensity of peaks gives information about the type and the positions of atoms in the crystal lattice. The refinement of intensities is the Rietveld refinement. Le Bail refinement fits automatically the intensities but doesn't take into consideration atomic positions;
- Volume of phases once Rietveld refinement is done.

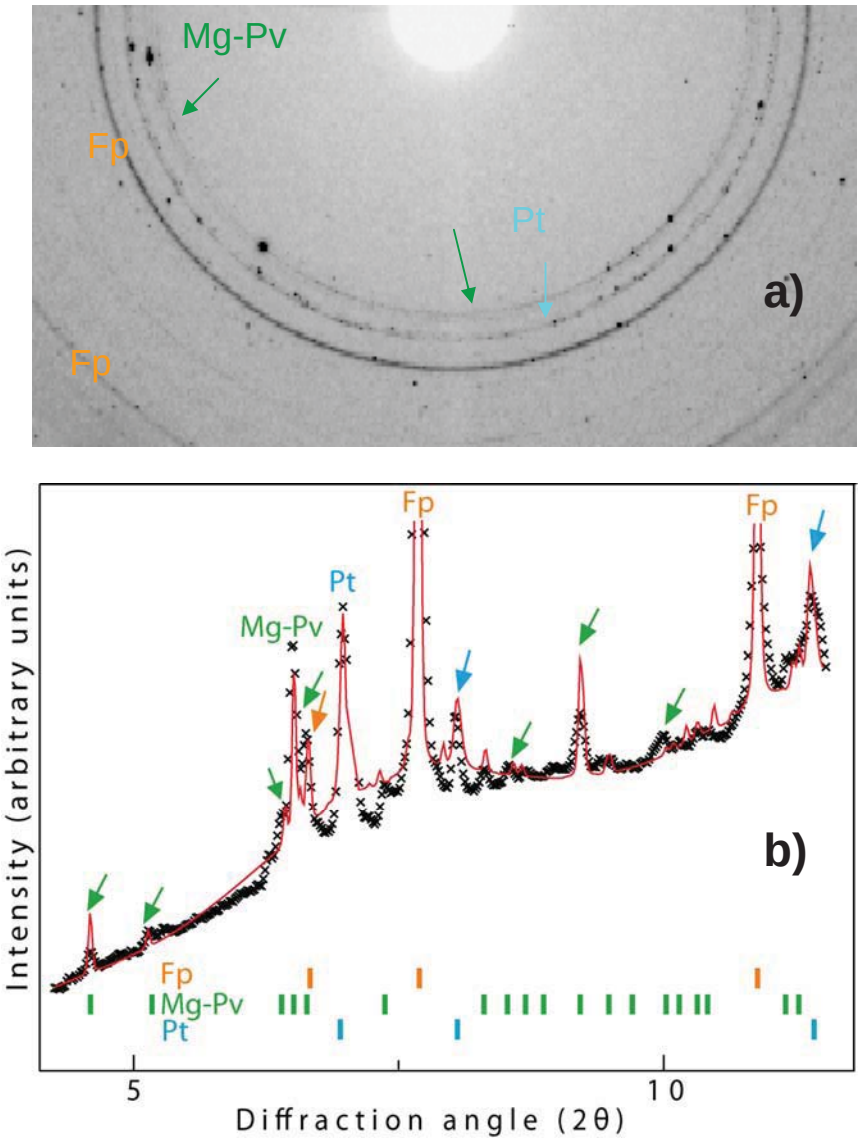


**Figure 2.16** a) X-ray diffraction pattern recorded at 300 K and 50 GPa. Dark spots and rings of diffraction correspond to phase crystallization; b) spectrum corresponding to diffraction pattern (Fig 2.16a), refined (Rietveld method) using GSAS program.

## 2.5 X-ray diffraction (XRD) procedure

### 2.5.1 XRD procedure: study of forsterite melting curve (chapter 3)

The sample properties were investigated *in situ* thanks to the use of the X-ray diffraction set-up available at the ID27 beamline of the ESRF (Mezouar et al., 2005). Wavelength was fixed to 0.3738 Å (HE3084 experiments) or 0.2647 Å (HS3258 experiments). The X-ray beam has been focused to 2x3 $\mu m^2$ using two bent KB-mirrors. Typical acquisition time was 20-30 seconds using imaging plate or MAR345 detector. Position of the X-ray beam was determined from optical observations of the Re-gasket fluorescence. For integration of 2D-images and further data treatment we used the Fit2d (Hammersley, 1996) and GSAS packages (Larson and Von Freele, 1988), respectively.

Melting criteria can be defined according to changes in the X-ray diffraction pattern. We search for first order changes such as (i) disappearance from the imaging plate of diffraction rings of Mg-Pv, (ii) reappearance of these diffraction rings after temperature quench, (iii) major variation of the intensity of diffraction lines on integrated spectra (Figures 3.1 to 3.4). These criteria can be complemented with observations of the sample optical changes as well as analysis of relationship between laser-power and sample temperature. In particular, crossing of flash temperatures (when increasing of temperature is very abrupt) is indicative of sample melting.

For determination of the Pt melting curve, it is the disappearance of the diffraction lines that represents the main criterion.

### 2.5.2 XRD procedure: study of chondrite melting curves (chapter 4)

Ultra-brilliant X-ray beams are now available from Synchrotron ring for in situ investigation of the melting behavior in the laser-heated diamond anvil cell (LH-DAC). We used a membrane-type DAC mounted with 250 μm or 75/300 μm culet-diameter diamonds. Re gaskets were pre-indented to 40 μm or 20 μm and laser-drilled to 80 μm or 50 μm, respectively.

In order to probe the sample properties in-situ, we used the X-ray diffraction set-up available for LH-DAC at the ID27 beamline (Mezouar et al., 2005). Wavelength was fixed to 0.3738 Å. X-ray focusing to better than 2x3 $\mu m^2$ was achieved by two bent KB-mirrors. Typical acquisition time is 20-30 seconds using an imaging plate or a CCD detector. The X-ray beam position was determined from optical observations of the Re-gasket fluorescence. Therefore, combined images of X-ray beam and YAG lasers could be perfectly positioned on the pinhole of the entrance of the spectrometer used for temperature measurements. Integration of 2D-images and further data treatment were performed using the Fit2d and the GSAS packages, respectively.

In general, the onset of melting can be detected using X-ray diffraction by the appearance of a diffuse x-ray scattering band typical of liquids. Such band is easily observed if the sample is composed of relatively high Z elements such as iron (Andrault et al., 2006; Shen et al., 2004). If the sample is composed of low Z-elements, such as is the case for a mantle silicate, the sample thickness should be important to enable observation of the diffuse band. This is not the case of our samples, which are intentionally thin in order to minimize axial thermal gradients.

Additional criteria based on X-ray observations are (1) the rapid re-crystallization of the sample at high temperature, with appearance and disappearance of X-ray spots, indicative of coexistence of crystal and melt. (2) At the same time as solid and liquid coexist, the temperature reaches a plateau while laser power is continuously increased, just before the liquid diffuse scattering

appears and temperature simultaneously increases (Dewaele et al., 2007). In the following we used the fast disappearance of diffraction peaks of the solidus phase and re-crystallization as a sign of solidus temperature and the end of the temperature-power plateau as the sign of liquidus temperature.

### 2.5.3 XRD procedure: study of chondrite (chapter 5)

We performed experiments at high pressure and high temperature using the LH-DAC technique. We used diamond anvils with flat culets of 250 μm diameter or bevel type 100-300 μm culets. We used tungsten gaskets pre-indented to a thickness of 30-45 μm and laser-drilled to diameters of 50-80 μm.

Our procedure for the samples synthesis is as follows: we compressed each sample to the target pressure at ambient temperature. We then adjusted the optical path for the lasers and the temperature measurements, keeping the two lasers at minimum power. We then observed the sample crystallization at a moderate temperature and verified the sample quality (mineralogical content and chemical composition), using X-ray diffraction and X-ray fluorescence (see details below). Finally, we increased the laser power until the liquidus temperature was reached at the center of the sample. The laser power was maintained for a couple of minutes before shut-down. We report typical microphotographs of the recovered samples (Figure 5.2). For some samples, we also performed sample analyzes using scanning electron microscope (JEOL JSM-5910 LV). Prior to the measurement, we immersed the W-gasket in water in order to remove the NaCl pressure medium. We then extracted the sample using a needle and positioned the sample chip on a graphite adhesive foil (Figure 5.3).

We then investigated the sample properties using X-ray diffraction (2.5.3) and X-ray fluorescence (2.7). Some of the X-ray measurements were performed *in situ* in the DAC at high P and T: XRD to monitor the sample evolution during laser heating; X-ray fluorescence (XRF) in order to check the sample composition. However, most of the measurements reported in this study were recorded after pressure release on samples trapped in the W-gasket. It insures a better signal, for XRF in particular, due to the strong absorption of the diamond-windows at low energies. All X-ray measurements were performed at the ID27 beamline of the ESRF. The X-ray beam generated by the ondulator was tuned to 0.3738 Å wavelength and focused by two Kirkpatrick-Baez (KB) mirrors to a 2*2 $\mu m^2$ FWHM spot on the sample.

For X-ray diffraction, we used the MAR345 image plate detector. Typical acquisition time was 20-30 seconds. Diffraction images were analyzed and integrated using the Fit2d program (Hammersley, 1996). We refined phase contents by performing multiphase Rietveld refinements using the GSAS code (Larson and Von Dreele, 1988). We note (i) a weak Ca-Pv signal for some of the samples, firstly because the Ca-Pv amorphorizes partially upon decompression and also because rapid quenching from the molten state could lead to other Ca-rich polymorphs, such as the calcium-ferrite form, and (ii) a weak precision for the determination of Fp contents, since its major diffraction peaks overlap with those of the major Mg-Pv phase.

## 2.6 X-ray fluorescence

Photon is an elementary particle, the quantum of the electromagnetic interaction and the basic unit of light. Photons are emitted in many natural processes. For example, when a charge is accelerated it emits synchrotron radiation. Planck's energy formula

$$E=h\nu \tag{2.4}$$

is used to define the energy of a photon, where E is energy, h is Planck constant and ν is the frequency.

### 2.6.1 Principle of absorption

When a X-ray beam hits a material, photons can interact with it. This interaction is photon/electron or photon/core interaction and is related to one type of physical process: absorption, scattering (Compton or Rayleigh) or pair production (Fig. 2.17).

When an X-ray beam interacts with matter, a certain fraction of the photons will be absorbed inside the material or scattered away from the original path. The intensity $I_0$ of an X-ray beam transmitted through a layer of thickness $x$ and density $\rho$ is reduced to intensity $I$ according to the well-known law of Lambert-Beer:

$$I(x) = I_0 e^{-\mu_L x} = I_0 e^{-\frac{x}{\lambda}} \tag{2.5}$$

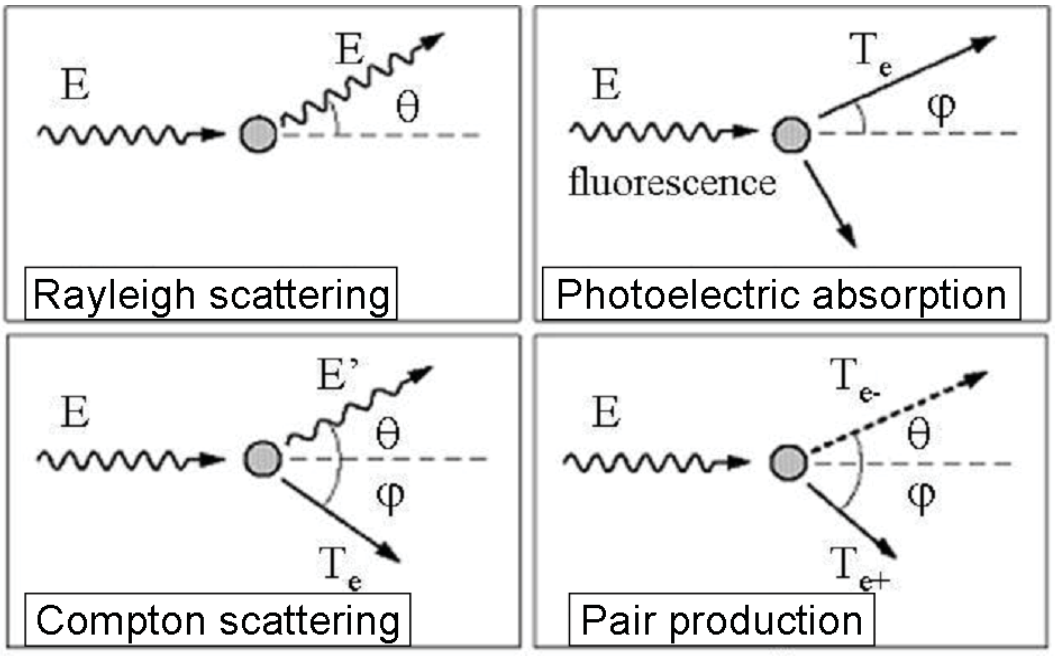


**Figure 2.17** Different processes of photon-matter interaction.

Where $\mu_L[cm^{-1}]$ is called the linear attenuation coefficient, $\lambda = 1/\mu_L[cm]$ is the attenuation length and $\mu = \mu_L/\rho[cm^2/g]$ is the mass attenuation coefficient. In the energy range of 1-100 KeV the mass attenuation coefficient can be described as:

$$\mu = \tau + \sigma_R + \sigma_C \tag{2.6}$$

where $\tau$(E,Z) is the photo-electric effect, $\sigma_R$(E,Z) is the Rayleigh (elastic/coherent) scattering and $\sigma_C$(E,Z) is the Compton (inelastic/incoherent) scattering (Van Grieken and Markowicz, 2002). At most X-ray energies, the mass attenuation coefficient $\mu$ is a smooth function of energy, with a value that depends on the sample density $\rho$, the atomic number Z, atomic mass A, and the X-ray energy E approximately as (Newville, 2009):

$$\mu \approx \frac{\rho Z^4}{AE^3} \tag{2.7}$$

When the sample consists of a mixture of several chemical elements, the mass attenuation coefficient $\mu$ can be calculated from the mass attenuation coefficients of the $n$ constituting elements:

$$\mu(compound) = \sum_{i=1}^{n} w_i \mu_i \tag{2.8}$$

where $w_i$ is the weight fraction of element $i$.

Fig. 2.18 shows the contributions of the photo-electric, Rayleigh and Compton scattering to the photon mass attenuation coefficient of *Fe* within the energy range of $10^{-3}$-$10^{4}$ MeV. A sharp absorption K-edge can be observed at 7.112 keV.

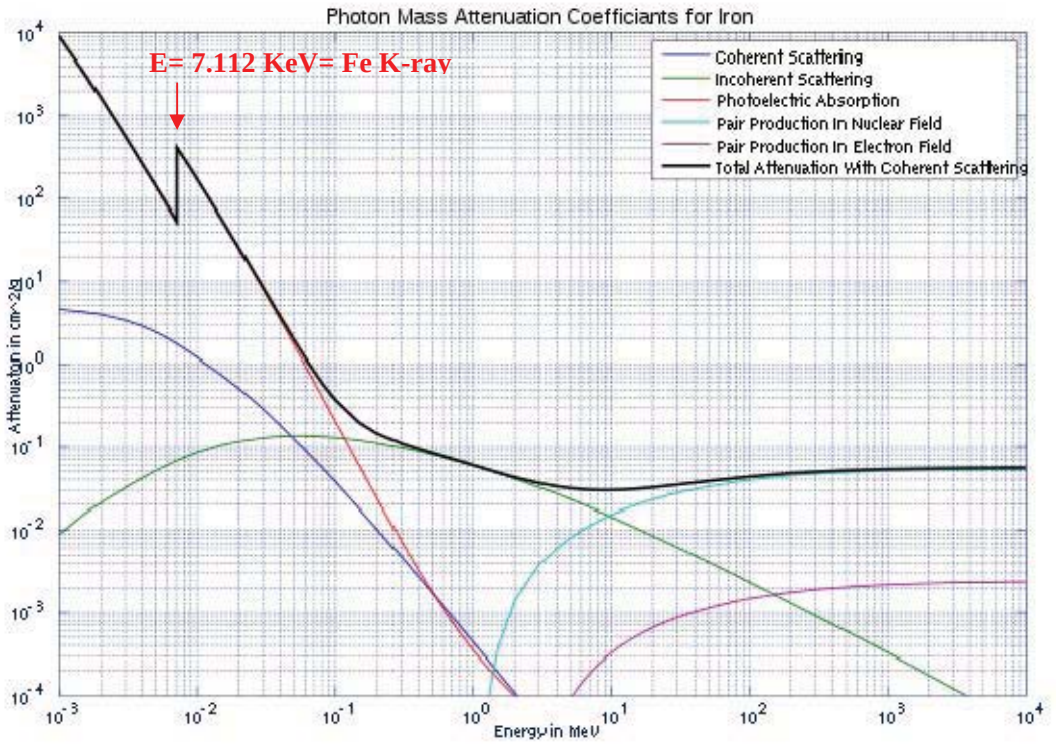


**Figure 2.18** Mass attenuation coefficients for iron provided by NIST's XCOM database. E=7.112 KeV is coicident to iron X-ray emission energy and correspond to a peak of Fe in a spectrum of fluorescence.

Each type of interaction is associated with an effective cross section depending on incident photon energy and atomic number *Z* of the target atom. These interactions in function of *E* and *Z* are shown in Fig. 2.19, where $\sigma_{ph}$, $\sigma_c$ and $\sigma_{pair}$ are the effective cross section for photoelectric effect, Compton effect and pair production respectively. Cross section for photon interaction with matter corresponds to the sum of the cross sections:

$$\sigma_{tot} = \sigma_{ph} + \sigma_c + \sigma_{pair} \tag{2.9}$$

Probability of interaction for Compton effect is quite independent of the target atomic number. On the other hand, photoelectric effect and pair production are proportional to the atomic number. Then, the range of energy corresponding to Compton effect is more important when target atomic number is little.

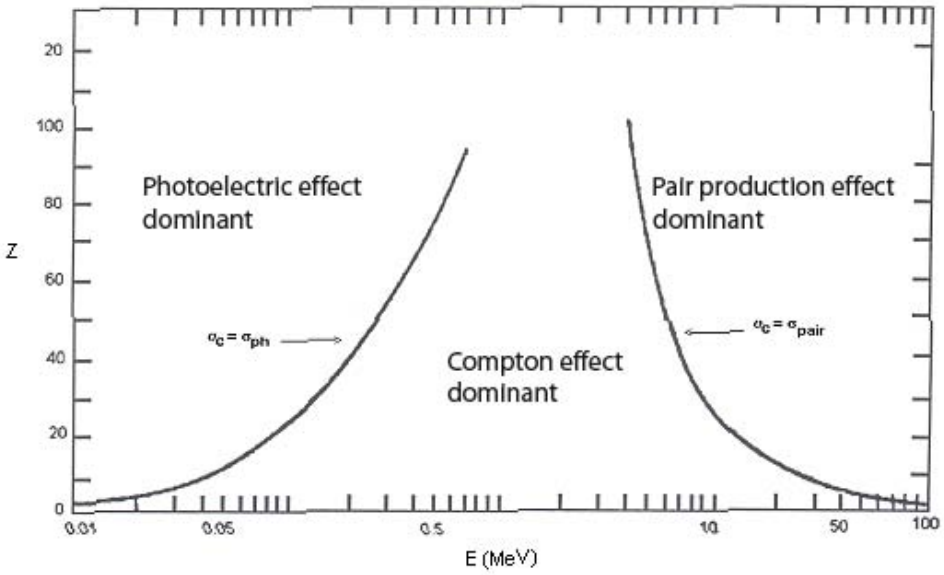


**Figure 2.19** Photon cross sections of interaction with the matter.

### 2.6.2 Photoelectric effect

In the photoelectric effect, the incoming X-ray photon with energy $E_x$ interacts with a bound atomic electron and is absorbed as shown in Fig. 2.20a. The excited atom emits a photoelectron with energy $E=E_x-E_{shell}$, where $E_{shell}$ is the binding energy of the electron. As a secondary effect, the hole in the atomic shell is immediately filled by less bound electrons from outer shells, resulting in a cascade process involving the emission of fluorescence X-rays characteristic for the absorbing atom as in illustrated in Fig. 2.20b. A fraction of the absorbed energy is also emitted by ejection of Auger electrons. The intensity of this characteristic radiation is directly related to the amount of each element in the material (Beckhoff et al., 2005).

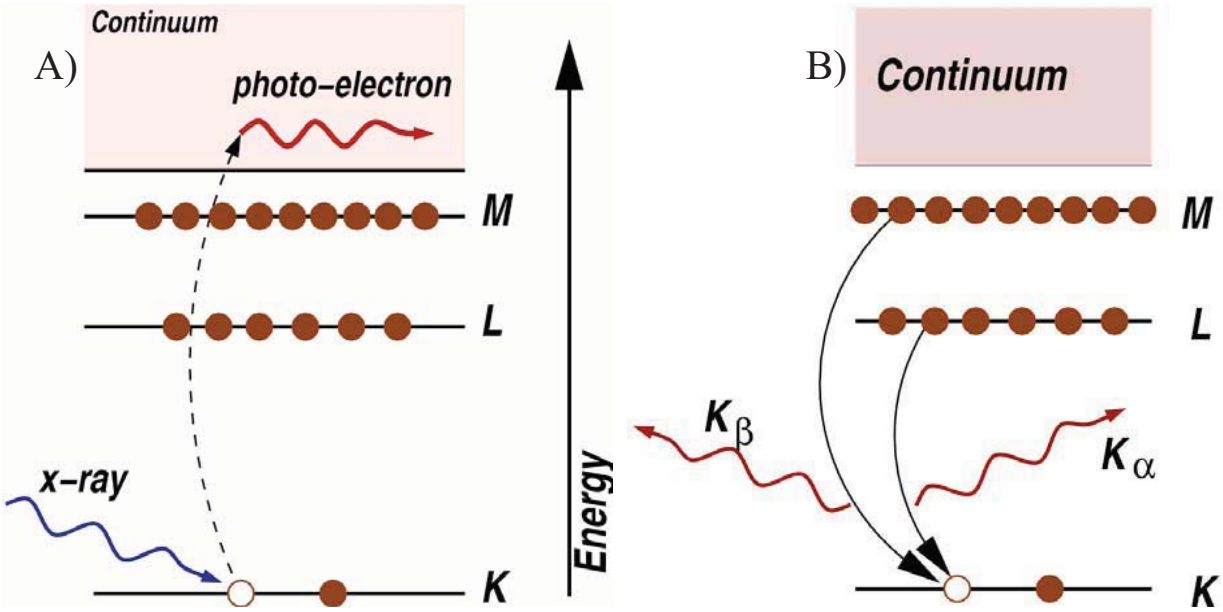


**Figure 2.20** In Fig 2.20A is shown the photo-electric effect, in which an X-ray is absorbed and a core-level electron is promoted out of the atom. When a less bound electron from the L or M shell falls back to a hole created in the K-shell by the photo-electric effect, causing X-ray fluorescence as a secondary effect (fig. 2.20B). Reproduced from Newville (2009).

### 2.6.3 Fluorescence yield

An atom in an excited state emits an X-ray photon in its first transition rather than an Auger electron. For K-lines is given by:

$$\omega_K = \frac{\sigma_K^X}{\sigma_K^I} \tag{2.10}$$

where $\sigma_K^X$ , is the efficient section to producing emitted photons and $\sigma_K^I$ is the efficient section of ionization (Fig. 2.21). The measurement of the fluorescence yield is more complicated for the higher orbitals because are composed of several sub-shells. What's more, Coster-Kronig transitions can occur: Coster-Kronig transition is an Auger transition in which the vacant electron level is filled by an electron from a higher sub-shell of the same shell. In case of absence of Coster-Kronig transitions, the yield for the sub-shell I of the s-shell (s=K, L, M,…) is given by:

$$\omega_{S_i} = \frac{\sigma_{S_i}^X}{\sigma_{S_i}^I} \tag{2.11}$$

And total yield $\omega_s$ of the s-shell is:

$$\omega_S = \sum_{i=1}^{K} N_{S_i} \omega_{S_i} \tag{2.12}$$

Where $N_{S_i}$ are the efficient sections of ionization for the sub-shell I of the s-shell and corresponds to:

$$N_{S_i} = \frac{\sigma_{S_i}^I}{\sum_i \sigma_{S_i}^I} \tag{2.13}$$

moreover the sum of $N_{S_i}$ is equal to 1.

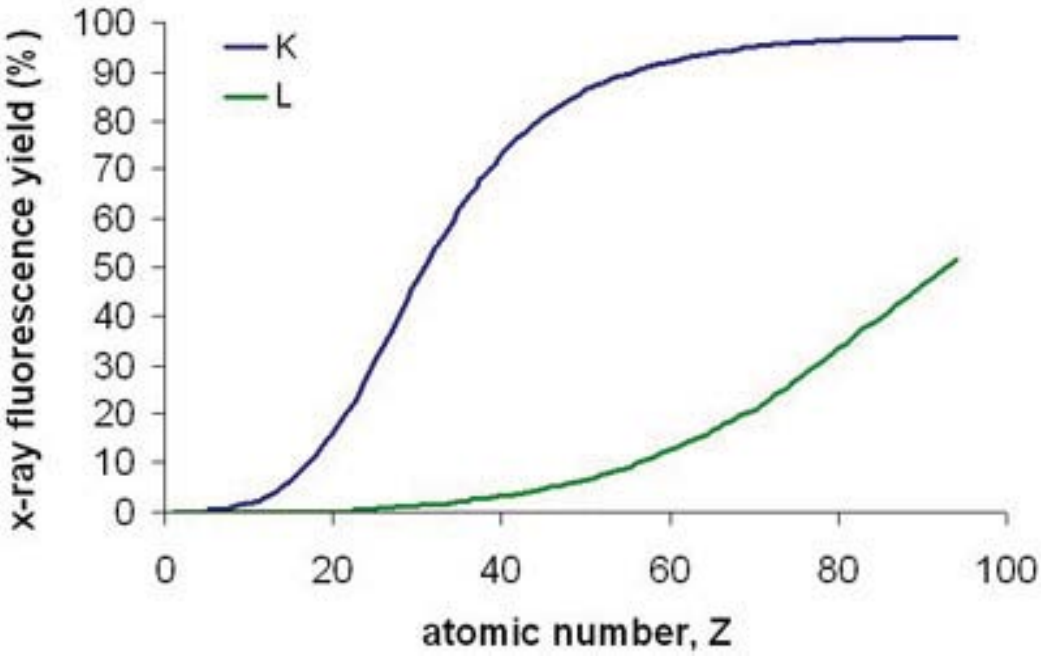


**Figure 2.21** X-ray fluorescence yield (%) in function of the atomic number (Z). It is clear that the yield for the light elements is very low, and this is reflected in achievable sensitivity for these elements (Z is 20 and 26 for Ca and Fe, respectively).

### 2.6.4 Anisotropic fluorescence emission

While photoelectric interactions result in an isotropic emission of characteristic radiation, scattering produce photons having highly anisotropic angular distributions. Therefore the ratio of fluorescence/scatter intensities can be strongly influenced by the choice of excitation/detection geometry. Quantitatively, the intensity of Rayleigh/Compton scattered radiation can be characterized by the so-called differential scattering cross-sections $d\sigma / d\Omega$, which characterize the angular distribution for the scattered photons. For the description of a linearly polarized photon beam, the local coordinate system is chosen in such a way that the photon beam (heaving an initial propagation vector $\overrightarrow{k_0}$ ) travels along the Z-axis prior to the interaction and its (net) electric field vector $\overrightarrow{\varepsilon_0}$ is parallel with the X-axis (Fig. 2.22). After the scattering event, the new

direction of photon propagation is characterized by the (unit) propagation vector $\vec{k}_1$ and the net vector $\vec{\varepsilon}_1$ (Vincze, 2004).

In case of linearly polarized radiation having a degree of polarization *p* with respect to the reference plane XZ, the expression for the Rayleigh ($d\sigma_R / d\Omega$) and Compton ($d\sigma_C / d\Omega$) differential scattering cross-sections are, respectively, given by:

$$\frac{d\sigma_R}{d\Omega}(\theta,\phi,E) = \frac{d\sigma_T}{d\Omega}(\theta,\phi)F^2(x,z) = \frac{r_e^2}{2}[2-\sin^2\theta(1-p+2\cos^2\phi)]F^2(x,Z) \qquad (2.14)$$

$$\frac{d\sigma_C}{d\Omega}(\theta,\phi,E) = \frac{d\sigma_{KN}}{d\Omega}(\theta,\phi)S(x,z) = \qquad (2.15)$$

$$= \frac{r_e^2}{2}\left(\frac{E}{E_0}\right)^2\left[\frac{E}{E_0}+\frac{E_0}{E}-\sin^2\theta(1-p+2\cos^2\phi)\right]S(x,Z) \qquad (2.16)$$

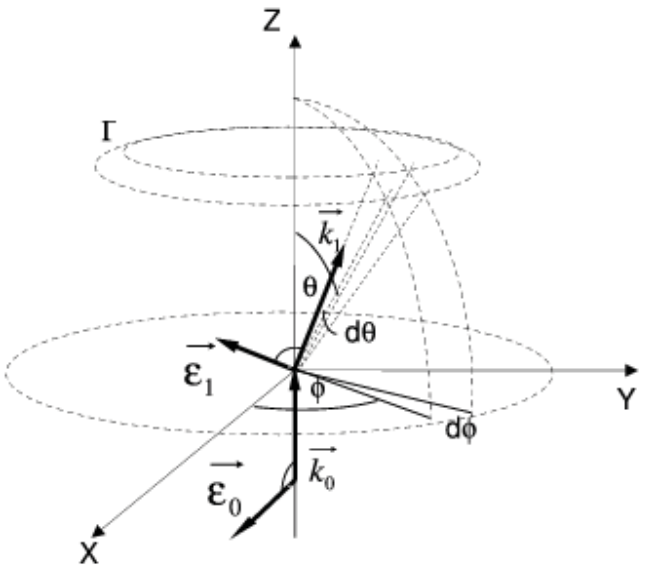


**Figure 2.22** The coordinate system attached to the photon used to describe the scattering phenomenon (from Vincze et al., 1999).

where $d\sigma_T / d\Omega$ denotes the Thomson, $d\sigma_{KN} / d\Omega$ the Klein-Nishina (1928) differential cross-section. $F(x,Z)$ and $S(x,Z)$ are the atomic form factor and the incoherent scattering function respectively, for an element with atomic number *Z*. $x = \sin(\theta/2)E(keV)/12.39$ is the momentum transfer of the photon and $r_e$ is the classical electron radius (Vincze, 2004).

The previous equations show that $\frac{d\sigma_R}{d\Omega} = 0$ and that $\frac{d\sigma_C}{d\Omega}$ reaches a minimum for *p*=1, $\theta$=90° and $\phi$=0°. Since the degree of linear polarization can approach 99.8% at 3rd generation synchrotron sources and also the angle between the incoming beam and the scattering angle is not exactly 90° for the complete detector surface, implying that there will still be an influence of the Rayleigh and Compton scatter. However, for X-ray fluorescence experiences in this study, the angle between the incoming beam and the detector in the plane of the synchrotron (assuming *p*~1) is set to ~60° (see chapter 5 for more details).

Photoelectic effect is dominant for low energy photons, in particular for elements with high *Z*. The cross section per atom at the K-line is:

$$\sigma_{ph}^{K} = \sigma_{Th} \frac{\alpha^4}{2} Z^5 (2/\varepsilon)^{7/2} \tag{2.17}$$

Where $\sigma_{Th}$=0.665 barn (1 barn=$10^{-24}$cm$^2$) is Thomson cross section per electron and $\alpha$=1/137 is the fine structure constant. Independently of lines this cross section can be estimated with:

$$\sigma_{ph} \propto \frac{Z^{4.35}}{E^3} \tag{2.18}$$

Photoelectric effect decreases at increasing energy of the incident photon for a given element (this is important for quantification of chemical contents). Most photoelectrons are emitted in the direction of polarization of the incident photon.

### 2.6.5 Processing of X-ray fluorescence data

Micro X-ray fluorescence (micro-XRF) has been developed very rapidly since 1990, mainly due to the use of synchrotron radiation (SR) (Janssens et al., 2010). Nowadays, micro-XRF is a well-established, non-destructive analytical method in a large variety of fields of application. Since the interaction of individual photons of a specific energy with individual atoms of specific atomic number can be very well described, in principle, any form of XRF has the potential to be used for quantitative analysis. Several calibration schemes and variants thereof have been developed since the 1970s and are used in many commercial and self-built instruments. These approaches are either based on the use of extensive sets of calibration standards that are similar to the materials to be investigated (so-called type standards) and empirical calibration models or make use of theoretical models that describe the interaction between X-rays and matter. These theoretical models allow the use of a smaller number of calibration standards. It is possible to calculate the theoretical X-ray intensities using fundamental parameters (e.g. tube excitation voltage, X-ray optical geometry). The fundamental parameter (FP) uses the calculated theoretical intensities and the measured intensities to determine the composition of a sample. In order to use a conventional FP method, one needs to have one or more standards with a matrix similar to the unknown samples or at least a set of standards that contain the analyze elements. There are many situations in which “standards” do not exist. This is particularly true in laboratories developing new materials and those involved in one of a kind and/or trouble shooting production problems. For this reason, the standardless fundamental parameter method has been developed. During the experiments on XRF (chapter 5), we used FP and standardless methods. When X-ray fluorescence analysis is performed with solid state detectors (e.g. Si(Li)) as shown in Figure 2.23,

method of choice is the energy-dispersive XRF (ED-XRF). Due to the relatively low resolving power of solid state detectors, the process of evaluating ED-XRF spectra is prone to many errors and requires dedicated software.

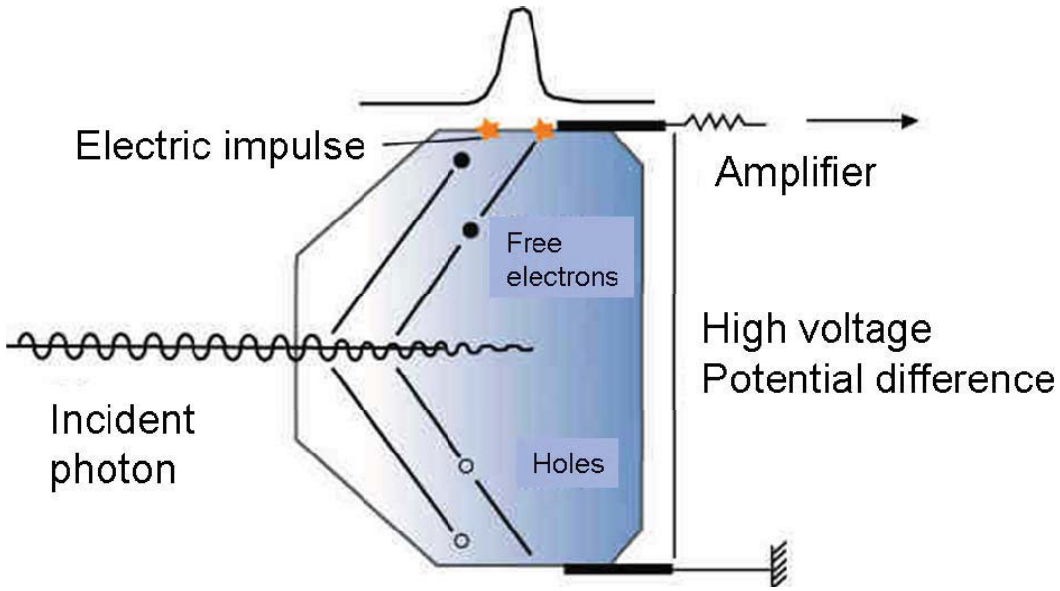


**Figure 2.23** Schematic diagram of an Energy Dispersive X-Ray Si(Li) detector. Incident photons create pair electron vacancies. Electrons emit an electric signal which is amplified and analyzed.

Whatever the detector used, it is essential a collimator to filter noise signals (scattering phenomena). In this work we used an Ag collimator. The need for a spectrum evaluation procedure which can be applied in an increasingly unsupervised manner, without having to compromise on the accuracy of the net peak area determination is critical for micro-XRF where vast amounts of spectra need to be processed. Therefore, several softwares were developed: e.g. AXIL (Analysis of X-Ray Spectra by Iterative Least Squares) which is based on the non-linear fitting of a mathematical function (Vekemans et al., 2004). PyMca (Python multichannel analyzer) program, developed by the Beamline Instrumentation Software Support (BLISS) group of the ESRF (Solé et al., 2007), was used in this work. This fitting application is based on the Levenberg-Marquardt algorithm (Levenberg, 1944; Marquardt, 1963). For the end user, PyMca is

a ready to use, and in many aspects state-of-the-art, set of applications implementing most of the needs of X-ray fluorescence data analysis. It allows the processing of large numbers of individual spectra generated during micro-XRF mapping experiments as well as manipulation and presentation of the resulting elemental maps in a variety of ways. Its implementation of a complete description of the M-lines of the elements is particularly helpful for analysis of data collected at low energies.

Measurement of intensity corresponds to calculating the area under the peak of fluorescence using a Gaussian function after subtracting background noise (Fig. 2.24). For these measurements I used PyMca program (Solé et al., 2007) thanks to the FP method.

A Gaussian peak is characterized by three parameters: the position, width and height or area. It is desirable to describe the peak in terms of its area rather than its height because the area is directly related to the number of X-ray photons detected, while the height depends on the spectrometer resolution. The first approximation to the profile of a single peak is then given by:

$$\frac{A}{s\sqrt{2\pi}}\exp\left[-\frac{(x_i - x_0)^2}{2s^2}\right] \tag{2.19}$$

where $A$ is the peak area (counts), $s$ the width of the Gaussian expressed in channels and $x_0$ the location of the peak maximum. The full-width-half-maximum (FWHM) is related to $s$ by FWHM=2.3548 $s$.

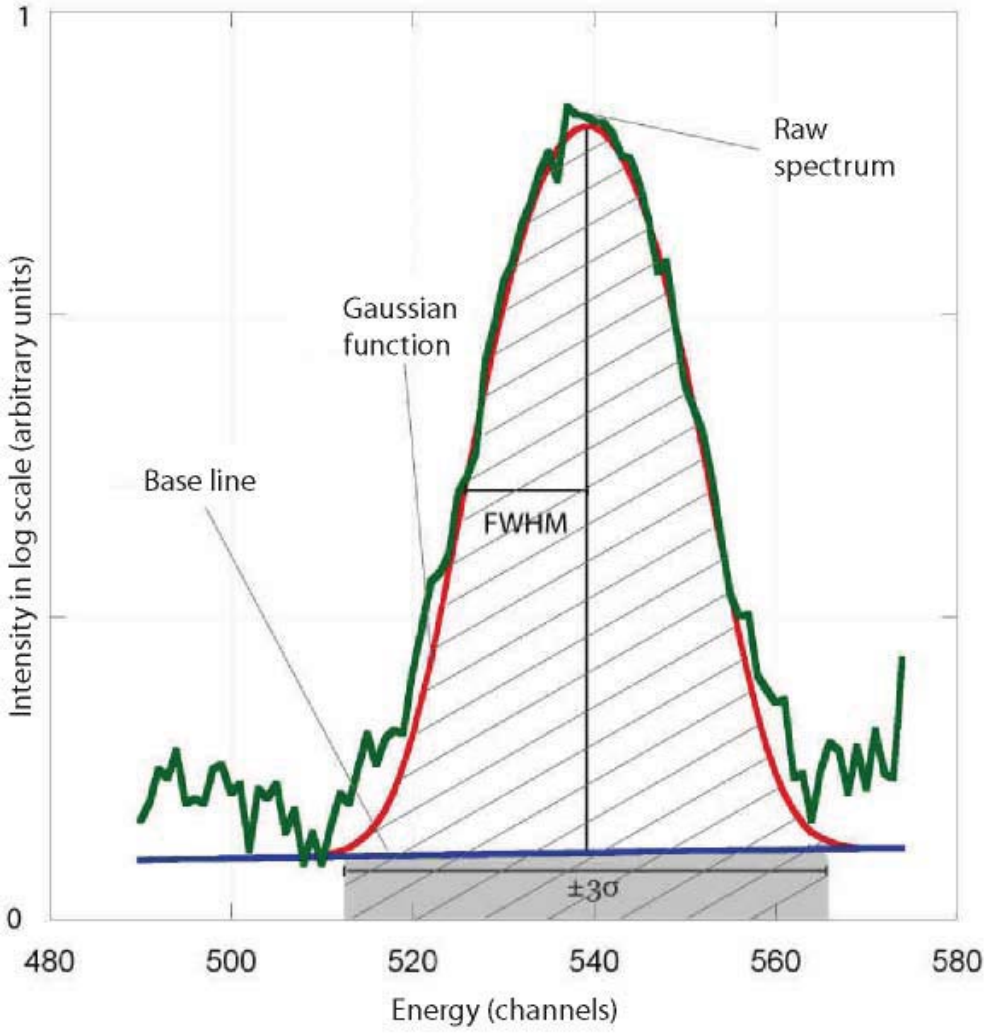


**Figure 2.24** Example of intensity measurements for a peak of fluorescence. Green curve corresponds to the raw spectrum. Red and blue curves are Gaussian function and base line respectively (from PyMca). Hatched zone is the area under the Gaussian after subtracting background noise (gray zone).

We are able to quantify X-ray fluorescence for an element only if its intensity is:

$$I_i = 3\sqrt{I_B} \tag{2.20}$$

where $I_i$ is the intensity of the element and $I_B$ intensity of the background noise.

### 2.6.6 Quantification methods

#### 2.6.6.1 Semi-quantitative elemental analysis

Analytical determinations with accuracy of 30-50% are known as semi-quantitative. A semi-quantitative analysis requires the measurement of a single multi-element standard reference material. Afterward, an element yield can be calculated for each element and element yield curves can be rendered, providing valuable information on how many fluorescence counts for a specific element are generated per second in the targeted area by the micro-beam. If standard reference material which contains an element $I$ in a concentration $C_i$ generates $I_i$ counts while measuring during a life time $T_{real}$, then the elemental yield $Y_i$ is for example given by:

$$Y_i = \frac{I_i}{T_{real}} / C_i \tag{2.21}$$

The elemental yields for elements that are not present in the calibration standard can be graphically derived by fitting a curve through the data points obtained for the calibration standard in a diagram where the intensity is plotted versus the analyte mass. These relative sensitivity factors will vary for each element depending on the photoelectric cross-section and the operating conditions selected for the determination. Concentrations of analyte in unknown samples can be estimated by dividing the measured netto line intensities by the elemental yields for the specific element under investigation. Because elemental yields are dependent on the specific operating conditions, they should be re-established whenever adjustments or modifications are made to instrumental parameters.

On the other hand, analytical determinations with accuracy of 10% are known as quantitative analyses. Below, four calibration approaches for quantitative analysis are discussed: (1) external standardization (2) internal standardization (3) fundamental parameter approach and (4) Monte

Carlo simulation. Statistical error calculation of the three procedures (Cauzid et al., 2006), shows that the standardless quantification method yields more accurate results than the internal or external standard procedures.

### 2.6.6.2 External standardization

In quantitative analysis via external standardization, several multiple concentration standards containing the analyte(s) of interest are involved. Scans of these standards are performed before, during, and after samples are scanned under the same operating conditions. The fluorescence intensities are obtained and then a calibration curve of intensity vs. concentration generated. Matrix-matched standards are required for improved accuracy which features same thickness, density and bulk composition. While this is the most accurate approach, matrix matched standards that are spatially homogeneous at the $\mu m$ scale are scarce.

### 2.6.6.3 Internal standardization

In this type of standardization one of the elements present in the sample is used as an internal standard, establishing that the Kα X-ray peak intensity of this element corresponds to a known concentration (Menez et al., 2002; Philippot et al., 2001). This method has been used to establish a calibration procedure potentially appropriate to all samples, for conducting quantitative analysis of fluid inclusions (Menez et al., 2002). Is important to point out that, owing to the strong sensitivity of light elements to absorption, the propagated error on calculated concentrations of the heaviest elements (Z>Mn) can be minimized using light elements (e.g. Cl or Ca in Menez et al., 2002) as internal standard. The internal standard method is based on the addition of an element (or a compound) in a known, constant proportion to a (series of) specimen(s), in order to

minimize the effect of variations in matrix effects. The same proportion has to be added to the standards as well as to the unknowns. The compound added is called an added internal standard. For the added internal standard, pure elements, pure compounds, mixtures, and solutions can be used. When using solutions or mixtures, it is vital that their composition be constant. There is basically only one selection criterion for the compound added: the added internal standard should have at least one characteristic line of sufficient intensity, which is subject to similar matrix effects as the analytical line(s) of interest.

### 2.6.6.4 Fundamental parameter (FP) methods

The expected count rate of an element group of lines can be written as:

$$A = I_0 C \frac{\Omega}{4\pi} \sum_j R_j'' \tag{2.22}$$

where $I_0$ is the incident beam rate, $C$ is the mass fraction of the element in the sample, $\Omega/4\pi$ represents the detector geometric efficiency and $R_j''$ the relative intensities of the lines. Measured the areas $A$, the only unknown terms to calculate the mass concentrations are the incident photon flux and the detector efficiency. These parameters are given by the user asking the program (PyMca in this work) to take one of the matrix elements as internal reference. Influence of secondary fluorescence excitation is neglected in all these calculations and should be estimated with standards or evaluated by Monte Carlo methods. This method needs the use of a standardization (external or internal) or standardless (such as in this work) method to verify relative intensities of the fluorescence lines.

### 2.6.6.5 Monte Carlo methods

Monte Carlo methods are numerical methods of statistical simulation. In XRF, they are sometimes used when a problem can be only (or more successfully) described by statistical models rather than by closed equations. Examples are inhomogeneous samples or samples with irregular shapes. Quantification is based on a Monte Carlo technique describing the relevant photon-matter interactions as a photon beam in the energy range of 1-100 KeV illuminates an arbitrary heterogeneous specimen. The exciting radiation can have any given energy distribution in the above energy range and can be either unpolarized or linearly polarized. The modeled multi-element sample can contain a maximum 92 elements from H to U. The simulated interaction types include (1) photoelectric effect (2) Rayleigh (elastic) scattering (3) Compton (inelastic) scattering. By simulating a statistically significant number of these interactions within the sample and its environment and calculating the probability of subsequent fluorescence or scattered X-ray emission within the solid angle of the modeled detector, the complete spectral response of a given sample can be calculated. The simulated spectrum can be compared directly to the experimental data in its entirety, including the scattered background of the XRF spectra, as well as the fluorescence line intensities (Vincze, 2004).

### 2.6.6.6 Standardless quantification

Any X-ray spectrometer will determine just intensities, i.e. the number of photons of a given energy which hit the detector in a given time. In other words, XRF is a relative analytical method and will always require an analytical function, which relates the measured intensities to concentrations of elements or compounds. A method without specific standards has to cover a maximum range of elements in as wide a variety of materials as possible, and there is clearly a

need for a universal and comprehensive matrix correction method. Empirical methods cannot fulfill these requirements; they are too limited in concentration range and element coverage. The only choice is the use of matrix corrections based on FPs. Any standardless method has to face a series of challenges: first of all, correct net intensities have to be determined. This task requires:

1. A set of measurements conditions covering concentrations from trace to 100% for all elements to be analyzed by XRF. One way is to adjust the tube power depending on the intensity of the current sample;
2. A reliable method for background determination and background subtraction;
3. A universal correction method for spectral interference (line overlaps).

Once these intensities are available, the concentrations can be determined. This will require:

a. The calculation of concentrations in the specimen as measured based on a universal calibration;
b. Ways to handle non-measured elements;
c. Correction procedures for size and thickness of the specimen;
d. Calculation of the composition of the original sample without preparation agents.

For many applications (e.g. this work), optimized standardless methods can ensure the same quality of results obtained using standardized methods without the need for a special calibration process.

### 2.6.7 Mapping

The software used (PyMca in this work) during the acquisition should allow to automatically make point analysis where the coordinates of each points of interest are stored in a file, line scans (not restricted to horizontal or vertical lines) simply by setting the coordinates of the end points and of course polygonal maps of various areas of the sample.

The program places the sample in the starting position, already referenced on the indexed external microscope, then starts the acquisition for a present time, stores the data, and repeats this cycle of operations until all points have been analyzed.

For some positions in the sample we may find locally very high concentrations of highly fluorescent elements. This will introduce dead time corrections and we must record for each analyzed point the exact real and live (active) times.

Below is presented some example of XRF mapping obtained during my experiments (Fig. 2.25); for a detailed description, see chapter 5.

This technique is most useful to visualize phase and elemental distributions, and consequently to partitioning coefficients determination of major elements between silicate phases (this study, chapter 5).

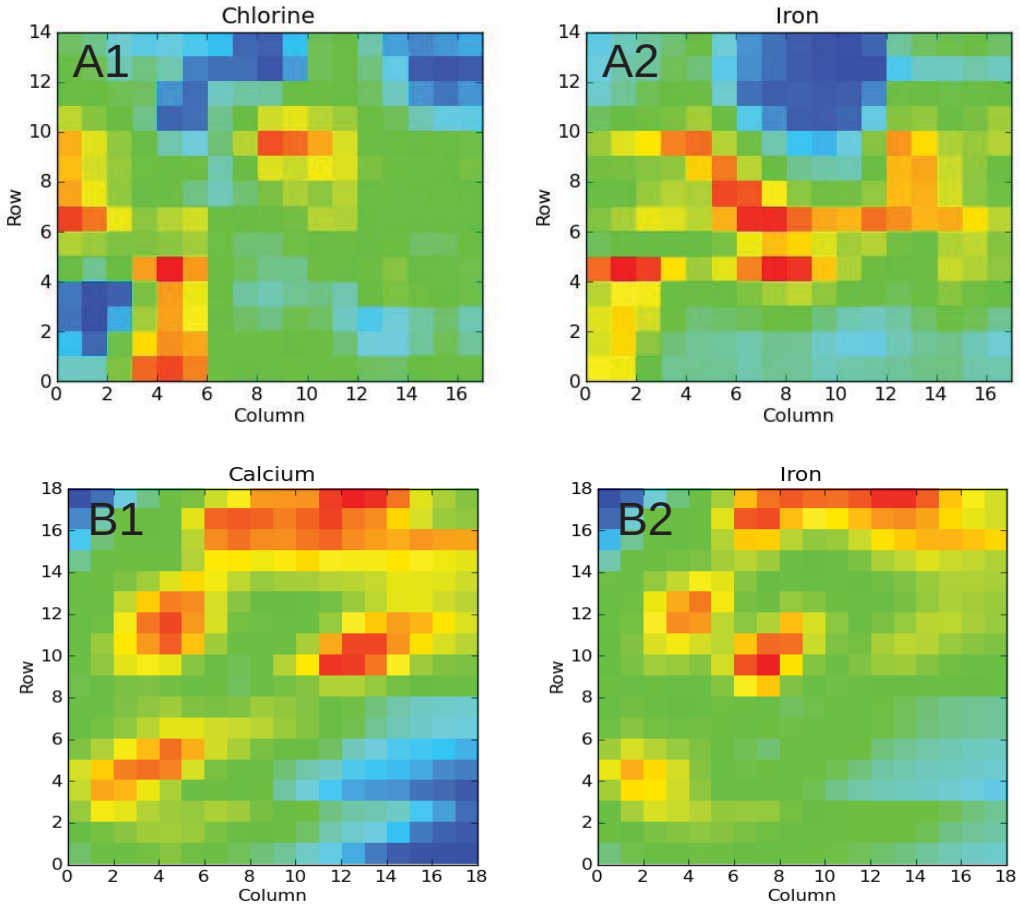


**Figure 2.25** X-ray fluorescence maps for samples recovered from 41 GPa (A1-A2) and 103 GPa (B1-B2). Each pixel is 2.5*2.5 µm and 1.5*1.5µm, respectively.

## 2.7 X-ray fluorescence (XRF) procedure: study of chondrite

We performed experiments at high pressure and high temperature using the LH-DAC technique. We used diamond anvils with flat culets of 250 μm diameter or bevel type 100-300 μm culets. We used tungsten gaskets pre-indented to a thickness of 30-45 μm and laser-drilled to diameters of 50-80 μm. Samples were loaded between two NaCl pellets. Our procedure for the samples synthesis is illustrated in 2.5.3.

For XRF measurements, we used an energy dispersive solid-state Si(Li) Vortex detector, set at around 60° from the incident beam. This angle position is the best that can be achieved in the transmission mode when using W-gaskets, in order to maximize the photoelectric effects and minimizes Compton and Rayleigh diffusions. The detector was protected from incoherent X-ray signal using an Ag collimator. We detected K-lines of Ca and Fe from the sample, K-line of Cl from the NaCl pressure medium, L-line of W from the gasket material, and L-line of Pb used as X-ray absorber on the beamline. Elemental analyzes are derived from fluorescence spectra using the PyMca program (Solé et al., 2007). We fixed the fundamental parameters to: X-ray flux= 8.4e+11 photons/s; Acquisition time= 100 or 150 sec.; Active area= 4 $\mu m^2$; Sample to detector distance= 20mm.

The XRF method usually requires the use of standards for quantitative determination of the element contents. In our samples, there are parts where the samples has not encountered melting or phase segregation and one could try to use these regions as an internal calibrant, since their chemical composition should be similar to that of the starting material. However, the presence of a thin NaCl layer above the sample makes the situation more complicated. Indeed, based on the intensity of the Cl fluorescence signal measured at the different sample positions, it is clear that this layer is heterogeneous in thickness in the recovered samples (Figure 5.3). We estimated the

NaCl thickness at all sample positions from the measured intensity of the Cl fluorescence signal and included a correction for NaCl absorption when refining the Ca and Fe contents from their respective XRF signals. This correction brings additional uncertainty for determination of the Ca contents, since 65% of the Ca fluorescence signal can absorbed by a 10 μm thick layer of NaCl. On the other hand, the correction for NaCl absorption is less than 20% at the Fe fluorescence energy. Altogether, our XRF measurements provide quantitative information for the relative variations of Fe and, to a minor extent, for Ca, for each given XRF map.

## 2.8 Scanning electron microscope

This electron microscope provides images of the sample surface by scanning a high-energy beam of electrons in a raster scan pattern. The electrons interaction with the sample produces signals that contain information about the sample's surface topography, composition and other properties such as electrical conductivity. A primary beam of incident electron exits the sample surface. Detectors collect either the secondary or backscattered electrons (imagery mode), or photons (analysis mode). The use of secondary electrons emitted by the sample surface provides an image of the surface topography (Secondary Electron Imaging, SEI). The backscattered electrons (Back Scattered Electrons Imaging, BSEI) are emitted from the effect of the primary beam penetration deeper in the sample, and their energy depends on the average atomic numbers of the elements it came across. The produced image roughly illustrates chemical contrast between different phases, or phase zoning in the sample: with the increasing average atomic number, the image becomes brighter. Using the analytical mode, photons emitted by the EDS detector are retrieved and picked up by a receptor.

For conventional imaging, the scanning electron microscope (SEM) requires that specimens be conductive for the electron beam to scan the surface and that the electrons have a path to ground. Our sample was coated with carbon by a low vacuum sputtering system, in order to prevent the accumulation of static electric charge on the specimen during electric irradiation and improve contrast and resolution.

SEM micrographs have a very large depth of focus yielding a characteristic three-dimensional appearance useful for understanding the surface structure of a sample. We used a JEOL JSM-5910 LV SEM equipped with a PGT microanalysis system at the Laboratory of Magmas and Volcanoes, Clermont-Ferrand, France (Fig. 2.26). Moreover there is an EDS micro-analysis

system with a Si(Li) captor and an ultra thin window (UTW) which permits the detection of light elements. The Spirit system of PGT gives semi-quantitative and quantitative chemical analyses, as do the concentration profiles and chemical EDS mapping. This type of SEM uses X-ray for imaging mode. The electron beam, which has energy of 20 KeV, is focused by one or two condenser lenses into a beam with a very fine focal spot.

The aim was obtain SEM micrographs of samples (Fig. 2.27 and 2.28) to compare it with X-ray diffraction and X-ray fluorescence maps, and at the same time to better understand the behavior of the samples when heated.

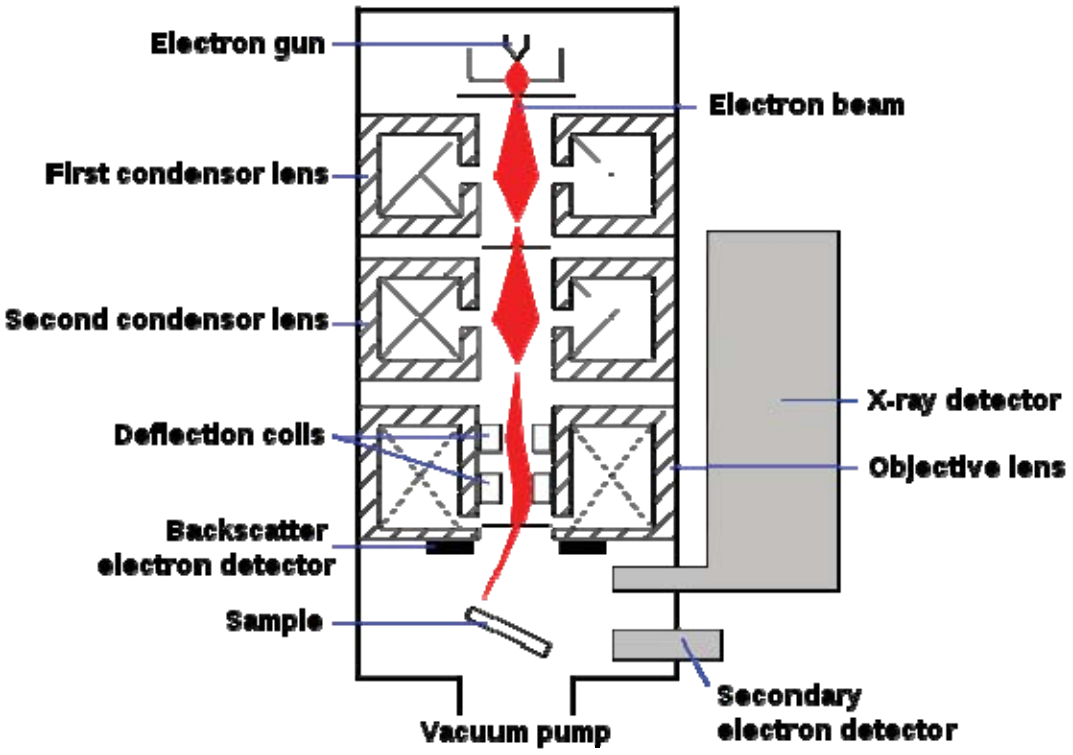


**Figure 2.26** Schematic diagram of a SEM microscope.

We get an energy spectrum that allows qualitative phase identifications. The comparison of the peak intensity on this spectrum identifies phases.

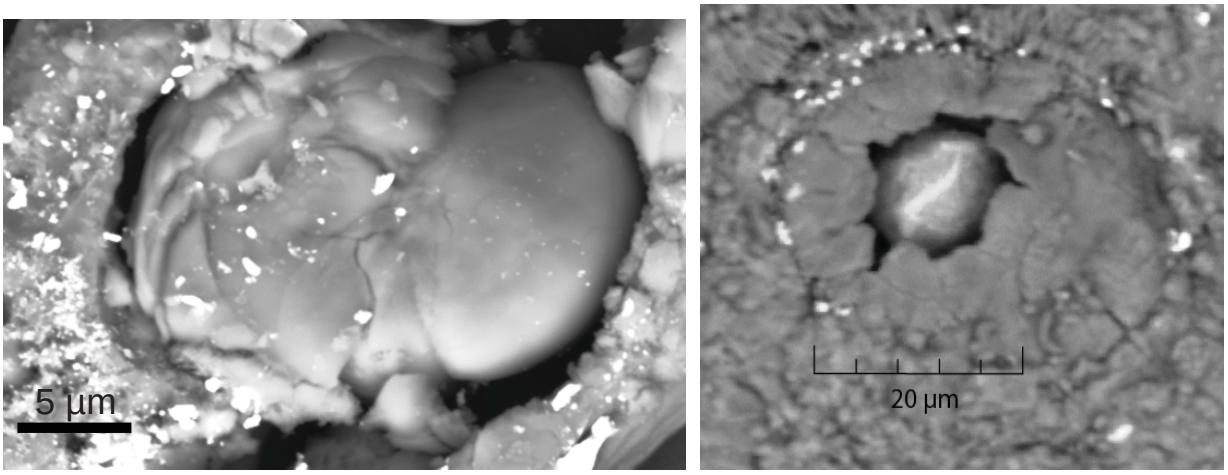


**Figure 2.27** Scanning electron microphotographs of two samples recovered from 30 and 48 GPa respectively, showing the central laser-heated zone that underwent complete melting. It formed an independent liquid ball separated from the rest of the sample.

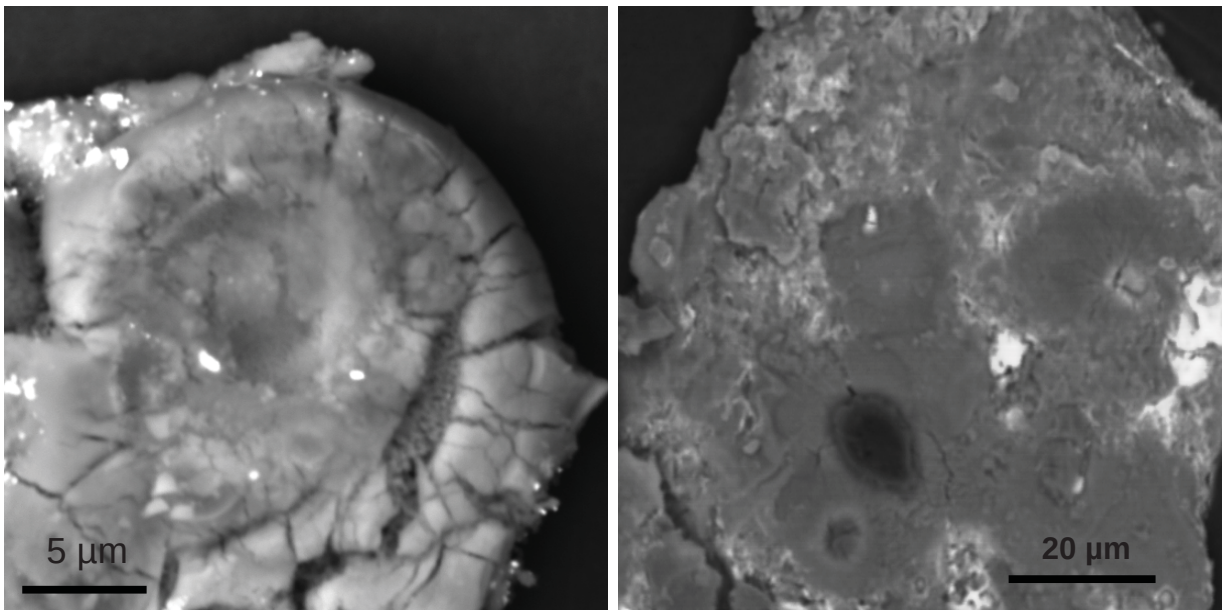


**Figure 2.28** Scanning electron microphotographs showing a central zone of two samples recovered from 30 and 53 GPa respectively. These samples encountered laser heating between the solidus and liquidus temperatures.

## 2.9 Inductively coupled plasma atomic emission spectroscopy (ICP-AES)

It is an analytical technique used to detect major, minor and trace elements. The spectrometer used in this study is a Horiba Jobin-Yvon ULTIMA C, at the Laboratory of Magmas and Volcanoes, Clermont-Ferrand, France. We used this technique in order to determine exactly the chemical composition of our chondritic samples.

This technique uses the inductively coupled plasma (ICP) to produce excited atoms and ions that give off electromagnetic radiation at wavelengths characteristic of a particular element. The detector within the ICP detects this wavelength and also its intensity and can therefore calculate the amount of each element present within the sample previously put in solution.

An ICP-AES is composed of an ICP and an optical spectrometer (Fig. 2.29). Argon gas was used to create the plasma. Then is generated a flame with a temperature of about 7000 K. A pump delivers the sample into a nebulizer where it is atomized and introduced directly inside the plasma flame. The sample collides with the electrons and charged ions in the plasma and is itself broken down into charged ions. The various molecules break up into their respective atoms which then lose electrons and recombine repeatedly in the plasma, giving off radiation at the characteristic wavelengths of the elements involved.

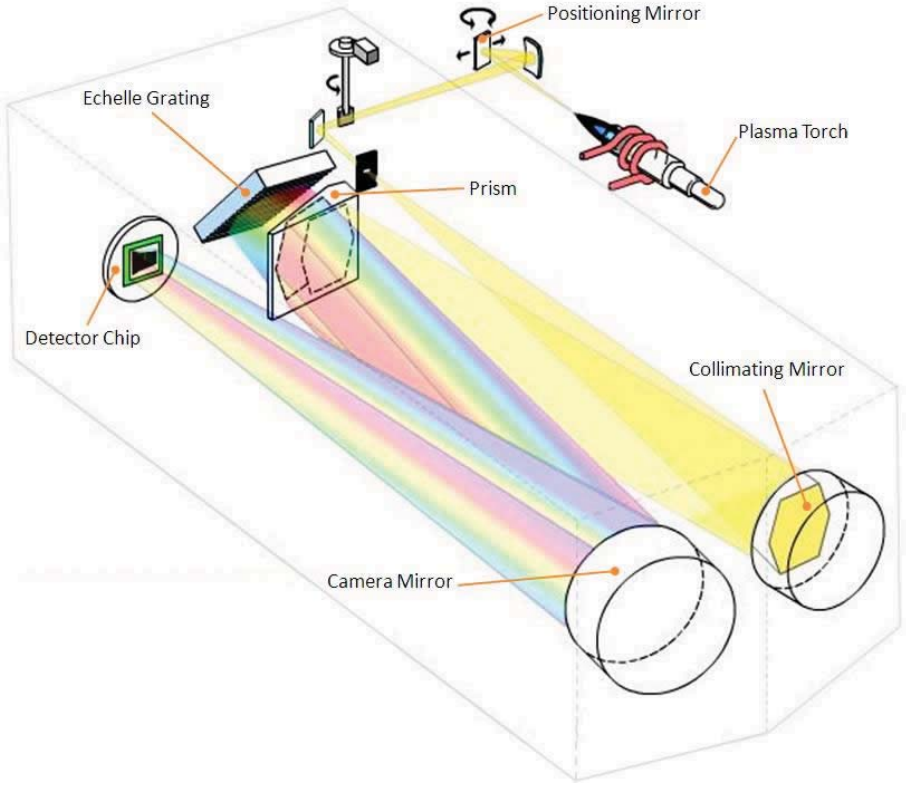


**Figure 2.29** A diagram showing the ICP-AES process.

## 2.10 Electron microprobe (EMP)

The electron microprobe is also known as an electron probe micro-analyzer (EPMA) or electron micro probe analyzer (EMPA). The electron microprobe is an analytical tool used to non-destructively determine the chemical composition of small volumes of solid materials.

The polished surface of the sample is bombarded with an electron beam accelerated by a 15 kV potential, emitting X-rays at wavelengths characteristic to the elements being analyzed. Intensity is measured with a detector and its wavelength is known thanks to the Bragg diffraction law (see paragraph 2.2). Comparing the wavelength and the intensity of X-rays emitted from the sample with those of standards, we are able to quantify elemental concentrations in the samples.

The type used during my thesis is the CAMECA SX 100, with four wavelength dispersive spectrometers (WDS) and twelve diffraction crystals (Fig. 2.30 and 2.31).

I used the electron microprobe to quantify the chemical composition of the some grain in the chondritic samples (Table 2.2).

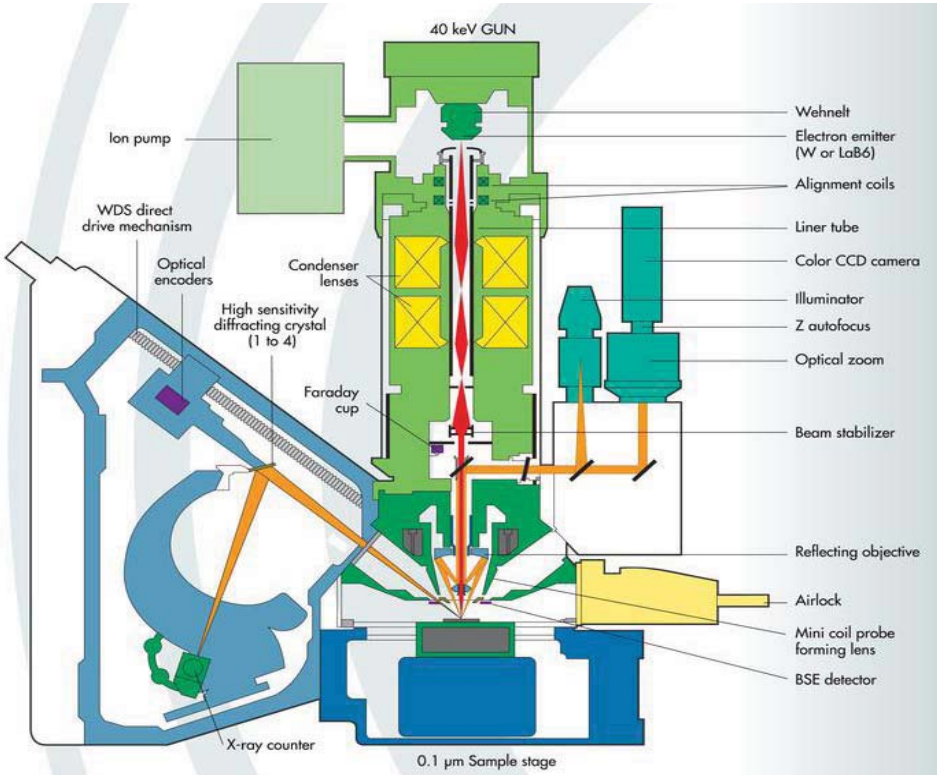


**Figure 2.30** Schematic cartoon of a Cameca SX 100; reproduced from the Cameca official site (www.cameca.com).


**Figure 2.31** Picture of a Cameca SX 100, available at the LMV, Clermont-Ferrand, France.

| | $SiO_2$ | MgO | FeO | $Al_2O_3$ | CaO |
|---|---|---|---|---|---|
| **grain1** | 51.859 | 33.538 | 6.3232 | 4.8961 | 3.3832 |
| **grain2** | 54.981 | 28.510 | 7.3195 | 5.0360 | 4.1531 |
| **grain3** | 43.387 | 53.960 | 2.0356 | 0.3168 | 0.3008 |
| **grain4** | 58.965 | 23.682 | 7.4602 | 5.6979 | 4.1950 |
| **grain5** | 44.018 | 53.227 | 2.5160 | 0.1127 | 0.1262 |
| **grain6** | 46.090 | 51.040 | 2.4255 | 0.2324 | 0.2128 |
| **grain7** | 52.443 | 32.156 | 6.6926 | 4.9690 | 3.7397 |
| **grain8** | 53.525 | 32.000 | 6.4000 | 4.3750 | 3.7000 |

**Table 2.2** Oxides Wt% for some grain of the chondritic glass (Chapter 4 and 5) obtained with EMP analyses (See Table 2.1 for starting composition).

# Chapter 3: Melting in the MgO-$MgSiO_3$ system: A simplified chemical model for the lower mantle

## 3.1 Abstract

In this chapter, we present melting relations in the system MgO-$MgSiO_3$ investigated using the laser-heated diamond anvil cell at typical lower mantle pressures. This binary chemical composition is used as a simplified model for the pyrolitic or chondritic mantle composition. We determined the pressure evolution of the eutectic temperature. Our melting curve plots in good agreement with previous work performed at lower pressures (Presnall et al., 1998). Also, as expected for this simplified system, it plots significantly higher than the solidus melting curves determined recently for chondritic (Andrault et al., 2011) or pyrolitic (Fiquet et al., 2010) mantle. The difference with our previous study increases from ~250 K to ~600 K with increasing pressure from 30 GPa to 135 GPa.

In the same experiments, we could also determine the melting curve of platinum which was use as an IR-laser absorber. The Pt melting curve is found in good agreement with the precedent determination performed up to 70 GPa (Kavner and Jeanloz, 1998).

## 3.2 Introduction

One of the most fundamental questions in the field of geology is related to the understanding of the physical and chemical processes that controlled formation and differentiation of the Earth's planet across its history (Wetherill, 1990). It is well accepted that our planet experienced partial melting early in its history as a consequence of energy release due to accretion. Investigating the melting properties is primordial to improve our knowledge on the segregation of the different Earth's reservoirs and the dynamics of our planet. Partial melting could still happen today in the lowermost mantle and could explain several chemical and thermal heterogeneities evidenced by seismic investigation (Lay et al., 2004; Garnero and McNamara, 2008; Stixrude et al., 2009), i.e. the ultra low velocity zone (ULVZ) at the core-mantle boundary (CMB).

For these reasons, melting relations at high pressure and high temperature have been investigated in the past by various techniques. For pressure below 35 GPa, melting relations have been extensively investigated using the multi-anvil press apparatus. These studies show that both solidus temperature, the liquidus temperature and the liquid compositions are affected by pressure (Presnall et al., 1998; Litasov and Ohtani, 2002; Ito et al., 2004). At higher pressures, using the laser heated diamond anvil cell (LH-DAC), Zerr et al. (1998) and Fiquet et al., (2010) determined the melting properties of pyrolite, then we determined those of a chondritic mantle (Andrault et al., 2011). While the solidus melting curves appear relatively similar and compatible between the different studies, the liquidus melting temperature of the mantle remains today largely controversial.

In this study, we investigate the eutectic melting temperature in the simplified MgO-$MgSiO_3$ system. Our interest is the change in melting temperature compared to the melting curves of pure MgO-periclase (Pe) and $MgSiO_3$-perovskite (Mg-Pv) lower mantle phases. Melting of forsterite

was previously reported at ~2700 K for a maximum pressure of 22.6 GPa (Presnall et al., 1998). No information exists about the melting properties in this system at very high pressures. Only one single point is reported for the melting of $(Mg,Fe)_2SiO_4$ olivine at 4300 K and ~130 GPa, using shock wave experiments (Holland and Ahrens, 1997). This temperature has been successively revised by Luo et al. (2004), suggesting that melting point of olivine at the CMB is 4000 ± 300 K.

Our experimental set-up also gave us the opportunity to discuss the melting curve of platinum. Melting curves of metals is of considerable importance in applied physics and geophysics. In particular, platinum (Pt) is used in high-pressure shock experiments and diamond anvil cell measurements as a pressure standard (as in this study). The use of Pt is due to its relative chemical inertness, structural stability in the face-centered-cubic (FCC) phase to very high pressure, high density, low strength, and easy availability. Its melting temperature was reported to increase from ~2500 K to ~3300 K with increasing pressure from 20 to 75 GPa, respectively, using spectroradiometric and visual observations in a LH-DAC (Kavner and Jeanloz, 1998). Computational methods also suggest a melting temperature of ~2600 and ~3300 K at the same pressure conditions (Wang et al., 2001).

## 3.3 Technical details

We used a membrane-type DAC mounted with 75/300 beveled diamonds. Temperatures were provided by two YAG lasers aligned on both sides of the sample. Axial temperature gradient was limited by the presence of MgO that provides good thermal insulation (Shen et al., 2001). Hot spot with diameter larger than 30 μm were obtained by defocusing the two YAG lasers, in order to minimize the radial temperature gradient. Temperatures were measured *in situ* from sample thermal emission using reflective lenses to prevent any chromatic aberration (Schultz et al., 2005). For solid samples, temperature stability was better than 20 K during the 20 to 30 seconds of data acquisition. The total temperature uncertainty is estimated to 50 K and 10 K for solid and molten samples respectively, including uncertainties on the thermal emissivity factors.

The sample properties were investigated *in situ* thanks to the use of the X-ray diffraction set-up available at the ID27 beamline of the ESRF (Mezouar et al., 2005). Wavelength was fixed to 0.3738 Å (HE3084 experiments) or 0.2647 Å (HS3258 experiments). The X-ray beam has been focused to 2x3 $\mu m^2$ using two bent KB-mirrors. Typical acquisition time was 20-30 seconds using imaging plate or MAR345 detector. Position of the X-ray beam was determined from optical observations of the Re-gasket fluorescence. For integration of 2D-images and further data treatment we used the Fit2d (Hammersley, 1996) and GSAS packages (Larson and Von Freele, 1988), respectively.

Our samples consisted of a thin pellet of $Mg_2SiO_4$ forsterite mixed with a few Wt% of Pt or W and loaded between two MgO pellets. Pt or W acts as a YAG absorber and pressure marker (Jamieson et al., 1982) at high pressure and temperature. Experiments with W were performed in order to check for artifacts potentially associated with the melting of Pt (Ono et al., 2005). We obtained melting temperatures very similar in both case. However, W tends to react with the

sample after long time heating, which limits the sample life time. To estimate pressure at high temperature, we applied a pressure correction (ΔP) for each heating temperature (ΔT) on the basis of the ΔP obtained for the experiments performed in the $MgSiO_3$-MgO system (because, as expected, $Mg_2SiO_4$ forsterite undergoes disproportionation into a mixture of Pc and Mg-Pv at lower mantle conditions (Presnall, 1995)). This is quantitatively equivalent to applying ΔP of ~50% of the theoretical thermal pressure ($\Delta P_{th} = \alpha K \Delta T$, where α and K are thermal expansion and bulk modulus, respectively) calculated from the thermoelastic parameters of the main Mg-Pv component (Andrault et al., 1998; Fiquet et al., 2000). The value of ΔP is ~2.5 $10^{-3}$ GPa/K. Both methods give results similar within a couple of GPa. Pressure error at high temperature is estimated to 3 GPa.

## 3.4 Experimental Methodology

Since our samples (Fig. 3.1) consisted of 5 to 10 μm thick pellets of $Mg_2SiO_4$-forsterite mixed with a YAG-laser absorber embedded between two MgO pellets, it represents a large MgO-excess in the pressure chamber. For this reason, eutectic melting in the $MgSiO_3$-MgO system can be detected by disappearance of the diffraction lines of the $MgSiO_3$-perovskite phase. In case the eutectic composition is enriched in $MgSiO_3$ compared to the forsterite pellet, extra-MgO can float in the partially molten sample until it joints (or not) the interface with the MgO pressure medium. In case the eutectic composition is enriched in MgO, melting of the entire forsterite pellet is achieved by dissolution of some MgO from the external pellets (the pressure medium) into the central liquid blob. According to previous studies, we expected the eutectic composition enriched in $MgSiO_3$ with increasing pressure (Liebske et al., 2005).

Melting criteria can be defined according to changes in the X-ray diffraction pattern. We search for first order changes such as (i) disappearance from the imaging plate of diffraction rings of Mg-Pv, (ii) reappearance of these diffraction rings after temperature quench, (iii) major variation of the intensity of diffraction lines on integrated spectra (Figures 3.2 to 3.5). These criteria can be complemented with observations of the sample optical changes as well as analysis of relationship between laser-power and sample temperature. In particular, crossing of flash temperatures (when increasing of temperature is very abrupt) is indicative of sample melting.

For determination of the Pt melting curve, it is the disappearance of the diffraction lines that represents the main criterion.

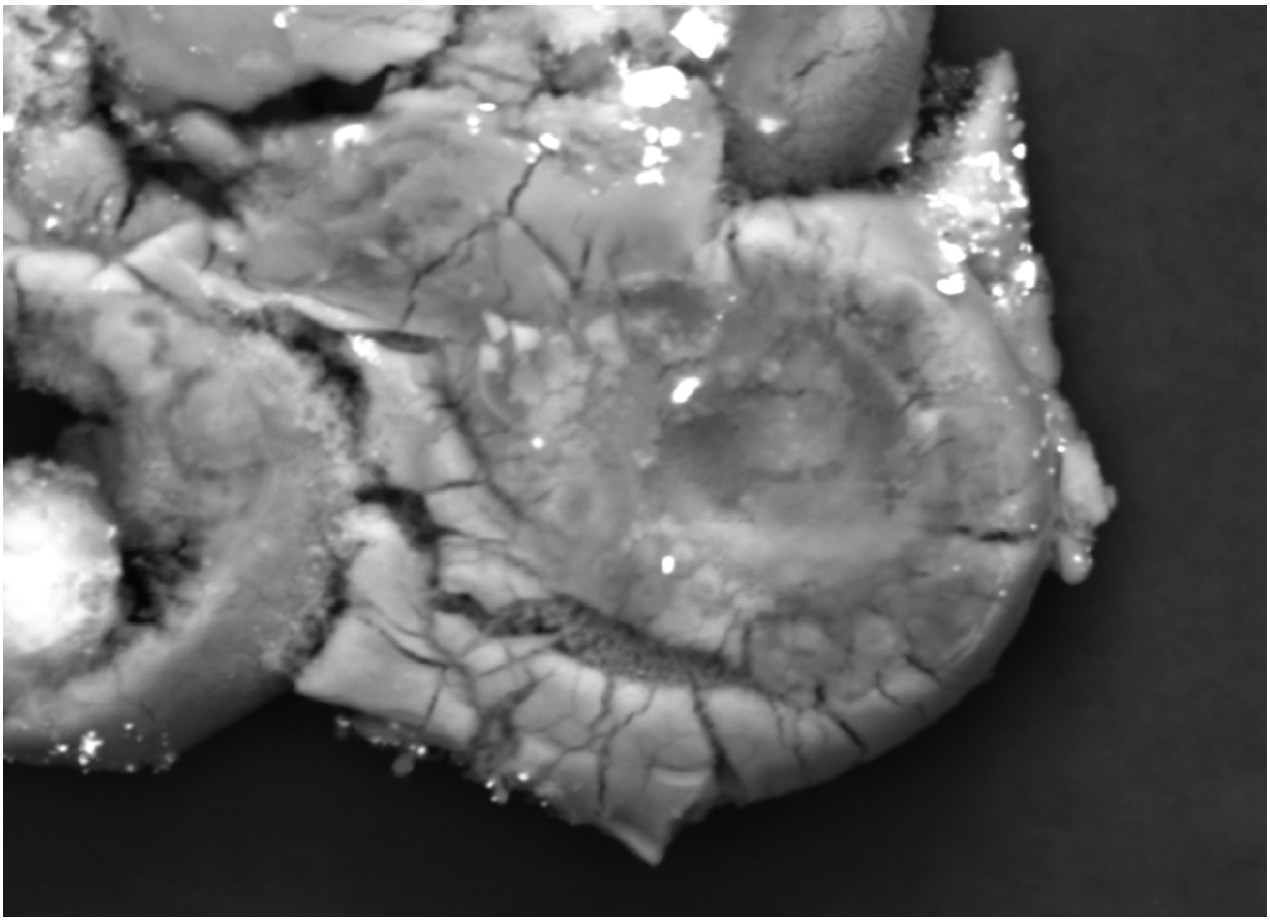

**Figure 3.1** Electron microphotograph of a forsteritic sample recovered from 30 GPa.

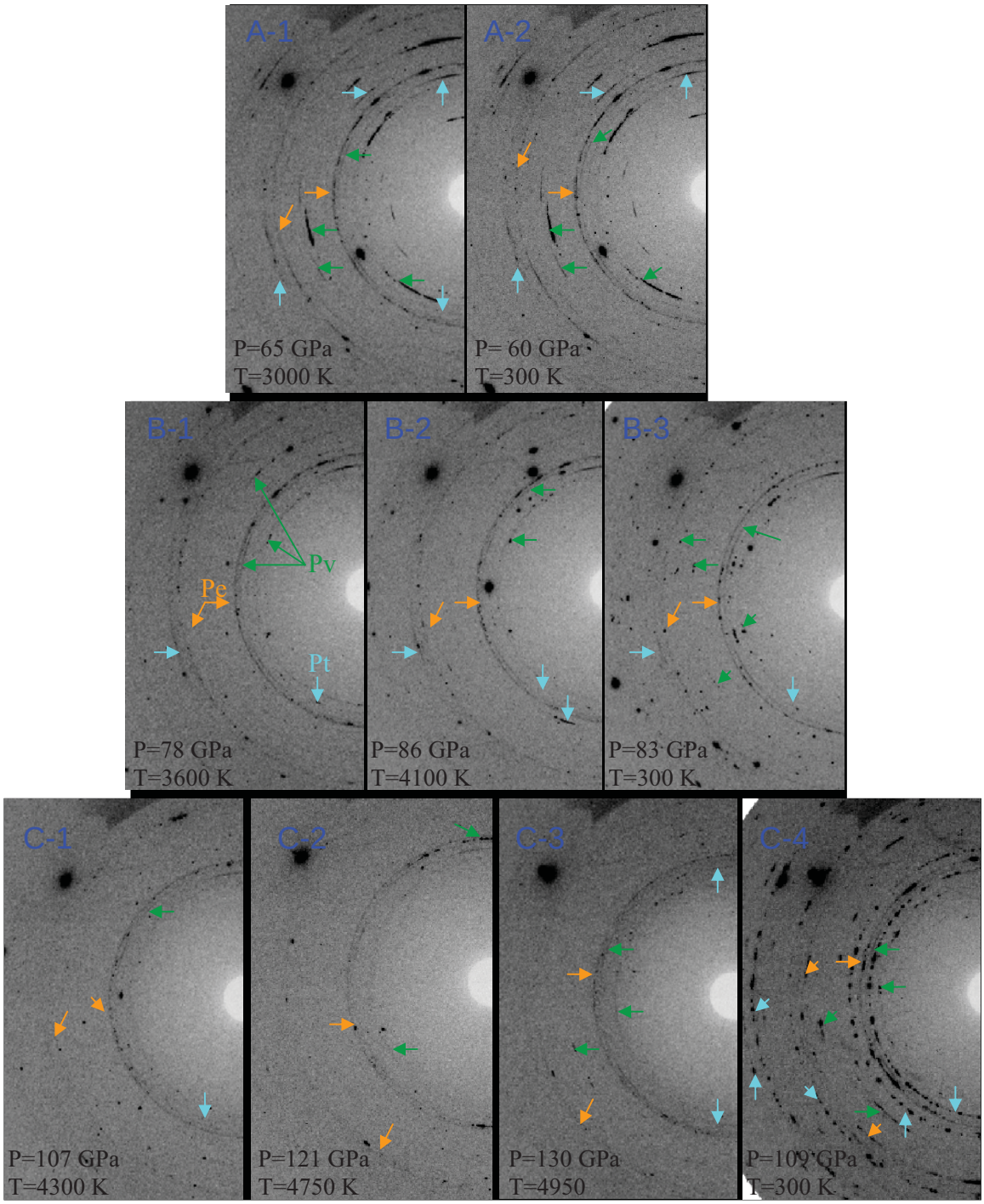


**Figure 3.2** Typical 2D-diffraction images recorded at increasing temperature at pressures of (a) ~65 GPa, (b) 78-86 GPa and (c) 107-130 GPa. Images at 300 K after laser heating are also reported. Orange, green, and blue arrows correspond MgO, Mg-Pv, and Pt, respectively. Diffraction rings are largely reduced in intensity (from B1 to B2), eventually disappear (from C2 to C3) and reappear after temperature quench (B3 and C4), as a proof of sample melting at very high temperature.

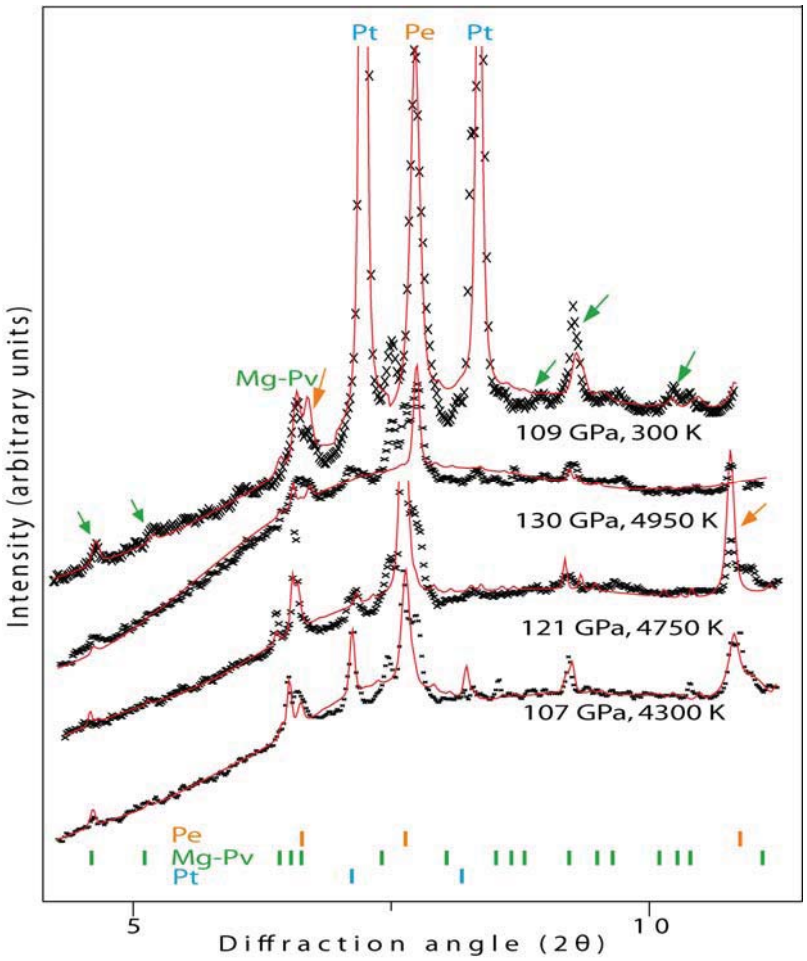


**Figure 3.3** X-ray diffraction spectra recorded at increasing pressure and temperature. Melting of Mg-Pv is evident above 130 GPa and 4750 K.

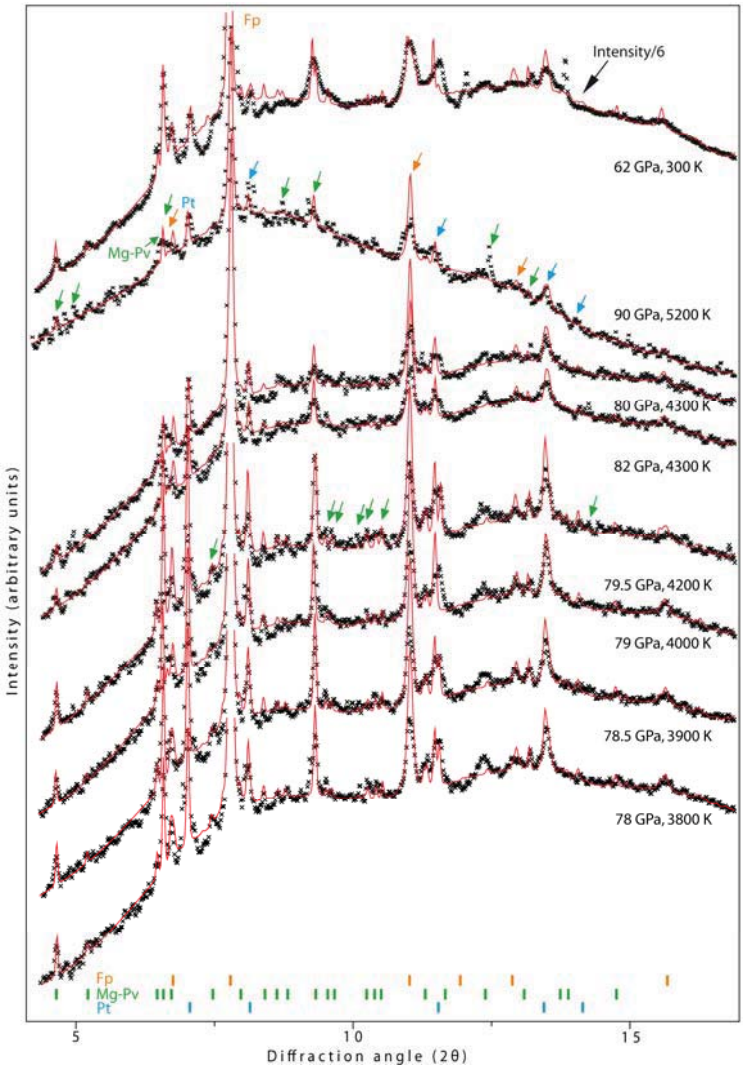


**Figure 3.4** X-ray diffraction spectra recorded at increasing pressure and temperature. Melting of Mg-Pv and Pt is clearly evident above ~80 GPa and 4300 K.

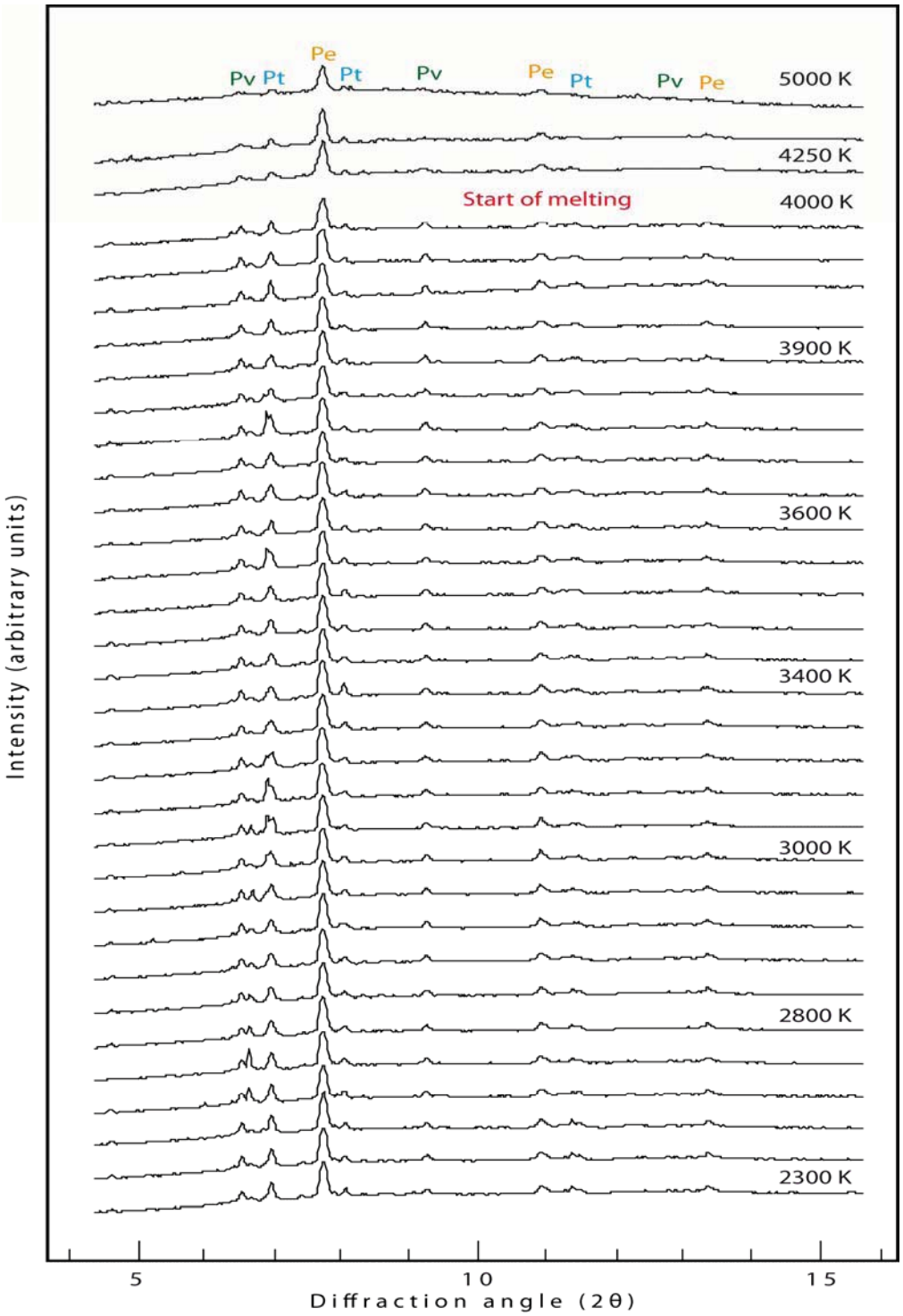


**Figure 3.5** Diffraction patterns as function of temperature, from 2300 K (bottom) to 5000 K (top). Sample pressure is simultaneously increased from 70 to 90 GPa, due to the thermal-pressure effect (see text). Melting is observed at ~4000 K, as evidenced by changes in peaks intensity of the Mg-Pv.

## 3.5 Results and Discussions

### 3.5.1. Silicate melting

Our new data set includes nine successful loadings in the LH-DAC. Each melting point has been determined after laser-heating of at least one fresh piece of sample (Figure 3.6). Eutectic temperature is found to increase smoothly from 2800 K to 4300 K with pressure increasing from 25 to 120 GPa. The melting curve is perfectly fitted by modified Simon and Glatzel equation (Simon and Glatzel, 1929) [$T=T_0*(P/(a+1))^{1/c}$] with a= 24 GPa and c= 1.75, and the extrapolated melting temperature at ambient pressure $T_0$=1650 K. Extrapolation to the CMB pressure of 135 GPa yields a melting temperature of ~4830±150 K. Our melting curve is not affected by the Pv to post-Pv phase transition that is expected to occur at a significantly higher pressure for 4830 K. Indeed, this $T_{CMB}$ is reported at 3500 K for 135 GPa (Tateno et al., 2009). Our eutectic melting curve plots well below the melting curves of the pure end-member phases $MgSiO_3$-perovskite, MgO and $CaSiO_3$-perovskite (Boehler, 2000) (Figure 3.7). The temperature difference is huge, about 1000 K at 60 GPa, for example. This behavior is not surprising, since it is an intrinsic property of eutectic liquids to show the lowest melting temperature in a given chemical system. At low pressures, our data set fits very well with the eutectic melting curve of the $Mg_2SiO_4$-$MgSiO_3$ system (Presnall et al., 1998). On the other hand, the data set plots about ~200 K higher than the melting curves for pyrolite determined in a large-volume press (Herzberg and Zhang, 1996; Litasov and Ohtani,, 2002; Trønnes and Frost, 2002). Finally, our melting curve plot ~750 K higher than the single data point reported at 4000±300 and ~130 GPa for melting of $(Mg,Fe)_2SiO_4$ olivine from shock-experiments (Luo et al., 2004). These comparisons between melting curves of Fe-free and Fe-bearing materials suggests important melting temperature depletion due to the presence of FeO in the sample.

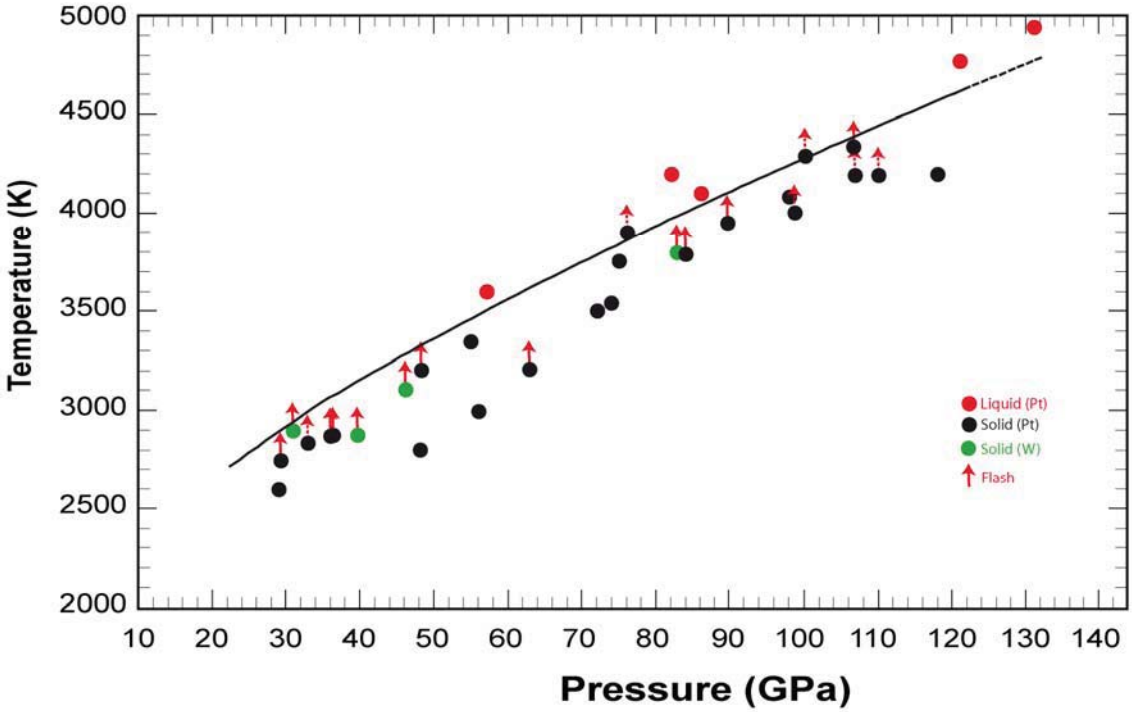


**Figure 3.6** Experimental determination of the eutectic melting curve of MgO-$MgSiO_3$ system. Black dots, green dots, red dots and red arrows correspond to P-T conditions where all phases are solid, where the Mg-Pv phase is mostly disappeared and where the temperature raises abruptly to extremely high temperatures, respectively. The interval between solid (black and green dots) and red dots corresponds to the melting curve and it is fitted with Simon-Glatzel equation (black line). Black and green dots correspond to solid for sample with Pt or W YAG absorber, respectively.

### 3.5.2. Platinum melting

We observed a smooth increase of the melting temperature of platinum from 2600 K to 3600 K with pressure increasing from 20 to ~100 GPa, respectively. Our melting curve is in good agreement with the melting curve of Kavner and Jeanloz (1998), expect at the highest pressure where our curve plots, and thus extrapolates, to higher melting temperatures (Figure 3.8). As for the $MgSiO_3$-MgO system, the melting curve is perfectly fitted by modified Simon and Glatzel equation with a=102 GPa, c=2.0, and $T_0$=2046 K. These parameters are similar to those previously reported for Pt (Babb, 1963).

We note that the melting curve of platinum plots below that of the MgO-$MgSiO_3$ system (Figure 3.9), which could potentially affect our determination of the melting curve in the MgO-$MgSiO_3$ system. However, we did not observe any significant change in the laser heating procedure after Pt-melting. We interpret this effect by stability in their positions of the submicronic Pt particles which remain well embedded in the silicate matrix, until the later stars to melt. No other diffraction lines than those representative of Pt, Pe and Mg-Pv are observed in the diffraction pattern after the laser shutdown, which confirms the Pt inertness toward Pe and Mg-Pv. Also, our results disagree with the recent suggestion that platinum could react with the carbon of the diamond anvils to form PtC (we did not find diffraction lines and peaks corresponding to PtC phase) at high pressure and temperature (Ono et al., 2005; Ono and Oganov, 2005). This discrepancy results from the use of MgO pellets to insulate the sample from the diamonds in our experiments.

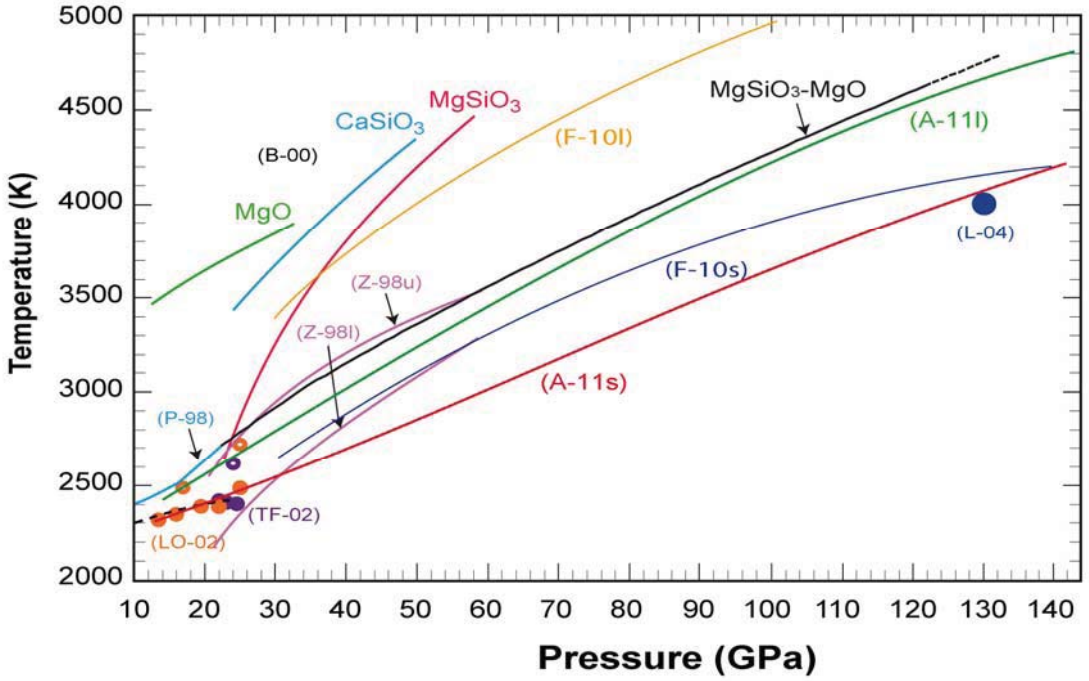


**Figure 3.7** Comparison between our MgO-$MgSiO_3$ eutectic melting curve and previous works performed for various materials: B-00 for simple oxide phases (Boehler, 2000); P-98 for melting of MgO-$MgSiO_3$ system (Presnall et al., 1998); L-04 for Olivine (Luo et al., 2004); A-11 for synthetic chondrite solidus and liquidus (Andrault et al., 2011); F-10 for peridotite liquidus and solidus (Fiquet et al., 2010); LO-02, TF-02 and Z-98 for melting of pyrolite by (Litasov and Ohtani, 2002), (Trønnes and Frost, 2002; full and open circle for solidus and liquidus, respectively) and (Zerr et al., 1998, upper and lower estimation of the solidus), respectively.

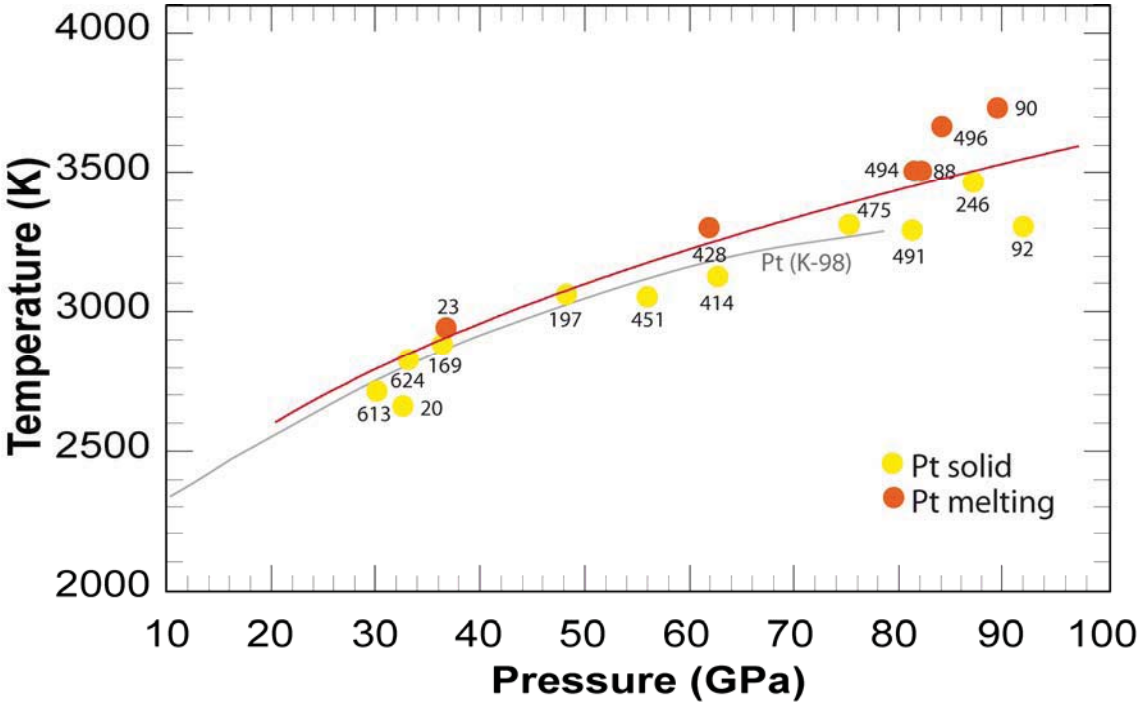


**Figure 3.8** Melting curve of platinum. Yellow and orange points correspond to solid and molten platinum, respectively. These results are fitted with the Simon-Glatzel model (red line) and compared with previous work (Grey line: Kavner and Jeanloz, 1998).

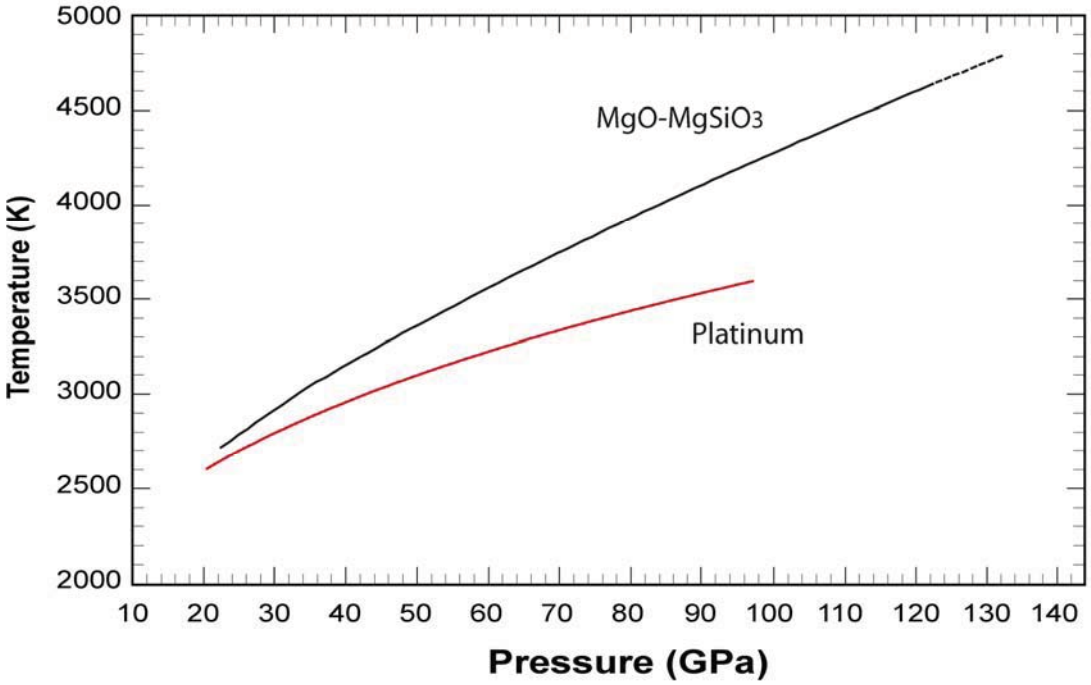


**Figure 3.9** Melting curve of $MgO\text{-}MgSiO_3$ system compared with that of platinum

## 3.6 Conclusions

We have determined the eutectic melting curve of the MgO-$MgSiO_3$ system for the lower mantle pressure conditions. Our measurements are in good agreement with all data sets, basically: (i) at low pressures with the multi-anvil experiments performed in the $Mg_2SiO_4$-$MgSiO_3$ system; (ii) at mid-mantle pressures with the melting curves of pure MgO and $MgSiO_3$ which plot at significantly higher temperatures; and (iii) at all pressures with the melting curve of Fe-bearing samples that plot at lower temperatures.

Beside the own interest of the $MgSiO_3$-MgO eutectic melting curve that is described above, our main goal while performing these experiments was to set-up an experimental procedure for *in situ* determination of the melting properties at extreme P-T conditions in the LH-DAC. The quality of our results demonstrated that this is done. The next two chapters present experimental results for geologically relevant sample compositions.

Finally, could be very important determine the weight percentage of MgO periclase and $MgSiO_3$ perovskite in the eutectic liquid.

In this way, we can be able to:

- Obtain a diagram weight perentage (wt%) versus pressure;
- Constrain the ocean magma properties.

# Chapter 4: Solidus and liquidus profiles of chondritic mantle: Implication for melting of the Earth across its history

This chapter introduces results of liquidus and solidus melting curves for a chondritic composition and implications for melting of the Earth from beginning to present day.

Those results are presented in the form of a paper published by Earth and Planetary Science Letters, in 2011.

In that study, we present:

1. Liquidus and solidus melting curves of chondritic mantle up to core-mantle boundary conditions;
2. Geophysical implications of melting curves for chondritic mantle;
3. Comparison of melting with the geotherm;
4. Discussions on an early magma ocean.

This work was made in collaboration with Denis Andrault (my advisor), Nathalie Bolfan-Casanova and Ali Bouhifd. This chapter must be considered as a first part of the work on chondritic mantle including iron partitioning (chapter 5).

## 4.1 Abstract

We investigated the melting properties of a synthetic primitive mantle up to core-mantle boundary (CMB) pressures, using laser-heated diamond cell. Melting criteria are essentially based on the use of X-rays provided by synchrotron radiation. We report a solidus melting curve lower than previously determined using optical methods. The liquidus curve is found between 300 and 600 K higher than the solidus over the entire lower mantle. At CMB pressures (135 GPa), the chondritic mantle solidus and liquidus reach 4150 (±150) K and 4725 (± 150) K, respectively.

We discuss that the lower mantle is unlikely to melt in the D"-layer, except if the highest estimate of the temperature profile at the base of the mantle, which is associated with a very hot core, is confirmed. Therefore, recent suggestions of partial melting in the lowermost mantle based on seismic observations of ultra-low velocity zones indicate either (1) a outer core exceeding 4150 K at the CMB or (2) the presence of chemical heterogeneities with high concentration of fusible elements.

Our observations of a high liquidus as well as a large temperature gap between solidus and liquidus temperatures have important implications for the properties of the magma ocean during accretion. Not only complete melting of the lower mantle would require excessively high temperatures, but also, below liquidus temperatures partial melting should take place over a much larger depth interval than previously thought. In addition, magma adiabats suggest very high surface temperatures in case of a magma ocean that would extend to more than 40 Gpa, as suggested by siderophile metal-silicate partitioning data. Such high surface temperature regime, where thermal blanketing is inefficient, points out to a transient character of the magma ocean, with a very fast cooling rate.

## 4.2 Introduction

A large proportion of our planet has experienced melting in the course of its accretion history as a consequence of the energy release associated with a large impacts, radioactive decay and core formation. Major unknowns remain about this early time, in particular the extension depth of the magma ocean and the chemical signature inherited from mantle crystallization during cooling. The melting curve of the primitive mantle thus has major consequences for the existence of chemical heterogeneities and the survival of primitive mantle reservoirs. In the modern Earth seismology evidences heterogeneous properties of the D"-region which extends from the core-mantle boundary (CMB) upwards 250 km (Lay et al., 1998). There are, indeed, evidences for large-scale patterns of heterogeneities, with anomalous set of $V_P$-$V_S$ sound velocities, which can hardly be explained by phase transitions in minerals or thermal anomalies. Instead, they seem to evidence chemical heterogeneities, which can be of different origins: (i) partial melting in the D"-layer (Lay et al., 2004), leading to chemical segregation of the mantle; (ii) relics of descending slabs rich in mid-ocean ridge basalts (MORB); (iii) zones enriched in incompatible elements associated to the progressive crystallization of an ancient magma ocean and trapped in the lowermost mantle (Labrosse et al., 2007).; and/or (iv) lower mantle material affected by chemical exchanges with outer core. Each hypothesis has specific implications for our comprehension of the dynamics of the Earth, as well as for elemental segregation between the different geological reservoirs. Unfortunately, it remains difficult to distinguish between the different scenarios. Indeed, the thermo-elastic parameters of the main lower mantle minerals are known with insufficient accuracy for inferring the mineralogy of this very remote using the seismic features. Especially, it remains a challenge to infer any chemical anomaly other than Mg/Si and Fe/(Mg+Fe) ratios.

In order to assess the potential occurrence of partial melting in the D"-region, one must refine the melting curves of the different geological materials. For pressures up to 25 GPa, melting curves of mantle silicates and phase relations in a partially molten mantle have been investigated using the multi-anvil press. It has been shown that pressure affects significantly the solidus and liquidus temperatures as well as composition of the eutectic liquids (Ito et al., 2004; Liebske et al., 2005; Litasov and Ohtani, 2002). At higher pressures, while the melting curve of end-member phases is relatively well documented using laser-heated diamond anvil cell (LH-DAC) (e.g. Boehler, 2000), shock wave experiments (e.g. Luo et al., 2004) or ab initio calculations (e.g. Stixrude and Karki, 2005), melting of material with relevant geological composition was much less investigated. For pyrolite, optical observations have been used to determine the melting curve as a function of pressure using the LH-DAC (Zerr et al., 1998), but only up to ~60 GPa. This pressure range remains too limited for quantitative extrapolation to the ~130 GPa representative of the D"-layer. On the other hand, using shock-wave experiments, melting of $(Mg,Fe)_2SiO_4$ olivine was reported at 4300 K and ~130 GPa (Holland and Ahrens, 1997). Recently, the same group corrected this value to 4000 (300) K, after improvement of the temperature estimation (Luo et al., 2004).

## 4.3 Methods

Ultra-brilliant X-ray beams are now available from Synchrotron ring for in situ investigation of the melting behavior in the laser-heated diamond anvil cell (LH-DAC). We used a membrane-type DAC mounted with 250 μm or 75/300 μm culet-diameter diamonds. Re gaskets were pre-indented to 40 μm or 20 μm and laser-drilled to 80 μm or 50 μm, respectively. Small glass flakes were loaded in between two NaCl or KCl pellets, and a few experiments were performed without pressure medium. Salts provide good thermal insulation from the diamond and can be used as pressure standards at 300 K (Sata et al., 2002; Walker et al., 2002). Hot spots with diameter larger than 30 μm were obtained by two YAG lasers aligned on both sides of the sample. Temperatures were measured from sample thermal emission reflective lenses to prevent any chromatic aberration (Benedetti and Loubeyre, 2004). The intrinsic temperature uncertainty is estimated to be 50 K, including uncertainties on the thermal emissivity factors. For solid samples, temperature stability was better than 20 K during the 20 to 30 seconds of data acquisition. However, when the sample starts melting, the temperature stability deteriorates. In this study, we discarded those measurements where temperature fluctuation exceeded 50 K. Also, the emissivity factor is less documented for liquid phases. Therefore, the temperature uncertainty is estimated to be 50 K and 100 K, for solid and molten samples, respectively.

Our sample consisted of a synthetic CMASF glass with oxide contents in chondritic proportions (except for iron) so as to model the primitive mantle after core segregation (Wasson and Kallemeyn, 1988) (Table 4.1). We did not include minor and trace elements, which most abundant are Na (4900 ppm) and K (560 ppm). We believe that their effect on solidus and liquidus curves can be neglected as a first approximation because these elements are easily inserted in the $CaSiO_3$ perovskite phase (Ca-Pv) (Corgne et al., 2003). We did not mix our

sample with any YAG-laser absorber or pressure standard, such as Pt or W, in order to avoid any chemical reaction. Finally, we estimate that the melting behavior of our starting material should be comparable to that of pyrolite, due to their related compositions (Ringwood, 1975) (Table 4.1).

| | Chondritic mantle (this study) | | Pyrolite |
|---|---|---|---|
| **Oxide** | **(Wt%)** | **(Mole %)** | **(Wt%)** |
| **$SiO_2$** | 49.6 | 43.5 | 45.1 |
| **$Al_2O_3$** | 3.4 | 1.8 | 3.3 |
| **FeO** | 8.48 | 6.2 | 8.0 |
| **CaO** | 3.3 | 2.6 | 3.1 |
| **MgO** | 35.1 | 45.9 | 38.1 |

**Table 4.1** Composition of starting material used in this study, as measured by electron microprobe analyses. At lower mantle P-T conditions, the Ca-Pv, Mg-Pv, and Fp phase proportions are expected to be 4.5, 75.7, and 19.8 mol%, respectively. This composition is representative of a chondritic-type mantle (Wassen and Kallemeyn, 1988), and it is also quite close to pyrolite (Ringwood, 1975).

In order to probe the sample properties in-situ, we used the X-ray diffraction set-up available for LH-DAC at the Id27 beamline (Mezouar et al., 2005). Wavelength was fixed to 0.3738 Å. X-ray focusing to better than 2x3 $\mu m^2$ was achieved by two bent KB-mirrors. Typical acquisition time is 20-30 seconds using an imaging plate or a CCD detector. The X-ray beam position was determined from optical observations of the Re-gasket fluorescence. Therefore, combined images

of x-ray beam and YAG lasers could be perfectly positioned on the pinhole of the entrance of the spectrometer used for temperature measurements. Integration of 2D-images and further data treatment were performed using the Fit2d and the GSAS packages, respectively.

For estimating pressure at high temperature, we used two different methods. The first one is based on the PVT equation of state (EoS) of $CaSiO_3$ (Shim et al., 2000) from which pressure is derived from the Ca-Pv volume at a known experimental temperature. Due to a non-negligible Al-solubility in Ca-Pv (Nishio-Hamane et al., 2007), its EoS could be affected, which would increase the experimental error. The second method is based on an estimation of the pressure correction ($\Delta P$), which is a fraction of the theoretical thermal pressure ($\Delta P_{th}$). The latter consists on an increase of pressure due to heating ($\Delta T$) at constant volume, $\Delta P_{th} = \alpha K \Delta T$, where $\alpha$ and K are thermal expansion and bulk modulus, respectively. Experiments and calculations show that, due to partial volume relaxation at high-temperature, the effective $\Delta P$ corresponds to about half of the theoretical thermal pressure (Andrault et al., 1998). According to the thermo-elastic parameters of the main Mg-Pv component (Fiquet et al., 2000), the value of $\Delta P$ is ~$2.5\ 10^{-3}$ GPa/K. Both methods give results similar within a couple of GPa. So, pressure error at high T is estimated to be about 3 GPa.

We investigated the melting temperature using NaCl and KCl as thermal insulators, but also tested without insulating pellets in a few experiments, in order to make sure that the results are not affected by the nature of the pressure transmitting medium. NaCl happens to melt at temperatures similar, or even below, the liquidus temperatures of the primitive chondritic mantle composition used. Therefore, all liquidus temperatures reported here were determined using KCl insulator. The data set presented in here includes 19 successful high-pressure loadings. Each melting point has been determined after laser-heating of at least one fresh piece of sample, i.e. melting at one single pressure.

## 4.4 Results

### 4.4.1 Melting criteria

In general, the onset of melting can be detected using X-ray diffraction by the appearance of a diffuse x-ray scattering band typical of liquids. Such band is easily observed if the sample is composed of relatively high Z elements such as iron (Andrault et al., 2006; Shen et al., 2004). If the sample is composed of low Z-elements, such as is the case for a mantle silicate, the sample thickness should be important to enable observation of the diffuse band. This is not the case of our samples, which are intentionally thin in order to minimize axial thermal gradients.

Additional criteria based on X-ray observations are (1) the rapid re-crystallization of the sample at high temperature, with appearance and disappearance of X-ray spots, indicative of coexistence of crystal and melt. (2) At the same time as solid and liquid coexist, the temperature reaches a plateau while laser power is continuously increased, just before the liquid diffuse scattering appears and temperature simultaneously increases (Dewaele et al., 2007). In the following we used the fast disappearance of diffraction peaks of the solidus phase and re-crystallization as a sign of solidus temperature and the end of the temperature-power plateau as the sign of liquidus temperature.

### 4.4.2 Determination of solidus temperature

At sub-solidus temperatures, the phases present are $CaSiO_3$-perovskite (Ca-Pv), (Mg,Fe)O ferropericlase (Fp), and Al-bearing $(Mg,Fe)SiO_3$ perovskite (Mg-Pv), in the order of increasing abundance. The first phase to disappear from the diffraction patterns when increasing temperature is Ca-Pv (Fig. 4.1), in agreement with a previous study using multi-anvil press (Ito et al., 2004). Concerning Fp, persistence or disappearance of this phase is difficult to detect, first because its

content is limited to 20 mole% for this chondritic-type composition and secondly because most of its diffraction lines overlap with those of Mg-Pv (Andrault, 2001). Thus, disappearance of Ca-Pv and Fp could be almost simultaneous. The Ca-Pv disappearance is concomitant with rapid grain growth of the Mg-Pv phase, as evidenced by larger diffraction spots on the diffraction image (Figs. 4.1A and 4.1B). Also, a number of diffraction peaks typical of the three phases reappear on the imaging plate after laser shut-down. Note that for such mineralogy, where at least three phases coexist, the kinetics of grain growth are extremely sluggish in the solid state (Yamazaki et al., 1996). Thus, changes of peak intensity can only be attributed to non-solid state diffusion, i.e. diffusion assisted by melt. Another source of information is based on the sample shape after laser-heating. In the case of heating to the solidus temperature, the shape of the sample is affected only moderately (Fig. 4.1D). Thermal expansion in the laser spot induced a circular-shaped structure, and some cracks in the surrounding material, at more than 10-15 microns from the center, where the material has not been heated at high temperatures. This shape contrasts largely with what is observed when heating to the liquidus temperatures (Fig. 4.2D).

We found that melting at the solidus temperature is very difficult to detect for those LH-DAC runs where we did not use any thermal insulator. The reason is that solidus melting is dispersed over a broad range of laser power, due to a large axial temperature gradient across the sample, given that the diamond remain basically cold compared to the center of the laser spot. Also, it is possible that a sample fraction remains below the solidus temperature at the diamond surface, before the central part of the sample reaches the liquidus temperature. Therefore, clear disappearance of $CaSiO_3$ (and/or Fp) diffraction lines cannot be observed in this case.

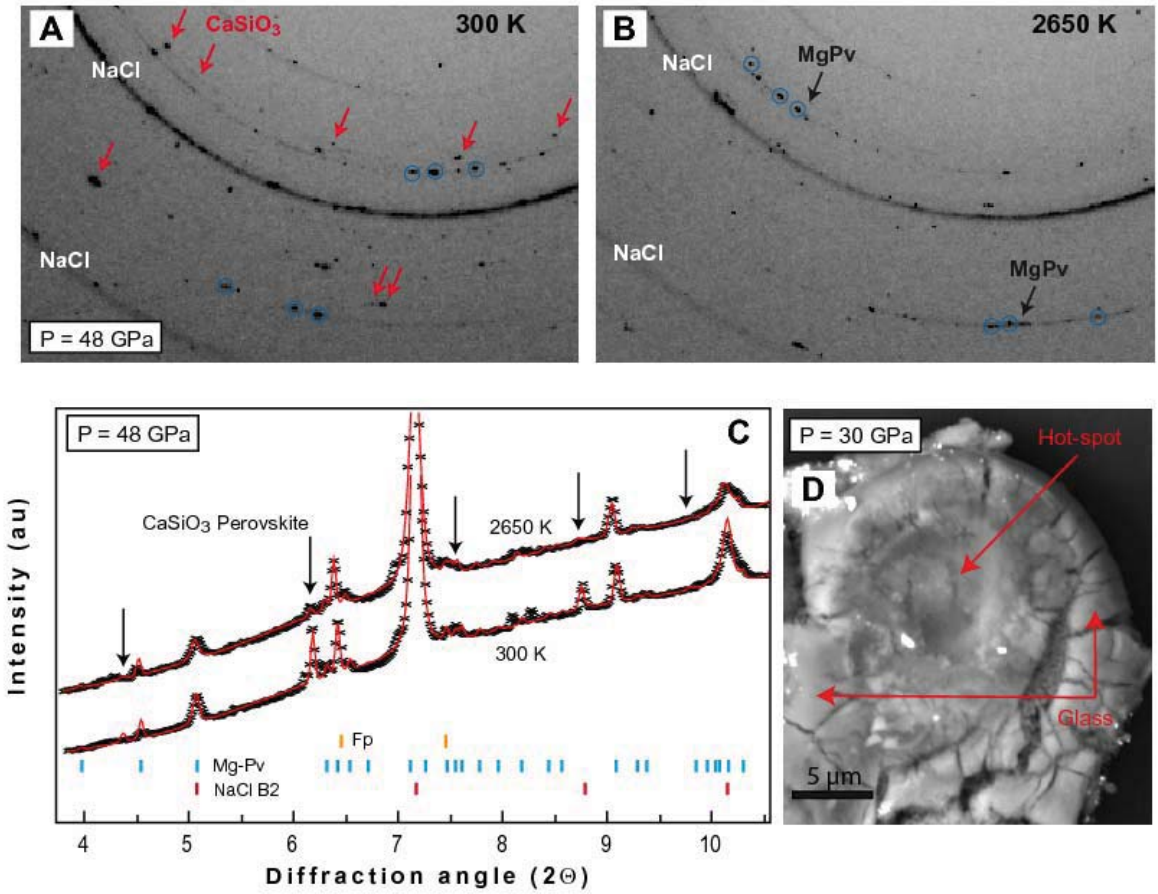


**Figure 4.1** Experimental evidences of sample partial melting and determination of the solidus temperature upon temperature increase from 300 K (A): at 2650 K (B) and a nominal pressure of 48 GPa, we observe first order changes in the position and intensity of diffraction peaks. First, disappearance of the $CaSiO_3$-perovskite diffraction peaks (pointed by arrows in (A) and (C)). Altogether, changes in peaks intensity are compatible with loss of 90% and 20% of the Ca-bearing and Mg-bearing perovskite phases, respectively. Simultaneously, we observe at 2650 K new spots of Mg-Pv phase (B) indicative of re-crystallization on a short time scale; this can only be due to the presence of melt at grain boundaries. (D) Electron microphotograph showing a central zone of a sample recovered from 30 GPa that encountered laser heating between the solidus and liquidus temperatures (see Fig. 4.2D for comparison).

### 4.4.3 Determination of liquidus temperature

When approaching the liquidus temperature, we first observe a plateau where increasing laser power does not yield an increase in temperature, just before a sudden temperature jump of more than 500 K (Fig. 4.2C). A similar criterion has been used for melting determination in metals (Dewaele et al., 2007). We explain the plateau by a progressive disappearance of Mg-Pv with increasing laser power, with a coexisting liquid phase absorbing the YAG-radiation less than Mg-Pv. Indeed, a higher absorption efficiency for the solid is expected since Al-bearing $(Mg,Fe)SiO_3$ perovskite contains high $Fe^{3+}$-content (Lauterbach et al., 2000). The last data point on the plateau corresponds to the laser power required to finally achieve a good coupling between YAG-radiation and the silicate melt, i.e. once the phase that absorbs the YAG-radiation better (i.e. the Mg-Pv) is consumed. Moreover, the flatness of the plateau indicates that the melt fraction has no significant effect on melting temperature. Such a high liquid productivity is expected when incompatible elements are not abundant in the bulk composition, which clearly is our case, and when the liquid composition gets closer to the remaining solid phase, which is also our case for high degree of partial melting due to the fact that Mg-Pv, the liquidus phase, is very abundant in our samples (Asimow et al., 1997) (Table 4.1).

A very important feature is the total disappearance of the fine and continuous diffraction lines of the Mg-Pv phase in the high-temperature X-ray spectrum, evidencing that this phase is completely molten at that temperature (Fig. 4.2A). The diffuse X-ray scattering is not clearly visible in our samples because the sample is too thin. The re-appearance of sparse and large diffraction spots upon temperature quench is typical of crystallization from a melt (Fig. 4.2B).

After quenching from the liquidus temperature, we observe a drastic change in the sample shape (Fig. 4.2D). The central part of the sample presents a round-shape with a diameter ~15-20

microns. This sample piece is detached from the rest of the sample. This part has undergone complete melting which induced deformation of the surrounding NaCl and KCl pressure medium to form a kind of sample droplet.

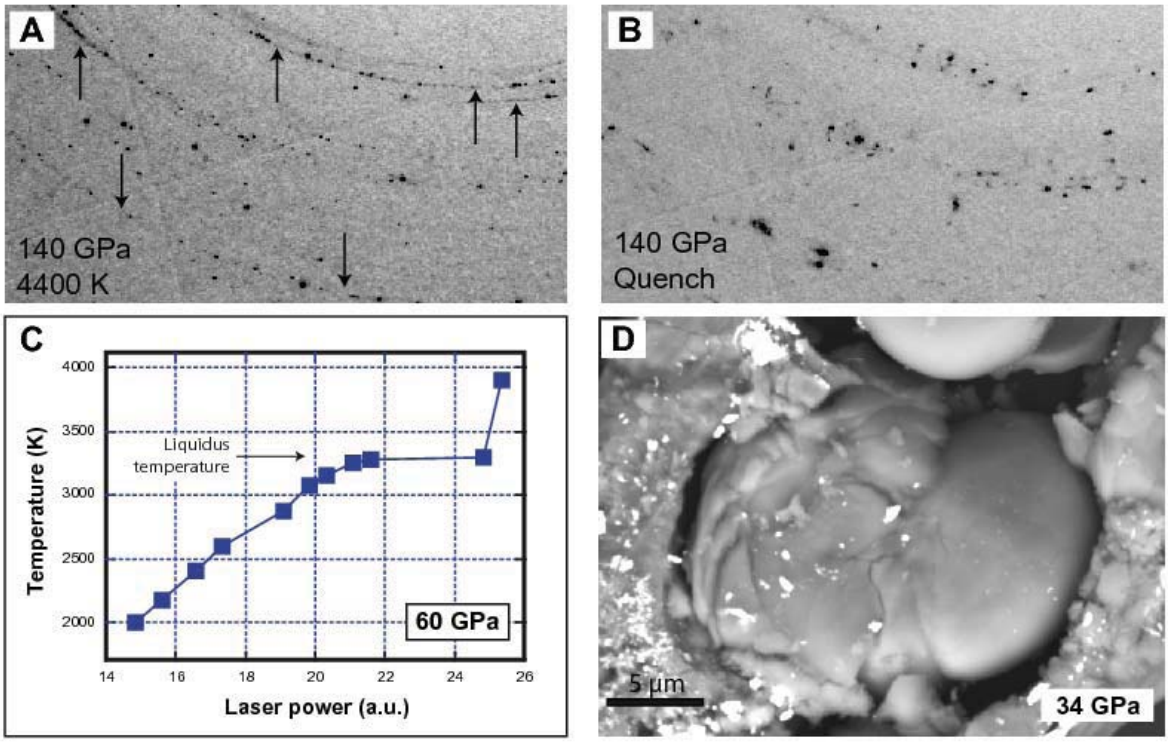


**Figure 4.2** Criterion used for determination of the liquidus temperature: X-ray diffraction pattern recorded (A) at 4400 K and (B) after quenching from 4800 K at a pressure of 100 GPa. Quench from the liquid phase (B) yields larger and new spots typical of sample re-crystallization from a fully molten sample. Indeed, while these two diffraction patterns were taken a few minutes apart from each other, the patterns are radically different in peak positions and intensities. Also, we observe total disappearance of all fine and continuous diffraction lines (indicates by arrows in (A)), which evidences the complete melting of Mg-Pv liquidus phase. (C) Sample temperature plotted as a function of the laser power. A discontinuity occurred at the liquidus temperature due to change in the absorption of the YAG-laser by the liquid sample. (D) Electron microphotograph of a sample recovered from 34 GPa showing the central laser-heated zone that underwent complete melting. It formed an independent liquid-ball separated from the rest of the sample.

### 4.4.4 Melting curves

The solidus temperature is found to increase smoothly with pressure from ~2500 K to ~4200 K at 30 to 140 GPa. The liquidus is found at 300 to 600 K above the solidus (Fig 4.3). Both melting curves are well fitted by modified Simon and Glatzel equation $\left[T = T_0 * \left(P/\left(a+1\right)\right)^{1/c}\right]$ with $T_0$ = 2045 K, a= 92 GPa and c= 1.3 for the solidus, $T_0$ = 1940 K, a= 29 GPa and c=1.9 for the liquidus, where $T_0$ is the virtual (this mineral assemblage is only stable above 24 GPa) melting temperature at ambient pressure (Simon and Glatzel, 1929). The interpolation to the CMB pressure of 135 GPa yields solidus and liquidus temperatures of 4150 ±150 K and 4725 ±150 K, respectively. At low pressures, both solidus and liquidus curves are compatible with previous determinations using multi-anvil press (Litasov and Ohtani, 2002; Trønnes and Frost, 2002). Our liquidus curve falls between upper and lower bounds of the solidus curve reported previously using LH-DAC (Zerr et al., 1998). However, it is unlikely that the speckle method used by Zerr et al. can precisely determine solidus and liquidus temperature in the absence of in-situ X-ray diffraction observation. In addition, their melting curves must be shifted to higher pressures because they neglected the effect of thermal pressure inherent to the use of LH-DAC (~2.5 GPa/1000 K, see above). Such uncertainties, leading to overestimation of the melting temperature using optical methods, explain why the MORB melting curve of Hirose et al. (1999) is observed at higher temperature than the solidus of our primitive mantle composition, although MORB is more fusible. Finally, the data point reported at 4300 K and ~125 GPa for melting of $(Mg,Fe)SiO_4$ olivine from shock-experiments (Holland and Ahrens, 1997) falls in between our solidus and liquidus melting curves, showing a relatively good agreement between the two different data sets. Indeed the forsterite liquidus is observed to be lower than that of enstatite at high-pressures (Mosenfelder et al., 2009). Most recently, liduidus and solidus melting curves for

a natural KLB-1 peridotite has been reported (Fig. 4.4) by Fiquet et al. (2010). Temperature differences on melting curves are supposed be due to: starting material composition and assembly (No thermal insulator in Fiquet et al. (2010) experiments) and experimental set-up.

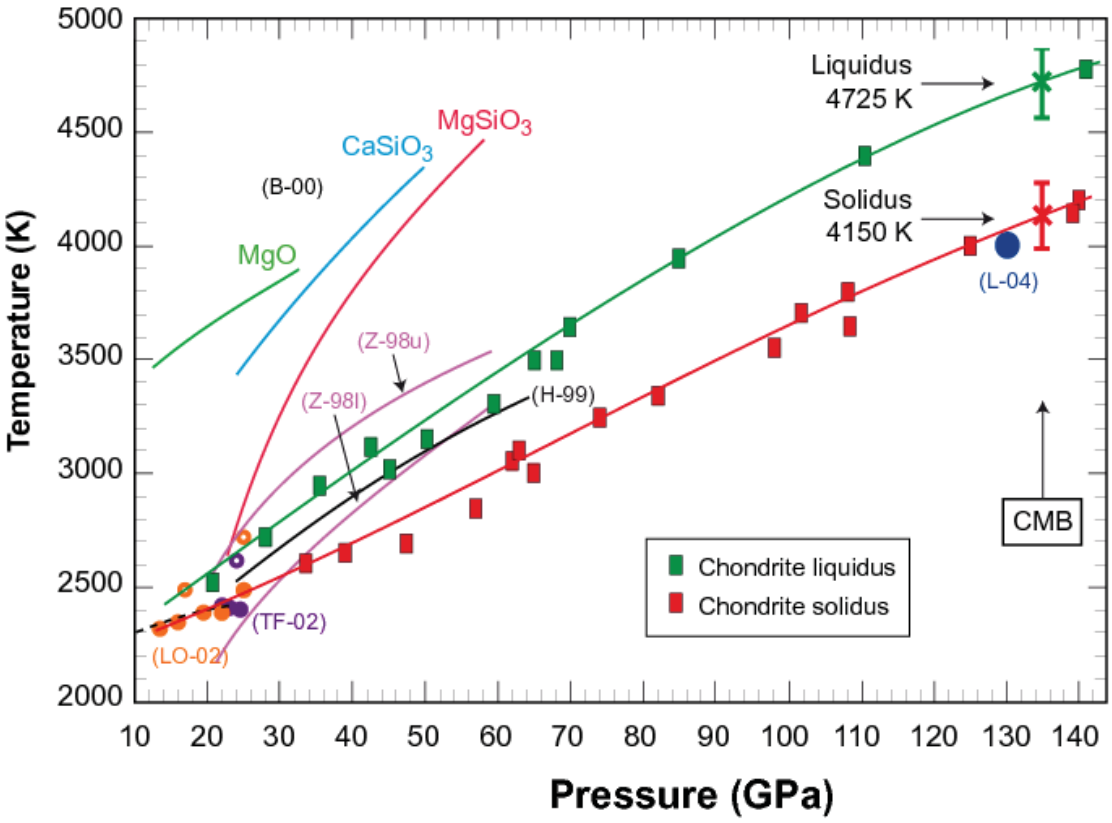


**Figure 4.3** Solidus (red squares) and liquidus (green squares) melting points and curve fits using the Simon-Glatzel model (continous red and green lines) obtained for our chondritic-type mantle composition. These results are compared with previous works on the melting of lower mantle materials (Pyrolite: LO-02 (Litasov and Ohtani, 2002) and TF-02 (Trønnes and Frost, 2002) (full and open circle for solidus and liquidus, respectively) and Z-98 (Zerr et al., 1998) upper and lower estimations of the solidus; Mid-ocean ridge basalt: H-99 (Hirose et al., 1999); Olivine: L-04 (Luo et al.; 2004); Simple oxides: B-00 (Boehler, 2000)).

| Liquidus | | Solidus | |
|---|---|---|---|
| *Pressure (Gpa)* | *Temperature (K)* | *Pressure (Gpa)* | *Temperature (K)* |
| 141 | 4750 | 140 | 4200 |
| 135 | 4725 | 139 | 4180 |
| 110 | 4400 | 135 | 4150 |
| 85 | 3950 | 125 | 4000 |
| 70 | 3650 | 109 | 3650 |
| 68 | 3500 | 108 | 3800 |
| 65 | 3500 | 102 | 3700 |
| 60 | 3300 | 98 | 3550 |
| 50 | 3150 | 82 | 3350 |
| 45 | 3050 | 74 | 3250 |
| 43 | 3120 | 65 | 3000 |
| 35 | 2950 | 63 | 3100 |
| 28 | 2750 | 62 | 3050 |
| 21 | 2550 | 57 | 2850 |
| | | 47 | 2700 |
| | | 39 | 2650 |
| | | 33 | 2620 |

**Table 4.2** Pressure-Temperature conditions for liquidus and solidus melting points (green and red squares, respectively in Fig. 4.3).

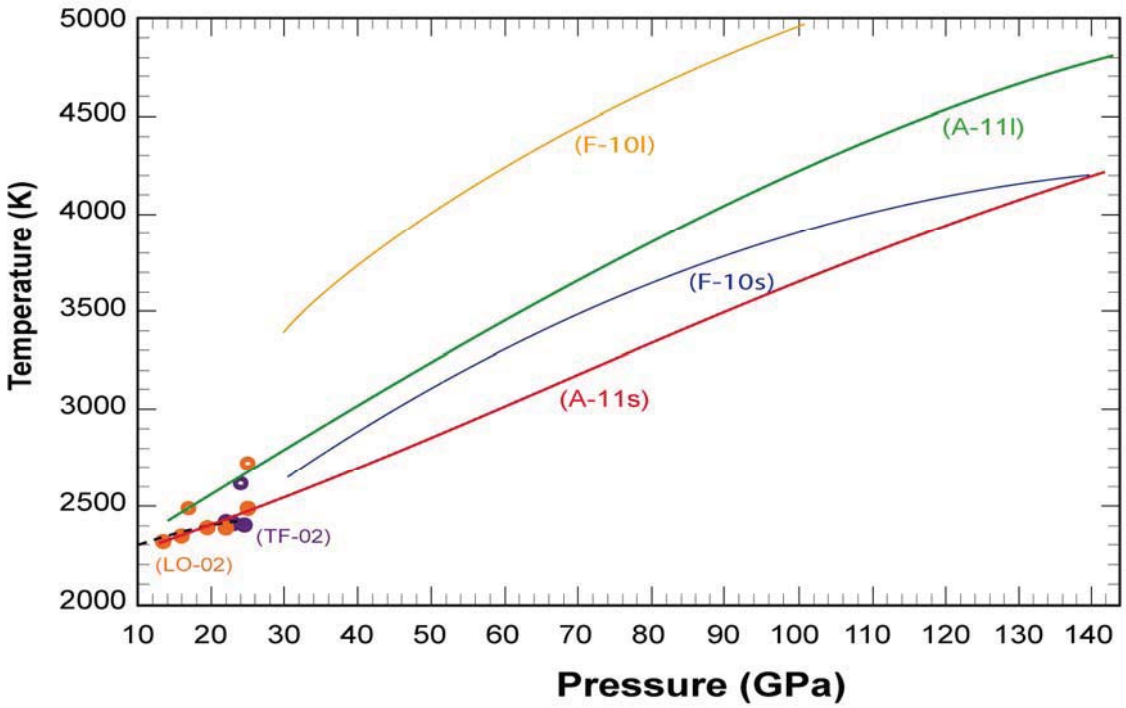


**Figure 4.4** Solidus (red squares) and liquidus (green squares) melting curves (this study) compared with previous works (Peridotite: F-10 (Fiquet et al., 2010) liquidus and solidus melting curves and Pyrolite: LO-02 (Litasov and Ohtani, 2002) and TF-02 (Trønnes and Frost, 2002)).

## 4.5 Discussions

### 4.5.1 Thermal structure of the D" layer

In order to identify melting in the mantle, melting curves must be compared to the geotherm. While temperatures are relatively well constrained in the shallow mantle due to anchoring by phase transitions at 410 and 670 km depth in $(Mg,Fe)_2SiO_4$ (Ito and Katsura, 1989), extrapolation of the adiabatic geotherm ($dT/dz = \alpha g T / C_p$, where α, g, $C_p$, are the thermal expansion, the gravity constant and heat capacity at constant pressure) to the base of the mantle using the elastic parameters of constitutive mantle minerals bears a much larger uncertainty (Fig. 4.5). Differences in adiabatic geotherms are often within 0.1 K/km but translate into up to 250 K difference at the bottom of the mantle yielding in general 2500 K ± 250 at 2700 km depth (Brown and Shankland, 1981; Bunge et al., 2001; Stacey and Davis, 2004). Whereas more sophisticated models using inversion of seismic radial profiles indicate hotter temperatures of 2800 to 3400 K at 2700 km depth (Matas et al., 2007), dependent on the Mg/Si ratio.

The temperature profile in the D"-layer should be much steeper accounting for the difference in temperature between the mean mantle above and the molten outer core. The present-time temperature gradient in this zone depends on the initial difference in temperature between the outer core and the mantle a few hundreds kilometres above the CMB, the core energy budget since its formation (Labrosse et al., 1997), the thickness of the boundary layer and the thermal conductivities. Recently, the thermal structure of the D" region has been tentatively constrained in light of the new post-perovskite phase of $MgSiO_3$ (Murakami et al., 2004; Oganov and Ono, 2004). It was proposed that the observation of pairs of positive and negative S-wave velocity jumps in the D" region are due to double-crossing of the perovskite to post-perovskite (PPv) transition (Hernlund et al., 2005). Based on the latest measurements of the Pv-PPv Clapeyron

slope in $MgSiO_3$, this would mean that the temperature at the CMB could be around 3700 K (Tateno et al., 2009). Still, it can be argued that the lower mantle contains Fe and Al that are known to influence the depth and thickness of phase transitions in general and have been demonstrated recently to considerably broaden the Pv-PPv transition due to the very different iron partitioning between the two phases (Andrault et al., 2010; Catalli et al., 2009). The interpretation of the seismic discontinuities in terms of temperature should thus be revised in order to take this into account.

In any case, refining the outer core temperature remains essential for our knowledge of the temperature profile in the D"-layer. This temperature is generally estimated by extrapolating the adiabatic temperature profile from the inner-core boundary (ICB) through the outer core. However, there are several sources of uncertainties. A first uncertainty arises from controversial melting curves for pure Fe determined firstly by LH-DAC, ranging from 4850±200 K (Boehler, 1993) to 7600±500 K (Williams et al., 1987) at ICB pressures. On the other hand, shock-wave experiments and ab-initio calculations suggest melting temperatures of more than 6000 K at 330 GPa (Alfè, 2009; Nguyen and Holmes, 2004). A second source of uncertainty is associated to the presence and nature of light elements, which should cause severe melting temperature depletion. Depending on the major light element considered for the outer core, extrapolations of the melting temperature to the ICB yields temperatures from 4100±100 K in the Fe-Si system (Asanuma et al., 2010) to 5500±500 K in the Fe-S eutectic system (Kamada et al., 2010), for example. And, if the outer core contains a mixture of light elements S, Si and O (Badro et al., 2007; Poirier, 1994), the resulting melting temperature should be lower than measured in binary compounds. Altogether, the broad range of ICB temperatures reported in the literature yields a large range of CMB temperatures and it is difficult to conclude if the outer core is indeed much hotter than the lower mantle at a fex hundreds kilometers above the CMB or not.

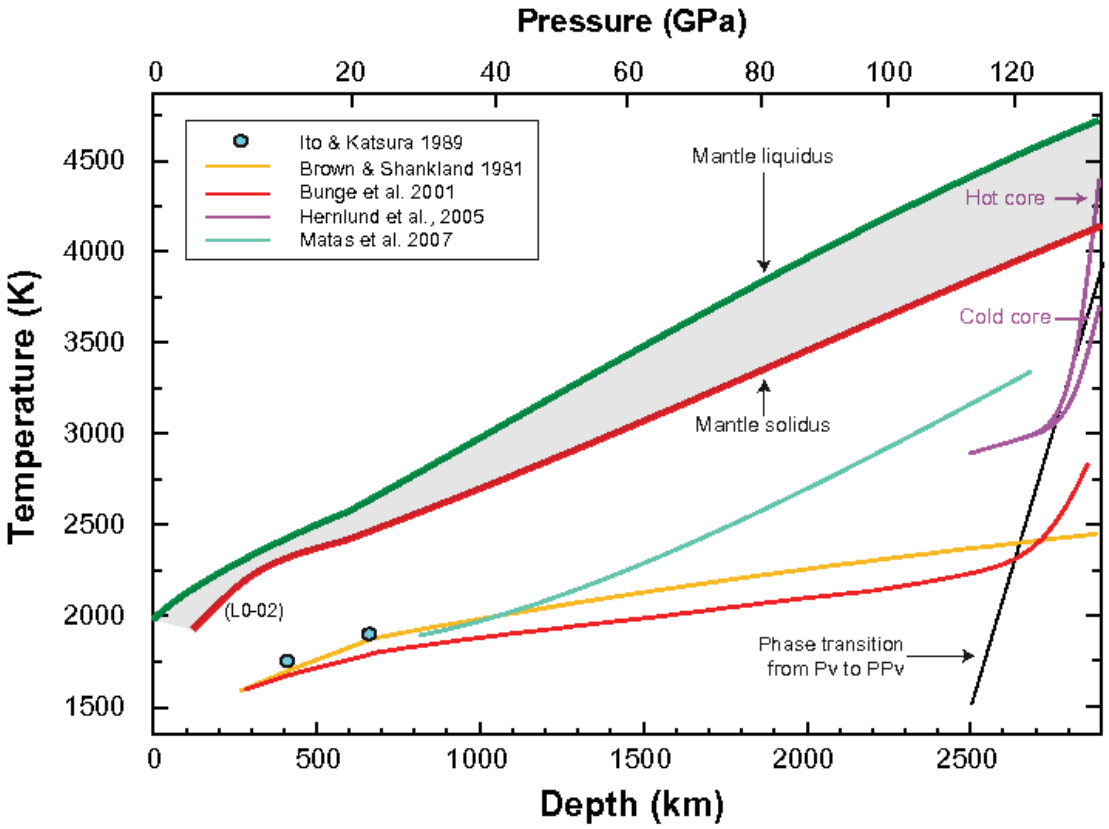


**Figure 4.5** The melting curves of synthetic chondritic mantle plotted together with available estimates of the mantle geotherm (Brown and Shankland, 1981; Bunge et al., 2001; Hernlund et al., 2005; Matas et al., 2007) and temperature anchor points (Ito and Katsura, 1989).

### 4.5.2 Melting in the D" region of the ULVZ

From the available geotherms, only the highest temperature estimation, based on an extremely steep temperature gradient in the D"-layer allows partial melting of a chondritic-type mantle in the D"-layer for which we report a solidus temperature of 4150 K (Fig. 4.5). However, we insist on tha fact that this very steep temperature profile is derived from the Clapeyron slope of the Pv-PPv transition for pure $MgSiO_3$ (Hernlund et al., 2005), and that in the mantle the transition does not occur at the same depths. Therefore, if partial melting of the chondritic (or pyrolitic) lower mantle is not totally precluded in the D"-layer, it remains unlikely as long as the occurrence of a very hot core is not better established.

The observation of ultra-low velocity zones (ULVZ) exhibiting P- and S-wave velocity reductions of 10 and 30% just above the CMB (Lay et al., 2004) has been interpreted as being the result of partial melting. Since the solidus and liquidus determined in this study are not in favor of partial melting of the chondritic (or pyrolitic) mantle, a probable way for inducing melting in the ULVZ of the D"-layer is a local enrichment in incompatible elements, in particular volatiles (Na, K, H $CO_2$) which are known to depress the solidus temperatures. Some of these elements (Na and K) may have a moderate effect on the solidus temperature, since they are easily inserted into the Ca-Pv at sub-solidus conditions (Corgne et al., 2003). In the case of water, however the effect could be large, becuase the solubility of H in the main lower mantle phases is low (Bolfan-Casanova et al., 2006). Once partial melting is induced, the degree of partial melting is difficult to estimate since solid-liquid phase relations are basically unknown at CMB conditions. Local concentration of the most fusible elements associated with chemical heterogeneities is compatible with the fact that ULVZ features are not ubiquitous but instead observed only in one third of investigated areas (Wen and Helmberger, 1998).

### 4.5.3 Depth extension of the early magma ocean

The energy deposited on the Earth during its accretion was sufficient to completely or partially melt it, especially just after the Moon-forming giant impact (Canup, 2008; Tonks and Melosh, 1993). Under such conditions, a magma ocean undoubtedly existed. It is interesting to discuss the implications of the new melting curve for our understanding of the nature of the magma ocean.

The inventory of siderophile elements in the modern indicates equilibration between silicates and iron at high pressures and temperatures (Li and Agee, 1996; Righter et al., 1997). In addition, in order to efficiently segregate the core, the silicate has to be molten in order to overcome the high surface tension of iron in a solid silicate matrix. Consequently, it was proposed that iron droplets sink through the molten silicate layer and pond at the base of a magma ocean, followed by metal descending through the solid mantle in the form of diapirs (Karato and Murthy, 1997; Stevenson, 1990). Thus, a widely accepted model is that equilibration occurred just before the iron droplets reach the Fe-pond at the floor of a magma ocean (Li and Agee, 1996; Wood et al., 2006). The apparent pressure of equilibrium is comprised between 30-60GPa, 45-85 GPa, or 20-50 GPa, based on metal-silicate partition coefficients of nickel and cobalt (Bouhifd and Jephcoat, 2003; Chabot et al., 2005), oxygen solubility in molten iron (Rubie et al., 2004), or metal-silicate partitioning of tungsten (Cottrell et al., 2009), respectively. A recent refinement of such model explains the mantle enrichment in several siderophile elements by a continuous accretion at a pressure of equilibrium of 40 GPa and 3150 K (Wood et al., 2006). The pressure of equilibrium is given by the partitioning of Ni and Co that is very sensitive to pressure while the temperature of equilibrium is estimated from the partitioning of V which is very sensitive to temperature. However, complications may arise from the fact that diffusion kinetics suggest metal-silicate equilibration during a “metal rainfall” so that the resulting chemical composition of the mantle

probably results from a polybaric process (Rubie et al., 2003), extending the pressure range of equilibrium to depths shallower than the base of the magma ocean.

We should also mention here that the model of equilibrium core segregation is challenged by numerical modeling results indicating that the core of the impactors possibly merged with the Earth's core or that the impact did not emulsify efficiently the metal and silicate liquids (Dahl and Stevenson, 2010). Both imply that the core segregated without equilibrating with the mantle. In this case, the pressure of equilibration is meaningless. Still, the geochemical constraints (Hf-W, U-Pb, siderophile elements) do not seem to be enough in order to conclude whether the core and mantle fully or partly equilibrated. It seems that the siderophile pattern of the mantle can be reproduced under non-equilibrium conditions assuming oxygen fugacity conditions higher than previously thought and embryos that have equilibrated at excessively high-temperatures (450 K above liquidus of chondritic mantle) (Rudge et al., 2010). In the following, since the disequilibrium core formation model creates more questions than answers, we will assume equilibrium core-mantle segregation at 45-50 GPa in agreement with metal-silicate partitioning experiments).

We report in Figure 4.6 liquidus and solidus curves measured for a chondritic mantle superimposed with the adiabats for the liquid (Mosenfelder et al., 2009; Stixrude and Karki, 2005). Here we focus on isentropes calculated by Mosenfelder et al. (2009), based on their latest shock-wave equation of state (EoS) of molten $MgSiO_3$. Such liquid is comparable to the chondritic mantle composition used here that contains ~70 mole% $MgSiO_3$ end-member. In the classical model of equilibrium at the base of a magma ocean, it is implicitly assumed that equilibrium occurs at 45-50 Gpa on the solidus (e.g. Wood et al., 2006). According to our measurements of the liquidus, a fully molten chondritic mantle that would extend to a pressure of 45-50 (±10) GPa exhibits a temperature of ~3175 (± 250) K at a depth of ~1175 (±250) km. Such

conditions correspond to a surface potential temperature of 2450 K (±150 K) (See red curves in Fig. 4.6). Such a hot surface is not stable and is only compatible with a transient magma ocean. Indeed, it has been demonstrated that surface temperatures significantly higher than 1700-1800 K prevent formation of an ($H_2O$-$CO_2$)-rich atmosphere required to produce an efficient thermal blanket to the magma ocean. Without such blanketing the magma ocean will cool down very rapidly (Abe and Matsui, 1988; Zahnle et al., 1988). Indeed, above 1700-1800 K significant silicate vaporization occurs (Nagahara and Ozawa, 1996) and such rock vapor atmosphere conducts heat easily so that the magma ocean would cool down in a few thousand years, before the magma ocean surface temperature comes back to 1700-1800 K (Sleep et al., 2001). Note that only shallow magma oceans (shallower than 5 GPa) are consistent with surface temperatures of 1700-1800 K (Miller et al., 1991) and can survive for long periods.

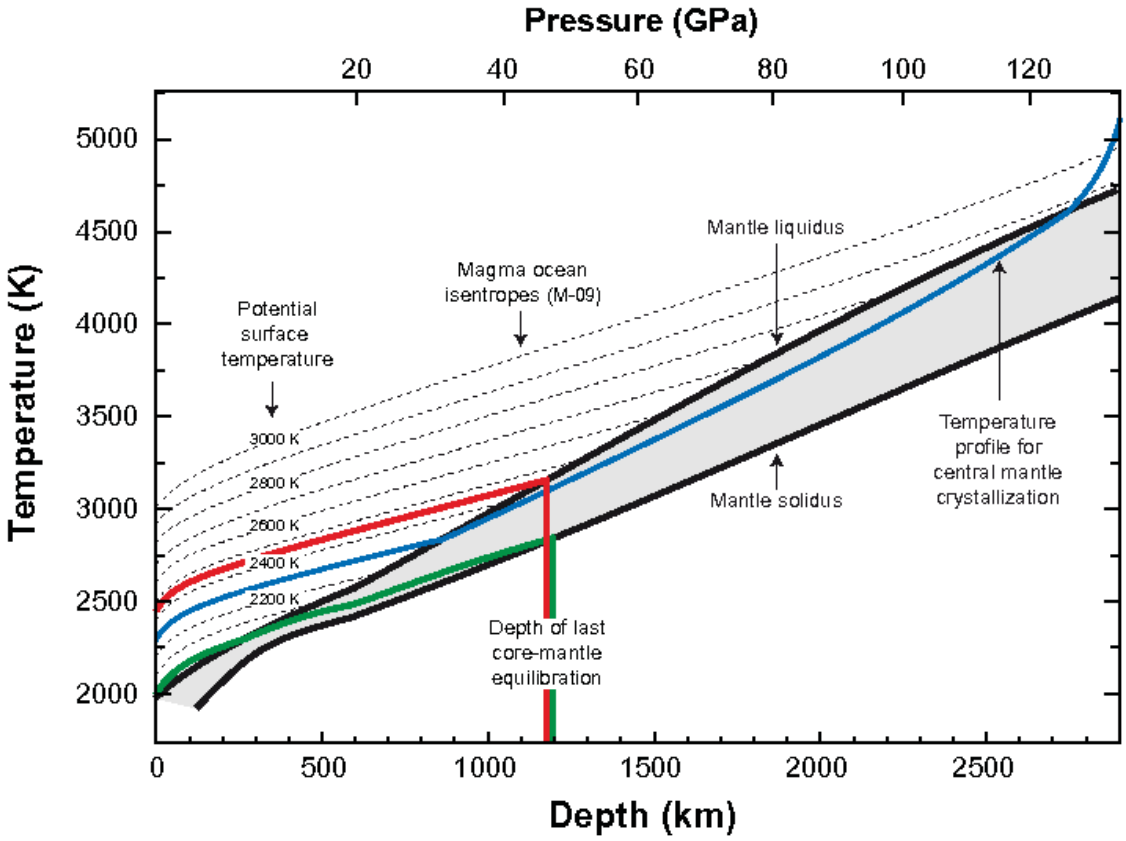


**Figure 4.6** The melting curves of synthetic chondritic mantle plotted together with isentropic temperature profiles of the magma ocean calculated for different potential surface temperatures (Mosenfelder et al., 2009). Green- and red- lines correspond to a surface temperature of ~2000 K and 2450 K respectively. Here is proposed a possible mantle geotherm (blue line, calculated interpolating and extrapolating Fig. 12A in Mosenfelder et al., 2009) compatible with crystallization of the liquidus phase Mg-Pv at the center of the mantle.

On the other hand, Hf-W chronology indicates that ~80% of the core formed within the first 30 million years of the earth's history (Kleine et al., 2002). As discussed above, deep mantle ocean extending to 45-50 GPa pressure can only last for a few thousand years, and such time scale is radically different from that inferred from Hf-W isotopes. Thus, one must refine the scenario of core-mantle segregation in order to explain these apparent contradictions:

a) If the metal droplets do not rain faster than the crystallization rate of the hot (transient) magma ocean (Rubie et al., 2003; Solomatov, 2000), they fall in the liquid mantle to intermediate depth until the silicate phases crystallize. Then, the metal remains embedded in the solid mantle until the next melting event. We note here that the descent of iron droplets is intrinsically associated with heat production by release of gravitational energy. Thus, in order to stop the Fe rain, the heat flux at the Earth's surface should be higher than the gravitational energy release. The droplet can also descend slowly by percolative flow (Yoshino et al., 2003). In this scenario (Fig. 4.7A), the equilibrium pressure of 45-50 GPa corresponds to the mean extension depth of the last magma ocean before the Fe droplets coalesce into larger diapirs and fall into the core.

b) A second possible scenario involves a magma ocean defined by its solidus located at ~1175 km depth (45-50 GPa) (Fig. 4.7b). From the base of this magma ocean upwards, coexistence of solid and melt is expected to occur over a broad depth interval due (i) to the large temperature difference between solidus and liquidus (Fig. 4.6) and (ii) to the fact that the adiabats of partially molten mantle are sub-parallel to the liquidus (Miller et al., 1991). It follows that this magma is on its liquidus at depth close to 300-400 km, corresponding to the actual upper mantle. As a consequence, the melt adiabats indicate a surface temperature approaching 2000 K, compatible with a blanketed magma ocean, which would thus cool down slowly. In this situation, the metal rains and equilibrates in a mush rather than in a completely molten magma ocean.

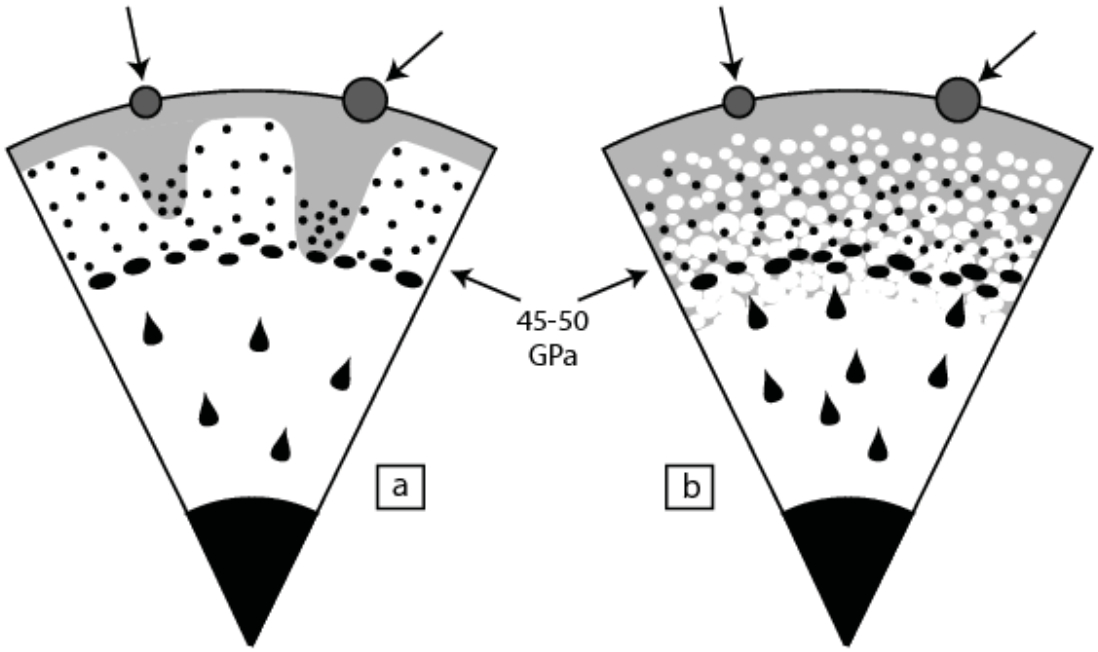


**Figure 4.7** Models for core-mantle segregation that respect (i) an equilibrium pressure of 45-50 GPa as suggested by metal-silicate partitioning experiments and (ii) a shallow completely molten magma ocean that can be compatible with a moderate surface temperature. In model (a) representative of transient magma oceans cooling very fast, the metal droplets remain embedded in the solid mantle and their progression to greater depths is aided by successive melting events. In model (b) representative of a sustained magma ocean cooling slowly, metal droplets fall in a partially molten mantle until the fraction of solid mantle becomes too high, at temperatures close to the solidus.

### 4.5.4 Formation of a basal magma ocean?

Finally, our new melting curve can be used to discuss the possible existence of an ancient magma ocean starting its crystallization in the mid-lower mantle, with formation of a basal magma ocean (Labrosse et al., 2007). First, we should note that complete melting of the Earth mantle implies a surface temperature higher than 2800 K (Fig. 4.6), wich is much above the vaporization temperature of the silicate mantle (Nagahara and Ozawa, 1996). Thus, cooling and crystallization of the mantle should occur very quickly, as discussed in the previous paragraph. In addition, this scenario implies temperatures higher than the liquidus in both the shallow and lowermost mantle, and temperatures becoming lower than the liquidus at intermediate depth due to secular cooling. Such a temperature profile requires a very hot core in order to induce a geotherm steeper than the liquidus in the lowermost mantle (see blue curve in Fig. 4.6). However, such temperature gradient is unlikely to be relevant to the primitive Earth for a long time. High thermal conductivities expected for both the liquid in the D"-layer and the partial melt at mid mantle depth should help to propagate heat from the CMB to shallower mantle depth and resolve a potential steep temperature gradient in the lowermost mantle. Therefore, it appears unlikely that the outer core temperature could exceed 4725 K at the CMB after crystallization of the magma ocean.

In the context of a complete (or almost complete) melting of the mantle, it is unlikely that the temperature profile could reach the solidus in the mid-lower mantle given (i) the large temperature difference found between solidus and liquidus temperatures; (ii) the fact that the solidus and liquidus are almost straight curves that remain steep at CMB conditions; and (iii) because the isentropes of partially molten mantle are steeper than melt adiabats (Fig. 4.6). Due to the later effect, it was argued that the partially molten mantle could extend up to the core mantle

boundary when the depth of a completely molten mantle to a pressure of more than 40 GPa (Kojitani and Akaogi, 1997; Miller et al., 1991; Stixrude et al., 2009). Therefore, the mantle fraction defined as "solid mantle" by Labrosse et al. (2007) could only correspond to a partially crystallized mantle, where the solid phase would essentially be the liquidus phase i.e. Mg-Pv (Fig. 4.1 and Ito et al., 2004). If Crystallization of the magma ocean from the middle is associated to formation of a perovskite layer, geochemical arguments constrain it to be at most 13% of the whole mantle, a minimum for which the upper mantle refractory elements budget still remains chondritic (Liebske et al., 2005).

Alternatively, a basal magma ocean could be possible if its composition is enriched in incompatible (i.e. fusible) elements, which would facilitate melting at lower temperatures at the base of the mantle. The persistence of such fusible material until today would be compatible with the observation of ULVZ, as mentioned in a previous paragraph. It could also explain major geochemical signatures, such as the one associated to "primitive mantle" with high $^{3}He$, for example (Allègre et al., 1995; Kurz et al., 1982).

## 4.6 Conclusions

Were have determined solidus and liquidus curves of a chondritic mantle up to CMB pressures. Our melting criteria include in-situ X-ray diffraction and temperature-power relationships. We confirm that the $MgSiO_3$-bearing perovskite is the liquidus phase in the deep lower mantle. The solidus melting curve is found at lower temperature than reported previously, especially at mid-lower mantle depth, while the liquidus is found at significantly higher temperatures at all mantle depths. At the CMB, we report solidus and liquidus melting at 4150 ± 150 K and 4725 ± 150 K, respectively.

We then discussed the geophysical implications of the new melting curve for chondritic mantle. First, it appears unlikely that the ULVZ, which is interpreted to experience ~20% partial melting, is of chondritic (or pyrolitic) composition. Indeed, the solidus of 4150 ± 150 K appears to be too high compared to estimates of the temperature profile in the D" region, except if the core is extremely hot. Thus, in order to be explained by melting the ULVZ should rather be associated to high concentration of fusible elements that decrease the melting point compared to the chondritic mantle.

We also show that the pressure of 45-50 GPa typical of metal-silicate equilibrium, as reported by several experimental studies in the context of core-mantle segregation, is associated to a magma ocean surface temperature incompatible with a sustained magma ocean. It strongly suggests that the metal-silicate equilibrium occurred in a partially molten mantle, covered by a fully molten magma ocean much thinner than 1000 km.

Finally, by examining the relationships between magma ocean temperatures at depth and potential surface temperatures, our melting diagram is compatible with the formation of a basal magma ocean only if the middle-depth solid mantle is mainly composed of Al-bearing

(Mg,Fe)$SiO_3$-perovskite and if the basal magma ocean has a chemical composition significantly different than the chondritic mantle.

# Chapter 5: Phase relations in partially molten lower mantle: A X-ray fluorescence study at very high-pressures

## 5.1 Abstract

We investigated melting relations in a model composition for chondritic mantle using X-ray diffraction (XRD) and X-ray fluorescence (XRF) methods at synchrotron facility ESRF. Samples were synthesized using the laser-heated diamond anvil cell between 19.5 GPa and 113 GPa, corresponding to conditions that extend from the mantle transition zone to the lowermost mantle. We recorded XRD and XRF maps which translate into maps of mineral fraction and maps of Fe and Ca contents, respectively. We observe (i) a good correlation between zones with maximum Ca and Fe contents and (ii) a clear mismatch between these zones and those with maximum Mg-bearing perovskite (Mg-Pv) content. Since Mg-Pv is the liquidus phase, we conclude that Ca and Fe have a similar incompatible behavior upon sample melting.

By comparing the different sample regions, we extracted the Fe partition coefficient ($D_{Fe}$) between melt and the solid at the liquidus temperature. The refined $D_{Fe} = X_{Fe}^{Pv} / X_{Fe}^{Melt}$ decreases slightly from 0.6-0.7 to 0.5-0.65 with increasing pressure. Our data set plots sightly higher than the previous data sets performed in multi-anvil press at low pressures, which could be due to a higher degree of melting in our experiments. Our $D_{Fe}$ are found at significantly higher values than a recent work performed in an Al-free system, a well-known effect for Fe partition coefficients when the Al-bearing silicate perovskite phase is involved. Altogether, the incompatible character of Fe is not very high, which put into questions the negative floatability of the liquids in the deep mantle.

## 5.2 Introduction

### 5.2.1 Mantle melting in the past and at present time?

Recently, melting of the lowermost mantle has been at the center of a number of experimental and theoretical studies. The great interest for this subject was enhanced after seismological studies suggested that partial melting in the lowermost mantle could explain the ultra-low velocity zones (Lay et al., 2004; Williams and Garnero, 1996). Indeed, it was suggested that 5 to 30% partial melting of the mantle would induce a reduction of P and S seismic wave velocities up to 10-30%, for specific geometry of liquid-enclaves in the solid-liquid mixture, in agreement with the seismological observations (Hernlund and Jellinek, 2010; Lay et al., 2004; Rost et al., 2005). Note, however, that this matter remains controversial, since other studies show that the presence of a melt layer does not explain satisfactorily all seismic features (McNamara et al., 2010; Stutzmann et al., 2000). Instead, mantle heterogeneities in the D”-layer could arise from other causes associated with core-mantle interactions (Buffett et al., 2000; Goarant et al., 1992) or large-scale convection of the mantle, leading to the presence of foreign material stored in this region. It was proposed, for example, that iron-rich Archean rocks could have subducted down to the core mantle boundary (CMB) (Dobson and Brodholt, 2005).

Still, partial melting remains a likely explanation for the D” seismic features and this hypothesis needs to be investigated. Its occurrence could be of major importance for the formation of distinct geochemical reservoirs, as a consequence of solid-liquid segregation at high mantle depth (McNamara et al., 2010). Solidus and liquidus melting curves were recently investigated in the P-T ranges covering the whole Earth's lower mantle (Andrault et al., 2011; Fiquet et al., 2010). Despite the fact that both studies are in significant disagreement with each other, especially for the liquidus temperature, the solidus melting temperature tend to converge to 4150 K at the core-

mantle boundary pressure of 135 GPa. The question of whether the temperature profile in this region is higher or not than the solidus melting temperature remains open.

At mid-mantle depths, solid-liquid segregation has probably occurred early in the Earth's history, when the planet experienced large degrees of melting due to giant impacts (Boyet and Carlson, 2005; Canup, 2008). The depth extension and the degree of melting in early magma oceans are still in discussion (Andrault et al., 2011; Miller et al., 1991). It was proposed recently that the actual ULVZ is a direct consequence of the dynamics of the early magma ocean, if a basal magma ocean took place in the primitive Earth (Labrosse et al., 2007).

### 5.2.2 Liquid floatability in the Earth mantle

A parameter of major importance for the fate of liquids in the mantle is their buoyancy. In this respect, density crossovers between solid and liquid phases should have a major impact on the dynamics of the mantle. Sinking of dense melts and accumulation at the CMB could explain, for example, the ULVZ in the D"-region. This would have enormous implications for thermal properties in the lowermost region and for the formation of deep mantle plumes.

At upper mantle pressures, various experimental techniques have been used to investigate the liquid floatability such as the relative sink-float method (Agee and Walker, 1988; Suzuki et al., 1998), the modeling of liquid density based on sound-velocity measurements (Ahrens et al., 1998; Stolper et al., 1981), and the measurement of the liquid equation of state (EoS) based on Hugoniot equation and shock-wave data (Miller et al., 1991; Ridgen et al., 1984). All these studies indicate that silicate liquids are less dense than PREM, and hence rise, at pressures lower than 10 GPa. A density crossover was suggested at 14 GPa, which would make the melt denser than the mantle material (Ohtani and Maeda, 2001). Then, phase transitions encountered by

minerals in the transition zone are likely to increase the solid-mantle density sufficiently to produce another density crossover in the transition zone (Lee et al., 2010). At lower mantle pressures, the silicate melts floatability remains uncertain. From a theoretical point of view, the liquid floatability at mantle P-T conditions depends mainly on the evolution with pressure of (i) the atomic packing of the liquid silicate network and (ii) the solid-liquid phase relations and thus the chemical composition of the melt, in particular its iron content.

### 5.2.3 Atomic packing

At shallow pressures, while silicate melts are less dense than the solid mantle, the liquids are more compressible than the minerals. In the transition zone, solids undergo a series of phase transitions that increase the atomic packing of their atomic structure, and thus their density. Similar changes in polyhedral linkage are also expected in the liquid phases, however, with a more progressive evolution. At lower mantle pressures, the liquid density was investigated by *ab initio* calculations. The different studies available agree for an increasing coordination number of the cations with increasing pressure: Si-Al-Mg coordination numbers are reported to change from 4-4-5 at room pressure to 6-6-8 with increasing pressure to 135 GPa. Also, polymerization of the melt is expected to increase with increases pressure, an effect potentially associated with changes in $SiO_2$-ring configurations in the liquid (Guillot and Sator, 2007; Karki, 2010; Stixrude and Karki, 2005).

Recently, polyamorphic phase transitions were reported experimentally in $MgSiO_3$-glass, in agreement with ab-initio calculations (Sanchez-Valle and Bass, 2010). On the other hand, shock wave experiments provide values for the melt density at extreme conditions of pressure and temperature. The P-V-T equation of state could be determined for $MgSiO_3$ and $Mg_2SiO_4$ liquids

up to the CMB pressure of 135 GPa (Mosenfelder et al., 2009). A major result is an increase with pressure of the Grüneisen parameter, in very good agreement with a molecular dynamic simulation based of first principles (Stixrude et al., 2009). For $MgSiO_3$, the density excess of the solid compared to the liquid is estimated to about 4% at the CMB (Mosenfelder et al., 2009; Stixrude and Karki, 2005). On the other hand, by comparing the compressibility difference between MgO and $SiO_2$ components in the liquid, it was suggested that the $MgO/SiO_2$ ratio has a major effect on the liquid floatability in the lower mantle, with increasing buoyancy for $SiO_2$-rich liquids (Funamori and Sato, 2010).

### 5.2.4 Melt composition

In previous melting experiments performed on various types of mantle composition, the liquidus phase was reported to change from majoritic garnet (Ito and Takahashi, 1987) to ferropericlase at 22-23 GPa (Zhang and Herzberg, 1994), before becoming Mg-bearing perovskite in the lowermost mantle (Ito et al., 2004). By itself, this change in nature of the liquidus phase is already a proof of change with pressure of the liquid composition in a partially molten mantle. In particular, the $MgO/SiO_2$ ratio is affected, as demonstrated in a previous experimental study performed up to 26 GPa (Liebske et al., 2005). While the $MgO/SiO_2$ ratio certainly plays a role in the liquid density (Funamori and Sato, 2010), the Fe partitioning coefficient between solid and liquid phases ($D_{Fe} = X_{Fe}^{Sol} / X_{Fe}^{Liq}$, where $X_{Fe}$ is the molar Fe-content) has been at the center of a number of studies. Using multi-anvil press apparatus, $D_{Fe}$ has been reported to vary from ~0.3 to ~0.6, when the solid phase considered is the liquidus phase, namely olivine, majoritic garnet and Mg-Pv, with increasing pressure from a few GPa to more than 25 GPa (see Figure 5.1a and references in Figure caption). We note that this figure compares experimental results obtained for

different starting materials, with model compositions being pyrolitic, peridotitic, or chondritic mantle. The figure shows that despite the phase transitions occurring in the 15-25 GPa pressure range and the change in nature of the liquidus phase (from olivine to Mg-Pv), the $D_{Fe}$ appears relatively constant up to 35 GPa. On this basis, Fe can be recognized as an incompatible element in the deep mantle, with a concentration ~1.5 to ~3.0 times higher in the melt.

At higher pressures, there are several reports on the Fe partition coefficient between Mg-Pv and ferropericlase, but much less exists about the Fe-partitioning between solid phases and silicate melts. A very recent work reports the solid-liquid phase relations up to 85 GPa in $(Mg,Fe)_2SiO_4$ using analytical transmission electron microscope (ATEM) on samples recovered from laser-heated diamond anvil cell (LH-DAC) (Nomura et al., 2011). This study reports a decrease of $D_{Fe}$ Pv/melt from ~0.4 to ~0.06, for pressures from 35 to 85 GPa, respectively. This corresponds to a strong increase of the incompatible character of Fe with increasing pressure. The authors also report a steep change of $D_{Fe}$ Pv/melt at ~75 GPa, which is interpreted to be due to the spin crossover of iron in the melt. We note that this previous study was performed on an Al-free system which could be too simplified to be fully representative to the lower mantle conditions (Andrault et al., 2010; Wood and Rubie, 1996). Here we present an alternative method based on LH-DAC coupled to *in situ* fluorescence measurements.

## 5.3 Experimental methods

### 5.3.1 Laser heating in the diamond anvil cell

The starting material consisted of a synthetic glass with a model composition for a C1-chondritic mantle (McDonough and Sun, 1995; Wasson and Kallemeyn, 1988). The bulk composition was prepared from oxide and carbonate mixes through repeated cycles of grinding and fusion at around 1800 K and rapidly cooled to obtain a glass of homogeneous composition. It is the same starting material than used in a previous study (Andrault et al., 2011).

We performed experiments at high pressure and high temperature using the LH-DAC technique. We used diamond anvils with flat culets of 250 μm diameter or bevel type 100-300 μm culets. We used tungsten gaskets pre-indented to a thickness of 30-45 μm and laser-drilled to diameters of 50-80 μm. Samples were loaded between two NaCl pellets. This material remains sufficiently soft at high pressure to insure hydrostatic pressure. NaCl does not melt and react with silicate phases. It insure a good thermal insulation between the laser-heated sample and the diamonds, and thus minimizes the axial temperature gradient in the sample. The thickness of the NaCl-layer between the sample and the diamond surfaces is estimated between 5 and 10 μm in our different experiments. Samples were heated by two Nd-YAG lasers with a laser spot size of more than 20 μm diameter. Temperatures were determined spectro-radiometrically using the Planck function.

We used the NaCl equation of state (EoS) to derive the pressure at room temperature, before and after laser heating. In this paper, we report experimental runs performed at 5 different nominal pressures, 14 GPa, 41 GPa, 48 GPa, 60.5 GPa and 103 GPa. We estimate the pressure correction ($\Delta P$) associated to the laser heating in a partially isochoric regime using the same technique than in a previous study (Andrault et al., 2011). This yields $\Delta P$ (GPa) = $2.5*10^{-3}$ $\Delta T$ (K), where $\Delta T = T-300$. The liquidus temperatures were observed at 2550 K, 3200 K, 3350 K, 3600 K and

4450 K for the nominal pressures reported above, in agreement with the melting criteria described elsewhere Andrault et al. (2011). Pressures encountered by the sample at high temperatures are therefore 19.5 GPa, 48 GPa, 55.5 GPa, 68.5 GPa and 113 GPa, respectively. These pressures extend from the transition zone to the deep lower mantle.

Our procedure for the samples synthesis is as follows: we compressed each sample to the target pressure at ambient temperature. We then adjusted the optical path for the lasers and the temperature measurements, keeping the two lasers at minimum power. We then observed the sample crystallization at a moderate temperature and verified the sample quality (mineralogical content and chemical composition), using X-ray diffraction and X-ray fluorescence (see details below). Finally, we increased the laser power until the liquidus temperature was reached at the center of the sample. The laser power was maintained for a couple of minutes before shut-down. We report typical microphotographs of the recovered samples (Figure 5.2). For some samples, we also performed sample analyzes using scanning electron microscope (JEOL JSM-5910 LV). Prior to the measurement, we immersed the W-gasket in water in order to remove the NaCl pressure medium. We then extracted the sample using a needle and positioned the sample chip on a graphite adhesive foil (Figure 5.3).

### 5.3.2 X-ray methods

We then investigated the sample properties using X-ray diffraction (XRD) and X-ray fluorescence (XRF). Some of the X-ray measurements were performed *in situ* in the DAC at high P and T: XRD to monitor the sample evolution during laser heating; XRF in order to check the sample composition. However, most of the measurements reported in this study were recorded after pressure release on samples trapped in the W-gasket. It insures a better signal, for XRF in

particular, due to the strong absorption of the diamond-windows at low energies. All X-ray measurements were performed at the ID27 beamline of the ESRF. The X-ray beam generated by the ondulator was tuned to 0.3738 Å wavelength and focused by two Kirkpatrick-Baez (KB) mirrors to a 2*2 $\mu m^2$ FWHM spot on the sample. For X-ray diffraction, we used the MAR345 image plate detector. Typical acquisition time was 20-30 seconds. Diffraction images were analyzed and integrated using the Fit2d program (Hammersley, 1996). We refined phase contents by performing multiphase Rietveld refinements using the GSAS code (Larson and Von Dreele, 1988). We note (i) a weak Ca-Pv signal for some of the samples, firstly because the Ca-Pv amorphizes partially upon decompression and also because rapid quenching from the molten state could lead to other Ca-rich polymorphs, such as the calcium-ferrite form, and (ii) a weak precision for the determination of Fp contents, since its major diffraction peaks overlap with those of the major Mg-Pv phase.

For XRF measurements, we used an energy dispersive solid-state Si(Li) Vortex detector, set at around 60° from the incident beam. This angle position is the best that can be achieved in the transmission mode when using W-gaskets, in order to maximize the photoelectric effects and minimizes Compton and Rayleigh diffusions. The detector was protected from incoherent X-ray signal using an Ag collimator. We detected K-lines of Ca and Fe from the sample, K-line of Cl from the NaCl pressure medium, L-line of W from the gasket material, and L-line of Pb used as X-ray absorber on the beamline. Elemental analyzes are derived from fluorescence spectra using the PyMca program (Solé et al., 2007). We fixed the fundamental parameters to: X-ray flux= 8.4e+11 photons/s; Acquisition time= 100 or 150 sec.; Active area= 4 $\mu m^2$; Sample to detector distance= 20mm.

The XRF method usually requires the use of standards for quantitative determination of the element contents. In our samples, there are parts where the samples has not encountered melting

or phase segregation and one could try to use these regions as an internal calibrant, since their chemical composition should be similar to that of the starting material. However, the presence of a thin NaCl layer above the sample makes the situation more complicated. Indeed, based on the intensity of the Cl fluorescence signal measured at the different sample positions, it is clear that this layer is heterogeneous in thickness in the recovered samples (Figure 5.3). We estimated the NaCl thickness at all sample positions from the measured intensity of the Cl fluorescence signal and included a correction for NaCl absorption when refining the Ca and Fe contents from their respective XRF signals. This correction brings additional uncertainty for determination of the Ca contents, since 65% of the Ca fluorescence signal can absorbed by a 10 μm thick layer of NaCl. On the other hand, the correction for NaCl absorption is less than 20% at the Fe fluorescence energy. Altogether, our XRF measurements provide quantitative information for the relative variations of Fe and, to a minor extent, for Ca, for each given XRF map.

## 5.4 Results

### 5.4.1 Diffraction results

Using XRD, we first followed the glass crystallization into the stable mineralogical assemblage at moderate laser-heating up to typically 2000 K. For a pressure of 19.5 GPa, the analysis reveals the presence of a majoritic garnet and Ca-perovskite, in agreement with previous reports (Zhang and Herzberg, 1994). Three phases are present for samples synthesized at higher pressures; Ca-Pv, the ferromagnesian perovskite (Mg-Pv) and ferropericlase (Fp). According to the composition of starting material, proportions of Mg-Pv, Ca-Pv and Fp phases are expected to be 75.7, 4.5 and 19.8 mol%, respectively. Diffraction rings of the NaCl pressure medium are clearly visible on all diffraction patterns (Figure 5.4), which suggests good sample insulation from the sample. Weak diffraction lines of the W-gasket are sometimes visible.

After the samples had experienced melting, we performed X-ray diffraction measurements at several positions around the laser hot-spot (LHS). The result of this procedure is a clear variation of Bragg-line intensities as a function of sample position relative to LHS (Figure 5.5), which evidences the samples heterogeneity around the molten zone. Phase contents were refined at each sample positions, by performing multiphase Rietveld analysis on each diffraction patterns. The results are presented in form of a map presenting the mineralogical content as a function of the sample position (Figure 5.6). A circular shape around the LHS center is observed for all phase contents. There is also a large decrease of the diffraction signal intensity at long distances from the LHS center, where the glassy sample has not been sufficiently heated for recrystallization. The ring shape is particularly clear for the main phase, Mg-Pv or garnet, but it is also visible for the Ca-Pv phase in some of our samples (Figure 5.6c). Interestingly, the rings representative of

the different phases do not overlap with each other. The Ca-Pv phase appears to be more concentrated on the external part of the laser spot, compared to Mg-Pv.

### 5.4.2 Fluorescence results

We recorded various X-ray fluorescence spectra at same sample positions than for the XRD mapping. Visible peaks arise from Cl in NaCl, Ca and Fe in the sample and W in the gasket (Figure 5.7). As for XRD, we observe a clear variation of XRF peak intensities from one sample position to another (Figure 5.8). Refinement of the XRF spectra provides maps of contents in Cl, Ca, and Fe (Figure 5.9). The chemical zoning is clearly apparent for Fe and Ca. We first note the good correlation between zones where Ca and Fe are found at higher concentrations. It creates a circular ring around the LHS center, in a similar manner than for the diffraction features. This is first evidence that Fe and Ca have a similar incompatible character during partial melting. For some samples, there is a lack of Ca and Fe at the LHS center. For samples synthesized at 68.5 GPa and 113 GPa, there is a higher Fe-concentration at the center. This difference in behavior, for a harder NaCl pressure medium at increasingly high pressures, reduces the sample migration away from the LHS center (Figure 5.3).

## 5.5 Discussions

### 5.5.1 Sample heterogeneity

To explain the chemical zoning observed in our samples, one could invoke artifacts generated by strong thermal gradient in the LH-DAC, such as the Soret-diffusion (Lesher and Walker, 1988). However, it has been demonstrated in a previous study specifically devoted to the analysis of the Soret-effect that it is largely reduced by using the NaCl pressure medium (Sinmyo and Hirose, 2010). Also, convection in the liquid state is expected to be severely more efficient than Soret diffusion to produce a chemical segregation in our samples. In any case, it is clear that our samples have been fully molten at the LHS center, while they remained solid at the border, and partially molten in between those two sample regions (Figure 5.3). Similar sample configuration is also observed in multi-anvil press studies (Ito et al., 2004; Liebske et al., 2005; Zhang and Herzberg, 1994). In all these studies, a higher concentration of the liquidus phase is observed in contact with the zone that encountered the highest temperatures, while the solidus phases are concentrated in the region of lower temperatures. In our experiments, similar chemical gradient can be interpreted as a migration of the liquid toward zones at lower temperatures, while the liquidus Mg-Pv phase has remained very close to the center of the LHS. At this point, it is interesting to note that our samples synthesized at the lowest pressures show a hole with almost no sample at the LHS center, while the two samples synthesized above ~65 GPa show a ball of quenched-liquid at the center (Table 1). This effect could be due to the stiffness of the NaCl pressure medium which is severely increased with increasing pressure, an effect that could reduce the liquid mobility in the LH-DAC.

### 5.5.2 Fe Partition coefficient

The Fe partition coefficient ($D_{Fe}$) between melt and solid at the liquidus temperature can be derived from the difference in Fe-content at different sample positions. In order to do this, we combine maps of Fe-contents and liquidus Mg-Pv phase concentrations (Figure 5.10). It appears clear that the zones with major Fe concentration do not overlap with those of major Mg-Pv (or garnet) concentrations. The Mg-Pv (or garnet) appears severely depleted in Fe, at least in the most central part of the ring of major Mg-Pv (or garnet) concentration. This observation confirms the incompatible character of Fe. For the two samples presenting a central balls of fully molten sample (Figures 5.3, 5.10b, 5.10c), the Fe partition coefficient can be calculated by comparing the Fe-content in the inner part of the Mg-Pv ring and the Fe-content at the center. We obtain $D_{Fe}$ ball ( $X_{Fe}^{inner-ring} / X_{Fe}^{inner-ball}$ ) values of 0.50-0.59 and 0.62-0.64 for samples synthesized at 68 GPa and 113 GPa, respectively. We here report upper and lower bounds for $D_{Fe}$ which correspond to two different calculations using a smaller and a larger zone of selection in the Fe-maps, respectively. For these two samples, we also calculated the partition coefficient $D_{Fe}$ by comparing the Fe-content in the inner part of the Mg-Pv ring and the Fe-content at the most external part of the LHS. The refined $D_{Fe}$ outer-ring ( $X_{Fe}^{inner-ring} / X_{Fe}^{outer-ring}$ ) values in good agreement with the $D_{Fe}$ ball refined above (Table 1). The strong similitude between these two values validates our assumption of radial liquid migration in our samples. For the samples synthesized at low pressures, we refined $D_{Fe}$ outer-ring to values between 0.58 and 0.77 (Table 1).

Altogether, we find that DFe decreases slightly from 0.6-0.7 to 0.5-0.65 with increasing the pressure from 19.5 GPa to 113 GPa (Figure 5.1b). Our data set is in good agreement with the previous data sets, since they all point out to an incompatible character of Fe in the deep mantle. Our $D_{Fe}$ values also plot at about 30% higher than the multi-anvil press results obtained up to 35

GPa (Figure 5.1a; (Ito et al., 2004)). On the other hand, our results are significantly higher than the most recent data set using the ATEM technique on LH-DAC samples (Nomura et al., 2011). The discrepancy could be due to the fact that previous study used an Al-free starting material, which is known to affect significantly the Fe partition coefficient significantly. At ~65 GPa, the amplitude of the $D_{Fe}$ change due to the presence of Al, from ~0.2 to ~0.6 for previous study and our work, respectively, is similar to the amplitude of change from 0.36 to 1 reported in a previous study for the effect of Al at ~25 GPa (Wood and Rubie, 1996).

### 5.5.3 Geophysical consequences

As mentioned in the introduction, the knowledge of the liquid buoyancy is critical for our comprehension of the dynamic properties of the Earth lower mantle. Our results indicate a definite preference of Fe for the liquid phase, with $D_{Fe}$ around 0.5-0.7 for the entire lower mantle. This implies that one should expect a liquid Fe-content between 1.4 and 2 times that of Mg-Pv phase, which corresponds to $X_{Fe}^{Liq}$ ~0.15-0.2 for partial melting a pyrolitic or chondritic mantle. In order to translate this information in liquid buoyancy, one needs to evaluate the other contributions to the solid-liquid difference in density. Melting itself could contribute to a difference in density of +3-4 % generated by difference atomic structure and composition between solid and liquid phases (Mosenfelder et al., 2009; Stixrude et al., 2009). It was also demonstrated that the $MgO/SiO_2$ ratio should play a major role in the liquid density (Funamori and Sato, 2010). Based on this later study, our $D_{Fe}$ values are compatible with production of a buoyant liquid in most of the lower mantle. In the lowermost mantle, where our $D_{Fe}$ value is of 0.60(5), $X_{Fe}^{Liq}$ is expected to be 0.18(1), and silicate liquid could become denser than the mantle if its $SiO_2$-content is below 20%. This value is to be compared with the 40% $SiO_2$ reported at 33

GPa (Ito et al., 2004). Even if this value could be reached, since it is observed that the $SiO_2$ content increases with increasing pressure (Ito et al., 2004; Liebske et al., 2005), it is unlikely to expect a large density difference, even for pressures found in the D”-layer. This suggests that melts are unlikely to remain trapped at long geological times in the D”-layer, due to their excess density.

Nevertheless, our results confirm the incompatible character of Fe in the deep mantle. Partial melting in the lower mantle should therefore generate liquids with high Fe-concentrations, together with a high proportion of incompatible elements as expected for mantle liquids. In this framework, it is rather normal that geological material with high Fe-content can be present in the deep lower mantle, if this material is involved in the large scale mantle convection.

| | 03G | 04G | 01G | 02G (Ext.) | 02G (Ball) | 05G (Ext.) | 05G (Ball) |
|---|---|---|---|---|---|---|---|
| *Pressure at 300 K (GPa)* | 14 | 41 | 48 | 60.5 | 60.5 | 103 | 103 |
| *Liquidus temperature (K)* | 2550 | 3200 | 3350 | 3600 | 3600 | 4450 | 4450 |
| *Pressure at high T (GPa)* | 19.5 | 48 | 55.5 | 68.5 | 68.5 | 113 | 113 |
| $K_{Fe}$ *(lower bounds)* | 0.66 | 0.58 | 0.62 | 0.57 | 0.5 | 0.55 | 0.62 |
| $K_{Fe}$ *(upper bounds)* | 0.75 | 0.77 | 0.68 | 0.7 | 0.59 | 0.65 | 0.64 |
| *Map resolution (μm)* | 2.0x2.0 | 2.0x2.0 | 2.5x2.5 | 2.0x2.0 | 2.0x2.0 | 1.5x1.5 | 1.5x1.5 |

**Table 5.1** Experimental conditions and results summary for each of the 5 experiments performed in this study. (Ext.) and (Ball) concern the external and central parts, respectively, for the two samples showing a ball of quenched-liquid at the center of the laser spot.

| | Mg-Pv | Ca-Pv | Fp | NaCl-B1 | W | P (Gpa) |
|---|---|---|---|---|---|---|
| He3218_DAC_01G | 26.00 | 0.50 | 0.69 | 72.54 | 0.29 | 48 |
| He3218_DAC_02G | 18.91 | 0.03 | 0.98 | 62.19 | 16.89 | 60 |
| He3218_DAC_03G | 3.35 | 0.39 | 0.07 | 75.66 | 20.53 | 14 |
| He3218_DAC_04G | 12.60 | 0.11 | 1.44 | 72.73 | 13.12 | 41 |
| He3218_DAC_05G | 4.91 | 0.04 | 0.15 | 91.97 | 2.93 | 103 |

**Table 5.2** Phases amount (Wt%) for samples synthesized at different pressures.

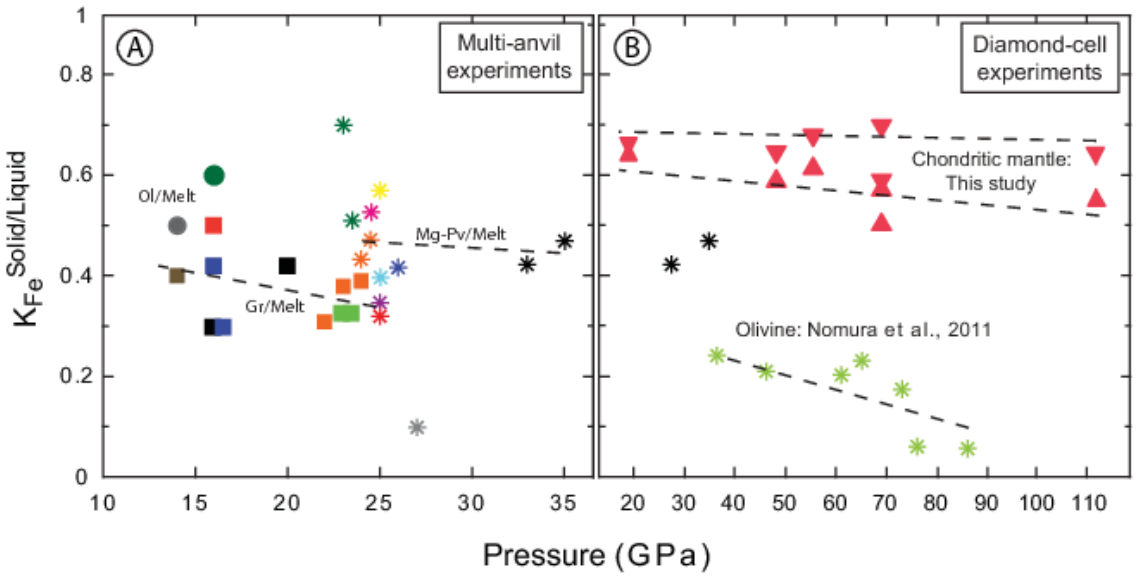


**Figure 5.1** Change of Fe-partition coefficients between silicate melts and liquidus phases as a function of pressure for various mantle compositions. (a) Results obtained from multi-anvil press experiments. The liquidus phases are olivine (Circles: green (Ohtani et al., 1989), grey (Zhang and Herzberg, 1994)), majoritic garnet (Squares: black (Kato et al., 1988), red (Ohtani et al., 1989), blue (McFarlane and Drake, 1992), brown (Zhang and Herzberg, 1994), orange (Tronnes and Frost, 2002), green (Walter et al., 2004)) and Mg-bearing perovskite (stars: yellow (Ohtani et al., 1998), light blue (Drake et al., 1993), pink (McFarlane et al., 1994), purple (Hirose et al., 2004), red (Corgne et al., 2005), orange (Tronnes and Frost, 2002), green (Walter et al., 2004), black (Ito et al., 2004), dark blue (Liebske et al., 2005)). (b) Results obtained from LH-DAC experiments. Green stars (Nomura et al., 2011) correspond to melting of olivine. We also report one MAP data point (Ito et al., 2004). Upwards and downwards triangles stand for lower and upper bounds of our experimental determination of the $D_{Fe}$, respectively (see text).

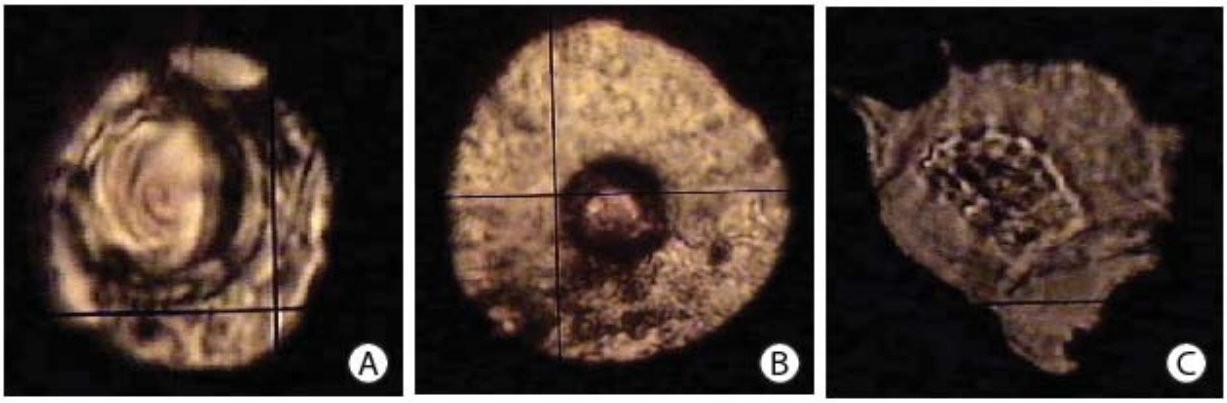


**Figure 5.2** Optical micro-photographs of samples synthesized at pressures of (a) 19.5 GPa, (b) 55.5 GPa, and (c) 113 GPa. All samples were first compressed to the target pressure before progressive laser-heating until melting at a temperature up to more than 2500 K.

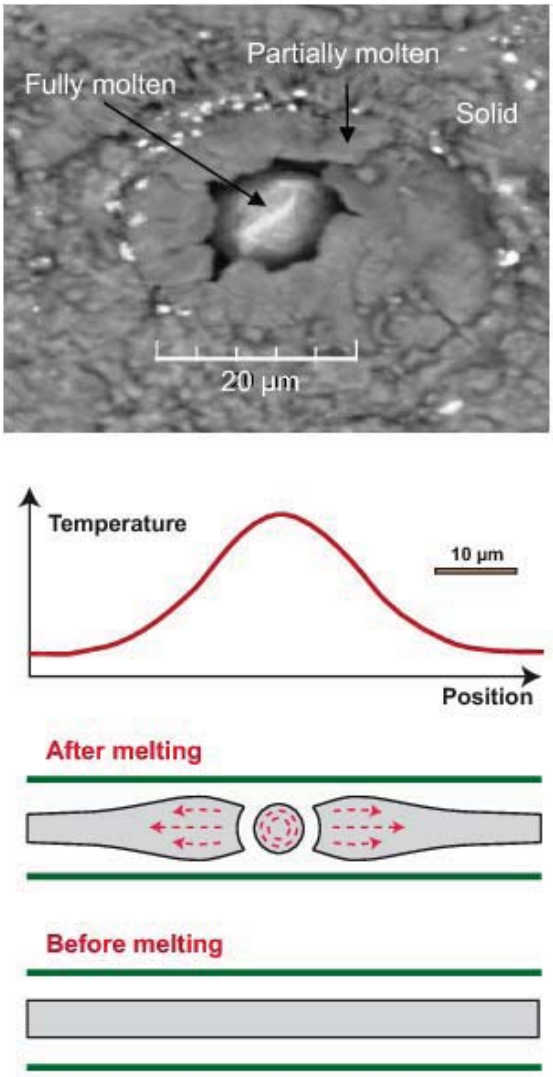


**Figure 5.3** Scanning electron microphotograph of the sample recovered from 55.5 GPa. We present below schematic representation of the temperature gradient and the sample shape in between the two diamonds. We used a NaCl pressure medium for all experiments.

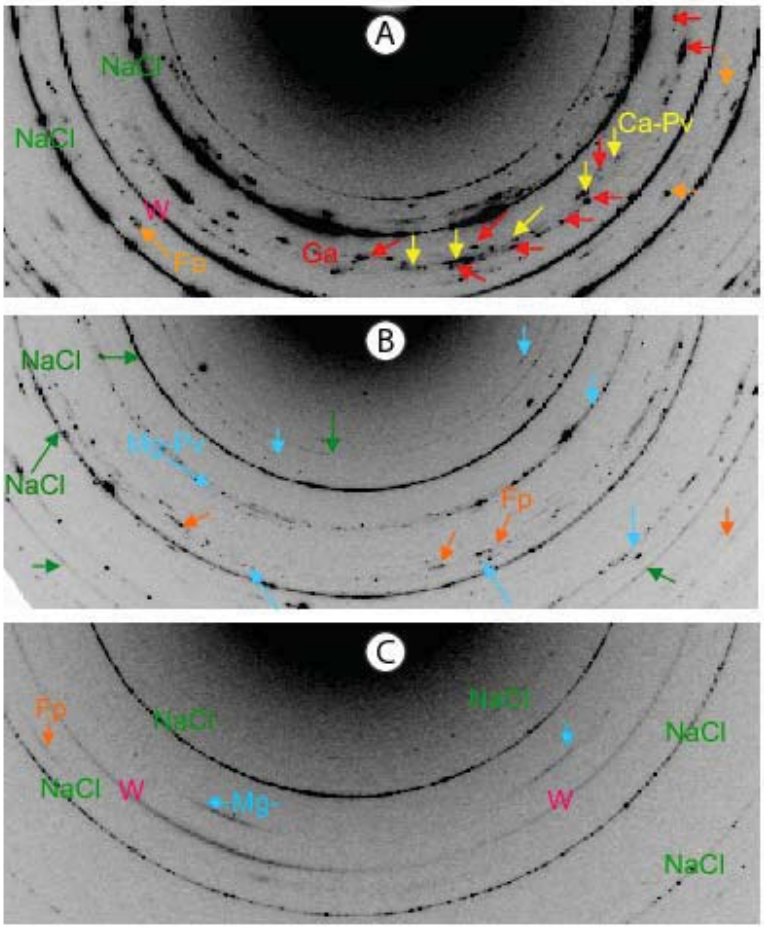


**Figure 5.4** Typical 2-dimensional X-ray diffraction images recorded for samples synthesized at (a) 19.5 GPa, (b) 55.5 GPa, and (c) 113 GPa. At a pressure of 19.5 GPa, the sample contains a mixture of majoritic garnet and wadsleyite phases. At all other pressures, the sample contains a mixture of Mg-Pv, Fp and Ca-Pv phases. Fp and Ca-Pv phases are relatively week, however, due to the composition of the starting material rich in Mg-Pv. Also, Ca-Pv is only visible in certain sample regions, and not close to the center of the laser spot, as discussed in the text.

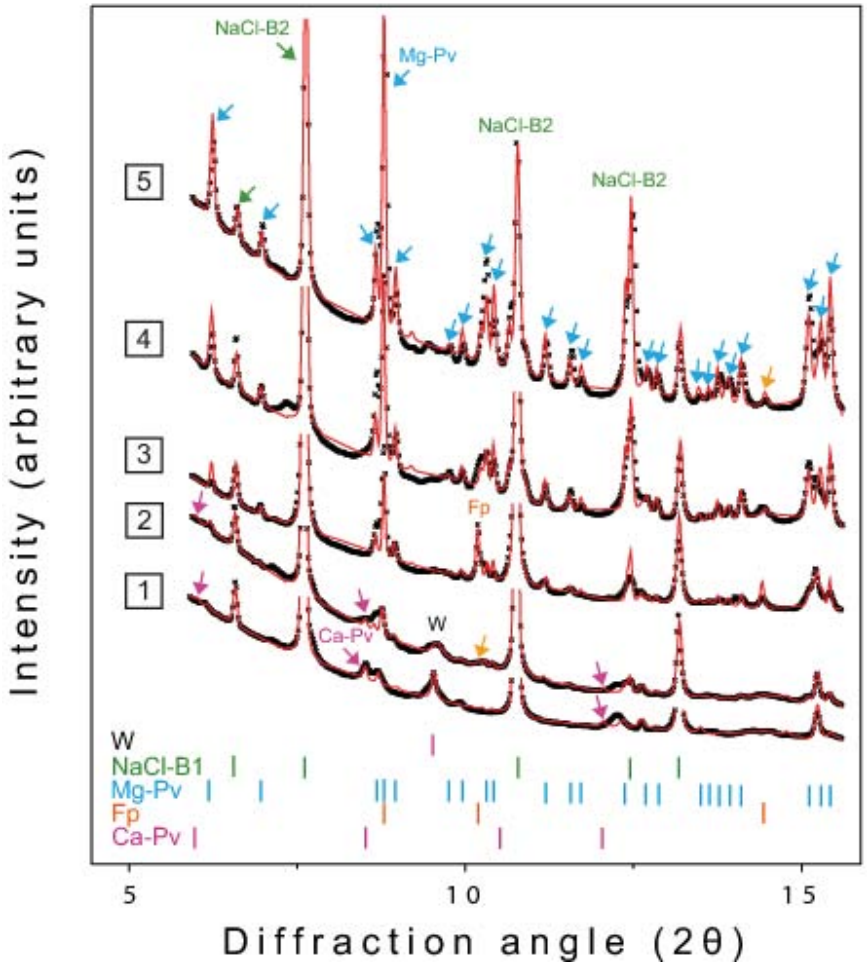


**Figure 5.5** Integrated X-ray diffraction patterns recorded at different positions for the sample synthesized at a pressure of 55.5 GPa. Spectra [1-2] show some Ca-bearing perovskite, spectra [3] show some ferropericlase, and spectra [4-5] show exclusively the major Mg-bearing perovskite.

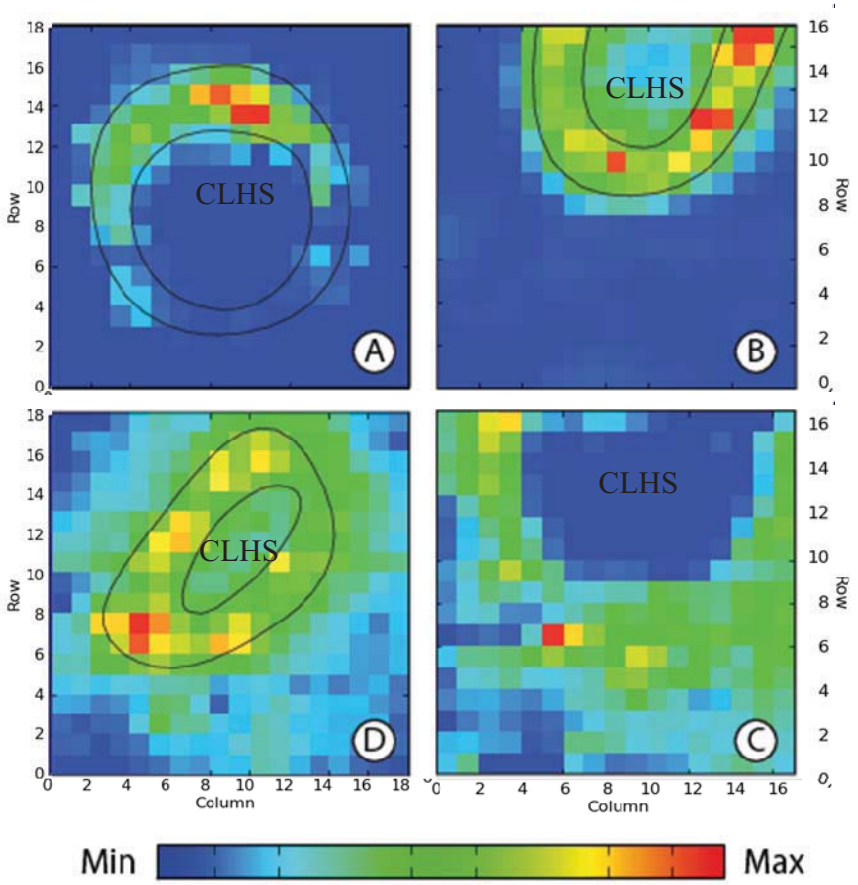


**Figure 5.6** Maps of relative phase contents extracted from the X-ray diffraction results using a Rietveld analysis. The intensity in the map corresponds directly to the intensity observed in the diffraction spectra, without any further method of normalization. Maps correspond to content of (a) Garnet at 19.5 GPa, (b) Mg-Pv and (c) Ca-Pv at 55.5 GPa, respectively, and (d) Mg-Pv at 113 GPa. Pixel size (in μm) is: 2.0x2.0 (a), 2.5x2.5 (b) and (c) and 1.5x1.5 (d), respectively. CLHS corresponds to the center of the laser hot-spot.

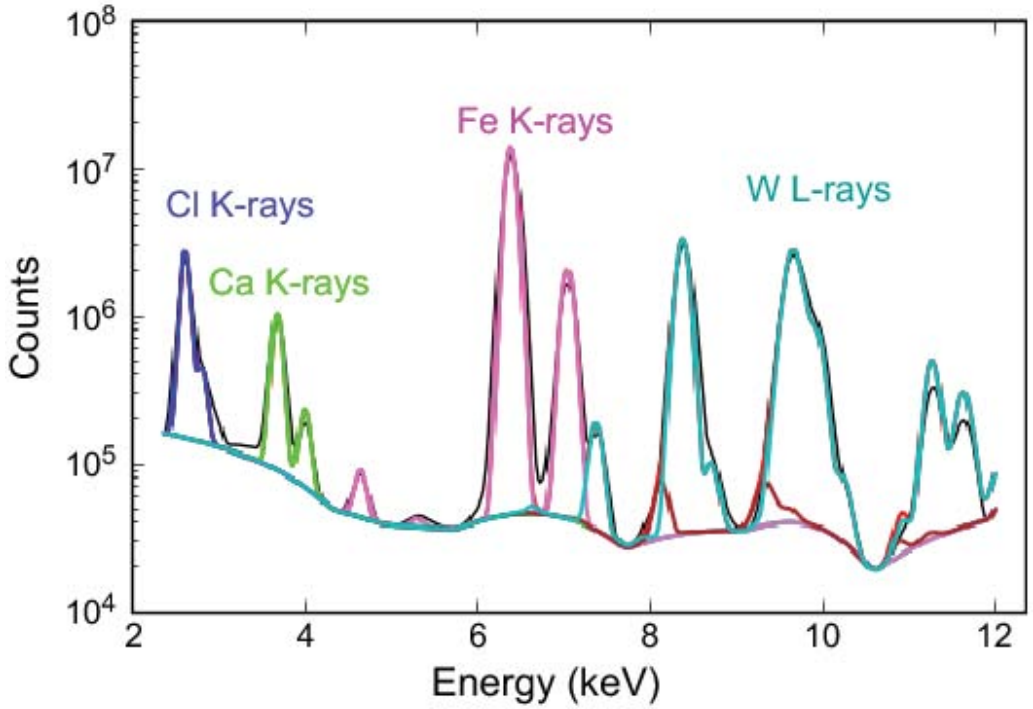


**Figure 5.7** Typical X-ray fluorescence spectrum measured on a sample recovered from 55.5 GPa. We report the experimental spectrum (black) as well as the adjusted theoretical profile including the Cl, Ca, Fe, and W contributions.

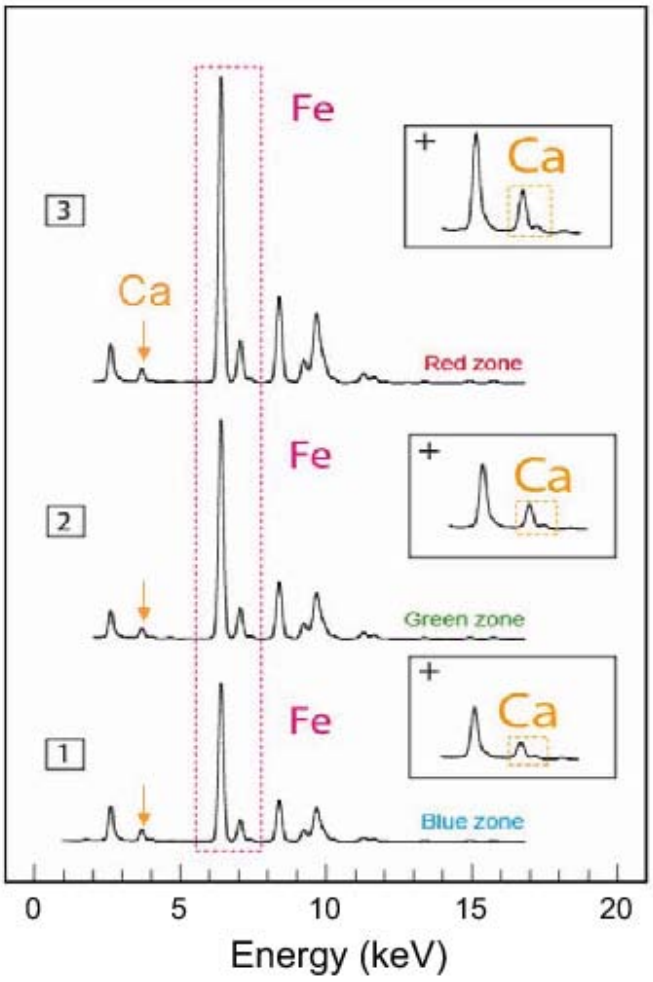


**Figure 5.8** Comparison of XRF spectra recorded at different location in the sample synthesized at 55.5 GPa. Blue, green and red zones correspond to the same colored zones in Figg. 5.10a.

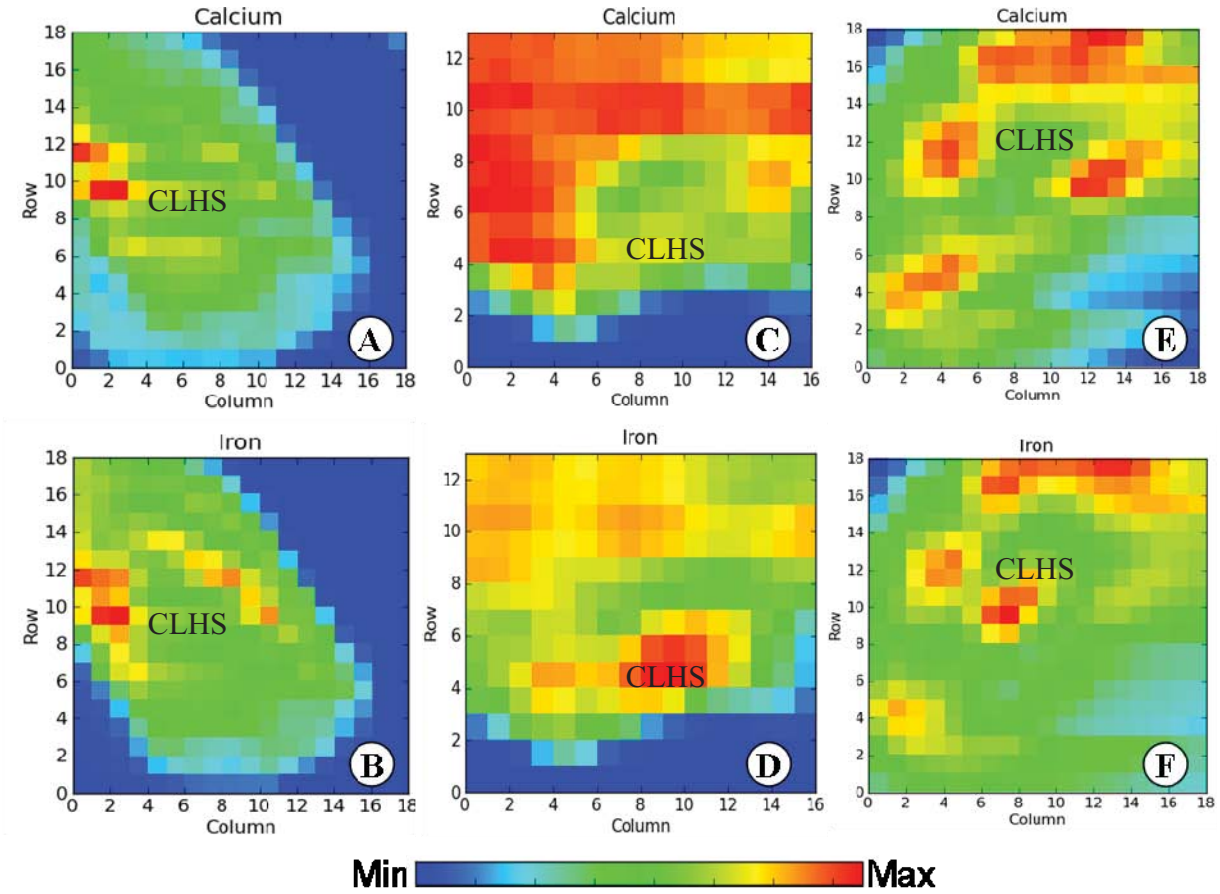


**Figure 5.9** Maps of relative elemental contents extracted from the X-ray fluorescence results. The intensity in the map corresponds directly to the intensity observed in the fluorescence spectra, without any further method of normalization. We report maps for Ca (upper) and Fe (lower) for sample synthesized at (a) (b) 19.5 GPa, (c) (d) 68.5 GPa and (e) (f) 113 GPa. Pixel size (in μm) is: 2.0x2.0 (a)-(b), 2.0x2.0 (c) and (d) and 1.5x1.5 (e) and (f), respectively.

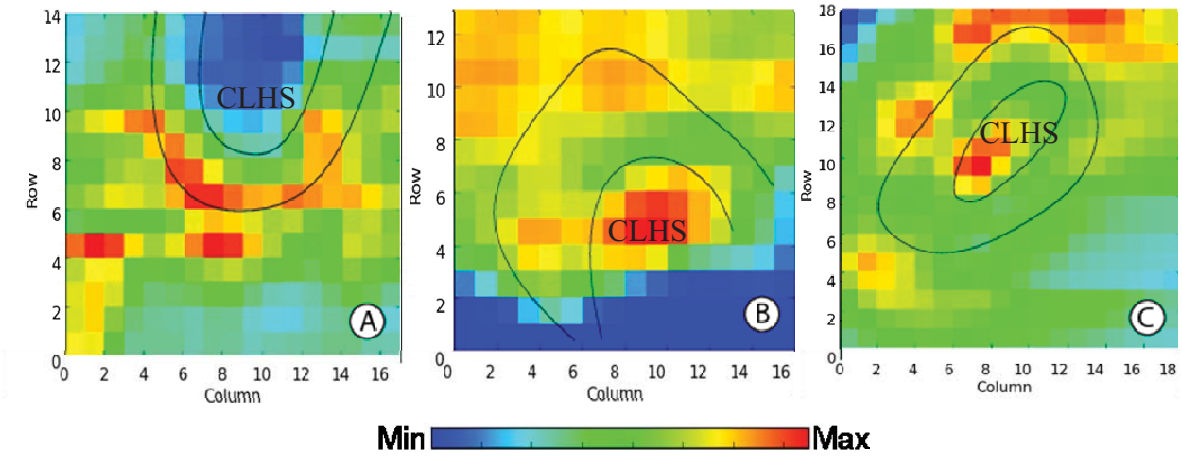


**Figure 5.10** Contours of Mg-bearing perovskite phase contents. Black lines are extracted from Figure 6 and plotted in superposition of Fe-contents maps for samples synthesized at (a) 55.5 GPa, (b) 68.5 GPa, and (c) 113 GPa. Pixel size (in μm) is: 2.5x2.5 (a), 2.0x2.0 (b) and 1.5x1.5 (c), respectively.

# Conclusions and Outlooks

My PhD work is an experimental investigation of the melting properties at lower mantle pressure and temperature conditions. Several melting experiments have been carried out in order to determine the melting profiles of the deep mantle and possible geophysical implications on Earth differentiation across its history. I determined also the partition coefficients between liquid and solid phases for iron major element, to investigate the behavior of mantle liquids as a function of partial melting and density up to core-mantle boundary (CMB) pressure conditions. In the following sections, I summarize the main results obtained in this work and I suggest new outlooks to pursue and improve this scientific work.

## Summary of the study melting in the MgO-$MgSiO_3$ system: A simplified chemical model for the lower mantle.

This study determined the melting relations for the system MgO-$MgSiO_3$ at pressures covering the entire lower mantle from the transition zone up to the base of lower mantle. I present the pressure-temperature eutectic melting curve for this compositional simplified model that provides basis for more complex systems such as peridotite and chondritic compositions.

Firstly, it is confirmed that $Mg_2SiO_4$-forsterite disproportionates in MgO+$MgSiO_3$ (Pc+Mg-Pv) at lower mantle pressure and temperature conditions. Eutectic melting curve has been determined for the reaction MgO+$MgSiO_3$=liquid, which was unknown for pressures higher than 26GPa. Eutectic temperature at 135 GPa, corresponding to the CMB, is found to be 4830±150 K that is ~700 K higher than the solidus for a chondritic type mantle composition (determined here, see

chapter four). Determination of periclase and Mg-perovskite weight percentages in the eutectic liquid would be of primary importance in order to better constrain early magma ocean properties. Moreover, I presented the melting curve of platinum up to ~100 GPa, whereas it was determined in a previous work only up to 70 GPa (Kavner and Jeanloz, 1998). In this work it was shown that melting of platinum does not affect the determination of the melting of $MgO+MgSiO_3$ material. Also no reaction between platinum and carbon of diamond anvils was detected (that is, PtC phase did not occur). These data agree with the main property of platinum: the inertness, which is the reason we use it in high pressure experiments.

## Summary of the study on implication of solidus and liquidus profiles of chondritic mantle for melting of the Earth across its history

The aim of this work was to determine liquidus and solidus curves for a chondritic mantle composition in order to investigate major implications on melting behavior of the Earth planet. Melting phase relations have been investigated at pressure and temperatures typical of the entire Earth's lower mantle, i.e. from 25 up to 135 GPa and up to more than 4000 K. Results show $MgSiO_3$-perovskite as the liquidus phase in the lower mantle, confirming previous works. Solidus and liquidus temperature at 135 GPa (CMB pressure) have reported to be of 4150±150 K and 4725±150 K, respectively. These data when compared with adiabatic profiles for Earth deep mantle and D" region indicate that partial melting in the lower mantle is unlikely because of highest temperatures required. Anyway, partial melting should be allowed in D" region if: 1) we consider an outer core very hot and/or 2) a mantle composition containing a high concentration of incompatible elements and in particular volatiles (i.e. Na, K, H, and CO2), whose effect is to

decrease the melting point compared to the lower mantle one. In these particular conditions we can assume ULVZs as a consequence of partial melting at the CMB.

Melting curves have been compared with isentropic temperature profiles of the magma ocean for different potential surface temperatures. We paid a particular attention to the pressure interval of 45-50 GPa, corresponding to metal-silicate equilibrium at the base of a magma ocean. In this range of pressures (at a depth of ~1750 (±250)), liquidus temperature for chondritic composition is ~3175 K (±250) and (according to isentropic profiles) 2450 K (±150) in surface (0 km depth). It is inferred that, complete melting of the Earth's mantle is incompatible with a reasonable surface temperature. Thus, it is the most unlikely that the early Earth mantle, after accretion of the planet, has experienced complete melting.

## Summary of the study on phase relations in partially molten lower mantle: A X-ray fluorescence study at very high-pressures

The objective of this work was to improve our knowledge on melting relations at lower mantle conditions of pressure and temperature for a chondritic composition starting material (see chapter 4). For this, partitioning coefficients for iron between liquid and solid silicate phases have been determined. An in-situ method, consisting in the use of coupled X-ray diffraction and X-ray fluorescence techniques, was developed. This work provides maps of elemental (Ca and Fe) and phase fractions for sample that have been partially molten in the laser-heated diamond anvil cell. $D_{Fe} = X_{Fe}^{Pv} / X_{Fe}^{Melt}$ was found decrease slightly from 0.6-0.7 to 0.5-0.65 at increasing pressure. These Fe partitioning coefficients extracted from the maps show incompatible character of Fe (Ca presents a similar incompatible character during partial melting). This incompatibility was not

found high enough to exclude that liquids tend to float in the deep mantle. But at the same time, it therefore confirms the incompatible character of Fe which, in turns, has a major effect on the liquid density. Liquids could have negative floatability and to sink down in the lower mantle.

These results on phase relations and partitioning coefficients have several implications:

- Affect directly the crystal-liquid density inversions (the so-called density crossovers): liquids produced by partial melting and rich in iron are denser than surroundings silicate crystals and thus are expected to sink down;
- Density crossovers could explain partial melting hypothesis for ULVZ, especially in light of the preference of calcium and iron for liquids;
- These denser liquids could accumulate at the CMB and float atop the ULVZ, with enormous implications for chemical and thermal heterogeneities;
- Would influence dynamics of the entire mantle and would have repercussions for mantle plumes and superplume upwellings and mantle convection.

It should be important to consider the participation of volatiles, especially water, since volatile amounts in silicate melts may cause density crossovers in the D" region and affect the floatability of hydrous melts which are likely to become negatively or neutrally buoyant.

The presence of neutrally or negatively buoyant melt in the deep mantle would have fundamental implications for our understanding of the Hadean Earth and of the structure and chemical evolution of the core-mantle boundary. If melting extended to the base of the mantle during accretion, perovskite may have floated in coexiting liquid as it crystallized out of the magma ocean, providing a possible means of large-scale chemical differentiation. In the present-day Earth, dense melt may provide a natural explanation for the ultralow velocity zone at the base of the mantle.

# -A-

Abe, Y., 1997. Thermal and chemical evolution of the terrestrial magma ocean. Physics of The Earth and Planetary Interiors Physical and Chemical Evolution of the Earth, 100(1-4): 27-39.

Abe, Y. and Matsui, T., 1988. Evolution of an impact-generated $H_2O$-$CO_2$ atmosphere and formation of a hot proto-ocean on Earth. Journal of Atmospheric Sciences, 45(21): 3081-3101.

Agee, C.B., 1990. A new look at differentiation of the Earth from melting experiments on the Allende meteorite. Nature, 346(6287): 834-837.

Agee, C.B. and Walker, D., 1988. Static compression and olivine floatation in ultrabasic silicate liquid. Journal of Geophysical Research, 93: 3437-3449.

Ahrens, T.J., Holland, K.G. and Chen, G., 1998. Shock temperature and the melting point of iron. In: S.e. al. (Editor), Shock Compression of Condensed Matter. AIP Press, Woodbury, NY, pp. 133-136.

Alfè, D., 2009. Temperature of the inner-core boundary of the Earth: Melting of iron at high pressure from first-principles coexistence simulations. Physical Review B, 79(6).

Allègre, J.A., Poirier, J.P., Humler, E. and Hofmann, A.W., 1995. The chemical composition of the Earth. Earth and Planetary Science Letters, 134: 515-526.

Allègre C.J., Manhès G. and Lewin E., Chemical composition of the Earth and the volatility control on planet genetics, Earth and Planetary Science Letters 185, 49-69, 2001.

Anderson, O.L., 1982. The Earth's Core and the Phase Diagram of Iron. Philosophical Transactions of the Royal Society of London. Series A, Mathematical and Physical Sciences, 306(1492): 21-35.

Andrault, D., 2001. Evaluation of (Mg,Fe) partitioning between perovskite and magnesiowustite up to 120 GPa. Journal of Geophysical Research, 106: 2079-2087.

Andrault, D. et al., 2011. Solidus and liquidus profiles of chondritic mantle: Implication for melting of the Earth across its history. Earth and Planetary Science Letters, 304(1-2): 251-259.

Andrault, D. et al., 1998. Thermal pressure in a laser-heated diamond-anvil cell: An x-ray diffraction study. European Journal of Mineralogy, 10: 931-940.

Andrault, D. et al., 2006. Study of partial melting at high pressure using *in situ* X-ray diffraction. High Pressure Research, 26(3): 267-276.

Andrault, D. et al., 2010. Experimental evidence for perovskite and post-perovskite coexistence throughout the whole D" region. Earth and Planetary Science Letters, 293: 90-96.

Arndt, N., 2000. Geochemistry: Hot heads and cold tails. Nature, 407(6803): 458-461.

Asanuma, H. et al., 2010. Melting of iron-silicon alloy up to the core-mantle boundary pressure: implications to the thermal structure of the Earth's core. Physics and Chemistry of Minerals, 37(6): 353-359.

Asimow, P.D., Hirschmann, M.M. and Stolper, E.M., 1997. An analysis of variations in isentropic melt productivity. Philosophical Transactions of the Royal Society London, 355: 255-281.

## -B-

Babb, S.E., 1963. Parameters in the Simon Equation Relating Pressure and Melting Temperature. Reviews of Modern Physics, 35(2): 400 LP - 413.

Badro, J. et al., 2007. Effect of light elements on the sound velocities in solid iron: Implications for the composition of Earth's core. Earth and Planetary Science Letters, 254(1-2): 233-238.

Ballentine, C.J., 2002. Tiny Tracers Tell Tall Tales. Science, 296(5571): 1247-1248.

Beckhoff, B., Kanngiesser, B., Langhof, N. and Wolff, H., 2005. Handbook of Practical X-ray Fluorescence Analysis. Springer.

Benedetti, R. and Loubeyre, P., 2004. Temperature gradients, wavelength-dependent emissivity, and accuracy of high and very-high temperatures measured in the laser heated diamond anvil cell. High Pressure Research, 24: 423-445.

Boehler, R., 1986. The phase diagram of iron to 430 kbar. Geophysical Research Letters, 13(11): 1153-1156.

Boehler, R., 1993. Temperatures in the Earth's core from melting-point measurements of iron at high static pressures. Nature, 363: 534-536.

Boehler, R., 2000. High-pressure experiments and the phase diagram of lower mantle and core materials. Review in Geophysics, 38(2): 221-245.

Bolfan-Casanova, N., McCammon, C.A. and Mackwell, S., 2006. Water in the transition zone and lower mantle minerals. In: S.J. Jacobsen and S. van der Lee (Editors), the Earth's deep water cycle. Geophysical Monographs, AGU, pp. 57-68.

Bouhifd, M.A. and Jephcoat, A.P., 2003. The effect of pressure on partitioning of Ni and Co between silicate and iron-rich metal liquids: a diamond anvil cell study. Earth and Planetary Science Letters, 209: 245-255.

Bouvet, T., Detlefs, C., Mitchell, E. and Revol, J., 2007. ESRF Science and Technology Programme 2008-2018. Technical report, European Synchrotron Radiation Facility.

Bower, D.J., Wicks, J.K., Gurnis, M. and Jackson, J.M., 2011. A geodynamic and mineral physics model of a solid-state ultralow-velocity zone. Earth and Planetary Science Letters, 303(3-4): 193-202.

Boyet, M. and Carlson, R.W., 2005. Nd-142 evidence for early (> 4.53 Ga) global differentiation of the silicate Earth. Science, 309(5734): 576-581.

Brown, J.M. and Shankland, T., 1981. Thermodynamic parameters in the Earth as determined from seismic profiles. Geophysical Journal of the Royal Astronomiacal Society, 66: 579-596.

Brunet, D. and Yuen, D.A., 2000. Mantle plumes pinched in the transition zone. Earth and Planetary Science Letters, 178(1-2): 13-27.

Buffett, B.A., Garnero, E.J. and Jeanloz, R., 2000. Sediments at the Top of Earth's Core. Science, 290(5495): 1338-1342.

Bullen, K.E., 1942. The density variation of the earth's central core. Bulletin of The Seismological Society of America, 32(1): 19-29.

Bullen, K.E., 1963. An Index of Degree of Chemical Inhomogeneity in the Earth. Geophysical Journal of the Royal Astronomical Society, 7(5): 584-592.

Bunge, H.P., Ricard, Y. and Matas, J., 2001. Non-adiabaticity in mantle convection. Geophysical Research Letters, 28: 879-882.

## -C-

Campbell, I.H. and Griffiths, R.W., 1990. Implications of mantle plume structure for the evolution of flood basalts. Earth and Planetary Science Letters, 99(1-2): 79-93.

Canil, D., 1994. Stability of clinopyroxene at pressure-temperature conditions of the transition region. Physics of The Earth and Planetary Interiors, 86(1-3): 25-34.

Canup, R.M., 2004. Simulations of a late lunar-forming impact. Icarus, 168(2): 433-456.

Canup, R.M., 2008. Accretion of the Earth. Philosophical Transactions of the Royal Society A: Mathematical, Physical and Engineering Sciences, 366(1883): 4061-4075.

Catalli, K., Shim, S.H. and Prakapenka, V.B., 2009. Thickness and Clapeyron slope of the post-perovskite boundary. Nature, 462: 782-785.

Cauzid, J. et al., 2006. Standardless quantification of single fluid inclusions using synchrotron radiation induced X-ray fluorescence. Chemical Geology, 227(3-4): 165-183.

Chabot, N.L., Draper, D.S. and Agee, C.B., 2005. Conditions of core formation in the Earth: Constraints from Nickel and Cobalt partitioning. Geochimica and Cosmochimica Acta, 69(8): 2141-2151.

Chervin, J.C., Canny, B. and Pruzan, P., 1995. A versatile diamond anvil cell for IR spectroscopy and X-ray diffraction analysis. Review of Scientific Instruments, 66(3): 2595-2598.

Christensen, U.R. and Hofmann, A.W., 1994. Segregation of subducted oceanic crust in the convecting mantle. Nature, 99: 19867-19884.

Corgne, A., Allan, N.L. and Wood, B.J., 2003. Atomistic simulations of trace element incorporation into the large site of $MgSiO_3$ and $CaSiO_3$ perovskites. Physics of the Earth and Planetary Interiors, 139(1-2): 113-127.

Corgne, A., Liebske, C., Wood, B.J., Rubie, D.C. and Frost, D.J., 2005. Silicate perovskite-melt partitioning of trace elements and geochemical signature of a deep perovskitic reservoir. Geochimica et Cosmochimica Acta, 69(2): 485-496.

Corgne, A. and Wood, B.J., 2002. CaSiO3 and CaTiO3 perovskite-melt partitioning of trace elements: Implications for gross mantle differentiation. Geophysical Research Letters, 29(19): 1933.

Cottrell, E., Walter, M.J. and Walker, D., 2009. Metal-silicate partitioning of tungsten at high pressure and temperature: Implications for equilibrium core formation in Earth. Earth and Planetary Science Letters, 281(3-4): 275-287.

## -D-

da Silva, C., Wentzcovitch, R.M., Patel, A., Price, G.D. and Karato, S., 2000. The composition and geotherm of the lower mantle: constraints from the elasticity of silicate perovskite. Physics of the Earth and Planetary Interiors, 118: 103-109.

Dahl, T.W. and Stevenson, D.J., 2010. Turbulent mixing of metal and silicate during planet accretion -- And interpretation of the Hf-W chronometer. Earth and Planetary Science Letters, 295(1-2): 177-186.

Dewaele, A., Mezouar, M., Guignot, N. and Loubeyre, P., 2007. Melting of lead under high pressure studied using second-scale time-resolved x-ray diffraction. Physical Review B, 76(1): 144106.

Dobson, D.P. and Brodholt, J.P., 2005. Subducted banded iron formations as a source of ultralow-velocity zones at the core-mantle boundary. Nature, 434(7031): 371-374.

Drake, M.J., McFarlane, E.A., Gasparik, T. and Rubie, D.C., 1992. Mg-perovskite/silicate melt partition coefficients in the system CaO-MgO-SiO2 at high temperature and pressure. Journal of Geophysical Research, 98: 5427-5431.

Drake, M.J., McFarlane, E.A., Gasparik, T. and Rubie, D.C., 1993. Mg-Perovskite/silicate melt and majorite garnet/silicate melt partition coefficients in the system CaO - MgO - SiO2 at high temperatures and pressures. Journal of Geophysical Research, 98(E3): 5427-5431.

Dziewonski, A. and Anderson, D., 1981. Preliminary reference Earth model. Physics of the Earth and Planetary Interiors, 25: 297-356.

## -E-

Elkins-Tanton, L.T., 2008. Linked magma ocean solidification and atmospheric growth for Earth and Mars. Earth and Planetary Science Letters, 271(1-4): 181-191.

Elkins-Tanton, L.T., Parmentier, E.M. and Hess, P.C., 2003. Magma ocean fractional crystallization and cumulate overturn in terrestrial planets: Implications for Mars. Meteoritics & Planetary Science, 38(12): 1753-1771.

## -F-

Fiquet, G. et al., 2010. Melting of Peridotite to 140 Gigapascals. Science 329 (5998 ): 1516-1518

Fiquet, G., Dewaele, A., Andrault, D., Kunz, M. and Le Bihan, T., 2000. Thermoelastic properties and crystal structure of $MgSiO_3$ perovskite at lower mantle pressure and temperature conditions. Geophysical Research Letters, 27: 21-24.

Funamori, N. and Sato, T., 2010. Density contrast between silicate melts and crystals in the deep mantle: An integrated view based on static-compression data. Earth and Planetary Science Letters, 295(3-4): 435-440.

## -G-

Garnero, E.J. and McNamara, A.K., 2008. Structure and Dynamics of Earth's Lower Mantle. Science 320 (5876 ): 626-628

Gasparik, T., 1990. Phase Relations in the Transition Zone. Journal of Geophysical Research, 95(B10): 15751-15769.

Gasparik, T. and Drake, M.J., 1995. Partitioning of elements among two silicate perovskites, superphase B, and volatile-bearing melt at 23 GPa and 1500-1600°C. Earth and Planetary Science Letters, 134(3-4): 307-318.

Gibson, W.M. and Kumakhov, M.A., 1992. Application of X-ray and Neutron Optics. Proceedings of SPIE, 1736, 172-186.

Gillet, P., Richet P. and Guyot F., 1991. High-Temperature Thermodynamic Properties of Forsterite. Journal Geophysical Research 96 (B7): 11805-11816.

Green D.H., Hibberson W.O. and Jaques A.L., 1979. Petrogenesis of mid-ocean ridge basalts. In M. W. MCElhinny, editor, The Earth in origin, structure and evolution, Academic Press, London, 265-299.

Goarant, F., Guyot, F. and Poirier, J.P., 1992. High-pressure and high-temperature reactions between silicates and liquid iron alloys, in the diamond anvil cell, studied by analytical electron microscopy. Journal of Geophysical Research, 97: 4477-4487.

Guillot, B. and Sator, N., 2007. A computer simulation study of natural silicate melts. Part II: High pressure properties. Geochimica et Cosmochimica Acta, 71(18): 4538-4556.

## -H-

Hammersley, J., 1996. Fit2d user manual, ESRF, Grenoble, France.

Hayashi, C., Nakazawa, K. and Mizuno, H., 1979. Earth's melting due to the blanketing effect of the primordial dense atmosphere. Earth and Planetary Science Letters, 43(1): 22-28.

Hernlund, J.W. and Jellinek, A.M., 2010. Dynamics and structure of a stirred partially molten ultralow-velocity zone. Earth and Planetary Science Letters, 296(1-2): 1-8.

Hernlund, J.W., Thomas, C. and Tackley, P.J., 2005. A doubling of the post-perovskite phase boundary and structure of the Earth's lowermost mantle. Nature, 434: 882-886.

Herzberg, C., Gasparik, T. and Sawamoto, H., 1990. Origin of Mantle Peridotite: Constraints From Melting Experiments to 16.5 GPa. Journal of Geophysical Research, 95(B10): 15779-15803.

Herzberg, C. and Zhang, J., 1996. Melting experiments on anhydrous peridotite KLB-1: compositions of magmas in the upper mantle and transition zone. Nature, 101: 8271-8295.

Hignette, O., Cloetens, P., Rostaing, G., Bernard, P. and Morawe, C., 2005. Efficient sub 100 nm focusing of hard x rays. Review of Scientific Instruments, 76(6): 063709.

Hirose, K., Shimizu, N., van Westrenen, W. and Fei, Y., 2004. Trace element partitioning in Earth's lower mantle and implications for geochemical consequences of partial melting at the core-mantle boundary. Physics of the Earth and Planetary Interiors, 146(1-2): 249-260.

Holland, K.G. and Ahrens, T.J., 1997. Melting of $(Mg,Fe)_2SiO_4$ at the core-mantle boundary of the Earth. Science, 275: 1623-1625.

Holmes, N.C., Moriarty, J.A., Gathers, G.R. and Nellis, W.J., 1989. Equations of state of platinum to 660 GPa (6.6 Mbar). Journal of Applied Physics, 66: 2962-2967.

## -I-

Ito, E. and Katsura, T., 1989. A temperature profile of the mantle transition zone. Geophysical Research Letters, 16(5): 425-428.

Ito, E., Kubo, A., Katsura, T. and Walter, M.J., 2004. Melting experiments of mantle materials under lower mantle conditions with implications for magma ocean differentiation. Physics of The Earth and Planetary Interiors, 143-144: 397-406.

Ito, E. and Takahashi, E., 1987. Melting of peridotite at uppermost lower-mantle conditions. Nature, 328: 514-517.

Ito, E. and Takahashi, E., 1989. Post-spinel transformation in the system $Mg_2SiO_4$-$Fe_2SiO_4$ and some geophysical implications. Journal of Geophysical Research, 94(88): 10637-10646.

## -J-

Jagoutz E., Palme H., Baddenhausen H., Blum K., Cendales M., Dreibus G., Spettel B., Lorenz V. and Wänke H., The abundances of major, minor and trace elements in the Earth's mantle as derived from primitive ultramafic nodules, Proceeding 10th Lunar Planetary Science Conference 76, 2031-2050, 1979.

Jamieson, J.C., Fritz, J.N. and Manghnani, M.H., 1982. Pressure measurement at high temperature in x-ray diffraction studies: gold as a primary standard. In: S. Akimoto and M.H. Manghnani (Editors), High Pressure Research in Geophysics. Riedel, Boston, pp. 27-48.

Janssens, K. et al., 2010. Recent trends in quantitative aspects of microscopic X-ray fluorescence analysis. TrAC Trends in Analytical Chemistry Analytical applications of synchrotron radiation, 29(6): 464-478.

Jephcoat, A.P. and Besedin, S.P. Temperature Measurement and Melting Determination in the Laser-Heated Diamond-Anvil Cell, Philosophical Transactions of the Royal Society of London. Series A: Mathematical, Physical and Engineering Sciences 354(1711), 1333-1360, 1996.

## -K-

Kamada, S. et al., 2010. Phase relationships of the Fe-FeS system in conditions up to the Earth's outer core. Earth and Planetary Science Letters, 294(1-2): 94-100.

Kanda, R.V.S. and Stevenson, D.J., 2006. Suction mechanism for iron entrainment into the lower mantle. Geophysical Research Letters, 33(2): L02310.

Karato, S. and Murthy, V.R., 1997. Core formation and chemical equilibrium in the Earth I. Physical considerations. Physics of the Earth and Planetary Interiors, 100: 61-79.

Karki, B.B. and Stixrude, L.P., 2010. Viscosity of MgSiO3 Liquid at Earth's Mantle Conditions: Implications for an Early Magma Ocean. Science, 328(5979): 740-742.

Kato, T., Ohtani, E., Ito, Y. and Onuma, K., 1996. Element partitioning between silicate perovskites and calcic ultrabasic melt. Physics of The Earth and Planetary Interiors. High

Pressure Mineral Physics and Petrochemistry in Memory of Professor Ted Ringwood, 96(2-3): 201-207.

Kato, T., Ringwood, A.E. and Irifune, T., 1988. Experimental determination of element partitioning between silicate perovskites, garnets and liquids : constraints on early differentiation of the mantle, Earth and Planetary Science Letters, pp. 123-145.

Katsura, T. and Ito, E., 1989. The System $Mg_2SiO4$-$Fe_2SiO4$ at High Pressures and Temperatures: Precise Determination of Stabilities of Olivine, Modified Spinel, and Spinel. Journal of Geophysical Research, 94(B11): 15663-15670.

Katsura, T., Yoneda, A., Yamazaki, D., Yoshino, T. and Ito, E., 2010. Adiabatic temperature profile in the mantle. Physics of the Earth and Planetary Interiors. Special Issue on Deep Slab and Mantle Dynamics, 183(1-2): 212-218.

Kavner, A. and Jeanloz, R., 1998. High-pressure melting curve of platinum. Journal of Applied Physics, 83(12): 7553.

Kellogg, L.H., Hager, B.H. and van der Hilst, R.D., 1999. Compositional Stratification in the Deep Mantle. Science, 283: 1881-1884.

Klein, O. and Nishina, Y., 1928. Über die Streuung von Strahlung durch freie Elektronen nach der neuen relativistischen Quantendynamik von Dirac. Zeitschrift für Physik, 52: 852-869.

Kleine, T., Munker, C., Mezger, K. and Palme, H., 2002. Rapid accretion and early core formation on asteroids and the terrestrial planets from Hf-W chronometry. Nature, 418: 952-955.

Knittle, E. and Jeanloz, R., 1987. Synthesis and equation of state of $(Mg,Fe)SiO_3$ perovskite to over 100 GPa. Science, 235: 669-670.

Knittle, E. and Jeanloz, R., 1991. Earth's Core-Mantle Boundary: Results of Experiments at High Pressures and Temperatures. Science, 251(5000): 1438-1443.

Kojitani, H. and Akaogi, M., 1997. Melting enthalpies of mantle peridotite: calorimetric determinations in the system CaO-MgO-Al2O3-SiO2 and application to magma generation. Earth and Planetary Science Letters, 153(3-4): 209-222.

Komabayashi, T., Hirose, K., Nagaya, Y., Sugimura, E. and Ohishi, Y., 2010. High-temperature compression of ferropericlase and the effect of temperature on iron spin transition. Earth and Planetary Science Letters, 297(3-4): 691-699.

Kumagai, I., Davaille, A., Kurita, K. and Stutzmann, E., 2008. Mantle plumes: Thin, fat, successful, or failing? Constraints to explain hot spot volcanism through time and space. Geophysical Research Letters, 35(16): L16301.

Kurz, M.D., Jenkins, W.J. and Hart, S.R., 1982. Helium isotopic systematics of ocean islands and mantle heterogeneity. Nature, 297: 43-46.

## -L-

Labrosse, S., Hernlund, J.W. and Coltice, N., 2007. A crystallizing dense magma ocean at the base of the Earth's mantle. Nature, 450(7171): 866-869.

Lange, R.A. and Carmichael, I.S.E., 1987. Densities of $Na_2O$-$K_2O$-CaO-MgO-FeO-$Fe_2O_3$-$Al_2O_3$-$TiO_2$-$SiO_2$ liquids: new measurements and derived partial molar properties. Nature, 51: 2931-2946.

Larson, A.C. and Von Dreele, R.B., 1988. GSAS Manual, Los Alamos National Laboratory.

Lauterbach, S., McCammon, C.A., van Aken, P., Langenhorst, F. and Seifert, F., 2000. Mössbauer and ELNES spectroscopy of (Mg,Fe)(Si,Al)$O_3$ perovskite: a highly oxidized component of the lower mantle. Contribution in Mineralogy and Petrology, 138: 17-26.

Lay, T., Garnero, E.J. and Williams, Q., 2004. Partial melting in a thermo-chemical boundary layer at the base of the mantle. Physics of the Earth and Planetary Interior, 146: 441-467.

Lay, T., Williams, Q. and Garnero, E.J., 1998. The core–mantle boundary layer and deep Earth dynamics. Nature, 392: 461-468.

Lee, C.-T.A. et al., 2010. Upside-down differentiation and generation of a 'primordial' lower mantle. Science, 463(7283): 930-933.

Lesher, C.E. and Walker, D., 1988. Cumulate Maturation and Melt Migration in a Temperature Gradient. Journal of Geophysical Research, 93(B9): 10295-10311.

Letoullec, R., Pinceaux, J.P. and Loubeyre, P., 1988. The membrane diamond anvil cell: A new device for generating continuous pressure and temperature variations. High Pressure Research: An International Journal, 1(1): 77 - 90.

Levenberg, K., 1944. A method for the solution of certain problems in least squares. Quarterly of Applied Mathematics, 2: 164-168.

Li, J. and Agee, C.B., 1996. Geochemistry of mantle-core differentiation at high pressure. Nature, 381: 686-689.

Li, X., Manga, M., Nguyen, J. H., Jeanloz, R., 1996. Temperature distribution in the laser-heated diamond cell with external heating, and implications for the thermal conductivity of perovskite. Geophysical Research Letters, Vol. 23, NO. 25 (3775-3778).

Liebske, C., Corgne, A., Frost, D.J., Rubie, D.C. and Wood, B.J., 2005. Compositional effects on element partitioning between Mg-silicate perovskite and silicate melts. Contribution in Mineralogy and Petrology, 149(113-128).

Litasov, K. and Ohtani, E., 2002. Phase relations and melt compositions in CMAS–pyrolite–H2O system up to 25 GPa. Physics of The Earth and Planetary Interiors, 134(1-2): 105-127.

Longhi, J., 1995. Liquidus equilibria of some primary lunar and terrestrial melts in the garnet stability field. Geochimica et Cosmochimica Acta, 59(11): 2375-2386.

Luo, S.N., Akins, J.A., Ahrens, T.J. and Asimow, P.D., 2004. Shock-compressed MgSiO3 glass, enstatite, olivine, and quartz: Optical emission, temperatures, and melting. Journal of Geophysical Research-Solid Earth, 109 (B05205).

## -M-

Mao, W.L. et al., 2006. Iron-Rich Post-Perovskite and the Origin of Ultralow-Velocity Zones. Science, 312(5773): 564-565.

Marquardt, D., 1963. An algorithm for least-squares estimation of nonlinear parameters. SIAM Journal on Applied Mathematics, 11(2): 431-441.

Masters, G., 1979. Observational constraints on the chemical and thermal structure of the Earth's deep interior. Geophysical Journal of the Royal Astronomical Society, 57(2): 507-534.

Matas, J., Bass, J.D., Ricard, Y., Mattern, E. and Bukowinsky, M.S., 2007. On the bulk composition of the lower mantle: predictions and limitations from generalized inversion of radial seismic profiles. Geophysical Journal International, 170: 764-780.

McDonough, W.F. and Sun, S.S., 1995. The composition of the Earth. Chemical Geology, 120: 223-253.

McFarlane, E.A. and Drake, M.J., 1990. Olivine, beta spinel and majorite/melt partitioning and the early thermal history of the earth. Lunar and Planetary Sciences, XXI: 759-760.

McFarlane, E.A., Drake, M.J. and Rubie, D.C., 1991. Magnesiowüstite/melt and majorite/melt partitioning and the early thermal history of the earth. Lunar and Planetary Sciences, XXII: 875-876.

McFarlane, E.A., Drake, M.J. and Rubie, D.C., 1992. Mantle mineral/silicate melt partition coefficients. Lunar and Planetary Sciences, XXIII: 875-876.

McFarlane, E.A., Drake, M.J. and Rubie, D.C., 1994. Element partitioning between Mg-perovskite, magnesiowüstite, and silicate melt at conditions of the Earth's mantle. Geochimica et Cosmochimica Acta, 58(23): 5161-5172.

McNamara, A.K., Garnero, E.J. and Rost, S., 2010. Tracking deep mantle reservoirs with ultra-low velocity zones. Earth and Planetary Science Letters, 299(1-2): 1-9.

Melosh, H.J., 1990. Giant impacts and the thermal state of the early earth. In: H.E. Newsom and J.H. Jones (Editors), Origin of the Earth, Oxford University Press, New York, pp. 69-83.

Ménez, B., Philippot, P., Bonnin-Mosbah, M., Simionovici, A. and Gibert, F., 2002. Analysis of individual fluid inclusions using synchrotron X-ray fluorescence microprobe: progress toward calibration for trace elements. Geochimica et Cosmochimica Acta, 66(4): 561-576.

Merkel, S. et al., 2007. Deformation of $(Mg,Fe)SiO_3$ Post-Perovskite and D" Anisotropy. Science, 316(5832): 1729-1732.

Mezouar, M., 2010. Synchrotron High-Pressure High-Temperature Techniques. In: E. Boldyreva and P. Dera (Editors), High-Pressure Crystallography. NATO Science for Peace and Security Series B: Physics and Biophysics. Springer Netherlands, pp. 23-33.

Mezouar, M. et al., 2005. Development of a new state-of-the-art beamline optimized for monochromatic single-crystal and powder X-ray diffraction under extreme conditions at the ESRF. Journal of Synchrotron Radiation, 12(5): 659-664.

Miller, G.H., Stolper, E.M. and Ahrens, T.J., 1991. The Equation of State of a Molten Komatiite 2. Application to Komatiite Petrogenesis and the Hadean Mantle. Journal of Geophysical Research, 96(B7): 11,849-11,864.

Montelli, R. et al., 2004 Finite-Frequency Tomography Reveals a Variety of Plumes in the Mantle. Science, 303 (5656): 338-343

Morishima, H. et al., 1994. The Phase Boundary Between alpha- and beta-Mg2SiO4 Determined by in Situ X-ray Observation. Science, 265(5176): 1202-1203.

Mosenfelder, J.L., Asimow, P.D., Frost, D.J., Rubie, D.C. and Ahrens, T.J., 2009. The $MgSiO_3$ system at high pressure: Thermodynamic properties of perovskite, postperovskite, and melt from global inversion of shock and static compression data. Journal of Geophysical Research, 114: B01203.

Murakami, M., Hirose, K., Kawamura, K., Sata, N. and Ohishi, Y., 2004. Post-perovskite phase transition in $MgSiO_3$. Science, 304: 855-858.

## -N-

Nagahara, H. and Ozawa, K., 1996. Evaporation of forsterite in H-2 gas. Geochimica Et Cosmochimica Acta, 60(8): 1445-1459.

Newville, M., 2009. Fundamentals of X-ray Absorption Spectroscopy. URL http://cars9.uchicago.edu/xafs/xas_fun/xas_fundamentals.pdf.

Nguyen, J.H. and Holmes, N.C., 2004. Melting of iron at the physical conditions of the Earth's core. Nature, 427(6972): 339-342.

Nishio-Hamane, D., Seto, Y., Nagai, T. and Fujino, K., 2007. Ferric iron and aluminum partitioning between $MgSiO_3$ and $CaSiO_3$ perovskites under oxydizing conditions. Journal of Mineralogical and Petrological Sciences, 102: 291-297.

Nomura, R. et al., 2011. Spin crossover and iron-rich silicate melt in the Earth's deep mantle. Nature, 473(7346), 199-202, 2011.

## -O-

Ohtani, E., Kato, T. and Ito, E., 1991. Transition metal partitioning between lower mantle and core materials at 27 GPa. Geophysical Research Letters, 18(1): 85-88.

Ohtani, E., Kato, T. and Sawamoto, H., 1986. Melting of a model chondritic mantle to 20 GPa. Nature, 322(6077): 352-353.

Ohtani, E., Kawabe, I., Moriyama, J. and Nagata, Y., 1989. Partitioning of elements between majorite garnet and melt implications for petrogenesis of komatiite. Nature, 103: 263-269.

Ohtani, E. and Maeda, M., 2001. Density of basaltic melt at high pressure and stability of the melt at the base of the lower mantle. Nature, 193: 69-75.

Ohtani, E., Moriwaki, K., Kato, T. and Onuma, K., 1998. Melting and crystal-liquid partitioning in the system $Mg_2SiO_4$-$Fe_2SiO_4$ to 25 GPa. Physics of the Earth and Planetary Interiors, 107(1-3): 75-82.

Ohtani, E., Yurimoto, H., Segawa, T. and Kato, T., 1995. Element Partitioning between MgSiO3 Perovskite, Magma, and Molten Iron: Constraints for the Earliest Processes of the Earth-Moon System. The Earth's Central Part: Its Structure and Dynamics, edited by T. Yukutake. TERRAPUB, Tokyo: 287-300.

Ono, S., Kikegawa, T. and Ohishi, Y., 2005. A high-pressure and high-temperature synthesis of platinum carbide. Solid State Communications, 133(1): 55-59.

Ono, S. and Oganov, A.R., 2005. In situ observations of phase transition between perovskite and $CaIrO_3$-type phase in $MgSiO_3$ and pyrolitic mantle composition. Earth and Planetary Science Letters, 236: 914-932.

## -P-

Philippot, P. et al., 2001. Mapping trace-metal (Cu, Zn, As) distribution in a single fluid inclusion using a third generation synchrotron light source. Chemical Geology, 173(1-3): 151-158.

Poirier, J.P., 1994. Light elements in the Earth's outer core: A critical review. Physics of the Earth and Planetary Interiors, 85: 319-337.

Presnall, D.C., 1995. Phase Diagrams of Earth-forming minerals. Mineral Physics and Crystallography, A Handbook of Physical Constants, vol. 2, edited by T. J. Ahren, pp 248-268, AGU, Washington, D. C.

Presnall, D.C., Weng, Y.-H., Milholland, C.S. and Walter, M.J., 1998. Liquidus phase relations in the system MgO-$MgSiO_3$ at pressures up to 25 GPa--constraints on crystallization of a molten Hadean mantle. Physics of The Earth and Planetary Interiors, 107(1-3): 83-95.

## -R-

Revenaugh, J. and Meyer, R., 1997. Seismic Evidence of Partial Melt Within a Possibly Ubiquitous Low-Velocity Layer at the Base of the Mantle. Science, 277(5326): 670-673.

Revenaugh, J. and Sipkin, S.A., 1994. Seismic evidence for silicate melt atop the 410-km mantle discontinuity. 369(6480): 474-476.

Ricolleau, A. et al., 2009. Density profile of pyrolite under the lower mantle conditions. Geophysical Research Letters, 36 (L06302).

Rigden, S.M., Ahrens, T.J. and Stolper, E.M., 1984. Densities of Liquid Silicates at High Pressures. Science, 226(4678): 1071-1074.

Righter, K. and Drake, M.J., 1997. Metal-silicate equilibrium in a homogeneously accreting earth: new results for Re. Earth and Planetary Science Letters, 146(3-4): 541-553.

Righter, K., Drake, M.J. and Yaxley, G., 1997. Prediction of siderophile element metal-silicate partition coefficients to 20 GPa and 2800°C: the effects of pressure, temperature, oxygen fugacity and silicate and metallic melt compositions. Physics of the Earth and Planetary Interiors, 100: 115-134.

Ringwood, A.E., 1962. A model for the upper mantle. Journal of Geophysical Research, 67 (2): 857-867.

Ringwood, A.E., 1975. Pyrolite and the Chondritic Earth Model. In: M. GrawHill (Editor), International series in the Earth's and Planetary Sciences, 189-194.

Rost, S., Garnero, E.J., Williams, Q. and Manga, M., 2005. Seismological constraints on a possible plume root at the core-mantle boundary. Nature, 435(7042): 666-669.

Rubie, D.C., Gessmann, C.K. and Frost, D.J., 2004. Partitioning of oxygen during core formation on the Earth and Mars. Nature, 429: 58-62.

Rubie, D.C., Melosh, H.J., Reid, J.E., Liebske, C. and Righter, K., 2003. Mechanism of metal-silicate equilibration in the terrestrial magma ocean. Earth and Planetary Science Letters, 205: 239-255.

Rudge, J.F., Kleine, T. and Bourdon, B., 2010. Broad bounds on Earth's accretion and core formation constrained by geochemical models. 3(6): 439-443.

## -S-

Sanchez-Valle, C. and Bass, J.D., 2010. Elasticity and pressure-induced structural changes in vitreous $MgSiO_3$-enstatite to lower mantle pressures. Earth and Planetary Science Letters, 295(3-4): 523-530.

Sata, N., Shen, G., Rivers, M.L. and Sutton, S.R., 2002. Pressure-volume equation of state of the high-pressure B2 phase of NaCl. Physical Review B, 65: 114114-7.

Schultz, E. et al., 2005. Double-sided laser heating system for in situ high pressure-high temperature monochromatic x-ray diffraction at the ESRF. High Pressure Research, 25(1): 71-83.

Shankland, T.J. and Brown, J.M., 1985. Homogeneity and temperatures in the lower mantle. Earth and Planetary Science Letters, 38: 51-58.

Shen, G., Prakapenka, V.B., Rivers, M.L. and Sutton, S.R., 2004. Structure of liquid iron up to 58 GPa. Physical Review Letters, 92: 185701.

Shen, G., Rivers, M.L., Wang, Y. and Sutton, S.R., 2001. Laser heated diamond cell system at the Advanced Photon Source for in situ x-ray measurements at high pressure and temperature. Review of Scientific Instruments, 72(2): 1273-1282.

Shim, S.H., Duffy, T.S. and Shen, G., 2000. The equation of state of $CaSiO_3$ perovskite to 108 GPa at 300 K. Physics of the Earth and Planetary Interiors, 120: 327-338.

Simon, F. and Glatzel, G., 1929. Fusion-pressure curve. Zeitschrift für anorganische und allgemeine Chemie, 178: 309-316.

Sinmyo, R. and Hirose, K., 2010. The Soret diffusion in laser-heated diamond-anvil cell. Physics of the Earth and Planetary Interiors, 80(3-4), 172-178.

Sleep, N.H., Zahnle, K.J. and Neuhoff, P.S., 2001. Initiation of clement surface conditions on the earliest Earth. Proceedings of the National Academy of Sciences, 98(7): 3666-3672.

Solé, V.A., Papillon, E., Cotte, M., Walter, P. and Susini, J., 2007. A multiplatform code for the analysis of energy-dispersive X-ray fluorescence spectra. Spectrochimica Acta Part B: Atomic Spectroscopy, 62(1): 63-68.

Solomatov, V.S., 2000. Fluid Dynamics of a Terrestrial Magma Ocean. in Origin of the Earth and Moon, R. Canup and K. Righter, eds., p 323-338, University of Arizona Press, Tucson, Arizona.

Solomatov, V.S. and Stevenson, D.J., 1993. Suspension in Convective Layers and Style of Differentiation of a Terrestrial Magma Ocean. Journal of Geophysical Research, 98(E3): 5375-5390.

Stacey, F.D., 1992. Physics of the Earth. 3rd edn. Brookfield Press, Queensland: 459.

Stacey, F.D. and Davis, P.M., 2004. High pressure equations of state with applications to the lower mantle and core. Physics of The Earth and Planetary Interiors, 142(3-4): 137-184.

Stevenson, D.J., 1990. Fluid dynamics of core formation. In: H. Newsom and J.H. Jones (Editors), The origin of the Earth. Oxford Press, London, pp. 231-249.

Stixrude, L., de Koker, N., Sun, N., Mookherjee, M. and Karki, B.B., 2009. Thermodynamics of silicate liquids in the deep Earth. Nature, 278: 226-232.

Stixrude, L. and Karki, B.B., 2005. Structure and freezing of $MgSiO_3$ liquid in the Earth's lower mantle. Science, 310: 297-299.

Stolper, E., Walker, D., Hager, B.H. and Hays, J.F., 1981. Melt segregation from partially molten source regions: the importance of melt density and source region size. Nature, 86: 6261-6271.

Stutzmann, E., Vinnik, L., Ferreira, A. and Singh, S., 2000. Constraint on the S-wave velocity at the base of the mantle. Geophysical Research Letters, 27(11): 1571-1574.

Suzuki, A., Ohtani, E. and Kato, T., 1998. Density and thermal expansion of a peridotite melt at high pressure. Nature, 107: 53-61.

## -T-

Takahashi, E. and Scarfe, C.M., 1985. Melting of peridotite to 14 GPa and the genesis of komatiite. Nature, 315(6020): 566-568.

Tateno, S., Hirose, K., Sata, N. and Ohishi, Y., 2009. Determination of post-perovskite phase transition boundary up to 4400 K and implications for thermal structure in D" layer. Earth and Planetary Science Letters, 277(1-2): 130-136.

Taura, H., Yurimoto, H., Kato, T. and Sueno, S., 2001. Trace element partitioning between silicate perovskites and ultracalcic melt. Physics of The Earth and Planetary Interiors, 124(1-2): 25-32.

Taylor, S.R. and McLennan, S.M., The continental crust: its composition and evolution, Blackwell, Oxford, 1985.

Taylor, S.R. and Norman, M.D., 1990. Accretion of differentiated planetesimals to the Earth. LPI Conference on the Origin of the Earth, p. 29 - 43.

Terasaki, H. et al., 2011. Liquidus and solidus temperatures of a Fe-O-S alloy up to the pressures of the outer core: Implication for the thermal structure of the Earth's core. Earth and Planetary Science Letters, In Press, Corrected Proof.

Thompson, P.F. and Tackley, P.J., 1998. Generation of mega-plumes from the core-mantle boundary in a compressible mantle with temperature-dependent viscosity. Geophysical Research Letters, 25(11): 1999-2002.

Thorne, M.S. and Garnero, E.J., 2004. Inferences on ultralow-velocity zone structure from a global analysis of SPdKS waves. Journal Of Geophysical Research, 109, B08301.

Tonks, W.B. and Melosh, H.J., 1993. Magma Ocean Formation Due to Giant Impacts. Journal of Geophysical Research, 98(E3): 5319-5333.

Trønnes, R.G. and Frost, D.J., 2002. Peridotite melting and mineral-melt partitioning of major and minor elements at 22-24.5 GPa. Earth and Planetary Science Letters, 197(1-2): 117-131.

Turcotte, D.L. and Schubert, G., 1982. Geodynamics, Application of continuum physics to geological problems. New York: John Wiley and Sons: 450 pp.

## -V-

van der Hilst, R., Widiyantoro, S. and Engdahl, E.R., 1997. Evidence for deep mantle circulation from global tomography. Nature, 386: 578-584.

Van Grieken, R. and Markowicz, A., 2002. Handbook of X-Ray Spectrometry: Methods and Techniques. Marcel Dekker, Inc.

Vekemans, B. et al., 2003. Quantitative X-ray fluorescence analysis at the ESRF ID18F microprobe. Nuclear Instruments and Methods in Physics Research Section B: Beam Interactions with Materials and Atoms, 199: 396-401.

Vincze, L., 2004. X-Ray Spectrometry: Recent technological Advances, chapter 6. New Computerisation Methods. John Wiley & Sons, Ltd.: 435-461.

Vincze, L., Janssens, K., Vekemans, B. and Adams, F., 1999. Monte Carlo simulation of X-ray fluorescence spectra: Part 4. Photon scattering at high X-ray energies. Spectrochimica Acta Part B: Atomic Spectroscopy, 54: 1711-1722.

## -W-

Walker, D., Cranswick, L.M.D., Verma, P.K., Clark, S.M. and Buhre, S., 2002. Thermal equations of state for B1 and B2 KCl. American Mineralogist, 87(7): 805-812.

Walter, M.J., 1998 Melting of Garnet Peridotite and the Origin of Komatiite and Depleted Lithosphere. Journal of Petrology 39 (1): 29-60

Walter, M.J., Nakamura, E., Trønnes, R.G. and Frost, D.J., 2004. Experimental constraints on crystallization differentiation in a deep magma ocean. Geochimica et Cosmochimica Acta, 68(20): 4267-4284.

Walter, M.J. and Trønnes, R.G., 2004. Early Earth differentiation. Earth and Planetary Science Letters, 225(3-4): 253-269.

Wan, J.T.K., Duffy, T.S., Scandolo, S. and Car, R., 2007. First-principles study of density, viscosity, and diffusion coefficients of liquid MgSiO3 at conditions of the Earth's deep mantle. Journal of Geophysical Research, 112(B3): B03208.

Wang, C.-y., 1972. Temperature in the Lower Mantle. Geophysical Journal of the Royal Astronomical Society, 27(1): 29-36.

Wang, Z., Lazor, P. and Saxena, S.K., 2001. A simple model for assessing the high pressure melting of metals: nickel, aluminum and platinum. Physica B, 293: 408-416.

Wasson, J.T. and Kallemeyn, G.W., 1988. Composition of chondrites. Philosophical Transaction of the Royal Society of London, A325: 535-544.

Wen, L. and Helmberger, D.V., 1998. Ultra-low velocity zones near the core-mantle boundary from broadband PKP precursors. Science, 279: 1701-1703.

Wetherill, G.W., 1990. Formation of the Earth. Annual Review of Earth and Planetary Sciences, 18(1): 205-256.

White, R. and McKenzie, D., 1989. Magmatism at Rift Zones: The Generation of Volcanic Continental Margins and Flood Basalts. Journal of Geophysical Research, 94(B6): 7685-7729.

Wicks, J.K., Jackson, J.M. and Sturhahn, W., 2010. Very low sound velocities in iron-rich (Mg,Fe)O: Implications for the core-mantle boundary region. Geophysical Research Letters, 37(15): L15304.

Williams, Q. and Garnero, E.J., 1996. Seismic evidence for partial melt at the base of Earth's mantle. Science, 273: 1528-1530.

Williams, Q., Jeanloz, R., Bass, J., Svendsen, B. and Ahrens, T.J., 1987. The Melting Curve of Iron to 250 Gigapascals - a Constraint on the Temperature at Earths Center. Science, 236(4798): 181-182.

Williams, Q., Revenaugh, J. and Garnero, E., 1998. A Correlation Between Ultra-Low Basal Velocities in the Mantle and Hot Spots. Science, 281(5376): 546-549.

Wood, B.J. and Rubie, D.C., 1996. The effect of alumina on phase transformations at the 660-kilometer discontinuity from Fe-Mg partitioning experiments. Science, 273: 1522-1524.

Wood, B.J., Walter, M.J. and Wade, J., 2006. Accretion of the Earth and segregation of its core. Nature, 441(7095): 825-833.

## -Y-

Yamazaki, D., Kato, T., Ohtani, E. and Toriumi, M., 1996. Grain growth rates of $MgSiO_3$ perovskite and periclase under lower mantle conditions. Science, 274: 2052-2054.

Yin, Q. et al., 2002. A short timescale for terrestrial planet formation from Hf-W chronometry of meteorites. Nature, 418(6901): 949-952.

Yoshino, T., Walter, D. and Katsura, T., 2003. Core formation in planetesimals triggered by permeable flow. Nature, 422: 154-157.

## -Z-

Zahnle, K.J., Kastings, J.F. and Pollack, J.B., 1988. Evolution of a Steam Atmosphere during Earth's Accretion. Icarus, 74: 62-97.

Zerr, A., Diegeler, A. and Boehler, R., 1998. Solidus of earth's mantle. Science, 281: 243-246.

Zhang, J. and Herzberg, C., 1994. Melting experiments on anhydrous peridotite KLB-1 from 5.0 to 22.5 GPa. Journal of Geophysical Research, 99(B9): 17729-17742.

# Appendix

## *Andrault et al., 2011*

Earth and Planetary Science Letters 304 (2011) 251–259

Contents lists available at ScienceDirect

Earth and Planetary Science Letters

journal homepage: www.elsevier.com/locate/epsl

# Solidus and liquidus profiles of chondritic mantle: Implication for melting of the Earth across its history

Denis Andrault [a,*], Nathalie Bolfan-Casanova [a], Giacomo Lo Nigro [a], Mohamed A. Bouhifd [a], Gaston Garbarino [b], Mohamed Mezouar [b]

[a] Laboratoire Magmas et Volcans, Université Blaise Pascal, Clermont-Ferrand, France
[b] European Synchrotron Radiation Facility, Grenoble, France

ARTICLE INFO

*Article history:*
Received 11 August 2010
Received in revised form 2 December 2010
Accepted 2 February 2011
Available online 4 March 2011

Editor: L. Stixrude

*Keywords:*
lower-mantle melting-curves
properties of the magma ocean

ABSTRACT

We investigated the melting properties of a synthetic chondritic primitive mantle up to core–mantle boundary (CMB) pressures, using laser-heated diamond anvil cell. Melting criteria are essentially based on the use of X-rays provided by synchrotron radiation. We report a solidus melting curve lower than previously determined using optical methods. The liquidus curve is found between 300 and 600 K higher than the solidus over the entire lower mantle. At CMB pressures (135 GPa), the chondritic mantle solidus and liquidus reach 4150 (±150) K and 4725 (±150) K, respectively.

We discuss that the lower mantle is unlikely to melt in the D″-layer, except if the highest estimate of the temperature profile at the base of the mantle, which is associated with a very hot core, is confirmed. Therefore, recent suggestions of partial melting in the lowermost mantle based on seismic observations of ultra-low velocity zones indicate either (1) a outer core exceeding 4150 K at the CMB or (2) the presence of chemical heterogeneities with high concentration of fusible elements.

Our observations of a high liquidus temperature as well as a large gap between solidus and liquidus temperatures have important implications for the properties of the magma ocean during accretion. Not only complete melting of the lower mantle would require excessively high temperatures, but also, below liquidus temperatures partial melting should take place over a much larger depth interval than previously thought. In addition, magma adiabats suggest very high surface temperatures in case of a magma ocean that would extend to more than 40 GPa, as suggested by siderophile metal–silicate partitioning data. Such high surface temperature regime, where thermal blanketing is inefficient, points out to a transient character of the magma ocean, with a very fast cooling rate.



## 1. Introduction

A large proportion of our planet has experienced melting in the course of its accretion history as a consequence of the energy release associated with large impacts, radioactive decay and core formation. Major unknowns remain about this early time, in particular the extension depth of the magma ocean and the chemical signature inherited from mantle crystallization during cooling. The melting curve of the primitive mantle thus has major consequences for the existence of chemical heterogeneities and the survival of primitive mantle reservoirs. In the modern Earth, seismology evidences heterogeneous properties of the D″-region which extends from the core–mantle boundary (CMB) upwards 250 km (Lay et al., 1998). There are, indeed, evidences for large-scale patterns of heterogeneities, with anomalous set of $V_P$–$V_S$ seismic velocities, that can hardly be explained by phase transitions in minerals or thermal anomalies. Instead, they seem to evidence chemical heterogeneities, which can be of different origins: (i) partial melting in the D″-layer (Lay et al., 2004), leading to chemical segregation of the mantle; (ii) relics of descending slabs rich in mid-ocean ridge basalts (MORB); (iii) zones enriched in incompatible elements associated to the progressive crystallization of an ancient magma ocean and trapped in the lowermost mantle (Labrosse et al., 2007); and/or (iv) lower mantle material affected by chemical exchanges with the outer core. Each hypothesis has specific implications for our comprehension of the dynamics of the Earth, as well as for elemental segregation between the different geological reservoirs. Unfortunately, it remains difficult to distinguish between the different scenarios. Indeed, the thermo-elastic parameters of the main lower mantle minerals are known with insufficient accuracy for inferring the mineralogy of this very remote region using the seismic features. Especially, it remains a challenge to infer any chemical anomaly other than Mg/Si and Fe/(Mg + Fe) ratios.

In order to assess the potential occurrence of partial melting in the D″ region, one must refine the melting curves of the different geological

* Corresponding author.
*E-mail address:* D.Andrault@opgc.univ-bpclermont.fr (D. Andrault).

0012-821X/$ – see front matter © 2011 Elsevier B.V. All rights reserved.
doi:10.1016/j.epsl.2011.02.006

materials. For pressures up to 25 GPa, melting curves of mantle silicates and phase relations in a partially molten mantle have been investigated using the multi-anvil press. It has been shown that pressure affects significantly the solidus and liquidus temperatures as well as composition of the eutectic liquids (Ito et al., 2004; Liebske et al., 2005; Litasov and Ohtani, 2002). At higher pressures, while the melting curve of end-member phases is relatively well documented using laser-heated diamond anvil cells (LH-DAC) (e.g. Boehler, 2000), shock wave experiments (e.g. Luo et al., 2004) or ab initio calculations (e.g. Stixrude and Karki, 2005), melting of material with relevant geological composition was much less investigated. For pyrolite, optical observations have been used to determine the melting curve as a function of pressure using the LH-DAC (Zerr et al., 1998), but only up to ~60 GPa. This pressure range remains too limited for quantitative extrapolation to the ~135 GPa representative of the D″-layer. On the other hand, using shock-wave experiments, melting of $(Mg, Fe)_2SiO_4$ olivine was reported at 4300 K and ~130 GPa (Holland and Ahrens, 1997). Recently, the same group corrected this value to 4000 (300) K, after improvement of the temperature estimation (Luo et al., 2004).

## 2. Methods

Ultra-brillant X-ray beams are now available from synchrotron rings for in-situ investigation of the melting behavior in the LH-DAC. For these experiments, we used a membrane-type DAC mounted with 250 μm or 75/300 μm culet-diameter diamonds. Re gaskets were pre-indented to 40 μm or 20 μm and laser-drilled to 80 μm or 50 μm, respectively. Small glass flakes were loaded in between two NaCl or KCl pellets, and a few experiments were performed without pressure medium. Salts provide good thermal insulation from the diamonds and can be used as pressure standards at 300 K (Sata et al., 2002; Walker et al., 2002). Hot spots with diameter larger than 30 μm were obtained by two YAG lasers aligned on both sides of the sample. Temperatures were measured from sample thermal emission using reflective lenses to prevent any chromatic aberration (Benedetti and Loubeyre, 2004). The intrinsic temperature uncertainty is estimated to be 50 K, including uncertainties on the thermal emissivity factors. For solid samples, temperature stability was better than 20 K during the 20 to 30 s of data acquisition. However, when the sample starts melting, the temperature stability deteriorates. In this study, we discarded those measurements where temperature fluctuation exceeded 50 K. Also, the emissivity factor is less documented for liquid phases. Therefore, the temperature uncertainty is estimated to be 50 K and 100 K, for solid and molten samples, respectively.

Our sample consisted of a synthetic CMASF glass with oxide contents in chondritic proportions (except for iron) so as to model the primitive mantle after core segregation (Wasson and Kallemeyn, 1988) (Table 1). We did not include minor and trace elements, which most abundant are Na (4900 ppm) and K (560 ppm). We believe that their effect on solidus and liquidus curves can be neglected as a first approximation because these elements are easily inserted in the $CaSiO_3$ perovskite phase (Ca–Pv) (Corgne et al., 2003). We did not mix our sample with any YAG-laser absorber or pressure standard, such as Pt or W, in order to avoid any chemical reaction. Finally, we estimate that the melting behavior of our starting material should be comparable to that of pyrolite, due to their related compositions (Ringwood, 1975) (Table 1).

**Table 1**
Composition of starting material used in this study, as measured by electron microprobe analyses. At lower mantle P–T conditions, the Ca–Pv, Mg–Pv, and Fp phase proportions are expected to be 4.5, 75.7, and 19.8 mol%, respectively. This composition is representative of a chondritic-type mantle (Wasson and Kallemeyn, 1988), and it is also quite close to pyrolite (Ringwood, 1975).

| Oxide | Chondritic mantle (this study) | | Pyrolite |
|---|---|---|---|
| | (wt.%) | (mol%) | (wt.%) |
| $SiO_2$ | 49.6 | 43.5 | 45.1 |
| $Al_2O_3$ | 3.4 | 1.8 | 3.3 |
| FeO | 8.48 | 6.2 | 8.0 |
| CaO | 3.3 | 2.6 | 3.1 |
| MgO | 35.1 | 45.9 | 38.1 |

In order to probe the sample properties in-situ, we used the X-ray diffraction set-up available for LH-DAC at the ID27 beamline of ESRF (Mezouar et al., 2005). Wavelength was fixed to 0.3738 Å or 0.2647 Å. X-ray focusing to better than $2\times3$ μm$^2$ was achieved by two bent KB-mirrors. Typical acquisition time is 20–30 s using an imaging plate or a CCD detector. The X-ray beam position was determined from optical observations of the Re-gasket fluorescence. Therefore, combined images of X-ray beam and YAG lasers could be perfectly positioned on the pinhole of the entrance of the spectrometer used for temperature measurements. Integration of 2D-images and further data treatment were performed using the Fit2d and the GSAS packages, respectively.

For estimating pressure at high temperature, we used two different methods. The first one is based on the PVT equation of state (EoS) of $CaSiO_3$–perovskite (Shim et al., 2000) from which pressure is derived from the Ca–Pv volume at a known experimental temperature. Due to a non-negligible Al-solubility in Ca–Pv (Nishio-Hamane et al., 2007), its EoS could be affected, which would increase the experimental error. The second method is based on an estimation of the pressure correction ($\Delta P$), which is a fraction of the theoretical thermal pressure ($\Delta P_{th}$). The latter consists on an increase of pressure due to heating ($\Delta T$) at constant volume, $\Delta P_{th} = \alpha K \Delta T$, where $\alpha$ and $K$ are thermal expansion and bulk modulus, respectively. Experiments and calculations show that, due to partial volume relaxation at high-temperature, the effective $\Delta P$ corresponds to about half of the theoretical thermal pressure (Andrault et al., 1998). According to the thermo-elastic parameters of the main Mg–Pv component (Fiquet et al., 2000), the value of $\Delta P$ is $\sim 2.5 \cdot 10^{-3}$ GPa/K. Both methods give results similar within a couple of GPa. So, pressure error at high T is estimated to be about 3 GPa.

We investigated the melting temperature using NaCl and KCl as thermal insulators, but also tested without insulating pellets in a few experiments, in order to make sure that the results are not affected by the nature of the pressure transmitting medium. NaCl happens to melt at temperatures similar, or even below, the liquidus temperatures of the primitive chondritic mantle composition used. Therefore, all liquidus temperatures reported here were determined using KCl insulator. The data set presented in this paper includes 19 successful high-pressure loadings. Each melting point has been determined after laser-heating of at least one fresh piece of sample, i.e. melting at one single pressure.

## 3. Results

### 3.1. Melting criteria

In general, the onset of melting can be detected using X-ray diffraction by the appearance of a diffuse X-ray scattering band typical of liquids. Such band is easily observed if the sample is composed of relatively high-Z elements such as iron (Andrault et al., 2006; Shen et al., 2004). If the sample is composed of low Z-elements, such as is the case for a mantle silicate, the sample thickness should be important to enable observation of the diffuse band. This is not the case of our samples, which are intentionally thin in order to minimize axial thermal gradients.

Additional criteria based on X-ray observations are (1) the rapid re-crystallization of the sample at high-temperature, with appearance and disappearance of X-ray spots, indicative of coexistence of crystal and melt. (2) At the same time as solid and liquid coexist, the temperature reaches a plateau while laser power is continuously

increased, just before the liquid diffuse scattering appears and temperature simultaneously increases (Dewaele et al., 2007). In the following we used the fast disappearance of diffraction peaks of the solidus phase and re-crystallization as a sign of solidus temperature and the end of the temperature–power plateau as the sign of liquidus temperature.

### 3.2. Determination of solidus temperature

At sub-solidus temperatures, the phases present are $CaSiO_3$–perovskite (Ca–Pv), (Mg, Fe)O ferropericlase (Fp), and Al-bearing (Mg, Fe)$SiO_3$ perovskite (Mg–Pv), in the order of increasing abundance. The first phase to disappear from the diffraction patterns when increasing temperature is Ca–Pv (Fig. 1), in agreement with a previous study using multi-anvil press (Ito et al., 2004). Concerning Fp, persistence or disappearance of this phase is difficult to detect, first because its content is limited to 20 mol% for this chondritic-type composition and secondly because most of its diffraction lines overlap with those of Mg–Pv (Andrault, 2001). Thus, disappearance of Ca–Pv and Fp could be almost simultaneous. The Ca–Pv disappearance is concomitant with rapid grain growth of the Mg–Pv phase, as evidenced by larger diffraction spots on the diffraction image (Fig. 1A and B). Also, a number of diffraction peaks typical of the three phases reappear on the imaging plate after laser shut-down. Note that for such mineralogy, where at least three phases coexist, the kinetics of grain growth is extremely sluggish in the solid state (Yamazaki et al., 1996). Thus, changes of peak intensity can only be attributed to non-solid state diffusion, i.e. diffusion assisted by melt. Another source of information is based on the sample shape after laser-heating. In the case of heating to the solidus temperature, the shape of the sample is affected only moderately (Fig. 1D). Thermal expansion in the laser spot induced a circular-shaped structure, and some cracks in the surrounding material, at more than 10–15 μm from the center, where the material has not been heated at high temperatures. This shape contrasts largely with what is observed when heating to the liquidus temperatures (Fig. 2D).

We found that melting at the solidus temperature is very difficult to detect for those LH-DAC runs where we did not use any thermal insulator. The reason is that solidus melting is dispersed over a broad range of laser power, due to a large axial temperature gradient across the sample, given that the diamond remain basically cold compared to the center of the laser spot. Also, it is possible that a sample fraction remains below the solidus temperature at the diamond surface, before the central part of the sample reaches the liquidus temperature. Therefore, clear disappearance of $CaSiO_3$ (and/or Fp) diffraction lines cannot be observed in this case.

### 3.3. Determination of liquidus temperature

When approaching the liquidus temperature, we first observe a plateau where increasing laser power does not yield an increase

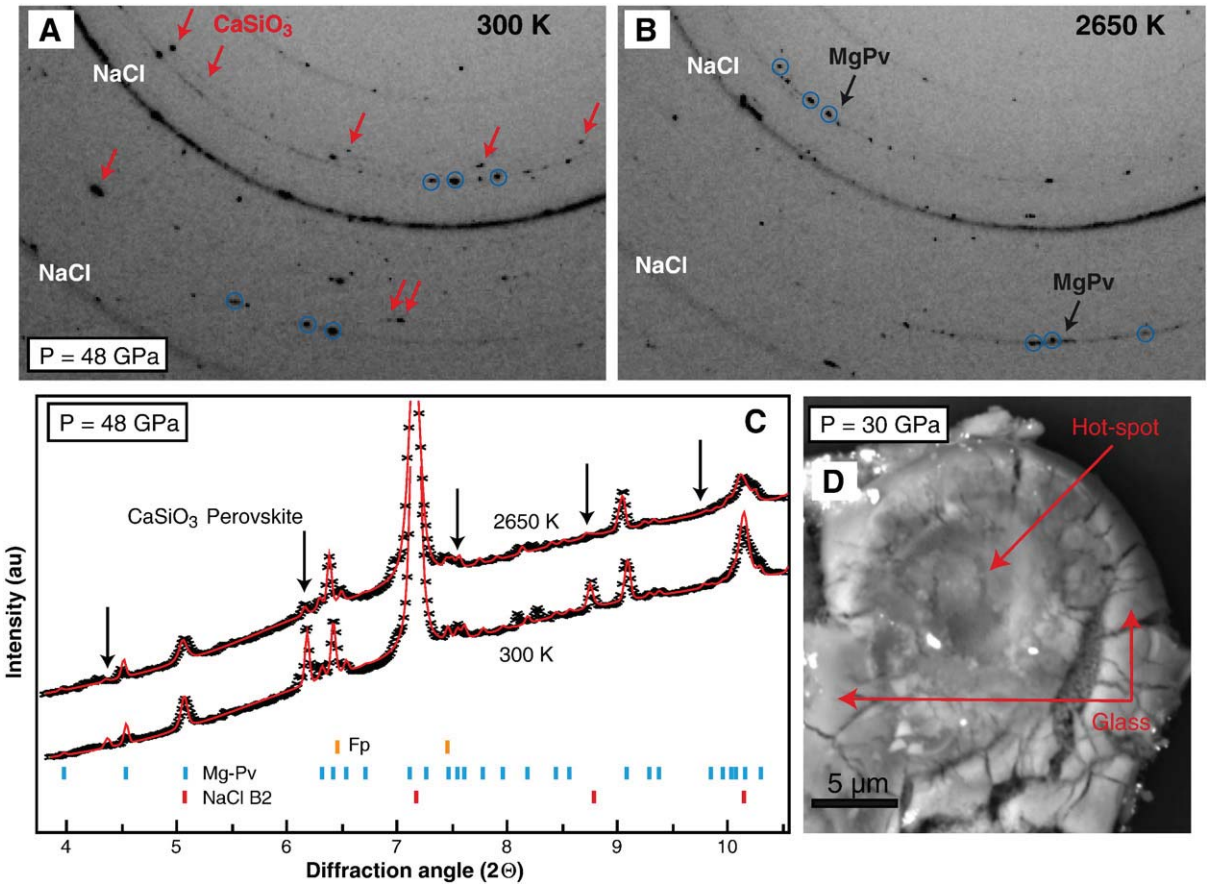


**Fig. 1.** Experimental evidences of sample partial melting and determination of the solidus temperature upon temperature increase from 300 K (A): at 2650 K (B) and a nominal pressure of 48 GPa, we observe first order changes in the position and intensity of diffraction peaks. First, disappearance of the $CaSiO_3$–perovskite diffraction peaks (pointed by arrows in (A) and (C)). Altogether, changes in peaks intensity are compatible with loss of 90% and 20% of the Ca-bearing and Mg-bearing perovskite phases, respectively. Simultaneously, we observe at 2650 K new spots of Mg–Pv phase (B) indicative of recrystallization on a short time scale, this can only be due to the presence of melt at grain boundaries. (D) Electron microphotograph showing a central zone of a sample recovered from 30 GPa that encountered laser heating between the solidus and liquidus temperatures (see Fig. 2D for comparison).

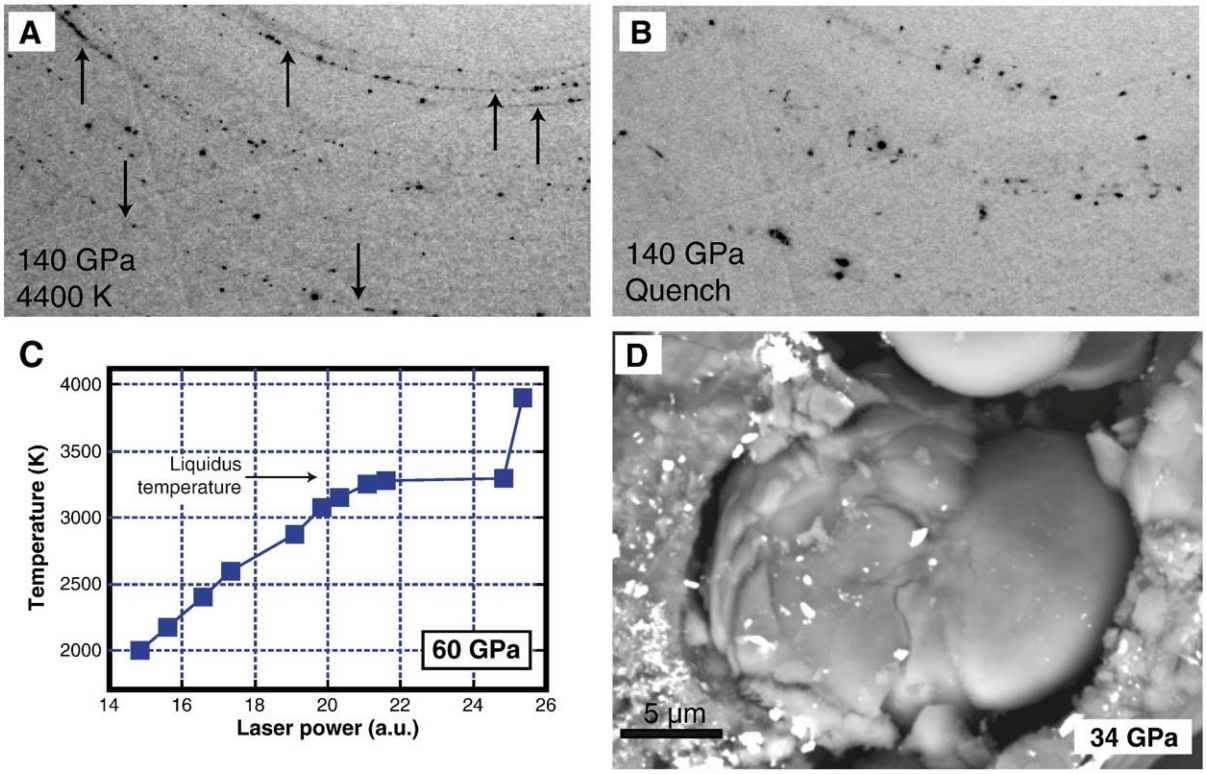


**Fig. 2.** Criterion used for determination of the liquidus temperature: X-ray diffraction pattern recorded (A) at 4400 K and (B) after quenching from 4800 K at a pressure of 140 GPa. Quench from the liquid phase (B) yields larger and new spots typical of sample recrystallization from a fully molten sample. Indeed, while these two diffraction patterns were taken a few minutes apart from each other, the patterns are radically different in peak positions and intensities. Also, we observe total disappearance of all fine and continuous diffraction lines (indicated by arrows in (A)), which evidences the complete melting of the Mg–Pv liquidus phase. (C) Sample temperature plotted as a function of the laser power. A discontinuity occurred at the liquidus temperature due to change in the absorption of the YAG-laser by the liquid sample. (D) Electron microphotograph of a sample recovered from 34 GPa showing the central laser-heated zone that underwent complete melting. It formed an independent liquid-ball separated from the rest of the sample.

in temperature, just before a sudden temperature jump of more than 500 K (Fig. 2C). A similar criterion has been used for melting determination in metals (Dewaele et al., 2007). We explain the plateau by a progressive disappearance of Mg–Pv with increasing laser power, with a coexisting liquid phase absorbing the YAG-radiation less than Mg–Pv. Indeed, a higher absorption efficiency for the solid is expected since Al-bearing (Mg, Fe)$SiO_3$ perovskite contains high $Fe^{3+}$-content (Lauterbach et al., 2000). The last data point on the plateau corresponds to the laser power required to finally achieve a good coupling between YAG-radiation and the silicate melt, i.e. once the phase that absorbs the YAG-radiation better (i.e. the Mg–Pv) is consumed. Moreover, the flatness of the plateau indicates that the melt fraction has no significant effect on melting temperature. Such a high liquid productivity is expected when incompatible elements are not abundant in the bulk composition, which clearly is our case, and when the liquid composition gets closer to the remaining solid phase, which is also our case for high degree of partial melting due to the fact that Mg–Pv, the liquidus phase, is very abundant in our samples (Asimow et al., 1997) (Table 1).

A very important feature is the total disappearance of the fine and continuous diffraction lines of the Mg–Pv phase in the high-temperature X-ray spectrum, evidencing that this phase is completely molten at that temperature (Fig. 2A). The diffuse X-ray scattering is not clearly visible in our samples because the sample is too thin. The reappearance of sparse and large diffraction spots upon temperature quench is typical of crystallization from a melt (Fig. 2B).

After quenching from the liquidus temperature, we observe a drastic change in the sample shape (Fig. 2D). The central part of the sample presents a round-shape with a diameter ~15–20 μm. This sample piece is detached from the rest of the sample. This part has undergone complete melting which induced deformation of the surrounding NaCl and KCl pressure medium to form a kind of sample droplet.

### 3.4. Melting curves

The solidus temperature is found to increase smoothly with pressure from ~2500 K to ~4200 K at 30 to 140 GPa. The liquidus is found at 300 to 600 K above the solidus (Fig. 3). Both melting curves are well fitted by modified Simon and Glatzel equation $[T = T_0\ (P/a+1)^{1/c}]$ with $T_0 = 2045$ K, $a = 92$ GPa and $c = 1.3$ for the solidus, $T_0 = 1940$ K, $a = 29$ GPa and $c = 1.9$ for the liquidus, where $T_0$ is the virtual (this mineral assemblage is only stable above 24 GPa) melting temperature at ambient pressure (Simon and Glatzel, 1929). The interpolation to the CMB pressure of 135 GPa yields solidus and liquidus temperatures of $4150 \pm 150$ K and $4725 \pm 150$ K, respectively. At low pressures, both solidus and liquidus curves are compatible with previous determinations using multi-anvil press (Litasov and Ohtani, 2002; Tronnes and Frost, 2002). Our liquidus curve falls between upper and lower bounds of the solidus curve reported previously using LH-DAC (Zerr et al., 1998). However, it is unlikely that the speckle method used by Zerr et al. can precisely determine solidus and liquidus temperature in the absence of in-situ X-ray diffraction observation. In addition, their melting curves must be shifted to higher pressures because they neglected the effect of thermal pressure inherent to the use of LH-DAC (~2.5 GPa/1000 K, see above). Such uncertainties, leading to overestimation of the melting temperature using optical methods, explain why the MORB melting curve of (Hirose et al., 1999) is observed at higher temperature than the solidus of our primitive mantle composition, although MORB is more fusible. Finally, the data point reported at 4300 K and ~125 GPa for melting of (Mg,

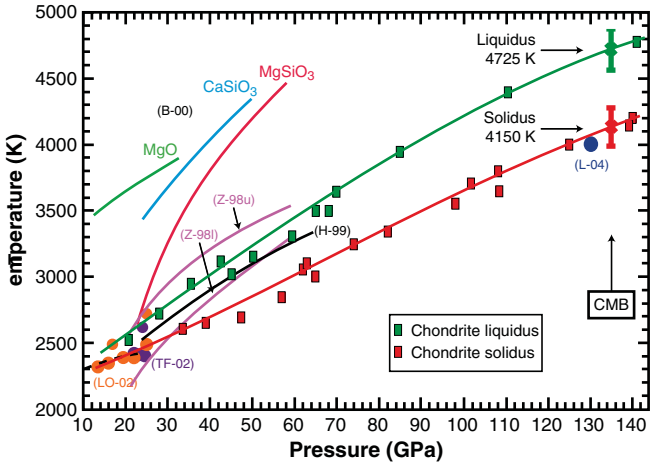


**Fig. 3.** Solidus (red squares) and liquidus (green squares) melting points and curve fits using the Simon–Glatzel model (continuous red and green lines) obtained for our chondritic-type mantle composition. These results are compared with previous works on the melting of lower mantle materials (Pyrolite: LO-02 (Litasov and Ohtani, 2002) and TF-02 (Tronnes and Frost, 2002) (full and open circle for solidus and liquidus, respectively) and Z-98 (Zerr et al., 1998) upper and lower estimations of the solidus; Mid-ocean ridge basalt: H-99 (Hirose et al., 1999); Olivine: L-04 (Luo et al., 2004); Simple oxides: B-00 (Boehler, 2000)). Melting criteria used in our experiments are described in Figs. 1 and 2. At the core–mantle boundary pressure of 135 GPa, we interpolate solidus and liquidus melting temperatures at 4150 K and 4725 K, respectively. Error bars for all points are shown at CMB pressures.

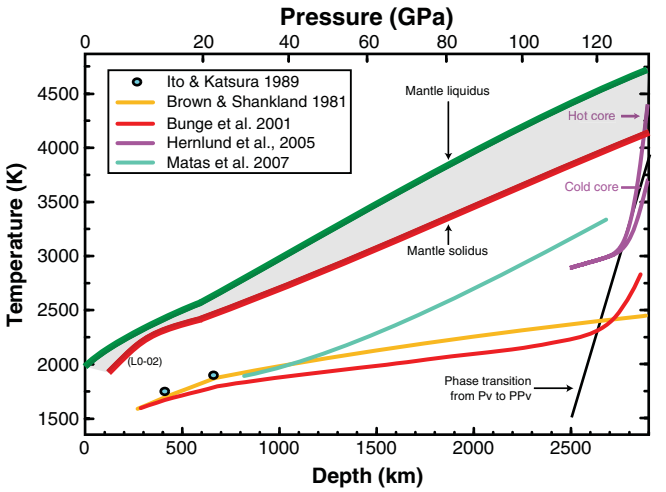


**Fig. 4.** The melting curves of synthetic chondritic mantle plotted together with available estimates of the mantle geotherm (Brown and Shankland, 1981; Bunge et al., 2001; Hernlund et al., 2005; Matas et al., 2007) and temperature anchor points (Ito and Katsura, 1989). Although the temperature estimates vary significantly from one work to another, there is only one estimate for the D″-layer temperatures (Hernlund et al., 2005) being higher than the experimentally determined melting curve for chondritic mantle. It is based on the double-crossing of the $MgSiO_3$ Pv to Post-Pv phase transition and remains controversial (see text).

$Fe)_2SiO_4$ olivine from shock-experiments (Holland and Ahrens, 1997) falls in between our solidus and liquidus melting curves, showing a relatively good agreement between the two different data sets. Indeed the forsterite liquidus is observed to be lower than that of enstatite at high-pressures (Mosenfelder et al., 2009).

## 4. Discussions

### 4.1. Thermal structure of the D″ layer

In order to identify melting in the mantle, melting curves must be compared to the geotherm. While temperatures are relatively well constrained in the shallow mantle due to anchoring by phase transitions at 410 and 670 km depth in $(Mg, Fe)_2SiO_4$ (Ito and Katsura, 1989), extrapolation of the adiabatic geotherm ($dT/dz = \alpha g T/Cp$, where $\alpha$, $g$, $Cp$ are thermal expansion, gravity and heat capacity at constant pressure) to the base of the mantle using the elastic parameters of constitutive mantle minerals bears a much larger uncertainty (Fig. 4). Differences in adiabatic geotherms are often within 0.1 K/km but translate into up to 250 K difference at the bottom of the mantle yielding in general 2500 K ± 250 at 2700 km depth (Brown and Shankland, 1981; Bunge et al., 2001; Stacey and Davis, 2004). Whereas more sophisticated models using inversion of seismic radial profiles indicate hotter temperatures of 2800 to 3400 K at 2700 km depth (Matas et al., 2007), dependent on the Mg/Si ratio.

The temperature profile in the D″-layer could be much steeper accounting for the difference in temperature between the mean mantle above and the molten outer core. The present-time temperature gradient in this zone depends on the initial difference in temperature between the outer core and the mantle a few hundreds kilometers above the CMB, the core energy budget since its formation (Labrosse et al., 1997), the thickness of the boundary layer and the thermal conductivities. Recently, the thermal structure of the D″ region has been tentatively constrained in light of the new post-perovskite phase of $MgSiO_3$ (Murakami et al., 2004; Oganov and Ono, 2004). It was proposed that the observation of pairs of positive and negative S-wave velocity jumps in the D″ region are due to double-crossing of the perovskite to post-perovskite (PPv) transition (Hernlund et al., 2005). Based on the latest measurements of the Pv-PPv Clapeyron slope in $MgSiO_3$, this would mean that the temperature at the CMB could be around 3700 K (Tateno et al., 2009). Still, it can be argued that the lower mantle contains Fe and Al that are known to influence the depth and thickness of phase transitions in general and have been demonstrated recently to considerably broaden the Pv—PPv transition due to the very different iron partitioning between the two phases (Andrault et al., 2010; Catalli et al., 2009). The interpretation of the seismic discontinuities in terms of temperature should thus be revised in order to take this into account.

In any case, refining the outer core temperature remains essential for our knowledge of the temperature profile in the D″-layer. This temperature is generally estimated by extrapolating the adiabatic temperature profile from the inner-core boundary (ICB) through the outer core. However, there are several sources of uncertainties. A first uncertainty arises from controversial melting curves for pure Fe determined firstly by LHDAC, ranging from 4850 ± 200 K (Boehler, 1993) to 7600 ± 500 K (Williams et al., 1987) at ICB pressures. On the other hand, shock-wave experiments and ab-initio calculations suggest melting temperatures of more than 6000 K at 330 GPa (Alfe, 2009; Nguyen and Holmes, 2004). A second source of uncertainty is associated to the presence and nature of light elements, which should cause a severe melting temperature depletion. Depending on the major light element considered for the outer core, extrapolations of the melting temperature to the ICB yields temperatures from 4100 ± 100 K in the Fe—Si system (Asanuma et al., 2010) to 5500 ± 500 K in the Fe—S eutectic system (Kamada et al., 2010), for example. And, if the outer core contains a mixture of light elements S, Si and O (Badro et al., 2007; Poirier, 1994), the resulting melting temperature should be lower than measured in binary compounds. Altogether, the broad range of ICB temperatures reported in the literature yields a large range of CMB temperatures and it is difficult to conclude if the outer core is indeed much hotter than the lower mantle at a few hundreds kilometers above the CMB or not.

### 4.2. Melting in the D″ region and origin of the ULVZ

From the available geotherms, only the highest temperature estimation, based on an extremely steep temperature gradient in

the D″-layer allows partial melting of a chondritic-type mantle in the D″-layer for which we report a solidus temperature of 4150 K (Fig. 4). However, we insist on the fact that this very steep temperature profile is derived from the Clapeyron slope of the Pv—PPv transition for pure $MgSiO_3$ (Hernlund et al., 2005), and that in the mantle the transition does not occur at the same depths. Therefore, if partial melting of the chondritic (or pyrolitic) lower mantle is not totally precluded in the D″-layer, it remains unlikely as long as the occurrence of a very hot core is not better established.

The observation of ultra-low velocity zones (ULVZ) exhibiting P- and S-wave velocity reductions of 10 and 30% just above the CMB (Lay et al., 2004) has been interpreted as being the result of partial melting. Since the solidus and liquidus profiles determined in this study are not in favor of partial melting of the chondritic (or pyrolitic) mantle, a probable way for inducing melting in the ULVZ of the D″-layer is a local enrichment in incompatible elements, in particular volatiles (Na, K, H or $CO_2$) which are known to depress the solidus temperatures. Some of these elements (Na and K) may have a moderate effect on the solidus temperature, since they are easily inserted into the Ca-Pv at sub-solidus conditions (Corgne et al., 2003). In the case of water, however, the effect could be large, because the solubility of H in the main lower mantle phases is low (Bolfan-Casanova et al., 2006). Once partial melting is induced, the degree of partial melting is difficult to estimate since solid–liquid phase relations are basically unknown at CMB conditions. Local concentration of the most fusible elements associated with chemical heterogeneities is compatible with the fact that ULVZ features are not ubiquitous but instead observed only in one third of investigated areas (Wen and Helmberger, 1998).

### 4.3. Depth extension of the early magma ocean

The energy deposited on the Earth during its accretion was sufficient to partially or completely melt it, especially just after the Moon-forming giant impact (Canup, 2008; Tonks and Melosh, 1993). Under such conditions, a magma ocean undoubtedly existed. It is interesting to discuss the implications of the new melting curve of chondritic mantle for our understanding of the nature of the magma ocean.

The inventory of siderophile elements in the modern mantle indicates equilibration between silicates and iron at high pressures and temperatures (Li and Agee, 1996; Righter et al., 1997). In addition, in order to efficiently segregate the core, the silicate has to be molten in order to overcome the high surface tension of iron in a solid silicate matrix. Consequently, it was proposed that iron droplets sink through the molten silicate layer and pond at the base of a magma ocean, followed by metal descending through the solid mantle in the form of diapirs (Karato and Murthy, 1997; Stevenson, 1990). Thus, a widely accepted model is that equilibration occurred just before the iron droplets reach the Fe-pond at the floor of a magma ocean (Li and Agee, 1996; Wood et al., 2006). The apparent pressure of equilibrium is comprised between 30 and 60 GPa, 45 and 85 GPa, or 20 and 50 GPa, based on metal–silicate partition coefficients of nickel and cobalt (Bouhifd and Jephcoat, 2003; Chabot et al., 2005), oxygen solubility in molten iron (Rubie et al., 2004), or metal–silicate partitioning of tungsten (Cottrell et al., 2009), respectively. A recent refinement of such model explains the mantle enrichment in several siderophile elements by a continuous accretion at a pressure of equilibrium of 40 GPa and 3150 K (Wood et al., 2006). The pressure of equilibrium is given by the partitioning of Ni and Co that is very sensitive to pressure while the temperature of equilibrium is estimated from the partitioning of V which is very sensitive to temperature. However, complications may arise from the fact that diffusion kinetics suggest metal–silicate equilibration during a “metal rainfall” so that the resulting chemical composition of the mantle probably results from a polybaric process (Rubie et al., 2003), extending the pressure range of equilibrium to depths shallower than the base of the magma ocean.

We should also mention here that the model of equilibrium core segregation is challenged by numerical modeling results indicating that the core of the impactors possibly merged with the Earth's core or that the impact did not emulsify efficiently the metal and silicate liquids (Dahl and Stevenson, 2010). Both imply that the core segregated without equilibrating with the mantle. In this case, the pressure of equilibration is meaningless. Still, the geochemical constraints (Hf–W, U–Pb, and siderophile elements) do not seem to be enough in order to conclude whether the core and mantle fully or partly equilibrated. It seems that the siderophile pattern of the mantle can be reproduced under non-equilibrium conditions assuming oxygen fugacity conditions higher than previously thought and embryos that have equilibrated at excessively high-temperatures (450 K above liquidus of chondritic mantle) (Rudge et al., 2010). In the following, since the disequilibrium core formation model creates more questions than answers, we will assume equilibrium core–mantle segregation at 45–50 GPa in agreement with metal–silicate partitioning experiments.

We report in Fig. 5 liquidus and solidus curves measured for a chondritic mantle superimposed with the adiabats for the liquid (Mosenfelder et al., 2009; Stixrude and Karki, 2005). Here we focus on isentropes calculated by Mosenfelder et al. (2009), based on their latest shock-wave equation of state (Eos) of molten $MgSiO_3$. Such liquid is comparable to the chondritic mantle composition used in this study that contains ~70 mol% $MgSiO_3$ end-member. In the classical model of equilibrium at the base of a magma ocean, it is implicitly assumed that equilibrium occurs at 45–50 GPa on the liquidus (e.g. (Wood et al., 2006)). According to our measurements of the liquidus, a fully molten chondritic mantle that would extend to a pressure of 45–50 (±10) GPa exhibits a temperature of ~3175 K (±250 K) at a depth of ~1175 (±250) km. Such conditions correspond to a surface potential temperature of 2450 K (±150 K) (See red curves in Fig. 5). Such a hot surface is not stable and is only compatible with a transient magma ocean. Indeed, it has been demonstrated that surface temperatures significantly higher than 1700–1800 K prevent formation of an ($H_2O$–$CO_2$)-rich atmosphere required to produce an efficient thermal blanket to the magma ocean. Without such blanketing the magma ocean will cool down very rapidly (Abe and

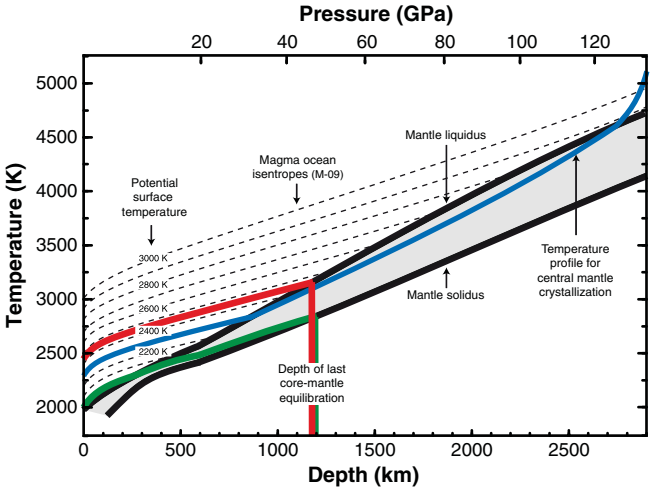


**Fig. 5.** The melting curves of synthetic chondritic mantle plotted together with isentropic temperature profiles of the magma ocean calculated for different potential surface temperatures (Mosenfelder et al., 2009). Metal–silicate partitioning coefficients determined experimentally evidence that core–mantle segregation occurred at a depth of ~1175 (±250) km. Such depth corresponds to a surface temperature of ~2000 K (green line) or 2450 K (red line) if this limit corresponds to solidus or liquidus temperature of the magma ocean, respectively. On the other hand, we propose a possible mantle geotherm (blue line) compatible with crystallization of the liquidus phase Mg–Pv at the center of the mantle.

Matsui, 1988; Zahnle et al., 1988). Indeed, above 1700–1800 K significant silicate vaporization occurs (Nagahara and Ozawa, 1996) and such rock vapor atmosphere conducts heat easily so that the magma ocean would cool down in a few thousand years, before the magma ocean surface temperature comes back to 1700–1800 K (Sleep et al., 2001). Note that only shallow magma oceans (shallower than 5 GPa) are consistent with surface temperatures of 1700–1800 K (Miller et al., 1991, see their Figure 8) and can survive for long periods.

On the other hand, Hf–W chronology indicates that ~80% of the core formed within the first 30 million years of the Earth's history (Kleine et al., 2002). As discussed above, deep magma ocean extending to 45–50 GPa pressure can only last for a few thousand years, and such time scale is radically different from that inferred from Hf–W isotopes. Thus, one must refine the scenario of core–mantle segregation in order to explain these apparent contradictions:

(a) If the metal droplets do not rain faster than the crystallization rate of the hot (transient) magma ocean (Rubie et al., 2003; Solomatov, 2000), they fall in the liquid mantle to intermediate depth until the silicate phases crystallize. Then, the metal remains embedded in the solid mantle until the next melting event. We note here that the descent of iron droplets is intrinsically associated with heat production by release of gravitational energy. Thus, in order to stop the Fe rain, the heat flux at the Earth's surface should be higher than the gravitational energy release. The droplet can also descend slowly by percolative flow (Yoshino et al., 2003). In this scenario (Fig. 6A), the equilibrium pressure of 45–50 GPa corresponds to the mean extension depth of the last magma ocean before the Fe droplets coalence into larger diapirs and fall into the core.

(b) A second possible scenario involves a magma ocean defined by its solidus located at ~1175 km depth (45–50 GPa) (Fig. 6B). From the base of this magma ocean upwards, coexistence of solid and melt is expected to occur over a broad depth interval due (i) to the large temperature difference between solidus and liquidus (Fig. 5) and (ii) to the fact that the adiabats of partially molten mantle are sub-parallel to the liquidus (Miller et al., 1991). It follows that this magma ocean is on its liquidus at depth close to 300–400 km. As a consequence, the melt adiabats indicate a surface temperature approaching 2000 K, compatible with a blanketed magma ocean, which would thus cool down slowly. In this situation, the metal rains and equilibrates in a mush rather than in a completely molten magma ocean.

### 4.4. Formation of a basal magma ocean?

Finally, our new melting curve can be used to discuss the possible existence of an ancient magma ocean starting its crystallization in the mid-lower mantle, with formation of a basal magma ocean (Labrosse et al., 2007). First, we should note that complete melting of the Earth mantle implies a surface temperature higher than 2800 K (Fig. 5), which is much above the vaporization temperature of the silicate mantle (Nagahara and Ozawa, 1996). Thus, cooling and crystallization of the mantle should occur very quickly, as discussed in the previous paragraph. In addition, this scenario implies temperatures higher than the liquidus in both the shallow and lowermost mantle, and temperatures becoming lower than the liquidus at intermediate depth due to secular cooling. Such a temperature profile requires a very hot core in order to induce a geotherm steeper than the liquidus in the lowermost mantle (see blue curve in Fig. 5). However, such temperature gradient is unlikely to be relevant to the primitive Earth for a long time. High thermal conductivities expected for both the liquid in the D″-layer and the partial melt at mid mantle depth should help to propagate heat from the CMB to shallower mantle depth and resolve a potential steep temperature gradient in the lowermost mantle. Therefore, it appears unlikely that the outer core temperature could exceed 4725 K at the CMB after crystallization of the magma ocean.

In the context of a complete (or almost complete) melting of the mantle, it is unlikely that the temperature profile could reach the solidus in the mid-lower mantle given (i) the large temperature difference found between solidus and liquidus temperatures; (ii) the fact that the solidus and liquidus are almost straight curves that remain steep at CMB conditions; and (iii) because the isentropes of partially molten mantle are steeper than melt adiabats (Fig. 5). Due to the later effect, it was argued that the partially molten mantle could extend up to the core mantle boundary when the depth of a completely molten mantle extends to a pressure of more than 40 GPa (Kojitani and Akaogi, 1997; Miller et al., 1991; Stixrude et al., 2009). Therefore, the mantle fraction defined as “solid mantle” by (Labrosse

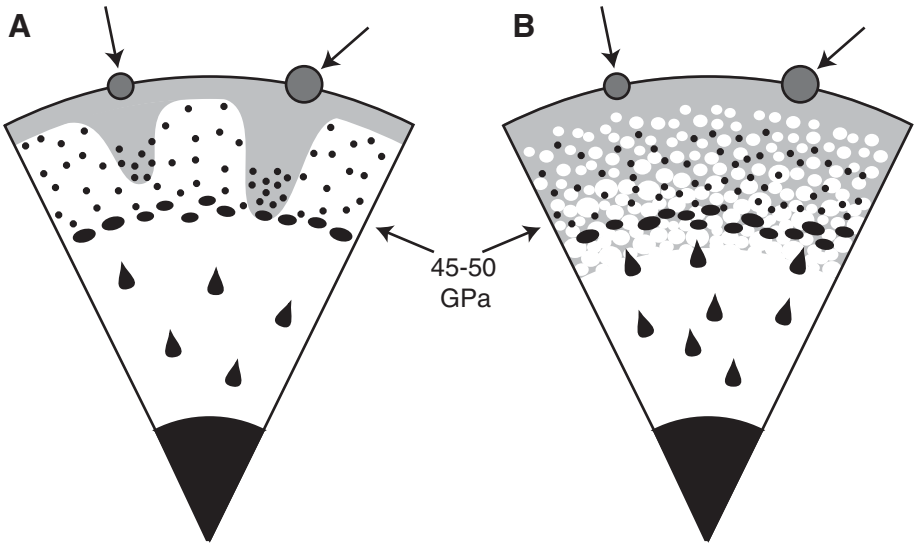


**Fig. 6.** Models for core–mantle segregation that respect (i) an equilibrium pressure of 45–50 GPa as suggested by metal–silicate partitioning experiments and (ii) a shallow completely molten magma ocean that can be compatible with a moderate surface temperature. In model (A) representative of transient magma oceans cooling very fast, the metal droplets remain embedded in the solid mantle and their progression to greater depths is aided by successive melting events. In model (B) representative of a sustained magma ocean cooling slowly, metal droplets fall in a partially molten mantle until the fraction of solid mantle becomes too high, at temperatures close to the solidus.

et al., 2007) could only correspond to a partially crystallized mantle, where the solid phase would essentially be the liquidus phase i.e. Mg–Pv (Fig. 1 and (Ito et al., 2004)). If crystallization of the magma ocean from the middle is associated to formation of a perovskitic layer, geochemical arguments constrain it to be at most 13% of the whole mantle, a minimum for which the upper mantle refractory elements budget still remains chondritic (Liebske et al., 2005).

Alternatively, a basal magma ocean could be possible if its composition is enriched in incompatible (i.e. fusible) elements, which would facilitate melting at lower temperatures at the base of the mantle. The persistence of such fusible material until today would be compatible with the observation of ULVZ, as mentioned in a previous paragraph. It could also explain major geochemical signatures, such as the one associated to "primitive mantle" with high $^3$He, for example (Allègre et al., 1995; Kurz et al., 1982).

## 5. Conclusions

We have determined the solidus and liquidus curves of a chondritic mantle up to CMB pressures. Our melting criteria include in-situ X-ray diffraction and temperature–power relationships. We confirm that the $MgSiO_3$-bearing perovskite is the liquidus phase in the deep lower mantle. The solidus melting curve is found at lower temperature than reported previously, especially at mid-lower mantle depth, while the liquidus is found at significantly higher temperatures at all mantle depths. At the CMB, we report solidus and liquidus melting at $4150 \pm 150$ K and $4725 \pm 150$ K, respectively.

We then discussed the geophysical implications of the new melting curve for chondritic mantle. First, it appears unlikely that the ULVZ, which is interpreted to experience ~20% partial melting, is of chondritic (or pyrolitic) composition. Indeed, the solidus of $4150 \pm 150$ K appears to be too high compared to estimates of the temperature profile in the D″ region, except if the core is extremely hot. Thus, in order to be explained by melting the ULVZ should rather be associated to high concentration of fusible elements that decrease the melting point compared to the chondritic mantle.

We also show that the pressure of 45–50 GPa typical of metal–silicate equilibrium, as reported by several experimental studies in the context of core–mantle segregation, is associated to a magma ocean surface temperature incompatible with a sustained magma ocean. It strongly suggests that the metal–silicate equilibrium occurred in a partially molten mantle, covered by a fully molten magma ocean much thinner than 1000 km.

Finally, by examining the relationships between magma ocean temperatures at depth and potential surface temperatures, our melting diagram is compatible with the formation of a basal magma ocean only if the middle-depth solid mantle is mainly composed of Al-bearing (Mg, Fe)$SiO_3$-perovskite and if the basal magma ocean has a chemical composition significantly different than the chondritic mantle.

## Acknowledgments

We thank N. Guignot, T. Hammouda, J.P. Perrillat and S. Petitgirard for participation to some experiments, S. Labrosse and H. Martin for fruitful discussions, and Paul Asimow for a fruitful review. This work is supported by Région Auvergne, INSU-CNRS, FEDER and the European C2C program.

## References

Abe, Y., Matsui, T., 1988. Evolution of an impact-generated $H_2O$–$CO_2$ atmosphere and formation of a hot proto-ocean on Earth. J. Atmos. Sci. 45, 3081–3101.
Alfe, D., 2009. Temperature of the inner-core boundary of the Earth: melting of iron at high pressure from first-principles coexistence simulations. Phys. Rev. B 79.
Allègre, C.J., Moreira, M., Staudacher, T., 1995. $^4$He/$^3$He dispersion and mantle convection. Geophys. Res. Lett. 22, 2325–2328.
Andrault, D., 2001. Evaluation of (Mg, Fe) partitioning between perovskite and magnesiowustite up to 120 GPa. J. Geophys. Res. 106, 2079–2087.
Andrault, D., Fiquet, G., Itié, J.P., Richet, P., Gillet, P., Häusermann, D., Hanfland, M., 1998. Thermal pressure in a laser-heated diamond-anvil cell: an X-ray diffraction study. Eur. J. Mineral. 10, 931–940.
Andrault, D., Morard, G., Bolfan-Casanova, N., Ohtaka, O., Fukui, H., Arima, H., Guignot, N., Funakoshi, K., Lazor, P., Mezouar, M., 2006. Study of partial melting at high pressure using *in situ* X-ray diffraction. High Pressure Res. 26, 267–276.
Andrault, D., Munoz, M., Bolfan-Casanova, N., Guignot, N., Perrillat, J.P., Aquilanti, G., Pascarelli, S., 2010. Experimental evidence for perovskite and post-perovskite coexistence throughout the whole D″ region. Earth Planet. Sci. 293, 90–96.
Asanuma, H., Ohtani, E., Sakai, T., Terasaki, H., Kamada, S., Kondo, T., Kikegawa, T., 2010. Melting of iron–silicon alloy up to the core–mantle boundary pressure: implications to the thermal structure of the Earth's core. Phys. Chem. Miner. 37, 353–359.
Asimow, P.D., Hirschmann, M.M., Stolper, E.M., 1997. An analysis of variations in isentropic melt productivity. Philos. Trans. R. Soc. Lond. 355, 255–281.
Badro, J., Fiquet, G., Guyot, F., Gregoryanz, E., Occelli, F., Antonangeli, D., d'Astuto, M., 2007. Effect of light elements on the sound velocities in solid iron: implications for the composition of Earth's core. Earth Planet. Sci. 254, 233–238.
Benedetti, R., Loubeyre, P., 2004. Temperature gradients, wavelength-dependent emissivity, and accuracy of high and very-high temperatures measured in the laser heated diamond anvil cell. High Pressure Res. 24, 423–445.
Boehler, R., 1993. Temperatures in the Earth's core from melting-point measurements of iron at high static pressures. Nature 363, 534–536.
Boehler, R., 2000. High-pressure experiments and the phase diagram of lower mantle and core materials. Rev. Geophys. 38, 221–245.
Bolfan-Casanova, N., McCammon, C.A., Mackwell, S., 2006. Water in the transition zone and lower mantle minerals. In: Jacobsen, S.J., van der Lee, S. (Eds.), The Earth's Deep Water Cycle: Geophysical Monographs, AGU, pp. 57–68.
Bouhifd, M.A., Jephcoat, A.P., 2003. The effect of pressure on partitioning of Ni and Co between silicate and iron-rich metal liquids: a diamond anvil cell study. Earth Planet. Sci. 209, 245–255.
Brown, J.M., Shankland, T., 1981. Thermodynamic parameters in the Earth as determined from seismic profiles. Geophys. J. R. Astron. Soc. 66, 579–596.
Bunge, H.P., Ricard, Y., Matas, J., 2001. Non-adiabaticity in mantle convection. Geophys. Res. Lett. 28, 879–882.
Canup, R.M., 2008. Accretion of the Earth. Phil. Trans. R. Soc. A 366, 4061–4075.
Catalli, K., Shim, S.H., Prakapenka, V.B., 2009. Thickness and Clarpyron slope of the post-perovskite boundary. Nature 462, 782–785.
Chabot, N.L., Draper, D.S., Agee, C.B., 2005. Conditions of core formation in the Earth: constraints from nickel and cobalt partitioning. Geochim. Cosmochim. Acta 69, 2141–2151.
Corgne, A., Allan, N.L., Wood, B.J., 2003. Atomistic simulations of trace element incorporation into the large site of $MgSiO_3$ and $CaSiO_3$ perovskites. Phys. Earth Planet. Inter. 139, 113–127.
Cottrell, E., Walter, M.J., Walker, D., 2009. Metal–silicate partitioning of tungsten at high pressure and temperature: implications for equilibrium core formation in Earth. Earth Planet. Sci. 281, 275–287.
Dahl, T.W., Stevenson, D.J., 2010. Turbulent mixing of metal and silicate during planet accretion- and interpretation of the Hf–W chronometer. Earth Planet. Sci. 295, 177–186.
Dewaele, A., Mezouar, M., Guignot, N., Loubeyre, P., 2007. Melting of lead under high pressure studied using second-scale time-resolved X-ray diffraction. Phys. Rev. B 76, 144106.
Fiquet, G., Dewaele, A., Andrault, D., Kunz, M., Le Bihan, T., 2000. Thermoelastic properties and crystal structure of $MgSiO_3$ perovskite at lower mantle pressure and temperature conditions. Geophys. Res. Lett. 27, 21–24.
Hernlund, J.W., Thomas, C., Tackley, P.J., 2005. A doubling of the post-perovskite phase boundary and structure of the Earth's lowermost mantle. Nature 434, 882–886.
Hirose, K., Fei, Y., Ma, P., Mao, H.K., 1999. The fate of subducted basaltic crust in the Earth's lower mantle. Nature 397, 53–56.
Holland, K.G., Ahrens, T.J., 1997. Melting of (Mg, Fe)2SiO4 at the core–mantle boundary of the Earth. Science 275, 1623–1625.
Ito, E., Katsura, T., 1989. A temperature profile for the mantle transition zone. Geophys. Res. Lett. 16, 425–428.
Ito, E., Kubo, A., Katsura, T., Walter, M.J., 2004. Melting experiments of mantle materials under lower mantle conditions with implications for magma ocean differentiation. Phys. Earth Planet. Inter. 143–144, 397–406.
Kamada, S., Terasaki, H., Ohtani, E., Sakai, T., Kikegawa, T., Ohishi, Y., Hirao, N., Sata, N., Kondo, T., 2010. Phase relationships of the Fe–FeS system in conditions up to the Earth's outer core. Earth Planet. Sci. 294, 94–100.
Karato, S., Murthy, V.R., 1997. Core formation and chemical equilibrium in the Earth I. Physical considerations. Phys. Earth Planet. Inter. 100, 61–79.
Kleine, T., Munker, C., Mezger, K., Palme, H., 2002. Rapid accretion and early core formation on asteroids and the terrestrial planets from Hf–W chronometry. Nature 418, 952–955.
Kojitani, H., Akaogi, M., 1997. Melting enthalpies of mantle peridotite: calorimetric determinations in the system CaO–MgO–$Al_2O_3$–$SiO_2$ and application to magma generation. Earth Planet. Sci. 153, 209–222.
Kurz, M.D., Jenkins, W.J., Hart, S.R., 1982. Helium isotopic systematics of oceanic islands and mantle heterogeneity. Nature 297, 43–47.
Labrosse, S., Poirier, J.P., Le Mouël, J.L., 1997. On cooling of the Earth's core. Phys. Earth Planet. Inter. 99, 1–17.
Labrosse, S., Hernlund, J.W., Coltice, N., 2007. A crystallizing dense magma ocean at the base of the Earth's mantle. Nature 450, 866–869.
Lauterbach, S., McCammon, C.A., van Aken, P., Langenhorst, F., Seifert, F., 2000. Mössbauer and ELNES spectroscopy of (Mg, Fe)(Si, Al)O3 perovskite: a highly oxidized component of the lower mantle. Contrib. Mineral. Petrol. 138, 17–26.

Lay, T., Williams, Q., Garnero, E.J., 1998. The core–mantle boundary layer and deep Earth dynamics. Nature 392, 461–468.
Lay, T., Garnero, E.J., Williams, Q., 2004. Partial melting in a thermo-chemical boundary layer at the base of the mantle. Phys. Earth Planet. Inter. 146, 441–467.
Li, J., Agee, C.B., 1996. Geochemistry of mantle–core differentiation at high pressure. Nature 381, 686–689.
Liebske, C., Corgne, A., Frost, D.J., Rubie, D.C., Wood, B.J., 2005. Compositional effects on element partitioning between Mg-silicate perovskite and silicate melts. Contrib. Mineral. Petrol. 149.
Litasov, K., Ohtani, E., 2002. Phase relations and melt compositions in CMAS–pyrolite–$H_2O$ system up to 25 GPa. Phys. Earth Planet. Inter. 134, 105–127.
Luo, S.N., Akins, J.A., Ahrens, T.J., Asimow, P.D., 2004. Shock-compressed $MgSiO_3$ glass, enstatite, olivine, and quartz: optical emission, temperatures, and melting. J. Geophys. Res. Solid Earth 109.
Matas, J., Bass, J.D., Ricard, Y., Mattern, E., Bukowinsky, M.S., 2007. On the bulk composition of the lower mantle: predictions and limitations from generalized inversion of radial seismic profiles. Geophys. J. Int. 170, 764–780.
Mezouar, M., Crichton, W.A., Bauchau, S., Thurel, F., Witsch, H., Torrecillas, F., Blattmann, S., Marion, P., Dabin, Y., Chavanne, J., Hignette, O., Morawe, C., Borel, C., 2005. Development of a new state-of-the-art beamline optimized for monochromatic single-crystal and powder X-ray diffraction under extreme conditions at the ESRF. J. Synchrotron Radiat. 12, 559–664.
Miller, G.H., Stolper, E.M., Ahrens, T.J., 1991. The equation of state of a molten komatiite 2. Application to komatiite petrogenesis and the Hadean mantle. J. Geophys. Res. 96, 11,849–11,864.
Mosenfelder, J.L., Asimow, P.D., Frost, D.J., Rubie, D.C., Ahrens, T.J., 2009. The $MgSiO_3$ system at high pressure: thermodynamic properties of perovskite, postperovskite, and melt from global inversion of shock and static compression data. J. Geophys. Res. 114, B01203.
Murakami, M., Hirose, K., Kawamura, K., Sata, N., Ohishi, Y., 2004. Post-perovskite phase transition in $MgSiO_3$. Science 304, 855–858.
Nagahara, H., Ozawa, K., 1996. Evaporation of forsterite in H-2 gas. Geochim. Cosmochim. Acta 60, 1445–1459.
Nguyen, J.H., Holmes, N.C., 2004. Melting of iron at the physical conditions of the Earth's core. Nature 427, 339–342.
Nishio-Hamane, D., Seto, Y., Nagai, T., Fujino, K., 2007. Ferric iron and aluminum partitioning between $MgSiO_3$ and $CaSiO_3$ perovskites under oxydizing conditions. J. Mineral. Petrol. Sci. 102, 291–297.
Oganov, A.R., Ono, S., 2004. Theoretical and experimental evidence for a post-perovskite phase of $MgSiO_3$ in the Earth's D″ layer. Nature 430, 445–448.
Poirier, J.P., 1994. Light elements in the Earth's outer core: a critical review. Phys. Earth Planet. Inter. 85, 319–337.
Righter, K., Drake, M.J., Yaxley, G., 1997. Prediction of siderophile element metal–silicate partition coefficients to 20 GPa and 2800 °C: the effects of pressure, temperature, oxygen fugacity and silicate and metallic melt compositions. Phys. Earth Planet. Inter. 100, 115–134.
Ringwood, A.E., 1975. Pyrolite and the chondritic Earth model. In: GrawHill, M. (Ed.), International series in the Earth's and Planetary Sciences, pp. 189–194.
Rubie, D.C., Melosh, H.J., Reid, J.E., Liebske, C., Righter, K., 2003. Mechanism of metal–silicate equilibration in the terrestrial magma ocean. Earth Planet. Sci. 205, 239–255.
Rubie, D.C., Gessmann, C.K., Frost, D.J., 2004. Partitioning of oxygen during core formation on the Earth and Mars. Nature 429, 58–62.
Rudge, J.F., Kleine, T., Bourdon, B., 2010. Broad bounds on Earth's accretion and core formation constrained by geochemical models. Nat. Geosci. 3, 439–443.
Sata, N., Shen, G., Rivers, M.L., Sutton, S.R., 2002. Pressure–volume equation of state of the high-pressure B2 phase of NaCl. Phys. Rev. B 65, 114114–114117.
Shen, G., Prakapenka, V.B., Rivers, M.L., Sutton, S.R., 2004. Structure of liquid iron up to 58 GPa. Phys. Rev. Lett. 92, 185701.
Shim, S.H., Duffy, T.S., Shen, G., 2000. The equation of state of $CaSiO_3$ perovskite to 108 GPa at 300 K. Phys. Earth Planet. Inter. 120, 327–338.
Simon, F., Glatzel, G., 1929. Fusion–pressure curve. Z. Anorg. Allg. Chem. 178, 309–316.
Sleep, N.H., Zahnle, K.J., Neuhoff, P.S., 2001. Initiation of clement surface conditions on the earliest Earth. Proc. Natl. Acad. Sci. 98, 3666–3672.
Solomatov, V.S., 2000. Fluid dynamics of terrestrial magma ocean. In: Canup, R.M., Righter, K. (Eds.), Origin of the Earth and Moon. The University of Arizona Press, Tucson, Arizona, pp. 323–338.
Stacey, F.D., Davis, P.M., 2004. High pressure equations of state with applications to the lower mantle and core. Phys. Earth Planet. Inter. 142, 137–184.
Stevenson, D.J., 1990. Fluid dynamics of core formation. In: Newsom, H., Jones, J.H. (Eds.), The Origin of the Earth. Oxford Press, London, pp. 231–249.
Stixrude, L., Karki, B.B., 2005. Structure and freezing of $MgSiO_3$ liquid in the Earth's lower mantle. Science 310, 297–299.
Stixrude, L., de Koker, N., Sun, N., Mookherjee, M., Karki, B.B., 2009. Thermodynamics of silicate liquids in the deep Earth. Earth Planet. Sci. 278, 226–232.
Tateno, S., Hirose, K., Sata, N., Ohishi, Y., 2009. Determination of post-perovskite phase transition boundary up to 4400 K and implications for thermal structure in D″ layer. Earth Planet. Sci. 277, 130–136.
Tonks, W.B., Melosh, H.J., 1993. Magma ocean formation due to giant impacts. J. Geophys. Res-Planet 98, 5319–5333.
Tronnes, R.G., Frost, D.J., 2002. Peridotite melting and mineral–melt partitioning of major and minor elements at 22–24.5 GPa. Earth Planet. Sci. 197, 117–131.
Walker, D., Cranswick, L.M.D., Verma, P.K., Clark, S.M., Buhre, S., 2002. Thermal equations of state for B1 and B2 KCl. Am. Mineral. 87, 805–812.
Wasson, J.T., Kallemeyn, G.W., 1988. Composition of chondrites. Philos. Trans. R. Soc. Lond. A325, 535–544.
Wen, L., Helmberger, D.V., 1998. Ultra-low velocity zones near the core–mantle boundary from broadband PKP precursors. Science 279, 1701–1703.
Williams, Q., Jeanloz, R., Bass, J., Svendsen, B., Ahrens, T.J., 1987. The melting curve of iron to 250 GPa — a constraint on the temperature at earths center. Science 236, 181–182.
Wood, B.J., Walter, M.J., Wade, J., 2006. Accretion of the Earth and segregation of its core. Nature 441, 825–832.
Yamazaki, D., Kato, T., Ohtani, E., Toriumi, M., 1996. Grain growth rates of $MgSiO_3$ perovskite and periclase under lower mantle conditions. Science 274, 2052–2054.
Yoshino, T., Walter, M.J., Katsura, T., 2003. Core formation in planetesimals triggered by permeable flow. Nature 422, 154–157.
Zahnle, K.J., Kastings, J.F., Pollack, J.B., 1988. Evolution of a steam atmosphere during Earth's accretion. Icarus 74, 62–97.
Zerr, A., Diegeler, A., Boehler, R., 1998. Solidus of earth's mantle. Science 281, 243–246.